MASSACHUSETTS INSTITUTE OF TECHNOLOGY

DEPARTMENT OF NUCLEAR ENGINEERING

Cambridge, Massachusetts

THE REACTOR PHYSICS OF THE MASSACHUSETTS INSTITUTE OF TECHNOLOGY REACTOR REDESIGN

by

A. K. Addae, D. D. Lanning, and T. J. Thompson

August, 1970

MITNE - 118

MASSACHUSETTS INSTITUTE OF TECHNOLOGY

DEPARTMENT OF NUCLEAR ENGINEERING

Cambridge, Massachusetts

THE REACTOR PHYSICS OF THE MASSACHUSETTS INSTITUTE OF TECHNOLOGY REACTOR REDESIGN

by

A. K. Addae, D. D. Lanning, and T. J. Thompson

August, 1970

MITNE - 118

THE REACTOR PHYSICS OF THE MIT REACTOR REDESIGN

ABSTRACT:

An H_2O cooled compact MITR-II core, reflected by D_2O, has been designed for the MITR to increase the reflector thermal neutron flux at tips of beam ports by a factor of 3 or better, without changing the operating power level of the reactor.

The diffusion approximation to the neutron transport equation has been used. A three neutron energy group scheme, that retains essential spatial effects, used in the studies has yielded satisfactory agreement with measured data.

The factors which affect the intensity as well as the quality of the reflector thermal neutron flux have been studied. These studies show that the permanent features of the MITR limit the maximum power densities in the MITR-II core to factors between 4.5 and 12 below the corresponding values in reactors employing a similar core concept

Nevertheless, the predicted unperturbed reflector thermal neutron flux of $1.1X10^{14}$ n/cm^2-sec in MITR-II yields a reflector flux per unit power that is competitive with the corresponding values available in reactors of its type and a factor of 5.0 higher than that in MITR-I.

Acknowledgments

Essentially the same material has been submitted by the principal author, A.K. Addae, in partial fulfillment of the requirements for the degree of doctor of science at the Massachusetts Institute of Technology.

The author thanks Dr. Theos. J. Thompson for his assistance and guidance as the first supervisor of this work. He also expresses his appreciation to Dr. David D. Lanning who became in charge of the redesign project as well as the supervisor of this thesis when Dr. Thompson was appointed a member of the U.S. Atomic Energy Commission in the summer of 1969. Thanks are also due to Dr. A. F. Henry for many invaluable suggestions regarding the computational methods.

The author is also grateful for the cooperation he has enjoyed from the members of the MIT Reactor Redesign group, and in particular for helpful suggestions and encouragement he has received from Dr. J. W. Gosnell, Mr. E. Barnet and Mr. D. Gwinn of this group. He also thanks Dr. N. C. Rasmussen, the thesis reader, for helpful suggestions in the writing of the manuscript.

The typing was done by Mrs. Carol Lindop, and the drawings by Mr. Leonard Andenler. Their assistance is appreciated. Thanks are also due to my wife for her assistance in preparing the final manuscript.

The computations for this thesis have been done in part at the MIT Information Processing Center on the IBM Operating System 360/65.

Table of Contents

Chapter VIII (Continued)

Appendix C (Continued)

List of Tables

List of Figures

CHAPTER I

INTRODUCTION

On July 20, 1969, the Massachusetts Institute of Technology Reactor (MITR-I) had been in power operation for ten years. During this period, it had served as a center of research and education for many of the departments of MIT and also supported medical and industrial research in the Greater Boston area.

Since MITR-I has been used primarily as a source of neutrons, its usefulness as a research tool will be greatly enhanced if the thermal neutron fluxes available in its experimental facilities can be improved. On this basis, it has now been proposed that the MITR be shut down for modifications that will permit the introduction of a new type of core designed to produce more intense thermal neutron fluxes with reduced fast neutron and gamma radiation background in the MITR experimental facilities, without altering the operating power level of the reactor.

The purpose of this thesis is twofold: first, to examine the principal reactor physics parameters that effect the reflector thermal neutron flux in order to optimize both the quality and the intensity of the maximum thermal neutron flux in the reflector; and secondly, to determine the principal reactor physics characteristics of the redesigned core in sufficient detail to permit its construction. This optimization and design study has been made within the constraints

imposed by the permanent features of the present reactor.

The remainder of this chapter is devoted to a brief description of the parts of the present reactor to be affected by the modifications as well as the principal features of the redesigned reactor. In addition, a brief outline of the method of solution employed is given.

1.1 PRESENT MITR (MITR-I)

The present MITR, designed to operate at power levels up to five megawatts, is moderated and cooled by heavy water and utilizes curved plate-type fuel elements of highly enriched uranium-235.

The reactor core is contained in an aluminum tank that is four feet in diameter and seven feet high, and is surrounded by a graphite reflector which extends two feet in the radial direction. The vertical section through the present system of Fig. 1.1 shows the general arrangement of the reactor; and the horizontal section of Fig. 1.2 shows the arrangement of eleven horizontal experimental beam-ports whose tips view the core radially at the wall of the core tank and have their centerlines slightly below the core centerline.

1.1.1 Diffuse Arrangement of Fuel Inside the Core Tank.

The fuel elements are arranged in a widely spaced manner

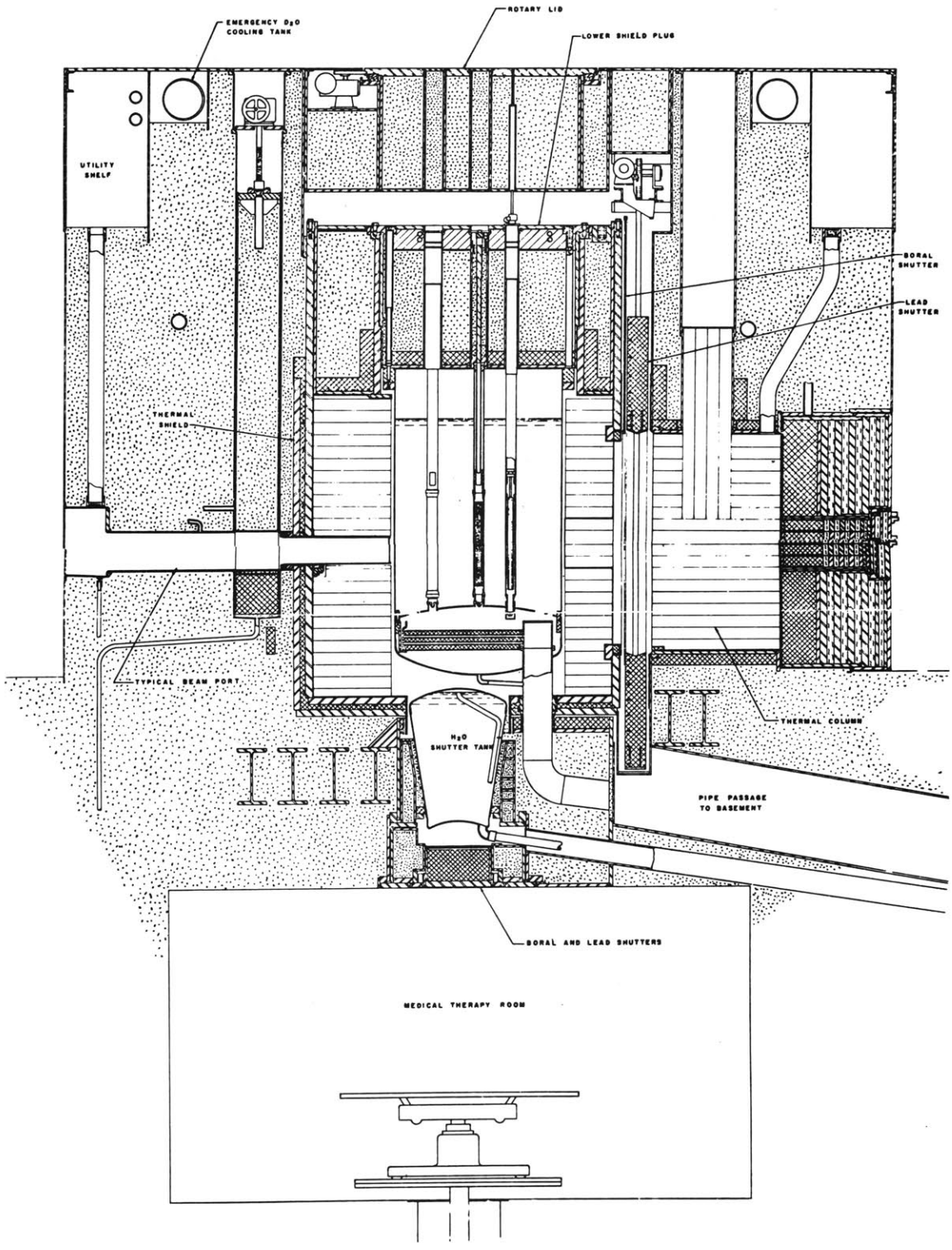

FIG. I.1 VERTICAL SECTION OF MITR-I

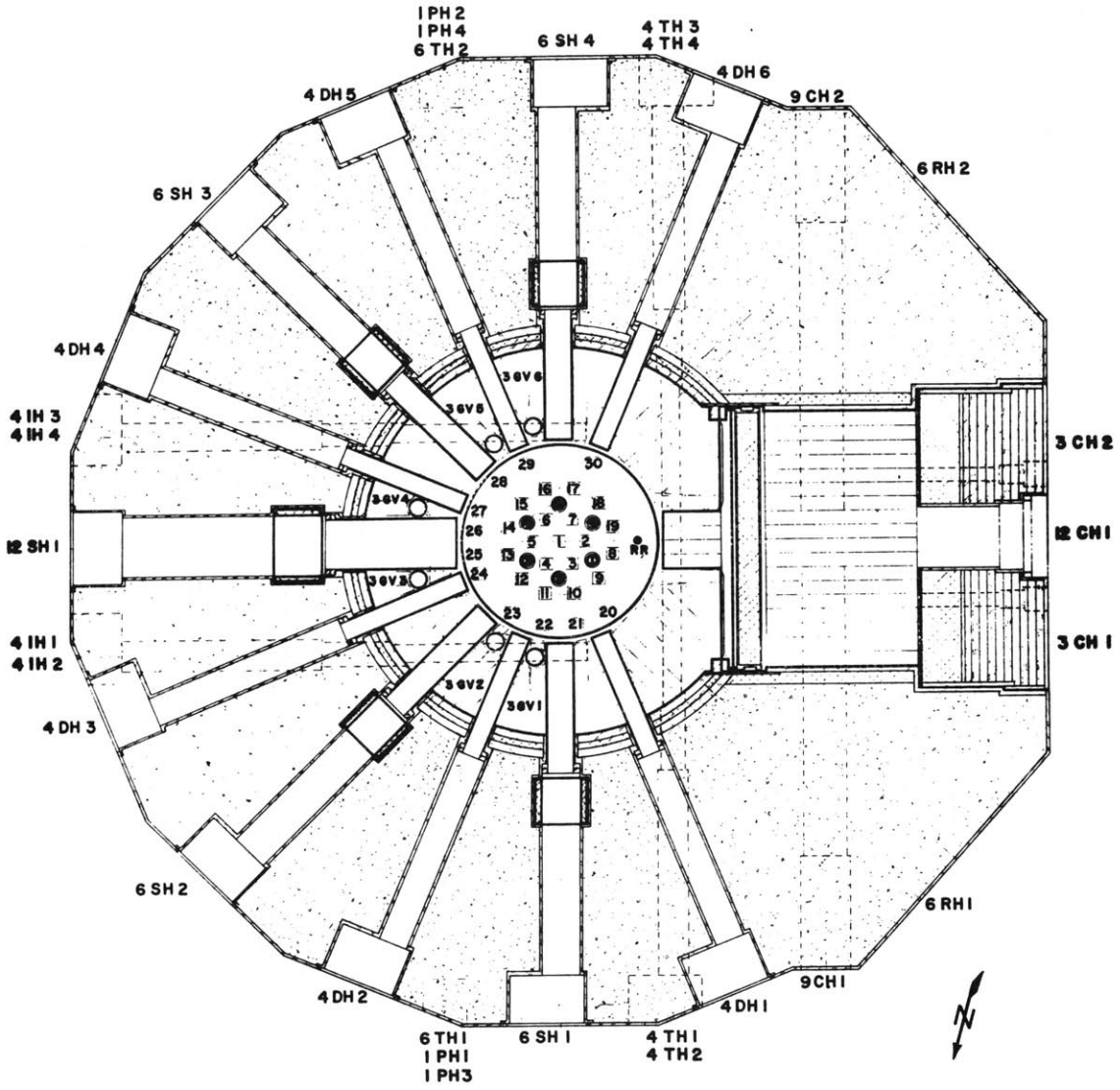

FIG. 1.2 HORIZONTAL SECTION OF MITR-1

inside the core tank. The central fuel element position is located at the radial center of the core tank; fuel element positions two through seven are equally spaced on a circle of 6.375 inches radius; fuel element positions eight through nineteen are equally spaced on a circle of 13.25 inches radius. Fuel element positions twenty through thirty are irregularly spaced on 20.94 inches radius. Fuel element positions one through nineteen constitute the normal loading for the operation of the reactor.

In addition to the fuel elements, one regulating rod and six shim safety rods are located inside the core tank. The six safety rods are arranged symmetrically on a circle of 9.25 inches radius; while the regulating rod is located at 19.5 inches radius on the inward projection of the thermal column centerline.

1.1.2 Thermal Flux Distribution.

The thermal flux distribution in the well moderated MITR core, with a widely spaced fuel arrangement, shows two important features. First, the local minimum thermal flux occurs inside an element, while the local maximum thermal flux occurs in the moderator surrounding that element. This feature is well illustrated on Fig. 1.3, which shows the thermal flux distribution in the present MITR, measured using foil activation techniques (28). The fuel, which absorbs thermal neutrons to produce fast neutrons, acts as a sink for the

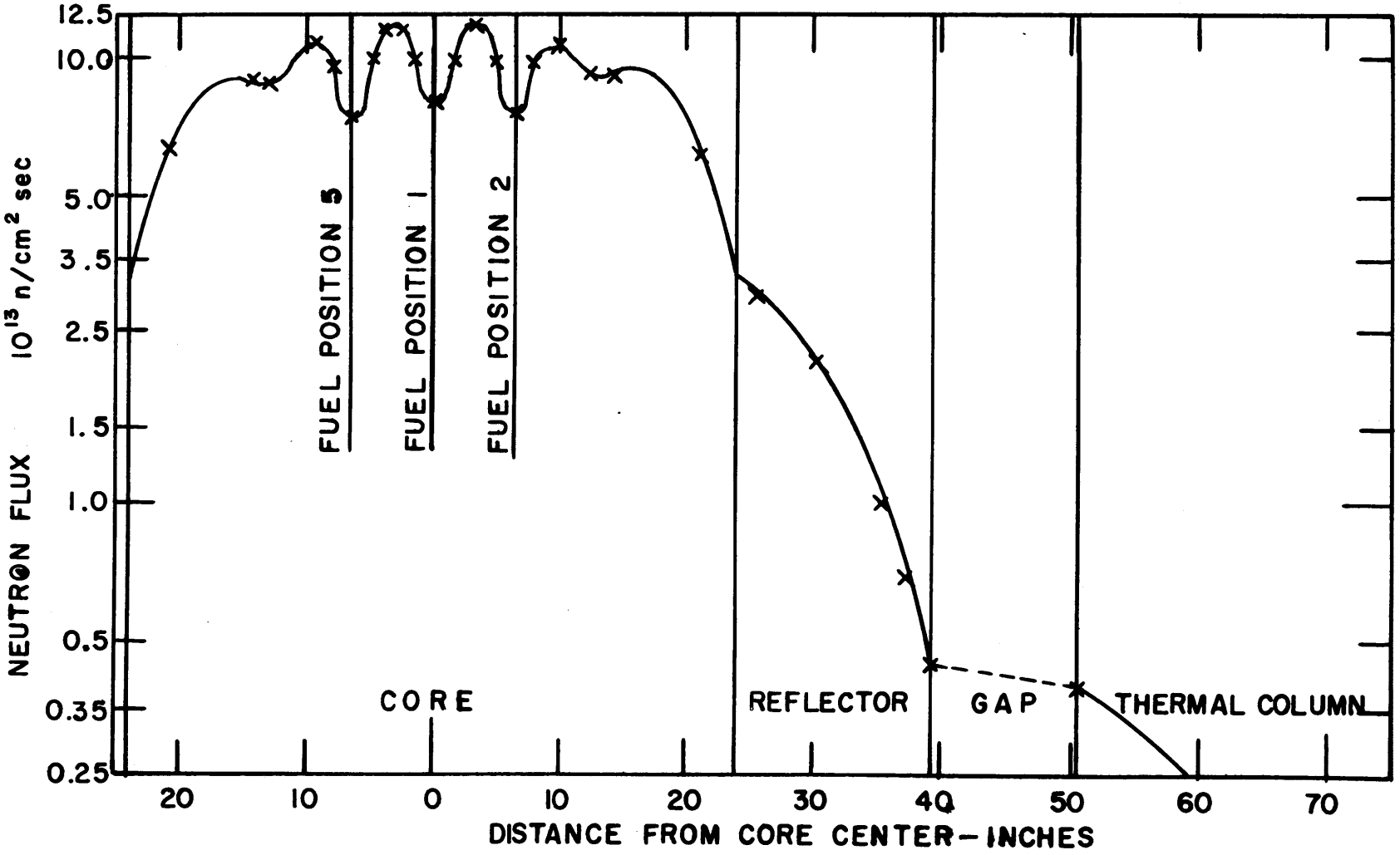

FIG. 1.3 MITR-I NEUTRON FLUX AT CORE AXIAL CENTERLINE THROUGH THE CORE AND THERMAL COLUMN AT 5.0 MW

thermal neutrons, whereas the surrounding moderator, which slows down and thermalizes the fast neutrons that leak from the fuel, act as a source of thermal neutrons.

The second important feature is that the maximum thermal neutron flux in this core occurs at the center of the core, where it is not available for out-of-core experimental facilities, because of the practical difficulties of making experimental beam-ports re-entrant into the core. A maximum thermal neutron flux of 1.2×10^{14} n/cm^2-sec is available at the center of the core, whereas only 2.2×10^{13} n/cm^2-sec is available at the wall of the tank, where the tips of experimental beam-ports view.

1.2 REDESIGNED MITR (MITR-II)

With reference to Fig. 1.1, the redesign of MITR has been limited to the region occupied by the aluminum core tank. In addition, the lower shield plug as well as the rotating plug above the core tank are to be removed and that region redesigned (2); the medical therapy room below it has also been redesigned (3).

1.2.1 Compact Arrangement of Fuel.

The fuel has been re-arranged to form a compact core of about 15 inches diameter surrounded by heavy water reflector. The proposed heavy water reflector tank is of the same

diameter (4 feet) as the present core tank. The experimental beam-ports have been made re-entrant into the heavy water tank. A horizontal section through the plane containing centerlines of beam-ports is shown in Fig. 1.4.

1.2.2 Advantages of the Compact Core Arrangement.

Re-arranging the fuel to form a compact core results in undermoderation of the core. A large fraction of the fission neutrons leak into the surrounding reflector, where they are thermalized. The undermoderated core, therefore, acts as a source of fast neutrons but as a sink for the thermal neutrons; whereas the reflector acts as a sink for the fast neutrons and as a source for the thermal neutrons. Consequently, the maximum fast flux region occurs in the center of the core, separated from the maximum thermal flux region which occurs in the reflector. The separation of the regions of maximum fast and thermal fluxes has two significant advantages.

First, the thermal to fast flux ratio, which is an important dimension of the quality of the thermal neutron fluxes available to the experimenter, is greatly improved in the reflector where thermal neutron beam is normally removed for experiments.

Secondly, the maximum thermal flux region, which occurs in the reflector instead of at the center of the core as it is in the present MITR, can be reached by re-entrant beam

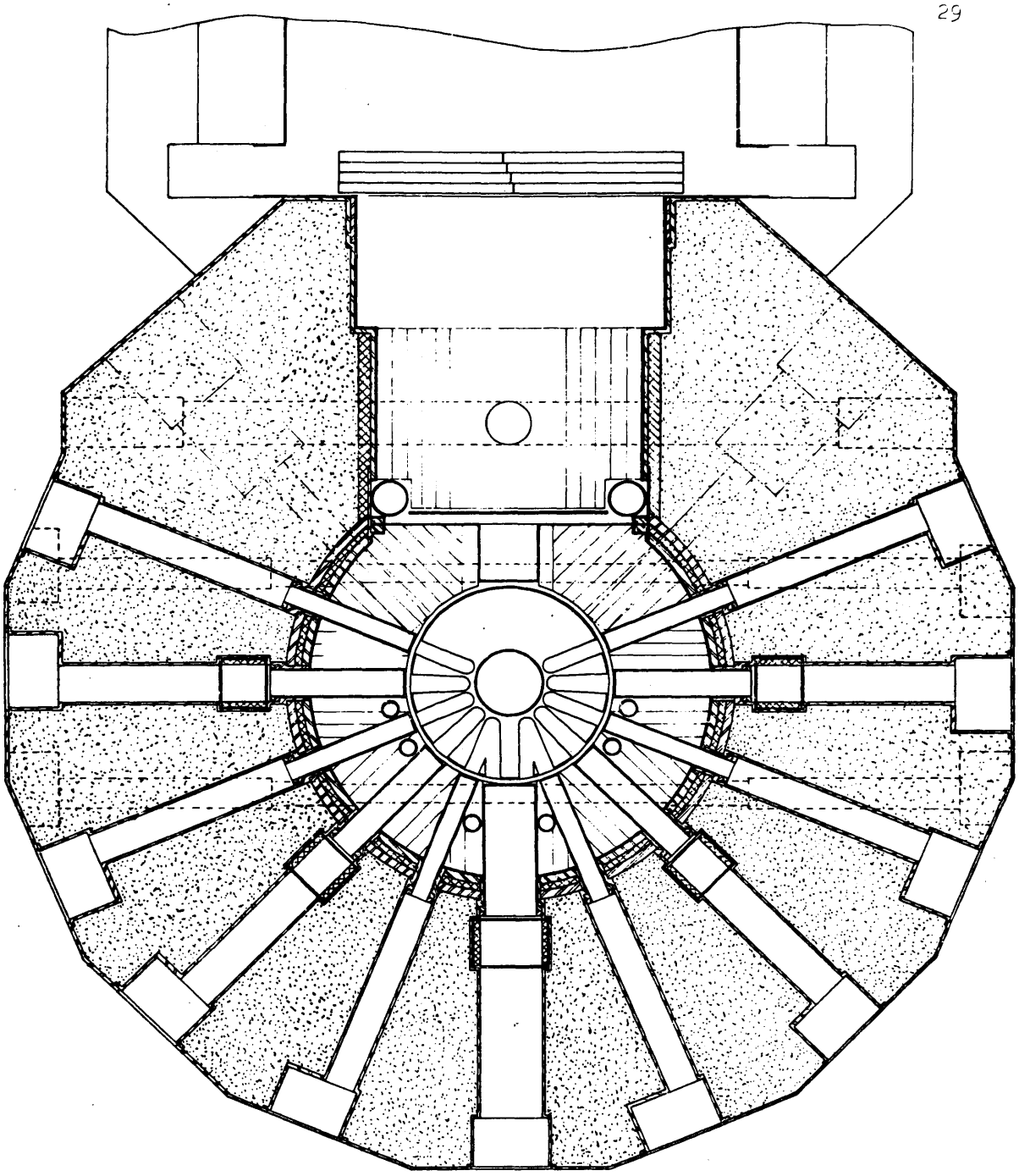

FIG. I.4 HORIZONTAL SECTION OF MITR – II

ports and extracted for experiments. In this way, the level of thermal neutron flux available to the experimenter can be significantly increased. Work to be discussed in later chapters show that the advantage of the redesign is derived from making the beam ports re-entrant into the heavy water tank. And this will result in an increase in the magnitude of the thermal neutron flux at the tips of beam ports by a factor of three or better, without altering the operating power level of the reactor.

1.2.3 Some Problems Inherent in the Redesign.

As the increase in the thermal neutron flux available to the experimenter in the redesigned MITR is derived from making the beam ports re-entrant into the heavy water tank, an optimum re-entrant beam port design is important. This problem was the subject of a doctoral thesis by Kennedy (4).

Regions of a compact core adjacent to the surrounding reflector present power peaking difficulties. Since a large fraction of the fission neutrons are slowed down external to the core, the fuel near the reflector-core interface sees a large re-entrant flux of thermal neutrons while fuel in the central region of the core sees a relatively weak flux of thermal neutrons. This results in a power peak region at the core-reflector interface. The larger the fraction of the fission neutrons that are slowed down external to the core, the higher the thermal neutron flux peak in the re-

flector. On the other hand, the more severe are the power peaking difficulties. High heat transfer rate in the power peak region will, therefore, enhance the reflector maximum thermal neutron flux level. The problem of augmenting the fuel plate heat transfer rate was the subject of other studies (5), (6); methods of reducing the power peaking difficulties without severely reducing the thermal neutron flux peak in the reflector are explored in this work.

1.3 REACTORS EMPLOYING THE COMPACT CORE CONCEPT

The Brookhaven High Flux Beam Research Reactor (HFBR) (7) is the first of the new generation of compact core reactors. Theoretical reactor physics studies on the HFBR started in 1956, and the reactor received its first loading of fuel in October, 1965 (8).

The HFBR, which operates at a nominal power of forty megawatts, is heavy water cooled, moderated and reflected. It uses curved-plate type fuel elements having fuel material made of fully enriched uranium alloyed in aluminum.

More than one thousand critical experiments were conducted to determine the detailed characteristics of HFBR. The theoretical reactor physics studies performed in support of these experiments employed the diffusion approximation to the transport equation in one dimensional spherical and cylindrical geometries. Experimental results were generally in good agreement with the predicted characteristics.

The Argonne Advanced Research Reactor (AARR) is the second of the compact core reactors (9)-(13). Although developmental work on the AARR reached an advanced stage, the design was changed in the 1966-67 fiscal year to make use of cores already being manufactured for the High Flux Isotope Reactor (HFIR) for budgetary reasons. Work on the AARR came to the attention of the author when the design of MITR was nearly complete. The geometry of the core radial section is hexagonal for both AARR and MITR-II; nevertheless, there are important differences between the two cores.

The AARR which is designed for a nominal power of 100 megawatts, has a central hexagonal thermal column, an annular fuel zone, and an external radial beryllium reflector. The core is cooled and moderated by light water, which also is the moderator in the central thermal column. Fuel assemblies are rhomboidal in radial section and consist of stainless steel-clad fuel-meat-matrix of stainless steel and UO_2 that is highly enriched in U-235. The fuel loading is graded, plate by plate, at the inner and outer hexagonal boundaries of the core to reduce power peaking difficulties.

Theoretical reactor physics studies for the AARR design employed the diffusion approximation to the transport equation in one and two dimensional cylindrical geometry. These calculations were generally in good agreement with the several critical assembly experiments which were made as a basis for the reactor physics design.

1.4 REACTOR PHYSICS DESIGN OF MITR-II

The reactor physics design of MITR-II has been based largely on theoretical studies, employing the diffusion approximation to the neutron transport equation in two space dimensional XY and RZ as well as three dimensional hexagonal geometries. Critical experiments are not envisaged as these will be both expensive and time consuming. For a thermal reactor, the diffusion approximation to the neutron transport equation often yields quite satisfactory agreement with experiment, provided the geometrical details can be treated conveniently by computation. Work discussed in Chapter 2 shows that the three energy group scheme used should indeed yield satisfactory results for redesigned MITR.

The details of the development of theory and computational techniques are discussed in Chapter 2. Chapters 3 through 6 relate to the study of the parameters that generally affect the quality and the level of the reflector maximum thermal neutron flux region; while Chapter 7 relates to the description of the arrangement of design base MITR-II core. Refinement of cross-section data showed that slight changes in core composition and dimensions were necessary. The characteristics of the resulting modified MITR-II core are discussed in Chapters 8 through 9. A comparison of selected characteristics of the present MITR-I core with redesigned MITR-II core constitutes the material for Chapter 10.

CHAPTER II
DEVELOPMENT OF THEORY AND COMPUTATIONAL TECHNIQUES

The reactor physics design of MITR has been based largely on theoretical studies employing the diffusion approximation to the transport equation. In this chapter, the computational techniques as well as the theory used in the different phases of the studies are discussed. Specifically, the problems discussed are:

2.1 The cross-section data employed

2.2 A comparison of the three group diffusion scheme with multigroup transport calculations

2.3 Method of homogenization of the core

2.4 A comparison of calculations with measured results

2.5 Method of representation of control rods

2.6 Computer codes used

2.1 CROSS-SECTION DATA

The basic cross-section data used is that of Hansen and Roach (14). The sixteen group set (14) as well as the modified twenty-three group set (15) were used. The energy structure of the sixteen and twenty-three energy group sets are shown in Tables 2.1 and 2.2 respectively.

The first fourteen energy groups, covering the energy range above 0.4 eV are identical on the two sets. As the energy range

TABLE 2.1

Sixteen Group Set

GROUP	ENERGY RANGE (eV)	VELOCITIES (CM/SHAKE)
1	10.0E+6 - 3.0E+6	28.5
2	3.0E+6 - 1.4E+6	19.9
3	1.4E+6 - 0.9E+6	14.7
4	0.9E+6 - 0.4E+6	11.0
5	0.4E+6 - 0.1E+6	6.7
6	0.1E+6 -17.0E+3	2.9
7	17.0E+3 - 3.0E+3	1.14
8	3.0E+3 - .55E+3	.48
9	.55E+3 - 100.0	.206
10	100.0 - 30.0	.101
11	30.0 - 10.0	.0566
12	10.0 - 3.0	.0319
13	3.0 - 1.0	.0179
14	1.0 - 0.40	.0109
15	0.40 - 0.10	.00606
16	0.10 - 0.001	.0022

TABLE 2.2

Twenty Three Group Set

GROUP	ENERGY RANGE (eV)	VELOCITIES (CM/SHAKE)
1	10.0E+6 - 3.0E+6	28.5
2	3.0E+6 - 1.4E+6	19.9
3	1.4E+6 - 0.9E+6	14.7
4	0.9E+6 - 0.4E+6	11.0
5	0.4E+6 - 0.1E+6	6.7
6	0.1E+6 - 17.0E+3	2.9
7	17.0E+3 - 3.0E+3	1.14
8	3.0E+3 - .55E+3	.48
9	550.0 -100.0	.206
10	100.0 - 30.0	.101
11	30.0 - 10.0	.0566
12	10.0 - 3.0	.0319
13	3.0 - 1.0	.0179
14	1.0 - 0.4	.0109
15	0.4 - 0.2	.00725
16	0.2 - 0.14	.00557
17	0.14 - 0.10	.00469
18	0.10 - 0.07	.00363
19	0.07 - 0.04	.00319
20	0.04 - 0.02	.00235
21	0.02 - 0.01	.00167
22	0.01 - 0.004	.00113
23	0.004 - 0.001	.00067

below 0.4 eV on the twenty-three set was divided into nine energy groups compared with two on the other set, the former was used primarily to study the effects of the different thermal cut-off energies discussed below in section 2.2.1.

The cross-section data for either lead or cadmium was not available from the above two sets. Those for lead were, therefore, collapsed from the twenty-six set of reference (16); while those of cadmium were collapsed from the six-hundred-and-forty energy group set of reference (17).

In the energy range above 1.0 eV, the diffusion length of neutrons were considered long enough so that the flux distribution would not be sensitive to the fine structure of material distribution in the core. Group macroscopic cross-sections for the unit cell in the core were computed, assuming the materials were homogeneously distributed. The exceptions were the fission and capture group cross-section for U-235 in the resonance region. Shielded cross-sections in the resonance region were computed, using figures 10 and 11 of reference (14).

In the energy range below 1.0 eV, the diffusion length of neutrons were of the same order as the thickness of fuel plates and hence self-shielding would be important. This energy range was treated by the integral neutron transport code, THERMOS (18), (19). The details of the procedure are discussed below in section 2.3.

The theoretical reactor physics studies reported by Brookhaven (7) and Argonne (12) employed energy groups of neutrons between five and sixteen. The need to represent the geometrical details in the present studies led to computations in two and three dimensions. Three energy groups of neutrons have been used in this work in order to save some computing time. For large water moderated thermal reactors, satisfactory results can often by obtained by using two, three, or four energy groups of neutrons (20).

Redesigned MITR is cooled by light water and reflected by heavy water. In addition, the light water coolant flows down the side of the core. A comparison of three group diffusion calculations with twenty-three group transport calculation was carried out, using spherical approximation of the core, to study the effects of thermal cut-off energy as well as the presence of the light water annulus outside the core.

2.2.1 Effect of Thermal Cut-Off Energy.

The spherical reactor model used had five regions and is shown in Fig. 2.1. Region one, the core, had the same material composition as MITR base core (defined in section 7.1). The radial dimensions as well as the materials of regions 3, 4, and 5 were the same as in the MITR base core.

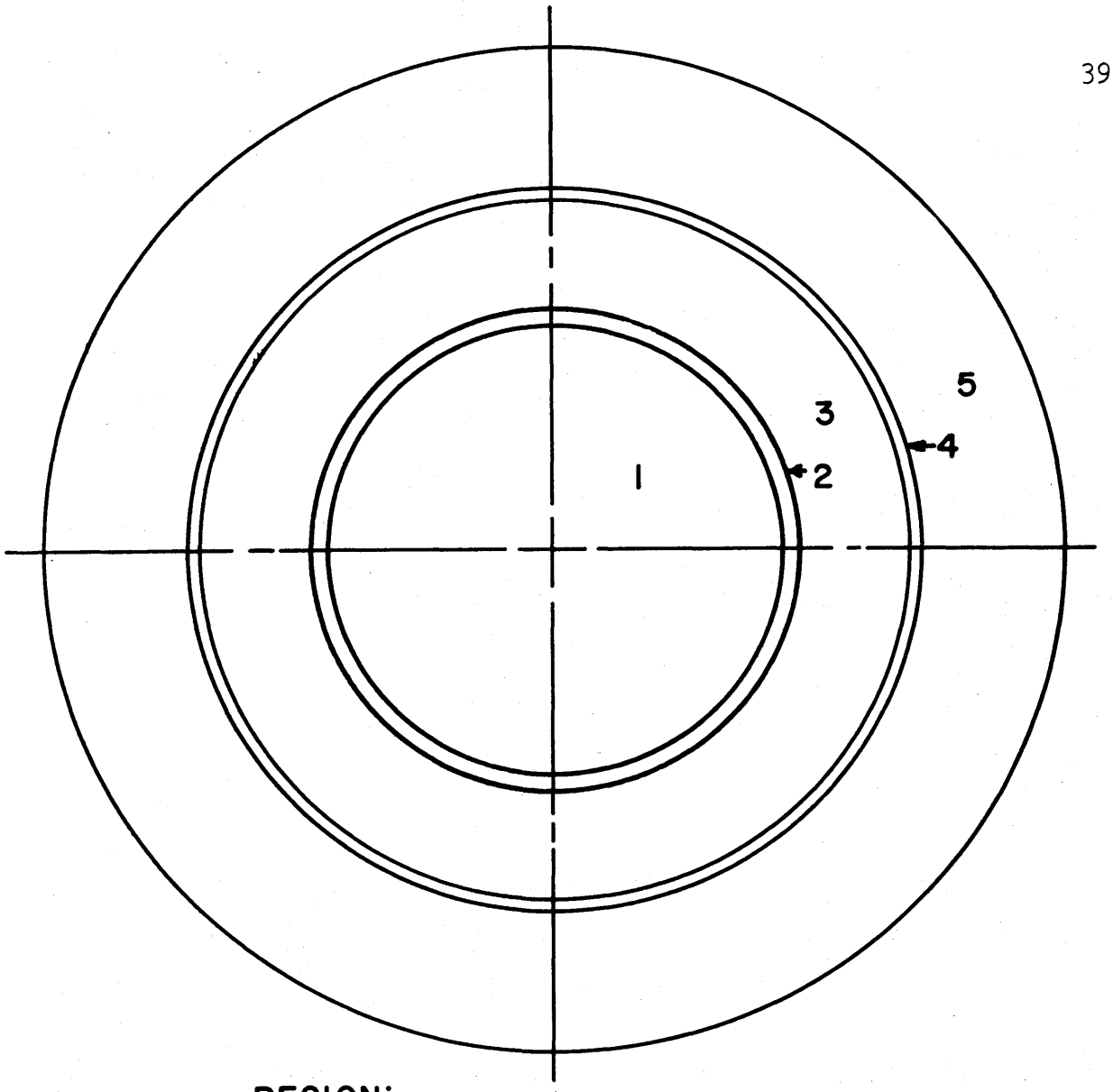

REGION:

1 CORE
2 ALUMINUM CORE TANK
3 HEAVY WATER REFLECTOR
4 HEAVY WATER TANK
5 GRAPHITE REFLECTOR

FIG. 2.1 5-REGION SPHERICAL REACTOR MODEL

The dimensions and composition of this spherical model of the core are given in Table 2.3.

The one dimensional discrete ordinate transport code, ANISN, described in section 2.6.1, was used. ANISN can also be used to make diffusion calculations with specified energy groups. The order of angular quadrature used for the transport solution was S8 with isotropic scattering.

The flux distribution in the core and part of the heavy water reflector for energy groups 1, 11, 16, and 23 are shown in Fig. 2.2 for 23 energy groups transport solution. In the high energy groups, such as groups 1 through 8, the flux level is nearly constant in the core but drops off very steeply in the reflector where neutrons are rapidly removed from these high energy groups due to slowing down.

In the epithermal region, such as groups 9 through 14, the flux level drops gently from the center of the core through the moderator. The net rate of removal of neutrons from the epithermal range is thus not markedly increased in the moderator compared to that in the core.

In the thermal energy region, such as groups 15 through 23, the flux distribution is in direct contrast to that of the fast energy region. The thermal flux level peaks in the reflector, where the slowing down source into this energy range is maximum; the flux level drops steeply at the edge of the core and remains nearly constant in the core. This contrast in the flux distribution in the fast and thermal energies is to be expected since an undermoderated core acts

TABLE 2.3

5-Region Core Model Data

Material Number Densities in Region One

U-235	2.498×10^{20}
U-238	1.880×10^{19}
Light Water	1.535×10^{22}
Aluminum	3.195×10^{22}

Outer Radii of Regions

Region	Outer Radius
1	14.03 cm.
2	16.15 cm.
3	52.91 cm.
4	57.82 cm.
5	123.82 cm.

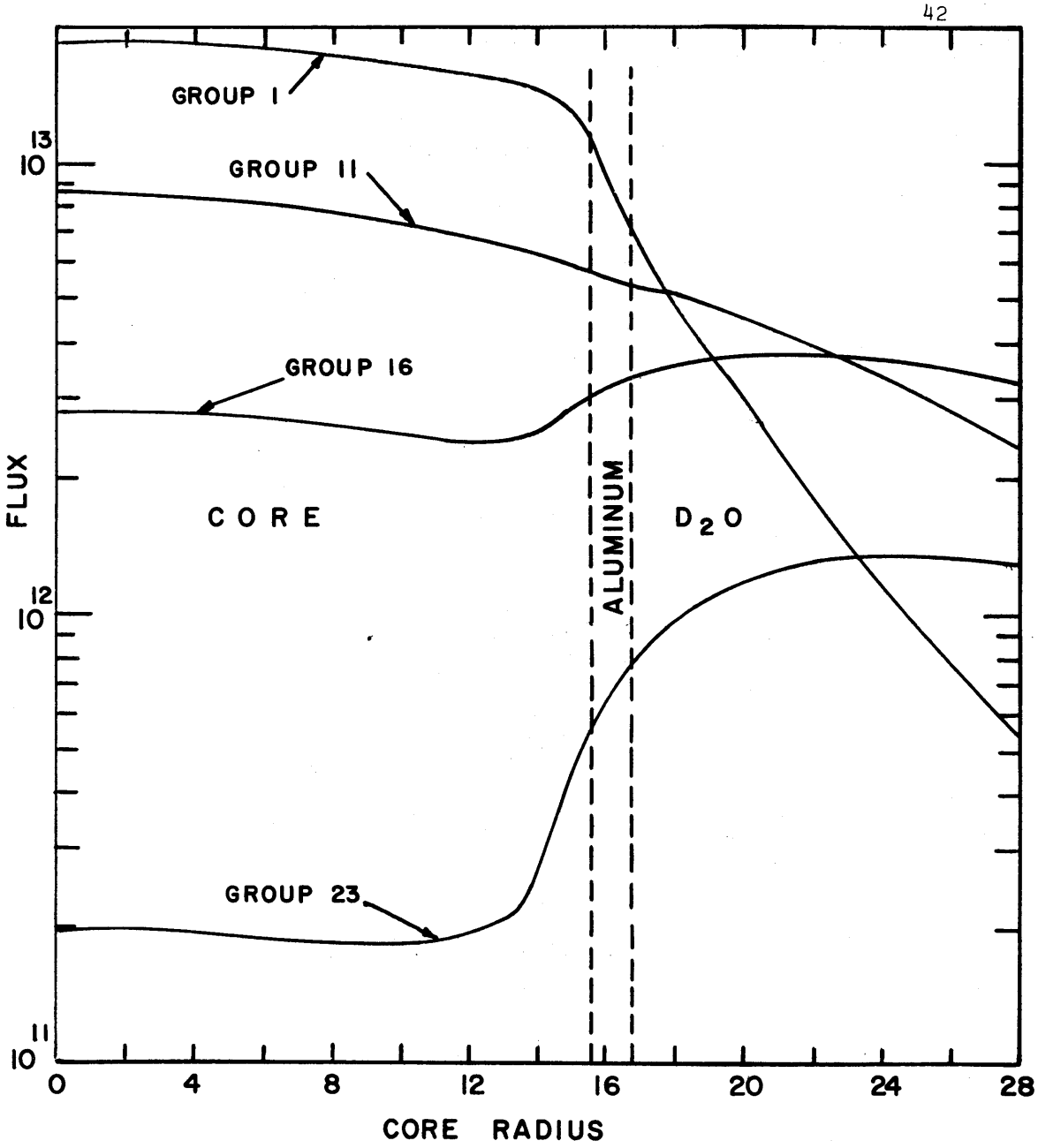

FIG. 2.2 FLUX DISTRIBUTION IN THE 5-REGION SPHERICAL REACTOR CORE

as a source of fast neutrons and a sink for the thermal neutrons, whereas the reflector acts as a source of thermal neutrons and a sink for the fast neutrons.

It may also be remarked that the flux level as well as the effective multiplication in the system for the diffusion solution were consistently lower than the corresponding transport solution result (see Table 2.4).

The general shape of the flux distribution in the fast, epithermal, and thermal energy ranges, point to the importance of the selection of the energy groups making up each of the collapsed few groups. A few trials showed that the lower cut-off of the collapsed fast group at 3.0 keV (multigroup 7) gave the best agreement between the few group diffusion and multigroup transport calculations. The effect of different schemes of thermal cut-off energy on the effective multiplication in the system as well as fission rate distribution in the core are summarized in Tables 2.4 and 2.5 and in Fig. 2.3

From Tables 2.4 and 2.5 as well as Fig. 2.3, a comparison of the first three cases shows that the four energy group scheme with two overlapping thermal groups below 0.4 eV energy range, gives a better agreement with the multigroup transport calculations than the twenty-three group diffusion results. The four group scheme overestimates the effective multiplication while the twenty-three group diffusion calculation underestimates the effective multiplication;

TABLE 2.4

Effects of Thermal Energy Cut-Off on K_{eff}

CASE	DESCRIPTION	K_{eff}	$1.0507-K_{eff}$
1	S-8 Transport--23 Groups	1.0507	0.0
2	Diffusion--23 Groups	1.0358	-0.0149
3	Diffusion--4 Groups (Two Overlapping Thermal Groups)	1.0535	+0.0028
4	Diffusion--3 Groups (0.4 eV Thermal Cut-Off)	1.0557	+0.0050
5	Diffusion--3 Groups (0.2 eV Thermal Cut-Off)	1.0665	+0.0158
6	Diffusion--3 Groups (1.0 eV Thermal Cut-Off)	1.0605	+0.0098

TABLE 2.5

Point Fission Rate (10^{12} fissions/cc-sec)

Point	Radius (cm)	CASES CORRESPONDING TO THOSE IN TABLE IV					
		1	2	3	4	5	6
1	1.4835	9.628	9.113	9.729	9.725	9.602	9.763
2	2.9670	9.592	9.071	9.675	9.664	9.547	9.691
3	4.4505	9.484	8.976	9.556	9.522	9.423	9.524
4	5.9340	9.351	8.844	9.376	9.284	9.225	9.238
5	7.5540	9.145	8.667	9.263	9.410	9.187	9.647
6	9.1740	8.989	8.509	9.007	9.112	8.910	9.318
7	10.794	8.856	8.437	8.853	8.976	8.757	9.204
8	12.414	9.222	8.825	9.078	9.239	9.028	9.497
9	14.034	10.242	10.174	10.434	10.590	1.057	10.782
10	15.654	15.029	15.307	15.032	14.784	15.568	14.440

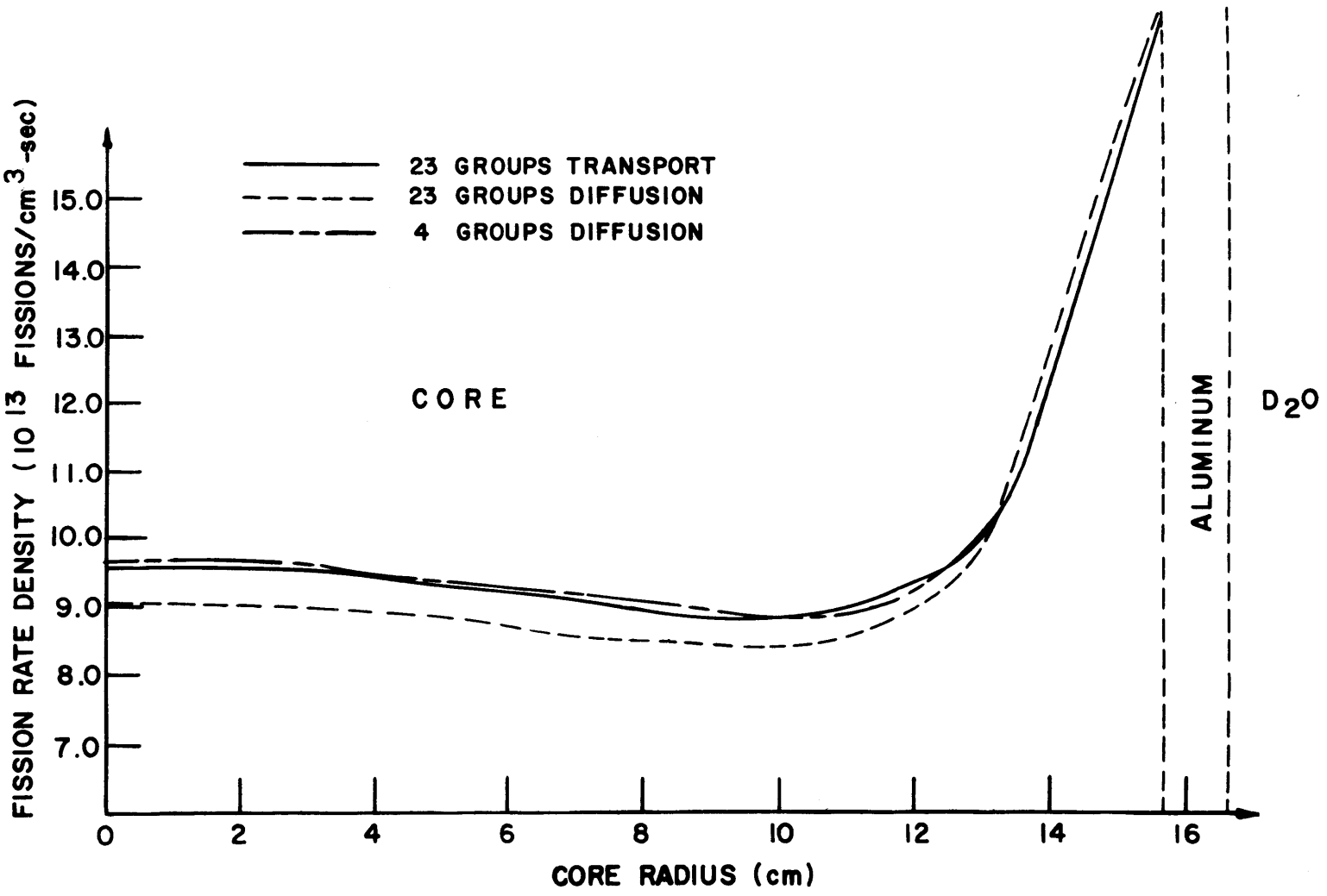

FIG. 2.3 POWER DENSITY DISTRIBUTION IN THE 5-REGION SPHERICAL REACTOR MODEL

but the excess reactivity predicted by the four groups scheme equals only a fifth of the reactivity underestimated by the twenty-three group diffusion results.

A comparison of the fission rate distribution in Fig. 2.3 also shows a better agreement between the four group diffusion and multigroup transport calculations than the agreement between the twenty-three group diffusion and transport results. The better agreement of the four group scheme may be due entirely to cancellation of errors but shows that the four group scheme does save some computing time as well as yield satisfactory results for this kind of core.

Cases four, five and six of Table 2.4 were included as further schemes of improving upon the four energy group scheme. In case four, the two overlapping thermal groups have been combined, resulting in one thermal group representation in the energy range below 0.4 eV. The reactivity overestimated by this scheme is one-third of that reactivity underestimated by the twenty-three energy group diffusion results. From Table 2.4, the agreement in the fission rate distribution is comparable to the four group scheme. For three space dimensional calculations, therefore, this three group scheme appears to be the method of choice, since the saving in computing time outweighs the slight loss in computational accuracy. A further disadvantage of the four group scheme compared with the three group scheme of case four is the difficulty of obtaining the up-scatter cross-section between the overlapping thermal groups, a quantity

that is slightly spatially dependent compared with the other cross-section data. This effect is illustrated by the aluminum average cross-sections for regions one, two, and four shown in Table 2.6.

Case five of Table 2.4 shows that, reducing the thermal cut-off energy from 0.4 eV to 0.2 eV results in poorer results; while case six shows that increasing the thermal cut-off energy to 1.0 eV also results in poorer results. In case six, Table 2.4 shows that the fission rate distribution is fairly flat and in poorer agreement with that distribution predicted by the multigroup transport calculations. The effect is primarily due to the inclusion of a large component of the epithermal flux, which is less sensitive to spectrum changes near the edge of the core, in the thermal spectrum.

2.2.2 Effect of Thin Light Water Regions.

Diffusion theory may not be expected to yield very satisfactory results in the alternating five thin regions of aluminum and light water outside the core. The gross effects of these regions on the power density distribution inside the core as well as the effective multiplication in the system were examined.

The spherical reactor model used is shown in Fig. 2.4. Regions two through six had radial dimensions similar to those of the design base MITR. The radial dimensions as well as region material compositions are given in Table 2.7.

TABLE 2.6

5-Region Core Model--Aluminum Up-Scatter Cross Sections for Regions 1, 2 and 4

Region	Aluminum Up-Scatter Cross Section for Group 4 to Group 3
1	3.9247×10^{-4}
2	2.8115×10^{-3}
4	2.29644×10^{-3}

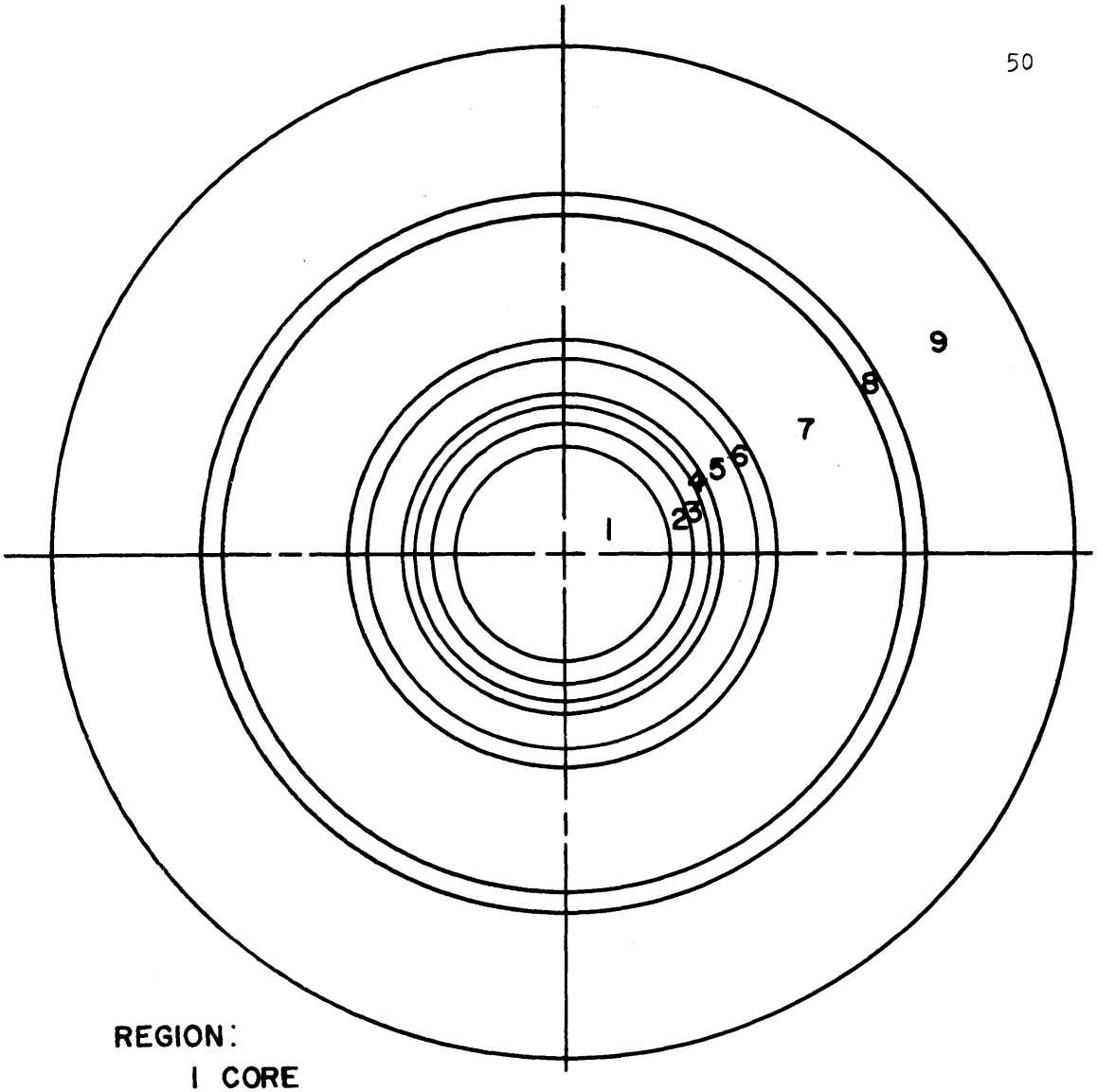

REGION:

1 CORE	
2 ALUMINUM	3 H_2O BELOW CONTROL RODS
4 ALUMINUM	5 H_2O COOLANT
6 ALUMINUM	7 H_2O REFLECTOR
8 ALUMINUM TANK	9 GRAPHITE

FIG. 2.4 NINE-REGION SPHERICAL REACTOR MODEL

TABLE 2.7

9-Region Core Model Data

Material Number Densities in Region One

U-235	2.6239×10^{20}
U-238	1.974×10^{19}
Light Water	1.535×10^{22}
Aluminum	3.195×10^{22}

Outer Radii of Regions

Region	Outer Radius
1	17.23 cm.
2	18.44 cm.
3	21.19 cm.
4	23.12 cm.
5	25.02 cm.
6	26.20 cm.
7	55.32 cm.
8	57.82 cm.
9	123.82 cm.

The effects on the effective multiplication in the system are summarized in Table 2.8. The twenty-three group diffusion calculation underestimates while the three group diffusion result overestimates the effective multiplication in the system as already observed in section 2.2.1. A comparison of Tables 2.4 and 2.8 shows that the presence of the thin regions increases the reactivity underestimated by the twenty-three group calculation by about fifty per cent, while that reactivity overestimated by the three group scheme increases by about the same fifty per cent. Nevertheless, the three group scheme gives a better agreement with the transport calculation.

The curves of power density given on Fig. 2.5 as well as the point fission rate given in Table 2.9 shows that the three group scheme gives a better agreement with the transport calculation.

2.2.3 Equivalent Homogeneous Diffusion Constant.

The flux-volume weighting procedure used in obtaining the equivalent few group homogeneous constants preserves the ratio of fission neutrons produced to those absorbed. This ratio is not sensitive to the average flux used; however, the equivalent few group homogeneous diffusion constant is sensitive to the choice of weighting scheme employed (21).

TABLE 2.8

Effective Multiplication

CASE	REMARKS	K_{eff}	$1.0026 - K_{eff}$
1	S-8 Transport--23 Energy Groups	1.0026	0.0
2	Diffusion--23 Energy Groups	0.9757	-0.269
3	Diffusion--3 Groups (0.4 eV Thermal Cut-Off)	1.0109	+0.0083

TABLE 2.9

Fission Rate (10^{12} Fissions/cc-sec)

POINT	RADIUS (cm)	CASE		
		1	2	3
1	2.237	6.21	5.78	6.14
2	4.474	6.13	5.69	6.05
3	6.710	5.93	5.51	5.85
4	8.947	5.64	5.23	5.54
5	11.18	5.26	4.88	5.12
6	12.39	4.95	4.59	4.98
7	13.60	4.72	4.40	4.74
8	14.81	4.55	4.25	4.56
9	16.02	4.45	4.23	4.50
10	17.23	4.62	4.46	4.70
11	18.44	5.17	5.24	5.41
12	19.65	7.11	7.37	7.16

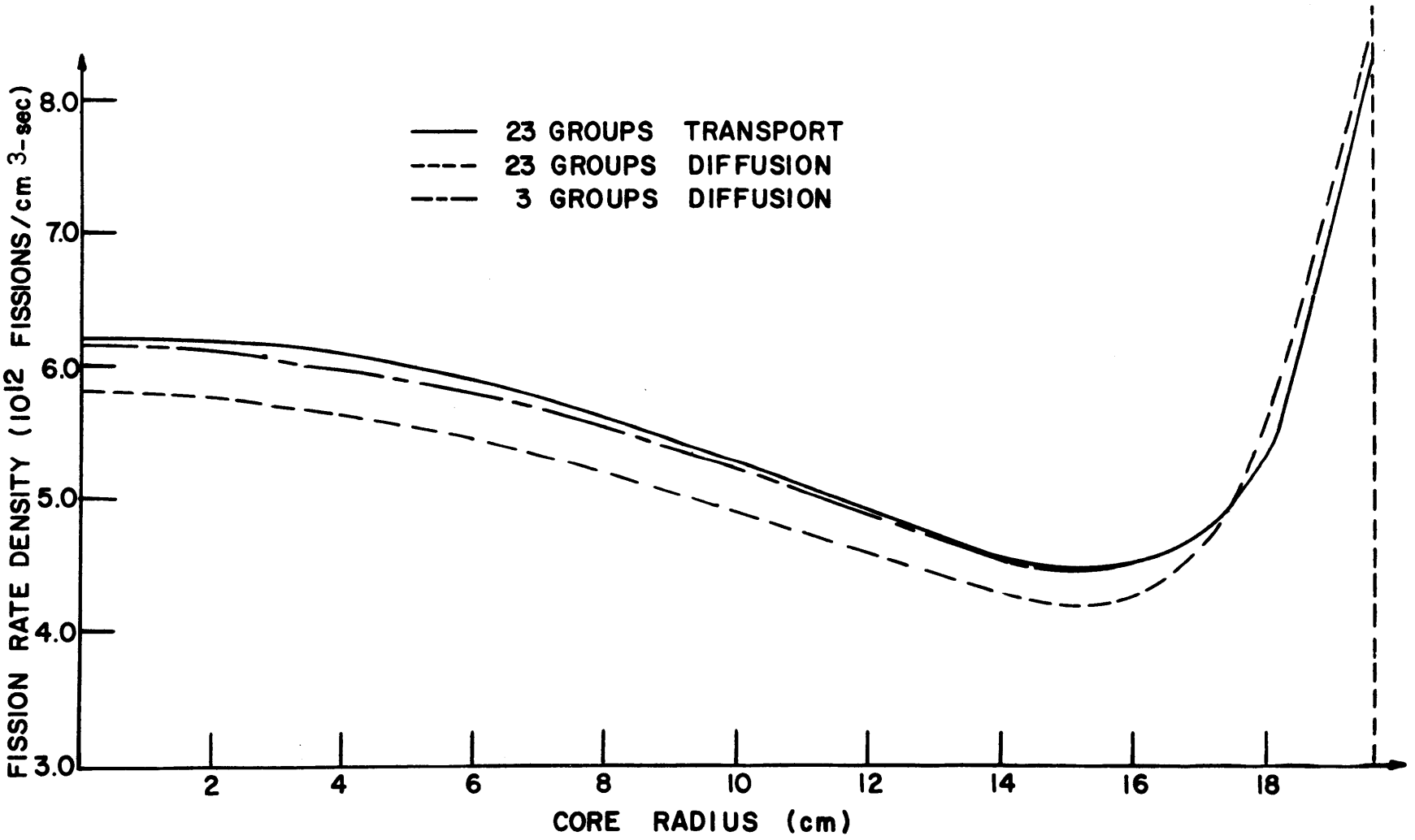

FIG. 2.5 POWER DENSITY DISTRIBUTION IN THE 9-REGION SPHERICAL REACTOR MODEL

The three common procedures for obtaining the equivalent homogeneous diffusion constant from a suitably weighted equivalent transport cross-section were compared. The Three methods used to obtain the equivalent transport cross-sections are:

1. Flux-volume weighting the macroscopic transport cross-section.
2. Flux-volume weighting the reciprocal of the macroscopic transport cross-section.
3. Flux-volume weighting the reciprocal of the microscopic transport cross-section, and combining the resulting equivalent microscopic transport cross-section with the appropriate number density to obtain the equivalent homogeneous macroscopic transport cross-section.

The converged group fluxes of the twenty-three group diffusion calculation described in section 2.2.2 (case 2 of Table 2.4) was the flux spectrum used. The equivalent homogeneous macroscopic transport cross-section was calculated for each of the nine regions shown in Fig. 2.4. The result for region one for the three groups is summarized in Table 2.10. In group two the equivalent transport cross-section is practically independent of the flux-volume weighting procedure used. In both groups one and three, the first procedure, namely flux-volume weighting the macroscopic transport cross-section, yields the largest numerical

TABLE 2.10

Effect of the Flux-Volume Weighting Scheme on the

Equivalent Homogeneous Transport Cross-Section

FLUX-VOLUME WEIGHTING SCHEME	EQUIVALENT HOMOGENEOUS TRANSPORT CROSS-SECTION FOR REGION ONE (CORE)		
	GROUP 1	GROUP 2	GROUP 3
1. Flux-volume weighting the macroscopic transport cross-section.	1.91073	3.2228	8.51094
2. Flux-volume weighting the reciprocal of the macroscopic transport cross-section.	1.66261	3.21975	8.04550
3. Flux-volume weighting the reciprocal of the microscopic transport cross-sections.	1.47046	3.17698	7.95262

value for the transport cross-section, while the third procedure results in the smallest numerical value, with the second procedure yielding an intermediate value.

The effect of the region neutron energy spectrum on the equivalent transport cross-section is illustrated by the values calculated for light water in regions one, three, and five and summarized in Table 2.11.

As the first and third procedures produced the smallest and the largest equivalent homogeneous diffusion constants respectively, the resulting effect on the effective multiplication was investigated. The results show that the third procedure yields the smaller effective multiplication of 0.9749 which agrees with that for the twenty-three group diffusion solution of 0.9757; while the first procedure yields the larger effective multiplication of 1.0109 which is slightly higher than that predicted by the twenty-three group transport solution of 1.0026. The three group results are, therefore, sensitive to the flux-volume weighting scheme used in obtaining the equivalent transport cross-section.

The equivalent macroscopic transport cross-section for the third group was obtained by combining the appropriate number densities with the effective microscopic transport cross-sections obtained from THERMOS (19) calculation. The effective microscopic transport cross-sections are calculated with the THERMOS code by flux-volume weighting the group transport cross-sections defined below. For all isotopes,

TABLE 2.11

The Effect of the Region Neutron Energy Spectrum on the Region Microscopic Transport Cross-Section for Light Water

	EFFECTIVE MICROSCOPIC TRANSPORT CROSS-SECTION FOR LIGHT WATER		
REGION	GROUP 1	GROUP 2	GROUP 3
1	1.7256	5.6493	13.9912
3	1.82779	5.65272	14.9239
5	1.82621	5.65429	15.0563

except hydrogen and deuterium, the group transport cross-section, σ_g^{tr}, is defined as

$$\sigma_g^{tr} = \sigma_g^a + (1-\bar{\mu}_o)\sigma_g^s \quad , \qquad \ldots 2.2.1.$$

where σ_g^a and σ_g^s are the group absorption and scattering scoss-sections respectively.

For hydrogen and deuterium, the Nelkin kernel (22) with transport correction defined by Honeck (23) was used and the group transport cross-section is then defined as

$$\sigma_g^{tr} = \sigma_g^a + \int_0^{E_c} dE' [\sigma_{so}(E,E') - \sigma_{si}(E)\delta(E-E')] \qquad \ldots 2.2.2.$$

where E_c is the thermal cut-off energy, $\sigma_{so}(E,E')$ is the isotropic scattering kernel and $\sigma_{si}(E)$ is the first order coefficient in the expansion of $\sigma_s(E,E';\bar{\Omega}\ \bar{\Omega}')$ in Legendre's polynomials of argument $\mu = \bar{\Omega}\cdot\bar{\Omega}'$.

As the first procedure, namely flux-volume weighting the macroscopic transport cross-sections directly, yielded results that agreed better with the transport calculations, this procedure, therefore, was used in obtaining the equivalent transport cross-sections for groups one and two.

2.3 HOMOGENIZATION OF THE CORE

In the energy range below 1.0 eV, the diffusion length of neutrons was of the same order as the thickness of the fuel plates and hence the flux distribution would be sensitive

to the fine structure of material distribution in the core. A homogenization scheme must, therefore, take the resulting self-shielding of the fuel into account. In addition, as the core is undermoderated, the thermal neutron spectrum at a point in the core is dependent on the radial distance from the external moderation in the neutron reflector surrounding the core; the shorter this radial distance, the softer the thermal neutron spectrum. These two effects were treated, by using the integral neutron transport code, THERMOS (18), (19).

The THERMOS code is described in section 2.6.4 below. The basic thermal library used was prepared from the thermal library tape of LAZER code (24). The thermal cut-off energy on this library is 1.855 eV and is divided into 35 energy groups. The scattering kernel used is the free gas kernel of Brown and St. John (25), except for light water and heavy water. For the bound proton in light water, the Nelkin kernel (22) with the transport correction defined by Honeck (23) was used. For the bound deuterium in heavy water, the kernel used was Honeck's extension of the Nelkin kernel to heavy water (26) with the transport correction defined by Honeck (23). The Nelkin kernel with the transport correction has been shown to account for anisotropic scattering effects if neutron flux gradients are not as large as to be expected near control rods (23), and has been found to yield satisfactory agreement with measured data (23), (27).

A fuel element of re-designed MITR is rhomboidal in section and has fifteen active fuel plates. Figure 2.6 shows the cross-sectional details of an element. The homogenization of an element was effected in two steps. First, a unit slab cell as shown in Fig. 2.7 was isolated and a THERMOS calculation performed to obtain cell homogenized constants. Secondly, the homogenized constants for this unit cell was used in the next step to homogenize the unit slab cell shown in Fig. 2.8 to obtain homogenized constants for the element.

The homogenized constants for an element were used to obtain spatially averaged effective constants for the core as described in section 2.3.2 below. It was found desirable to express the effective homogenized constants of a region in terms of the actual material microscopic constants available on the THERMOS library tape so that the homogenized constants of that region could be used in a subsequent step in which that region is further homogenized such as in the first and second steps described above.

The effective homogenized microscopic constants for each energy group were defined in terms of self-shielding factors such that in an energy group K, the ratio, f_k, of absorptions in the fuel to the total absorptions in the unit cell is preserved between the heterogeneous isolated region and the equivalent homogenized region.

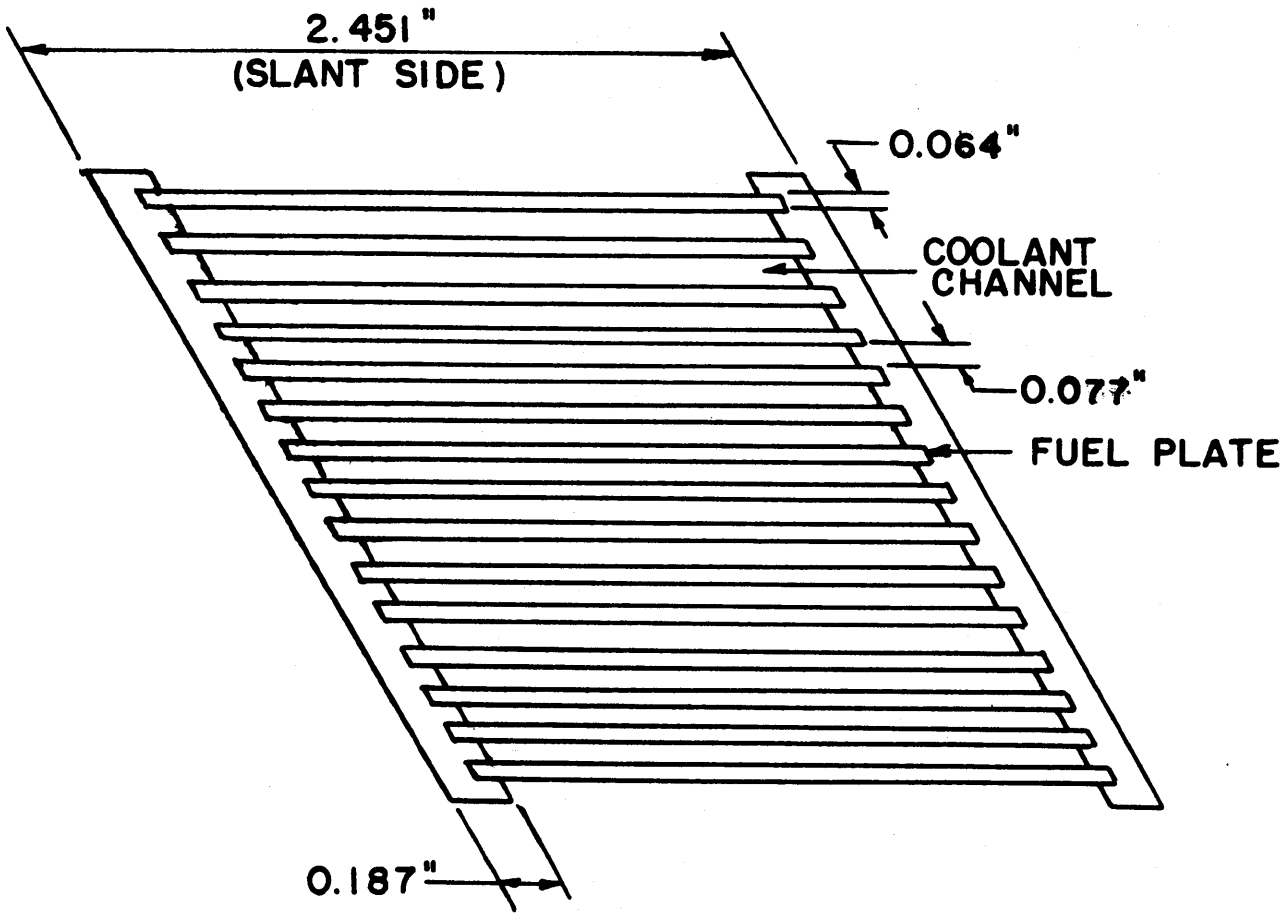

FIG. 2.6 DETAILS OF A FUEL ELEMENT CROSS-SECTION

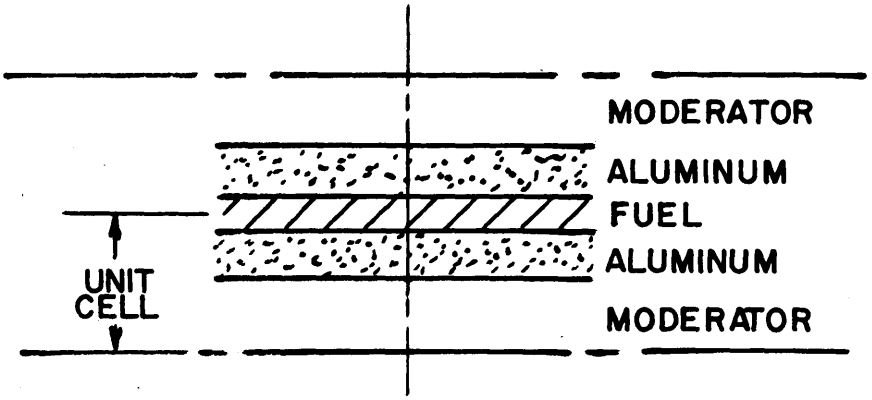

FIG. 2.7 FIRST UNIT CELL FOR HOMOGENIZATION

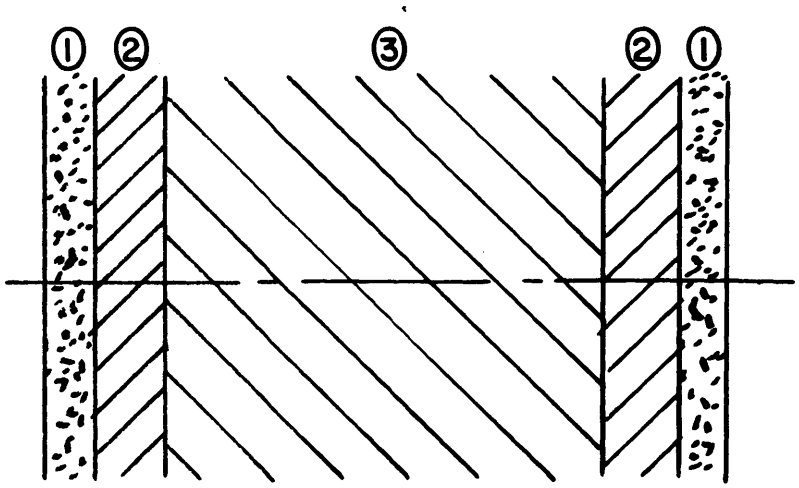

REGION:

1- ALUMINUM SIDE PLATE OF AN ELEMENT

2- HOMOGENIZED REGION OF ALUMINUM AND H_2O BETWEEN SIDE PLATE AND FUEL MEAT

3- HOMOGENIZED REGION CONSISTING OF UNIT SLAB CELLS SHOWN IN FIGURE 2.7

FIG. 2.8 SECOND UNIT CELL FOR HOMOGENIZATION

$$f_k = \frac{\text{Group K Absorptions in the Fuel}}{\text{Total Group K Absorptions in the Unit Cell}} \qquad \ldots 2.3.1.$$

In the homogenized region, as all the isotopes are exposed to the same average flux

$$f_k^{HOM} = \frac{N_F^{HOM}\ \sigma_F^{eff}}{N_F^{HOM}\ \sigma_F^{eff} + N_s^{HOM}\ \sigma_s^{eff} + N_M^{HOM}\ \sigma_M^{eff}} \qquad \ldots 2.3.2.$$

where the subscripts

F denotes fuel

S denotes unit cell structural material

M denotes moderator

K denotes neutron energy group

and N^{HOM}, σ^{eff} are respectively the homogenized number density and effective homogenized absorption cross-section.

In the heterogeneous cell,

$$f_K^{HET} = \frac{\int_{V_F} \sigma_F\ \phi_F^K(r)dr}{\int_{V_F} N_F\ \sigma_F\ \phi_F^K(r)dr + \int_{V_S} N_S\ \sigma_S\ \phi_S^K(r) + \int_{V_M} N_M\ \sigma_M\ \phi_M^K(r)dr} \qquad \ldots 2.3.3.$$

where v, σ, ϕ are respectively volume, unshielded microscopic absorption corss-section, and neutron flux.

$$= \frac{N_F \sigma_F \bar{\phi}_F^K V_F}{N_F \sigma_F \bar{\phi}_F^K V_F + N_S \sigma_S \bar{\phi}_F^K V_S + N_M \sigma_M \bar{\phi}_M^K V_M} \qquad \ldots 2.3.4.$$

$$\text{where } \bar{\phi}_i^K = \frac{1}{V_i} \int_{V_i} \phi_i^K(r) dr \qquad \ldots 2.3.5.$$

dividing the numerator and denomenator by $\bar{\phi}_M^K$ and V_{CELL}, the unit cell volume, yields

$$F_K^{HET} = \frac{N_F^{HOM}(F_F^K \sigma_F)}{N_F^{HOM}(F_F^K \sigma_F) + N_S^{HOM}(F_S^K \sigma_S) + N_M^{HOM} \sigma_M} \qquad \ldots 2.3.5.$$

$$\text{where } N_i^{HOM} = N_i V_i / V_{CELL}$$

$$F_i^K = \bar{\phi}_i^K / \bar{\phi}_M^K \qquad \ldots 2.3.6$$

F_i^K is the energy group K self-shielding factor for material i. Comparing equations 2.3.2 and 2.3.5, F_K^{HET} equals F_K^{HOM} provided the effective microscopic cross-sections are chosen such that

$$\sigma_i^{EFF} = F_i^K * \sigma_i \qquad \ldots 2.3.7.$$

THERMOS has now been modified to accept input self-shielding factors, F(J, K, M), for isotope J in mixture M for each neutron energy group K available on the THERMOS

library tape for isotope J. The effective microscopic cross-sections, $SIG(J, K, M)_{eff}$ of isotope J in mixture M used in the THERMOS calculation is computed as

$$SIG(J, K, M)_{eff} = F(J, K, M) * SIG(J, K) \quad ...2.3.8.$$

where SIG(J, K) is the actual microscopic cross-section for energy group K available on the THERMOS library tape for isotope J.

THERMOS has also been modified to compute (F(J, K, M) for the fissionable and structural materials in the cell:

$$F(J, K, M) = \frac{\sum_{N=NR1}^{NR2} CONT(J, N) * \phi(K, N) * DV(N)}{CONT(J) * \bar{\phi}(K) * VOL} \quad ...2.3.9.$$

where $$\bar{\phi}(K) = \frac{\sum_{N=M1}^{M2} \phi(K, N) * DV(N)}{\sum_{N=M1}^{M2} DV(N)} \quad ...2.3.10.$$

$$CONT(J) = \frac{\sum_{N=NR1}^{NR2} CONT(J, N) * DV(N)}{VOL} \quad ...2.3.11.$$

$$VOL = \sum_{N=NR1}^{NR2} (DV(N) \qquad \ldots 2.3.12.$$

NR1 to NR2 define the region over which homogenized constants are to be calculated; M1 to M2 define the cell moderator region; N is point index; j is the cell isotope index; K is the energy group index; CONT(J, N) is the atom number density of isotope J at point N in the cell; ϕ(K, N) is the group K average flux at point N; and DV(N) is the volume associated with point N in the cell.

2.3.2 Spatially Averaged Homogeneous Constants.

The neutron flux changes locally within an element as well as in an overall sense in going from one region of the core to another. The local flux variations within an element, principally in the thermal energy range, are accounted for by the self-shielding factors described in section 2.3.1 above.

For a compact core, the effect of the regions adjacent to an isolated unit cell, particularly the surrounding reflector, cannot be accounted for satisfactorily in cell calculations employing reflecting boundary conditions. Figure 2.9 shows a typical unit slab cell of the re-designed MITR. The half-thickness of the cell light water moderator,

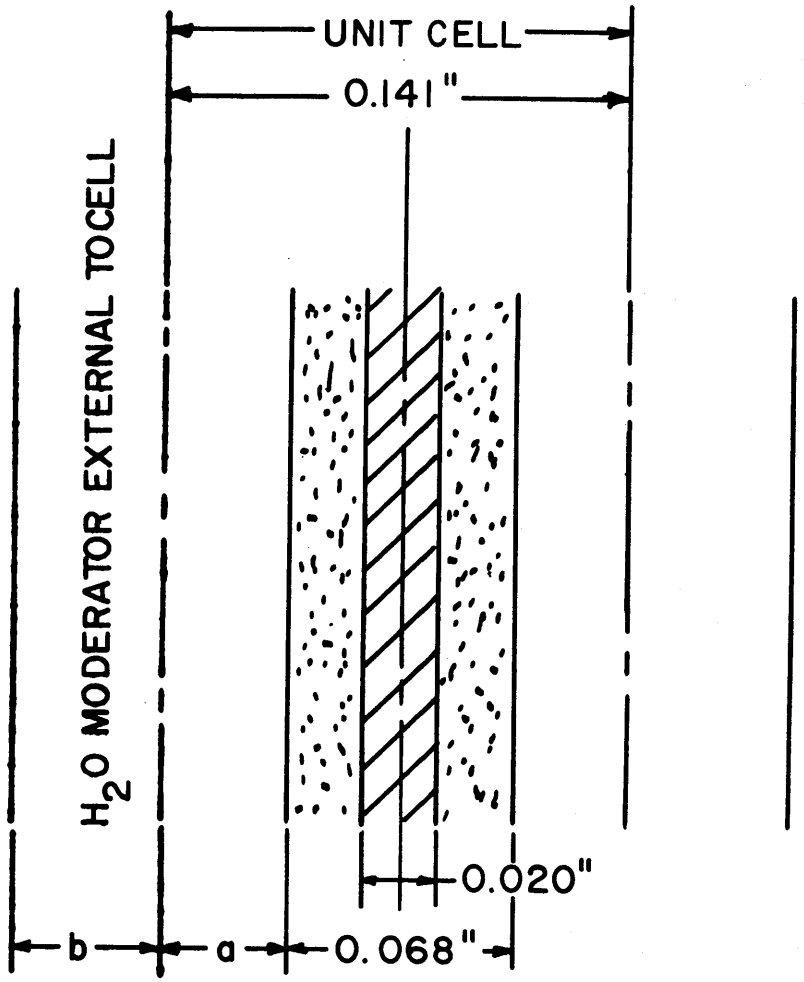

FIG. 2.9 UNIT SLAB CELL WITH EXTERNAL H_2O MODERATOR OF WIDTH b

a, is 0.0365 inches. The effects of external moderation in such a cell were examined by surrounding the unit slab cell with light water external moderator of width b inches. A series of THERMOS cell calculations were made in which the ratio b/a was varied from zero to nineteen. The slowing down source term in the THERMOS calculation was placed in the entire light water moderator only. The results of these calculations are summarized in Figs. 2.10 and 2.11.

Figure 2.10 shows graphs of the effective absorption cross-section in the cell for uranium-235 versus the moderation parameter (b/a) for twenty-seven and thirty weight per cent of uranium in the fuel meat. The curves for the two uranium percentages are similar. The effective cross-sections for the central part of the core would be about those for (b/a) = 0 while those for the core-relector interface region would be about those for (b/a) = 10. The curve for the twenty-seven uranium weight percentage shows that the effective absorption cross-section varies from about 400 barns in the center to about 470 at the edge of the core, nearly a change of 17.5 per cent.

Figure 2.11 shows the curves of the first moment of the spectrum in the cell moderator, $\bar{V}_M$, versus the moderation parameter (b/a). $\bar{V}_M$ is measured in units of 2200 m/sec., and defined as

$$\bar{V}_M = \int_o^{E_c} vN(V)dv / \int_o^{E_c} N(v)dv \qquad \ldots 2.3.13$$

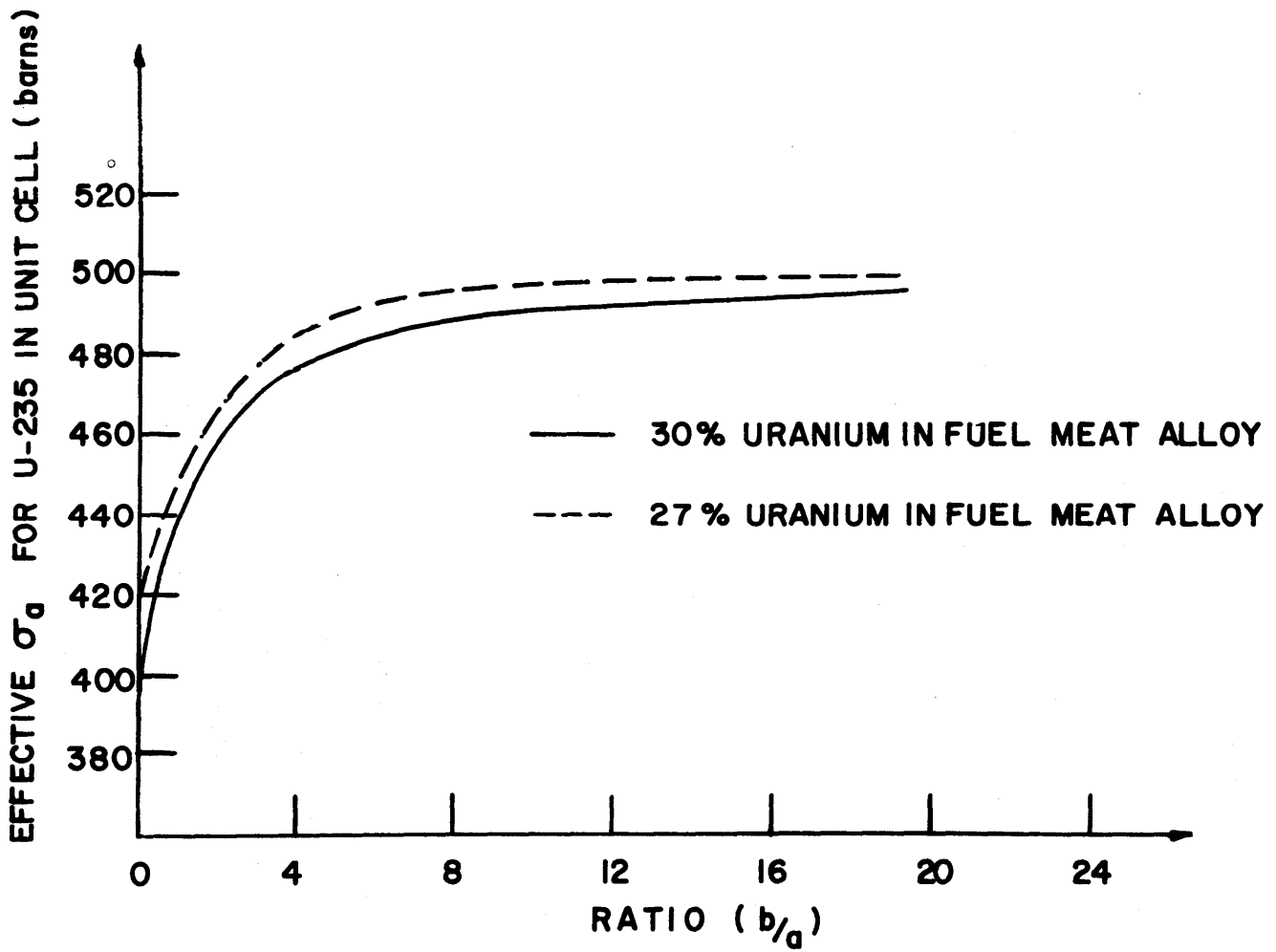

FIG. 2.10 EFFECTIVE σ_a FOR U-235 AS A FUNCTION OF THE MODERATION PARAMETER

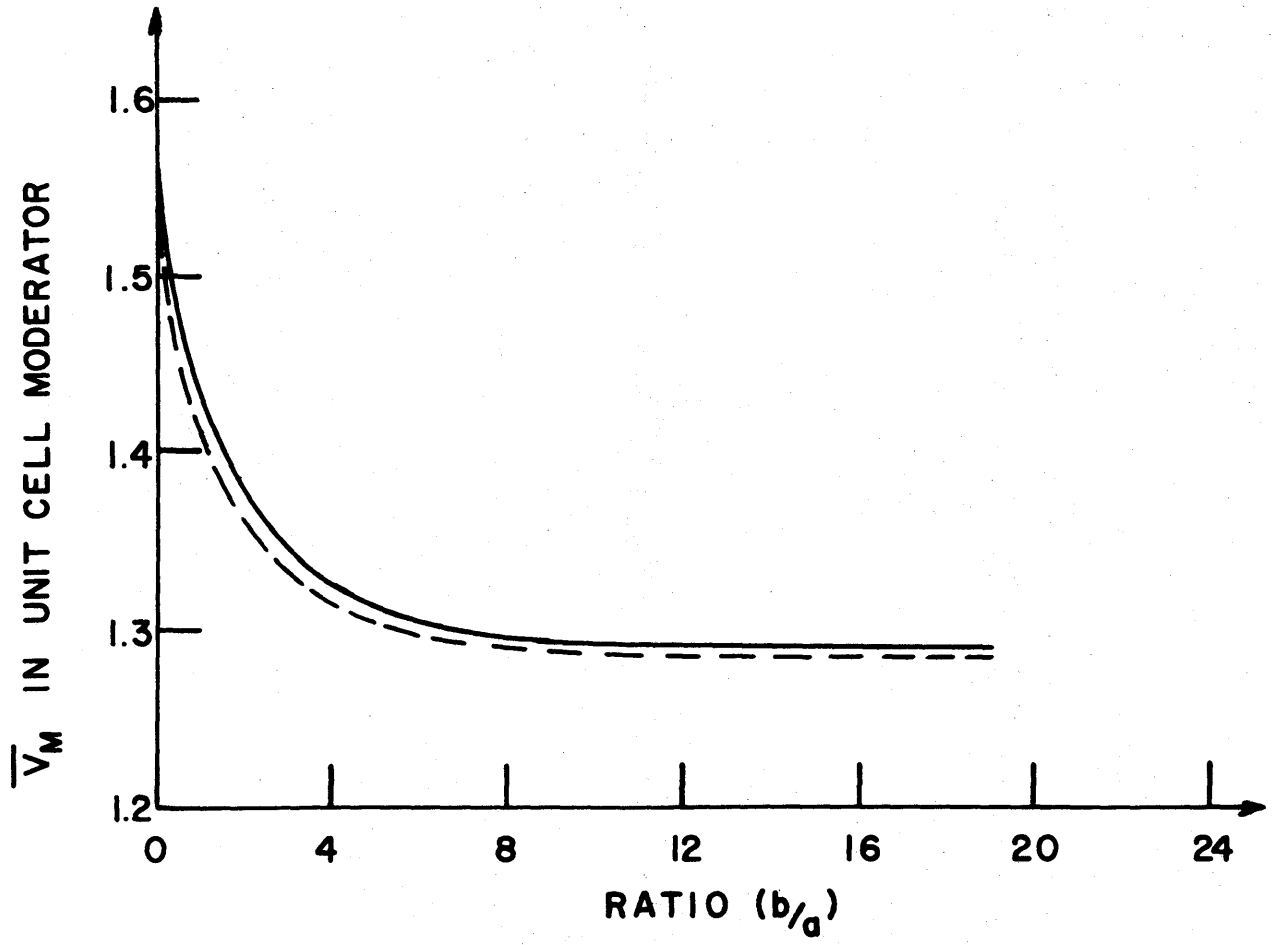

FIG. 2.11 THE FIRST MOMENT OF SPECTRUM AS A FUNCTION OF THE MODERATION PARAMETER

where E_c equals 0.4 eV, the thermal energy cut-off and N(V) is the integrated neutron number density in the cell moderator. $\bar{V}_M$ is also observed to vary from about 1.55 in the center to about 1.28 at the edge of the core. It is, therefore, necessary to treat the entire core with the surrounding reflector in order to obtain appropriate neutron flux spectrum to be used in flux-volume weighting the group constants to obtain the equivalent homogeneous constants over appropriate regions of the core.

In the energy range below 1.0 eV, THERMOS was used to obtain spatially averaged homogeneous constants over appropriate regions of the reactor. An entire element was homogenized and self-shielding factors as described in section 2.3.1. obtained for all isotopes in the core except light water. The calculated self-shielding factors were found to be only slightly sensitive to the moderation parameter b/a; the self-shielding factors for the slab cell with b/a = 0 are given in Table 2.12.

These calculated self-shielding factors were used as input to a THERMOS calculation in which the entire radial section of the active part of the core up to the wall tank was represented. The cylindrical approximation to the core described in section 7.1 was used and the radial material distribution corresponded to that at the active core mid-height.

The results for the twenty-seven and thirty uranium weight percentage in the fuel meat are summarized in Fig. 2.12 in the form of the effective absorption cross-section

TABLE 2.12

Calculated Self-Shielding Factors for U-235

ENERGY GROUP	SELF-SHIELDING FACTORS	
	PRESENT MITR	REDESIGNED MITR
1	0.7938	0.6467
2	0.8788	0.7870
3	0.9117	0.8434
4	0.9308	0.8769
5	0.9430	0.8991
6	0.9525	0.9158
7	0.9598	0.9281
8	0.9663	0.9404
9	0.9728	0.9503
10	0.9777	0.9574
11	0.9803	0.9611
12	0.9831	0.9635
13	0.9812	0.9586
14	0.9812	0.9560
15	0.9789	0.9551
16	0.9784	0.9547
17	0.9802	0.9570
18	0.9831	0.9651
19	0.9893	0.9708
20	0.9932	0.9767
21	0.9958	0.9820
22	0.9983	0.9825
23	0.9995	0.9871
24	0.9996	0.9872

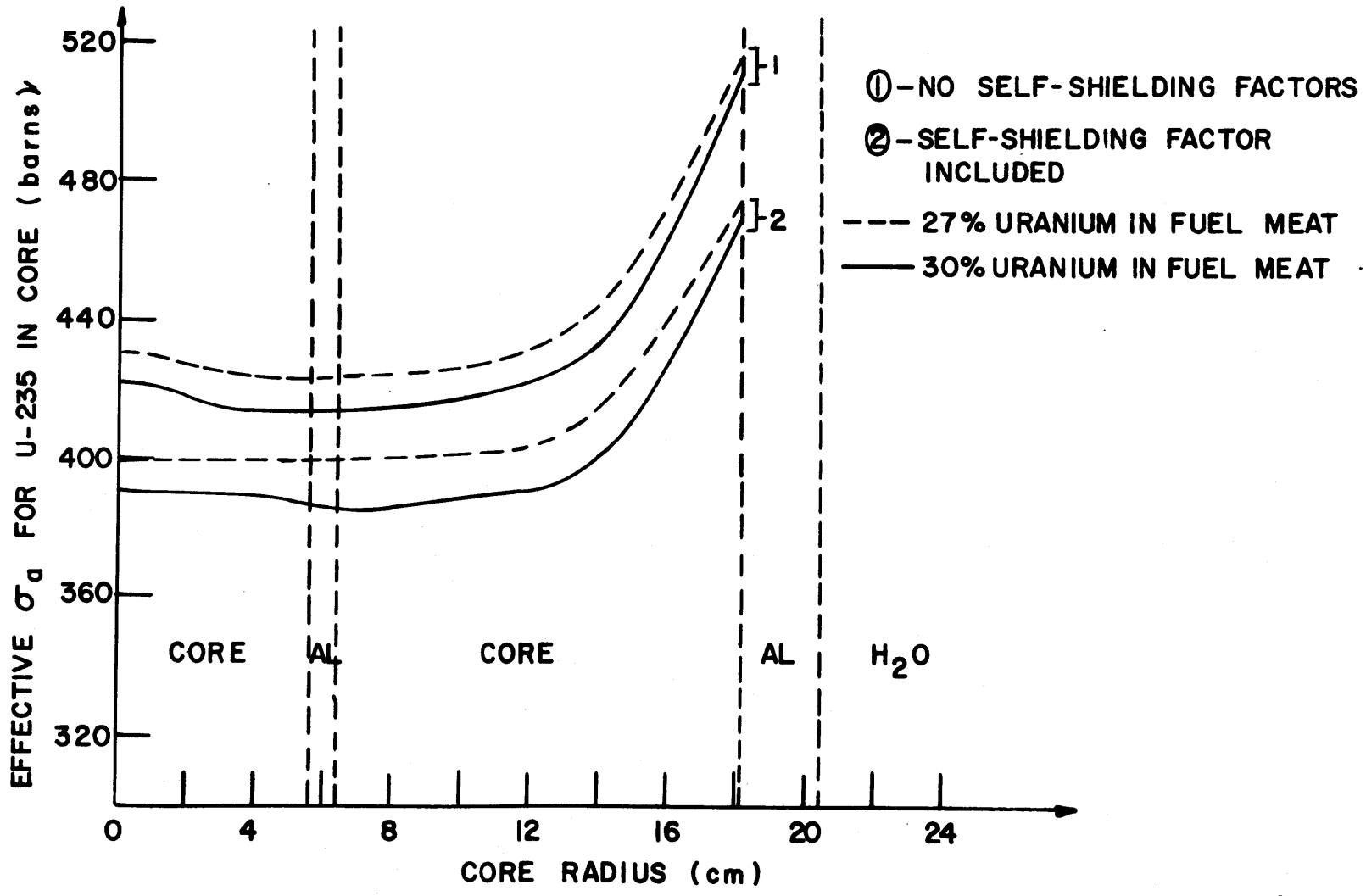

FIG. 2.12 EFFECTIVE σ_a FOR U-235 AS A FUNCTION OF THE CORE RADIUS

of uranium-235 versus core radius. The 2200 meter/second neutron absorption cross-section for uranium-235 is 679.2 barns; the effective value for the thermal neutrons at the center of the core for the twenty-seven uranium weight percentage in the fuel meat is about 400 barns and increases to about 475 barns at the edge of the core. If self-shielding factors are not included, the corresponding cross-sections are 430 at the center and 515 at the edge of the core.

Spatially averaged equivalent homogeneous constants over the core and other regions of the reactor were obtained for the energy range below 1.0 eV. This energy range was divided into two groups, namely 0.4 eV to 1.0 eV and thermal with cut-off energy of 0.4 eV. EXTERMINATOR II calculations showed that for the twenty-seven uranium weight percentage in the fuel meat, the effective multiplication in the system changed from 0.925 when self-shielding factors were not taken into account to .891 when these factors were included in obtaining the effective constants in the energy range below 1.0 eV.

To obtain the equivalent homogeneous constants for the fast and epithermal energy ranges, a fifteen-group diffusion calculation was performed. The neutron energy structure of the fifteen-group set used is shown in Table 2.13; the structure of the first fourteen groups is identical to the Hansen and Roach sets (14), (15). The cross-section data for groups one through thirteen were, therefore, taken from the sixteen group set (14); while those for groups fourteen and

TABLE 2.13

Energy Group Structure of the

Modified Hansen and Roach Fifteen Group Set

GROUP	NEUTRON ENERGY RANGE	FISSION SPECTRUM (X)
1	3 - ∞ MeV	0.204
2	1.4 - 3 MeV	0.344
3	0.9 - 1.4 MeV	0.168
4	0.4 - 0.9 MeV	0.180
5	0.1 - 0.4 MeV	0.090
6	17 -100 KeV	0.014
7	3 - 17 KeV	0.0
8	0.55- 3 KeV	0.0
9	100 -550 eV	0.0
10	30 -100 eV	0.0
11	100 - 10 eV	0.0
12	3 - 10 eV	0.0
13	1 - 10 eV	0.0
14	0.4 - 1.0 eV	0.0
15	Thermal	0.0

fifteen were obtained from the THERMOS calculations described above. The entire reactor was represented with the fewest number of mesh points necessary to obtain an adequate description of the flux spectrum in the reactor. A two dimensional cylindrical (RZ) geometry calculation was performed, using EXTERMINATOR-II code (41). The resulting flux spectrum was used to flux-volume weight the fifteen groups constants to obtain three groups equivalent homogeneous constants. The energy structure of the three group set is shown below:

FAST GROUP	3 KeV - ∞MeV
EPITHERMAL GROUP	0.4 eV - 3 KeV
THERMAL GROUP	0.00025 eV - 0.4 eV

2.4 A COMPARISON OF CALCULATIONS WITH MEASURED DATA

A comparison of calculated results with experimental data was carried out to determine whether the procedures used in obtaining spacially averaged homogeneous constants as well as the actual cross-section data employed and described in section 2.1 would yield satisfactory results.

There is adequate data on the present MITR taken during the initial low power tests carried out in 1959 (29), (30); in addition there is experimental criticality data on homogeneous systems in simple geometries (31) (32). The work on the present MITR is discussed in Chapter 10; in this section, a comparison of calculated results with experimental

criticality data on two cores of uranyl-fluoride (UO_2F_2) solutions are discussed.

The first core is a solution of uranyl-fluoride (UO_2F_2) in light water contained in an aluminum cylinder with effectively infinite light water full reflector. The core had H/U235 atomic ratio of 127, a height of 14.4 cm, a diameter of 25.4 cm, and critical mass of 1.45 Kg of uranium-235. The uranium enrichment was 93.2 weight per cent uranium-235. Although redesigned MITR had about 56 per cent by volume of aluminum in the core, the H/U-235 atomic ratio of this core with twenty-seven weight per cent in the fuel meat is 117 and hence only slightly less than the 127 for the above homogeneous core. The neutron energy spectra in the two cores, therefore, are not very different. The first moment of the spectrum, $\bar{V}$, in the center of redesigned MITR is 1.554 compared with 1.547 for the homogeneous core. The first homogeneous core is given in Table 5.9 of reference (32) as well as in reference (33).

The second homogeneous core is a solution of uranyl-fluoride (UO_2F_2) in heavy water contained in an unreflected steel cylinder. The core had D/U-235 atomic ratio of 856, a critical height of 60.83 cm, a diameter of 38.04 cm and critical mass of 8.31 Kg of U-235. The first moment of the spectrum, $\bar{V}$, in the center of this core is 1.601 compared with 1.554 for redesigned MITR. The neutron energy spectrum in this core is, therefore, only slightly harder with about eighty-four per cent of the fissions in the core occurring

below 0.4 eV compared with a corresponding figure of about eighty-nine per cent for the first homogeneous core. These three cores are, thus, quite thermal. This second homogeneous core is described by Olcott (34).

In the energy range below 1.0 eV, spatially averaged cross-sections were obtained from THERMOS calculation of the entire section of the cores as described in section 2.3.2. A fifteen group R-Z cylindrical calculations were performed, using the EXTERMINATOR II code. Three group calculations were performed, using the first and third schemes for obtaining the equivalent transport cross-section discussed in section 2.2.3.

The Hansen and Roach cross-section set (14) given for the bound proton in light water was found not to give very good results. Three versions are given for this isotope. The first version gave an effective multiplication of 0.9251, the second version gave 1.1646, while the third 0.7268 for the fully reflected light water system. A comparison showed that the first and second versions are practically identical, except the transport cross-section. The transport cross-sections are given in Table 2.14 for the first fourteen energy groups.

From the second column in Table 2.14, it is observed that the transport cross-section is constant between energy groups eight and thirteen, with the corresponding energy range of 10 eV. to 0.55 KeV. The detailed transport

TABLE 2.14

Microscopic Transport Cross-Sections for the Bound Proton in H_2O

	σ^{tr} FOR THE BOUND PROTON IN H_2O		
	HANSEN AND ROACH SET		NORMALIZED VALUES FROM THERMOS
ENERGY GROUP	VERSION ONE	VERSION TWO	
1	0.60	1.45	0.776
2	0.97	2.175	1.255
3	1.33	3.33	1.72
4	1.83	4.125	2.37
5	3.00	6.75	3.88
6	5.20	11.7	6.73
7	6.33	14.25	8.19
8	6.669	15.0	8.634
9	6.669	15.0	8.634
10	6.672	15.0	8.634
11	6.676	15.0	8.634
12	6.817	15.0	8.634
13	6.830	15.0	8.634
14	6.847	18.0	10.75

calculation performed by THERMOS, using the Nelkin kernel (22) with the transport correction defined by Honeck (23) should give the correct transport cross-section for the energy range below 1.0 eV. In addition, since the thermal library used for the THERMOS calculation has an upper cut-off energy of 1.85 eV, it should also be possible to obtain the correct transport cross-section in the energy range between 1.0 eV and 0.55 KeV.

This procedure was used to obtain the correct transport cross-section for the bound proton in hydrogen for the energy range below 0.55 KeV. The transport cross-section above 0.55 KeV was renormalized to agree with the correct value calculated for the energy range between 0.55 KeV and 1.0 eV. The resulting set of transport cross-sections actually used in the calculations are given in the third column of Table 2.14.

According to the results of section 2.2.3, the three group scheme using the third method to obtain the equivalent transport cross-section agrees better with the multigroup diffusion results, while the first method yields effective multiplication that is slightly higher than that obtained from multigroup transport calculations. The results for the two homogeneous systems are summarized in Table 2.15.

These results show that the three group scheme, using the simple flux-volume weighting procedure to obtain the equivalent transport cross-section, would over-predict the effective multiplication by about 1.0 percent, and these results are consistent with the results of section 2.2.3.

TABLE 2.15

Calculated Effective Multiplication

SYSTEM	CALCULATED EFFECTIVE MULTIPLICATION		
	15-GROUP DIFFUSION CALCULATIONS	3-GROUP DIFFUSION CALCULATIONS	
		FIRST SCHEME	THIRD SCHEME
1. Bare Homogeneous Heavy Water System	0.9910	1.0093	0.9898
2. Fully Reflected Homogeneous Light Water System	0.9933	1.0104	0.9803

Control rods and fixed absorbers in MITR-II are in the form of cadmium blades, 40 mils thick and clad with aluminum. In the two and three dimensional hexagonal calculations, the actual regions occupied by the cadmium absorbers were represented by fiticious diffusion regions have the same net absorption effect as the actual cadmium absorbers. The procedure used in obtaining the equivalent diffusion constants is that discussed by Henry (35) and Goldsmith (36).

In the thermal region, the equivalent diffusion constants of a slab of thickness 2t are defined in terms of blackness constants $\langle\alpha\rangle$,$\langle\beta\rangle$:

$$\langle\alpha\rangle_{th} = \frac{\langle j^+ + j^- \rangle}{\langle \phi^+ + \phi^- \rangle} = \frac{\int_o^{Ec} \alpha(E)\phi_{th}^{\infty}(E)dE}{\int_o^{Ec} \phi_{th}^{\infty}(E)dE} \qquad \ldots 2.5.1$$

$$\langle\beta\rangle \qquad \frac{\langle j^+ \oplus j^- \rangle}{\langle \phi^+ - \phi^- \rangle} = \frac{\int_o^{Ec} \beta(E)\phi_{th}^{\infty}(E)dE}{\int_o^{Ec} \phi_{th}^{\infty}(E)dE} \qquad \ldots 2.5.2.$$

$$\text{where } \alpha(E) = \frac{j^+ + j^-}{\phi^+ + \phi^-} = \frac{F_o(E)}{2[2-F_1(E)]} \qquad \ldots 2.5.3.$$

$$\beta(E) = \frac{j^+ - j^-}{\phi^+ - \phi^-} = \frac{2-F_o(E)}{2F_1(E)} \qquad \ldots 2.5.4.$$

$$F_{n+2}(E) = \int_0^1 \mu^n \mathrm{EXP}\ (-\frac{z}{\mu})\ d\mu \qquad \ldots 2.5.5.$$

$$z = 2t\ \Sigma_a(E) \qquad \ldots 2.5.6.$$

J^+, ϕ^+ and J^-, ϕ^- are the current and scaler flux at right and left-hand surfaces of the plate respectively; and ϕ^{∞}_{th} (E) is the scaler flux spectrum in the surrounding core away from the slab.

The mesh-corrected equivalent diffusion constants are then given by

$$D = \frac{(<\alpha>_{th}+<\beta>_{th})h}{2\ \mathrm{Sinh}\ (kh)} \cdot \tanh(2kt) \qquad \ldots 2.5.7.$$

$$\Sigma_a = \frac{2D}{h^2}[\mathrm{Cosh}(kh)-1] \qquad \ldots 2.5.8.$$

$$\text{where}\quad K = \frac{1}{2t}\left(\mathrm{Cosh}^{-1}\left(\frac{<\beta>_{th}+<\alpha>_{th}}{<\beta>_{th}-<\alpha>_{th}}\right)\right. \qquad \ldots 2.5.9.$$

h equals the mesh spacing inside the slab, with at least one internal point required.

The average blackness constants satisfy the relationship,

$$\frac{1}{4<\alpha>_{th}} \leq <\beta>_{th} \leq \frac{1}{<\alpha>_{th}} \qquad \ldots 2.5.10.$$

In the limit when the absorber is black over most of the thermal energy range,

$$<\alpha>_{th} = <\beta>_{th} = 1/2 \qquad \ldots 2.5.11.$$

In this case, if one internal mesh point is used such that h = t, then h is chosen such that

$$2kt = 10 \qquad \ldots 2.5.12.$$

Goldsmith (36) shows that less than 10 per cent error in the multiplication worth of 20 mils thick cadmium membrane bisecting a highly enriched slab core is incurred by representing the membrane in diffusion calculations with effective thermal diffusion constants in the energy range up to 0.625 eV calculated by using equation 2.5.11.

In the energy range up to 0.4 eV, equations 2.5.7 through 2.5.12 were used to calculate equivalent diffusion constants; above 0.4 eV, the spectrum weighted average cadmium cross-section data were used.

2.6 COMPUTER CODES USED

Computer codes employing finite difference analogs of the multigroup neutron transport equation or the diffusion approximation to the neutron transport equation were used in the computations. Prior to the summer of 1968, when the IBM system 360 was not available at MIT, the Modified Twenty Grand program was the main computational tool. A brief description of the computer codes used follows.

2.6.1 ANISN

The ANISN computer code was used primarily for the work described in sections 2.2 and 2.4. The IBM system 360

version of the code (37) was used.

The program solves the multigroup one-space dimension neutron transport equation in either slab, spherical or cylindrical geometrics using the SN approximation (37), (38). Isotropic or linear anisotropic scattering is permitted between all energy groups and upscattering is also allowed between any groups. In addition, a diffusion solution may be obtained for any or all neutron energy groups. The variable dimensioning technique is used so that parameters such as number of groups and total mesh points may be traded off one for the other, the only restriction on the size of the problem being the available computer core storage.

2.6.2 MODIFIED TWENTY GRAND

The Modified TWENTY GRAND computer program (39), (40), was used for the work described in Chapter 3 as well as section 4.1. The IBM computer 7090 version of the program was used.

The program solves the finite difference diffusion approximation to the transport equation in two dimensional RZ (cylindrical) XY (slab) geometries. It can handle up to six neutron energy groups; the maximum total mesh points allowed is 700 with a maximum of 20 mesh points in the X or R dimension.

2.6.3 EXTERMINATOR-II

The EXTERMINATOR-II computer program (41), (42), (43) was used for the work described in section 4.2 through Chapter 8. The IBM system 360 version was used.

The program is related to Modified TWENTY GRAND with many improvements. It solves the finite difference diffusion approximation to the transport equation in two dimensional X-Y, RZ or RΘ geometry. The code allows neutron upscatter from any group to any other group. The effect on the multiplication factor and fluxes due to pointwise equilibrium xenon concentrations may be taken into account. Flux-weighted few group microscopic cross-sections may be calculated. In addition, the code will calculate adjoint fluxes and do perturbation calculations (44). As variable dimensioning is used, parameters such as number of neutron energy groups and total mesh points may be traded off one for the other, the only restriction on the size of the problem being the available core memory.

A few modifications were made to the program. The input cards necessary to execute the code are basically those described in reference (41); the additional cards required by the modification are described in Appendix A.

2.6.4 THERMOS

THERMOS (18) was used to obtain spatially averaged few

group cross-sections in the energy range below 1.0 eV as described in sections 2.2 and 2.3. The IBM system 360 version (19) was used.

It is a thermalization transport theory code for reactor lattice calculations and computes the scaler thermal neutron spectrum as a function of position in a lattice by solving the integral transport equation with isotropic scattering. Anisotropic scattering effects may be accounted for by using a scattering kernel with transport correction (23). The code permits 20 maximum space points and 50 neutron energy groups. One dimensional X (slab) or R (cylindrical) geometry can be used.

A library tape containing scattering kernels and absorption cross-sections as primary input to THERMOS is prepared by the LIBP and GAKER codes (18), (19), (24). The LIBP code described by reference (24) was rewritten to produce a library tape format suitable for input to THERMOS described by reference (19).

The additional input cards necessary in order to make use of the modifications to THERMOS (19), discussed in section 2.3 are described in Appendix B.

2.6.5 PDQ-7

PDQ-7 computer code (45), (46), (47) was used for the work described in Chapters 9 and 10. The IBM system 360

version (47) as well as the CDC-6600 version (45) was used.

The program solves the finite difference diffusion approximation to the neutron transport equation in one, two, and three space dimensions. Two overlapping thermal groups may be used in one and two space dimensional problems, and either pointwise or regionwise depletion may be performed using the Harmony depletion system (48). The geometry may be rectangular, cylindrical or spherical in one dimension; rectangular, cylindrical or hexagonal in two dimensions; and rectangular or hexagonal in three dimensions.

The total number of neutron energy groups is limited to five. The product of groups and points cannot exceed 300,000 and the plane size in three dimensional problems is restricted to 8,000. In three dimensional problems, a block Guass-Seidel procedure is used, each block consisting of a single plane (45). The resulting inner iteration procedure may fail to converge if the planes are closely spaced and hence tightly coupled. In heavy water systems, in particular, the axial planes spacing must be greater than at least two and a half times the neutron transport mean free path.

2.7 CROSS-CHECKING OF COMPUTER CODES.

The principal computer codes used in the calculations

checked one against the other to determine the degree to which they agree in predicting the effective multiplication and neutron flux distribution. The same problem calculated by using both the Modified TWENTY GRAND and EXTERMINATOR-II codes showed agreement in K_{eff} up to the fifth significant figure while the neutron flux agreement was up to the fourth significant figure. PDQ-7 and EXTERMINATOR-II codes gave a similar agreement for the design base MITR-II core given in Fig. 7.1.

CHAPTER III

GEOMETRY OF THE CORE RADIAL SECTION

Regions of a compact core adjacent to the surrounding reflector can present power peaking difficulties. The larger the fraction of the fission neutrons that are slowed down external to the core, the higher the thermal neutron flux peak in the reflector, though the more severe are the power peaking difficulties. Different geometries of the core radial section were studied to determine the geometrical shape that reduced power peaking difficulties without severely reducing the thermal neutron flux peak in the reflector.

3.1 CORE RADIAL GEOMETRIES STUDIED

The first of the two core radial geometries studied is shown in Fig. 3.1. This design, proposed by Goebel (56), is approximately circular in section and utilizes nineteen fuel elements that are similar to the present MITR fuel elements.

The problem with this core configuration is that the fuel near the core-reflector interface sees a large re-entrant flux of thermal neutrons while fuel in the central region of the core sees a relatively weak flux of thermal neutrons. This results in a large ratio of maximum to core average power density and consequently severe power peaking difficulties at the core-reflector interface.

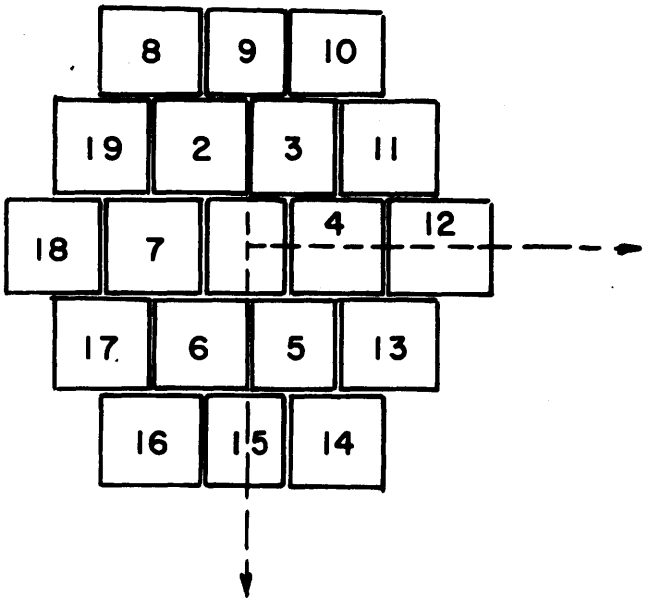

FIG. 3.1 APPROXIMATELY CIRCULAR CORE RADIAL SECTION

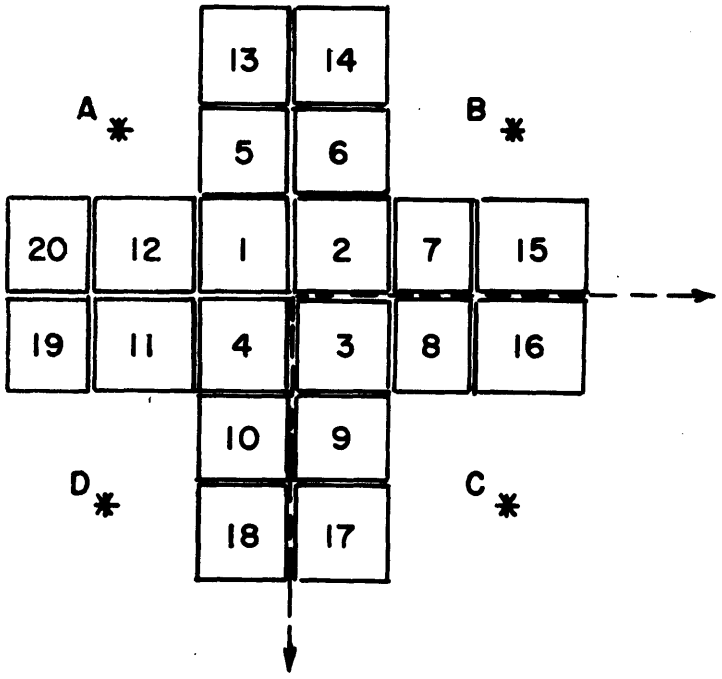

FIG. 3.2 CRISS-CROSS CORE RADIAL SECTION

The second core configuration, shown in Fig. 3.2, is criss-cross in section and utilizes twenty elements instead of nineteen used in the first core configuration. It has two interesting features. First, the core-reflector interface area is about thirty per cent larger than that of the core configuration of Fig. 3.1. This increased re-entrant area for the thermal neutrons will tend to reduce the power peaking difficulties at the core-reflector interface.

Secondly, this core geometrical arrangement tends to peak the reflector thermal neutron flux at four points, marked A, B, C, and D on Fig. 3.2. As the fast neutrons emitted nearly isotropically by the core into the reflector undergo scattering collisions that are not isotropic but peaked highly in the forward direction during slowing down, a suitable choice of the shape of the core boundary can exert a focusing effect in the resulting thermal neutron flux distribution in the reflector. The advantage of this latter core configuration depends on whether the core power distribution is flatter as well as the reflector thermal neutron flux peak at the four points is much greater than achievable with a cylindrical core.

3.2 COMPUTATIONAL MODEL

Because of the symmetry in the core radial sections shown in Figs. 3.1 and 3.2, only a quadrant of each core was

isolated for detailed comparison. The quadrants are marked in Figs. 3.1 and 3.2 respectively and the dimensions for the quadrant of the cylindrical section is shown in Fig. 3.3. The core was surrounded by heavy water and graphite reflector regions.

The fuel elements were taken to be 3.0 inches square in section and were homogenized by the procedure described in section 2.3 to obtain the one region homogenized core, cooled by heavy water.

A three energy group, two dimensional XY slab geometry calculation was made for each of the cores shown in Figs. 3.1 and 3.2. Leakage in the axial direction was accounted for by a group independent buckling which was taken from the work of Mathews (28). The calculated fluxes were normalized to the same power level for the two cores.

3.3 THERMAL FLUX AND POWER DENSITY PROFILES

The results of the calculations are summarized in the form of thermal flux and power density distribution profiles and given in Figs. 3.4 and 3.5 respectively. The corresponding effective multiplications are also given on the figures.

The $1.0X10^{14}$ thermal flux contour line for the criss-cross core, shown in Fig. 3.4, shows that an isolated high flux region occurs for this core as expected. However, this peak flux is only about ten per cent higher than the flux of about $9.5X10^{13}$ that is available around the entire core.

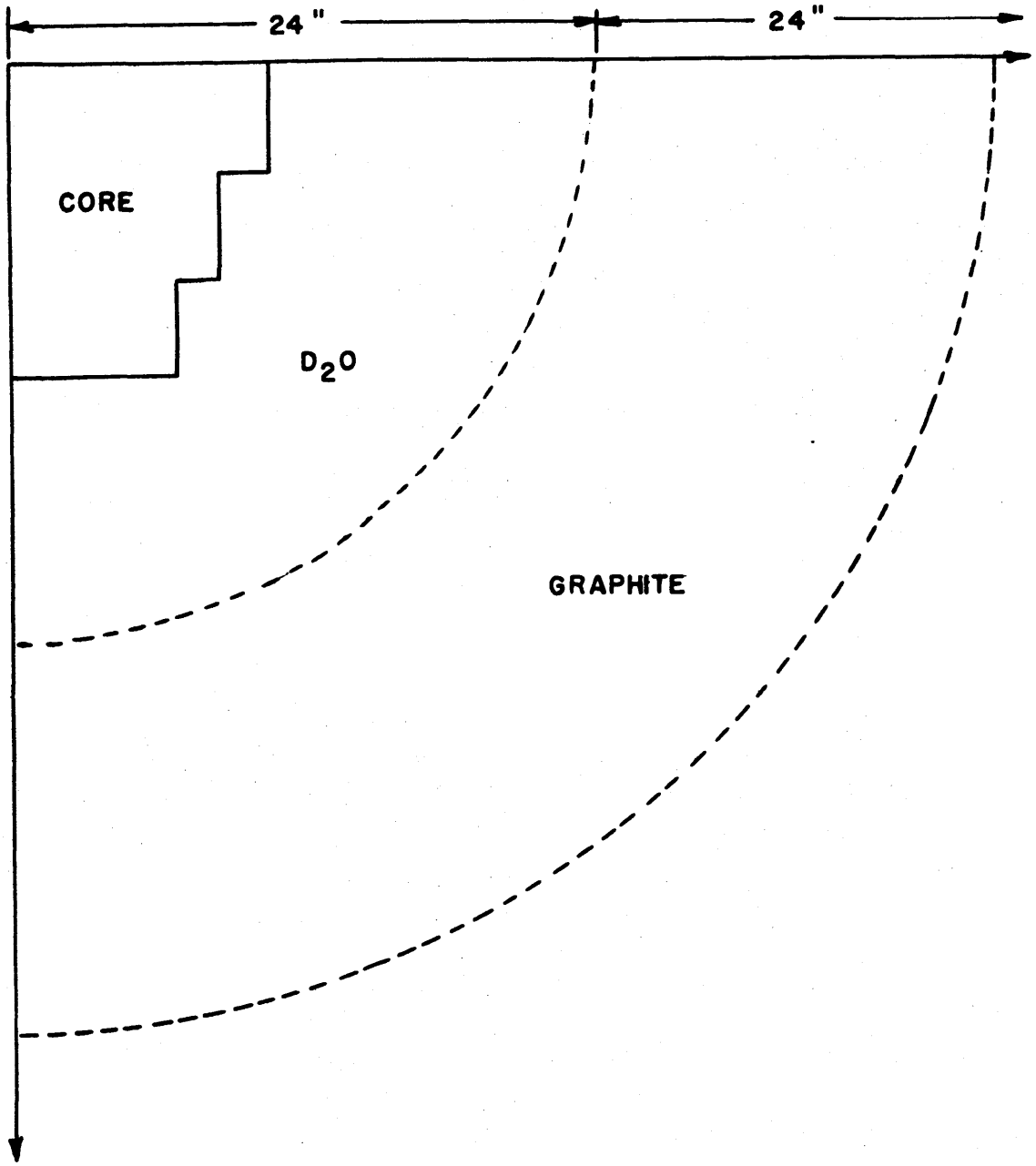

FIG. 3.3 CALCULATIONAL MODEL

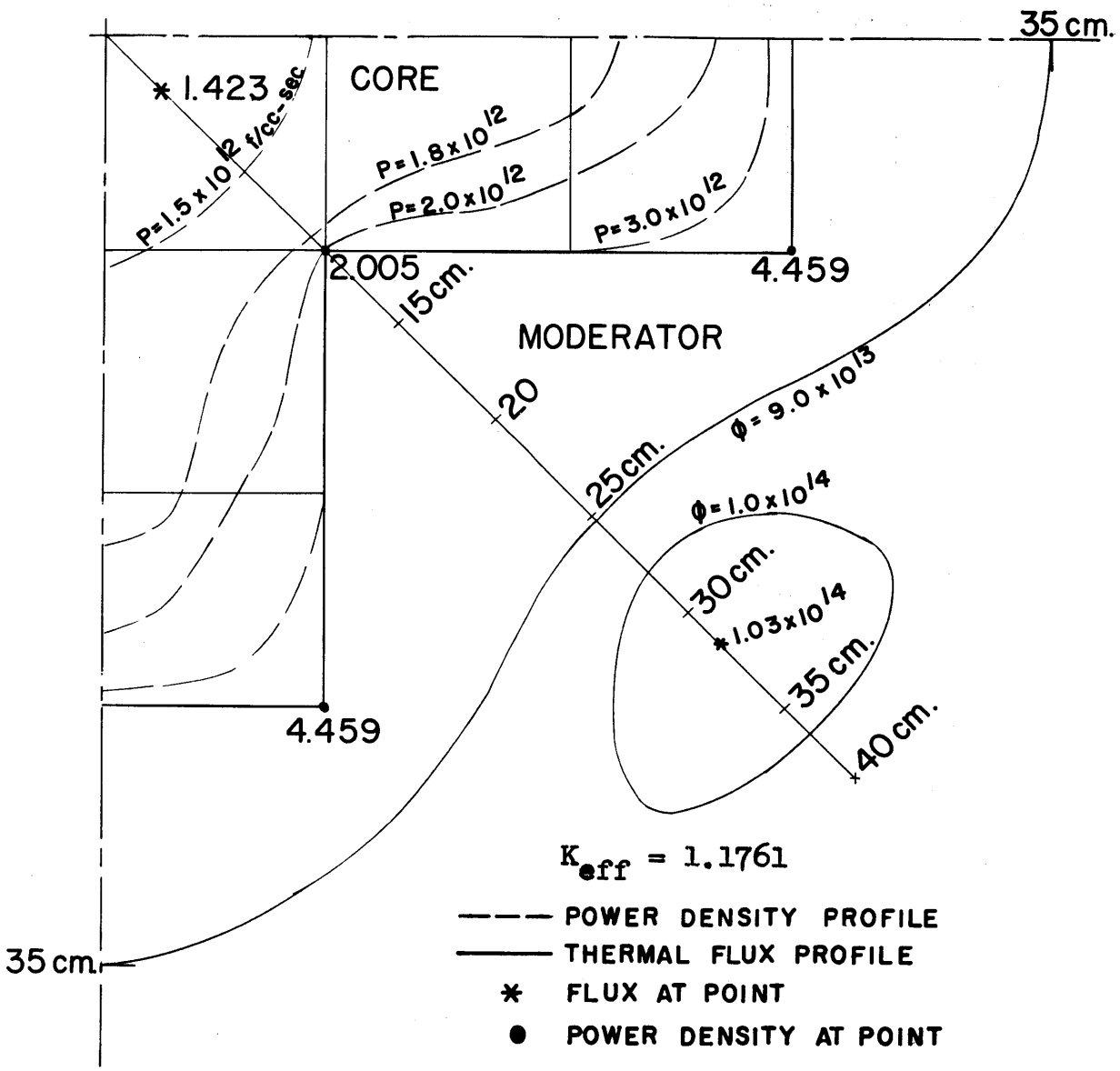

FIG. 3.4 FLUX AND POWER DENSITY PROFILES FOR THE CRISS–CROSS CORE

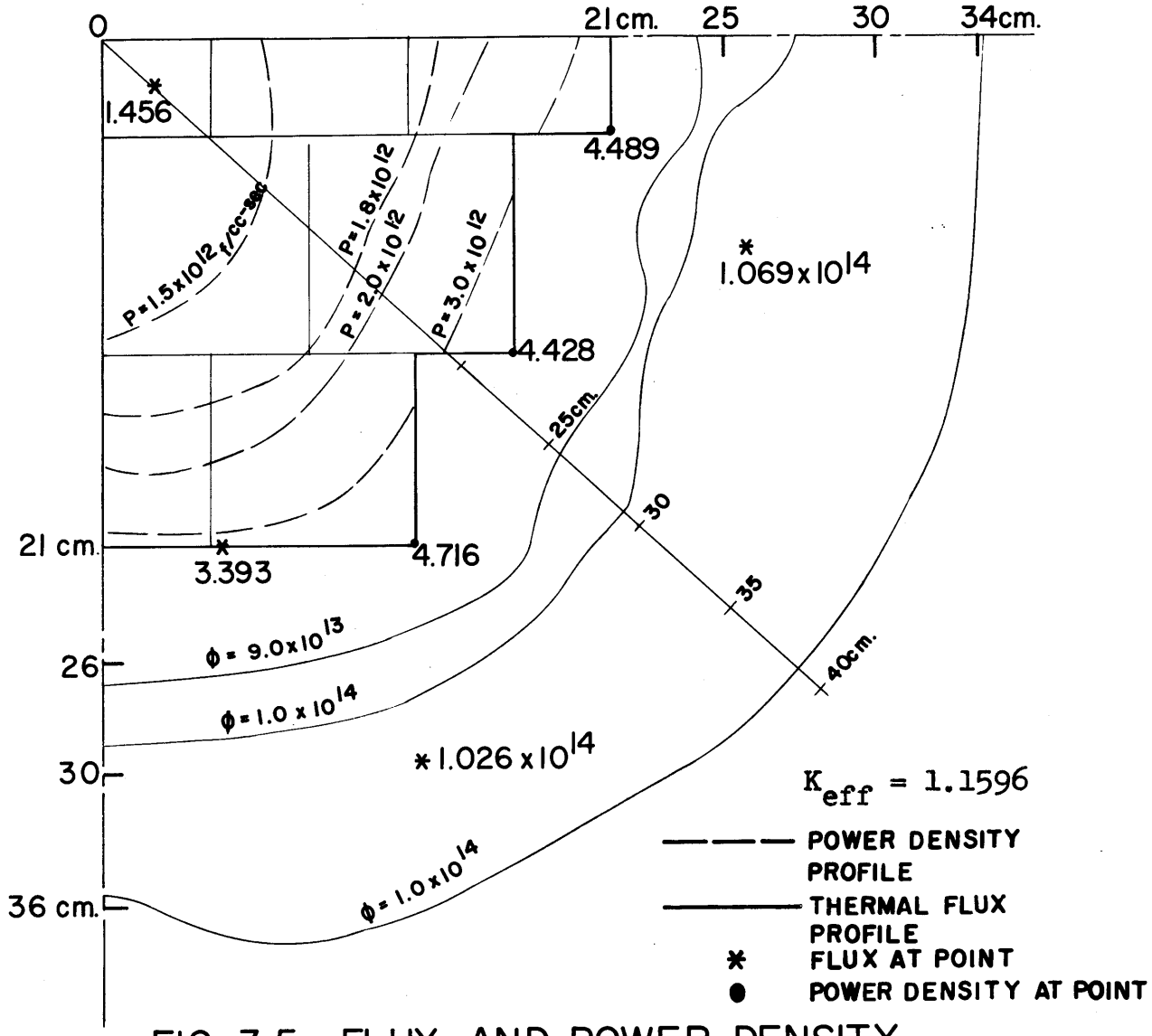

FIG. 3.5 FLUX AND POWER DENSITY PROFILES FOR NEAR CYLINDER CORE

The average radius of the flux contour lines and the size of the maximum flux regions are important features to be observed in comparing the thermal flux profiles for the two cores. First, the $9.0X10^{13}$ flux contour line is at an average radius of 25 centimeters for the cylindrical core; whereas the corresponding flux contour line for the criss-cross core occurs at a larger radius of 35 centimeters. The effective diameter of the criss-cross core is larger and this adversely affects the reflector thermal flux peak.

Secondly, an examination of the regions enclosed by the $1.0X10^{14}$ flux contour line shows that the maximum thermal flux for the two cores is about equal. However, the high flux region for the criss-cross core is restricted to a small region, whereas the corresponding region for the cylindrical geometry surrounds the entire core.

As discussed below in section 5.1, the heat transfer rate in the core sets an upper limit on the core maximum power density. In comparing the two cores, therefore, the power density distribution is important.

An examination of Figs. 3.4 and 3.5 shows that the maximum power densities occur at the corners of the elements and are about the same for the two cores. Furthermore, the $3.0X10^{12}$ fissions/cm^3-sec power density contour line shows that regions with power densities greater than $3.0X10^{12}$ fissions/cm^3-sec are distributed fairly evenly over all

the outer elements for the cylindrical core, whereas the corresponding region for the criss-cross core is limited to only the tips of elements at the outermost edges of the core.

Two important observations may be made about the maximum power density regions for the two cores. First, as the magnitude of the maximum power densities are about the same for the two cores, the limiting heat transfer rates are also equal. Secondly, the size of the high power density region at the edge of the core affects the maximum thermal flux region. This is so because the maximum thermal flux region occurs at a distance from the edge of the core equal to about the square root of the age of thermal neutrons in the reflector. The fast neutrons which thermalize in this region are principally those born at the edge of the core. The larger the fraction of the fast neutrons born near the edge of the core, the larger is the reflector thermal flux peak region as illustrated by Fig. 3.5. Spreading the power peak region over a large area near the edge of the core would, therefore, enhance the reflector thermal flux peak.

3.4 ADVANTAGES OF A CYLINDRICAL CORE

The cylindrical core appears to possess two distinct features which will be difficult to beat by other geometrical arrangements such as the criss-cross core considered.

First, the effective core radius is smallest when the fuel is arranged to form a cylinder in the radial section. Thus, although the criss-cross core does indeed exert a "focusing" effect on the thermal flux distribution in the reflector, the resulting increase in the effective core radius completely outweighs the gain in reflector flux peak. Secondly, the cylindrical core spreads out the power peak region evenly over a larger area. The importance of this feature is that a larger core region feed source neutrons into the reflector maximum thermal flux region. Thus, for the same upper limit on the core power density, the cylindrical core will not merely result in a reflector maximum thermal flux which is as high as can be achieved by other core geometrical arrangements, but also this maximum thermal flux region spreads symmetrically around the entire core to feed all experimental beam ports with the reflector maximum thermal flux.

CHAPTER IV

HEAVY WATER COOLED AND REFLECTED CORES

The purpose of redesigning MITR is to increase the magnitude of the reflector thermal neutron flux at the tips of experimental beam ports as well as cut down on the fast neutron and gamma radiation background. On the basis of the work discussed in Chapter 3 a cylindrical core radial section has been chosen. In this chapter, the thermal neutron flux distribution around a cylindrical core, cooled, moderated, and reflected by heavy water, is examined. The optimum core arrangement is sought to provide neutron beams for experiments with the maximum thermal neutron flux and simultaneously reduced in both the fast neutron and gamma radiation background.

4.1 COMPLETELY REFLECTED CYLINDRICAL CORE

The thermal flux distribution as well as the power density profiles for a completely reflected core without control rods was examined first.

4.1.1 Computational Model

Figure 4.1 shows the schematic of the six region reactor model used. The normal MITR fuel element (1)

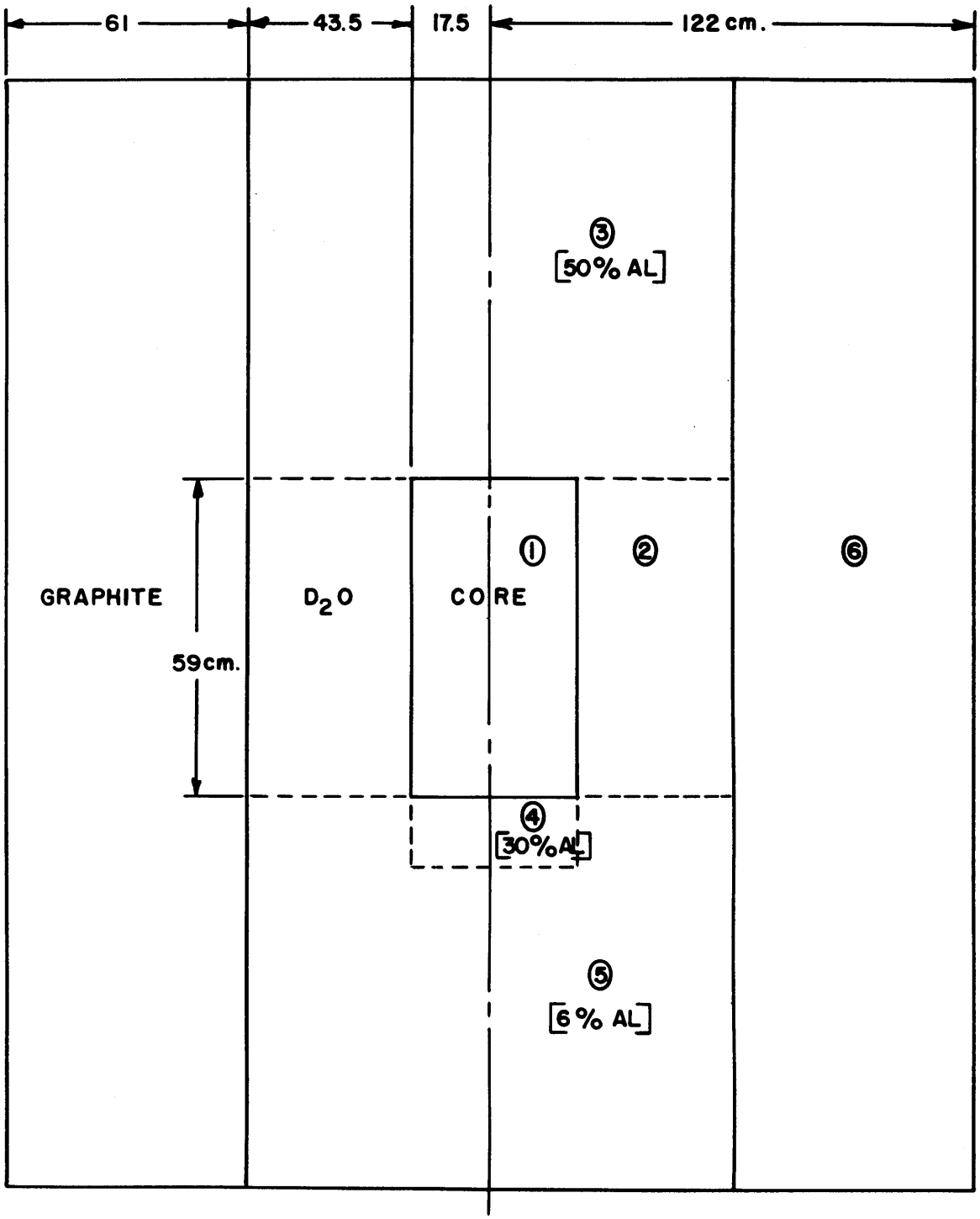

FIG. 4.1 D_2O COOLED AND REFLECTED CORE MODEL

which has 160 ± 5 grams of uranium-235 was homogenized. The resulting atom number densities are given in Table 4.1. The core, region one of Fig. 4.1, had a height of twenty-four inches and volume equivalent to that of nineteen fuel elements. The core was immersed in heavy water reflector of radius of two feet, equivalent to the radius of present MITR heavy water tank. This heavy water reflector was subdivided into four regions, namely regions two to five, and different volume fractions of aluminum included in regions three to five to represent the effect of structural material. The aluminum volume fractions in regions three to five were 50 per cent, 30 per cent, and 6 per cent respectively. The graphite reflector, region six, was of radial thickness of two feet, which is also the same dimension as that of the graphite in present MITR-I.

A three neutron energy group two dimensional RZ cylindrical calculation was performed, by using modified TWENTY GRAND code (40). The composition of the homogenized compact core was that of the homogenized fuel element composition given in Table 3.1 and the reactor power was normalized to five megawatts.

4.1.2 Thermal Flux and Power Density Profiles

Two cases were made. First, a run was made in which aluminum was excluded from regions three through five of the

TABLE 4.1

Calculated Atom Number Densities for an MITR-I 160-Gram Fuel Element with all 18 Plates Active

U-235	1.4565×10^{20}
U-238	1.0983×10^{19}
Heavy Water	1.8951×10^{22}
Aluminum	2.5518×10^{22}

heavy water reflector. Secondly, the run was repeated with 50 per cent, 30 per cent, and 6 per cent by volume of aluminum in regions three through five of the heavy water reflector. The results of these two runs are summarized in Figs. 4.2 and 4.3 respectively in the form of thermal neutron flux and power density distribution.

Two important features about the thermal flux distribution to be observed are the location of the reflector maximum thermal flux region and the effect of structural materials, simulated by the aluminum in the heavy water reflector, on the thermal neutron flux distribution. Both figures 4.2 and 4.3 show that the reflector maximum thermal flux region occurs about thirty centimeters from the core and centered about the plane through the core mid-height. This region can be reached by re-entrant beam ports to extract neutron beam for experiments. However, if the present radial beam ports are merely made re-entrant to extract the neutron beam at about thirty centimeters from the core, both fast neutron and gamma radiation background will be worse than the current levels.

There are two possible beam port arrangements that will permit re-entrant beam ports to extract neutron beam at a close distance from the core as well as cut down on the fast neutron and gamma radiation background. The first arrangement is to orient beam ports tangentially to the core at the mid-plane. Fast neutrons will then have to undergo large

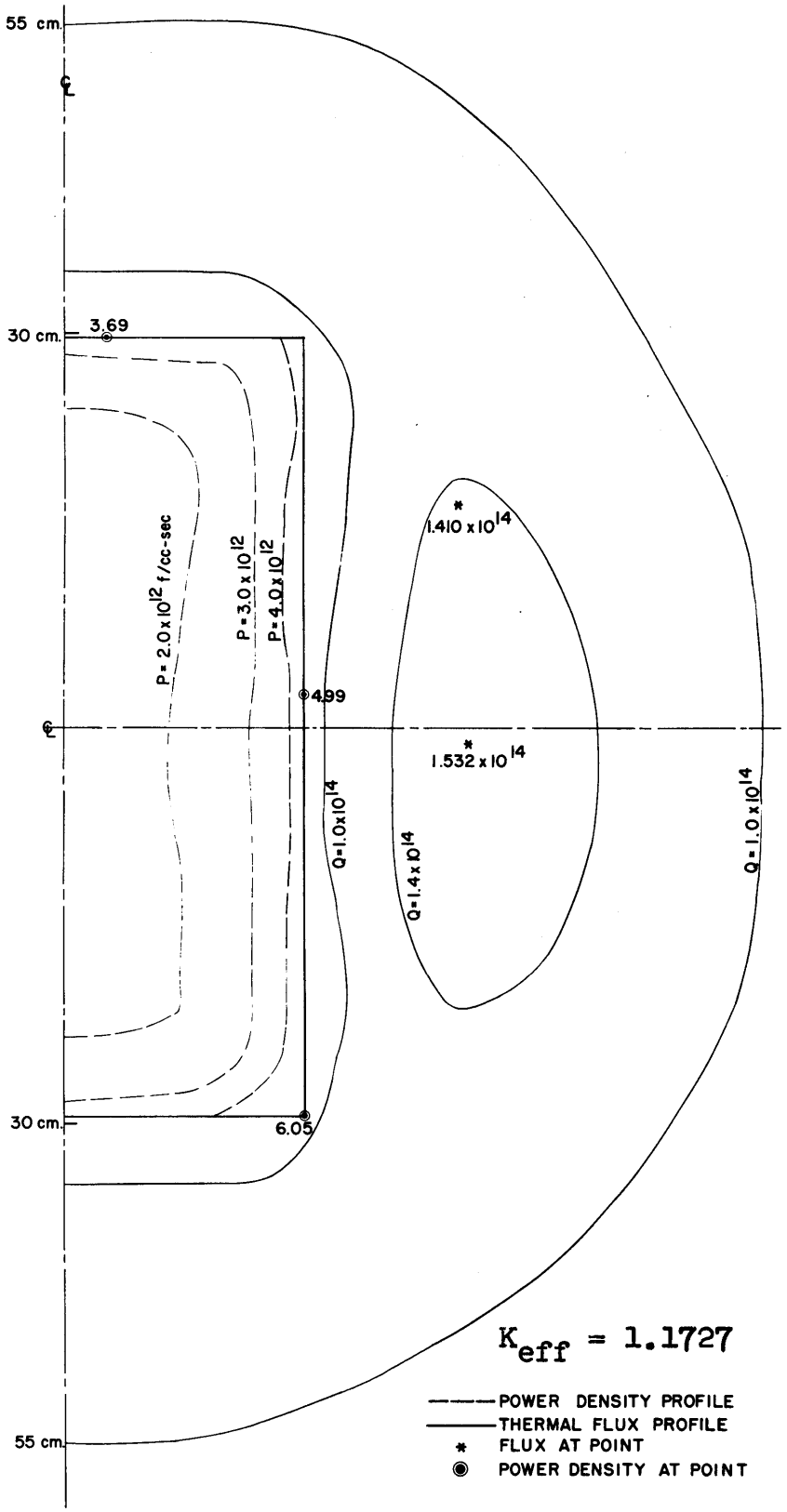

FIG. 4.2 FLUX AND POWER PROFILES
(NO ALUMINUM IN REFLECTOR)

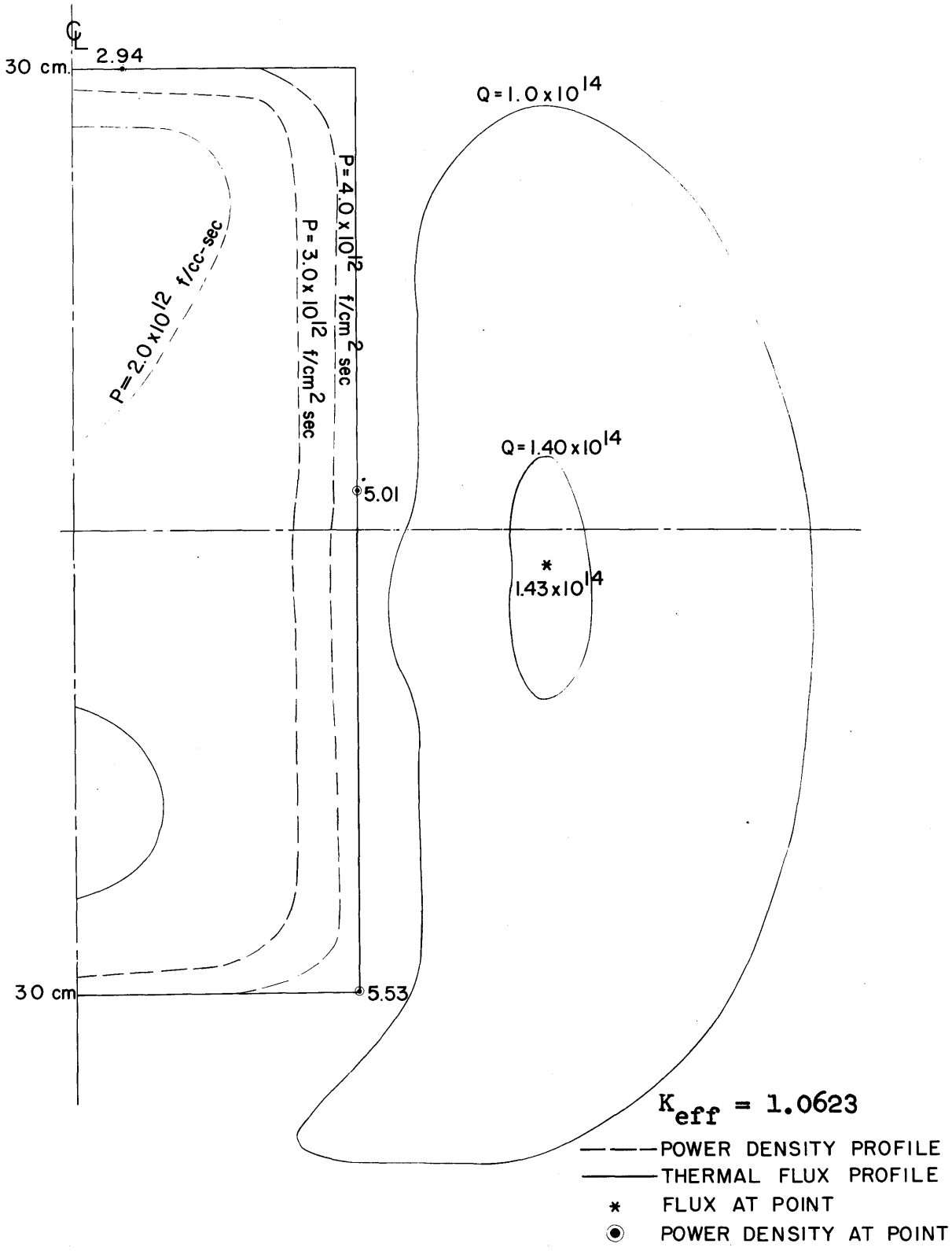

FIG. 4.3 FLUX AND POWER PROFILES (ALUMINUM IN REGIONS 3 TO 5)

angle scattering before entering the beam ports. This arrangement has been found to cut down significantly on the fast neutron and gamma radiation background (7). The second arrangement is to raise the core such that re-entrant radial beam ports view the reflector below the bottom of the core tangentially. Fast neutons will again have to undergo large angle scattering before entering the beam ports. Both methods will result in considerable reduction of the fast neutron and gamma radiation background.

A comparison of the $1.0X10^{14}$ thermal neutron flux contour line in Figs. 4.2 and 4.3 shows the effect of the presence of structural materials (simulated by the aluminum in the heavy water) on the thermal flux available in the two regions from which neutron beams may be extracted for experiments with the minimum fast neutron and gamma radiation background. For this completely reflected cylindrical core, therefore, in addition to the fact that the maximum thermal flux region occurs at the core mid-height rather than underneath the core, structural materials which normally occur at the ends of the core, cause a more significant decrease in the thermal neutron flux underneath the core than at the mid-height. For this type of core, beam ports oriented tangentially to the core at the mid-plane will extract the highest beam port current as well as cut down significantly on the fast neutron and gamma radiation background. These are the ideal types of beam ports for this kind of core.

4.2 CYLINDRICAL CORE WITH THE UPPER-HALF POISONED

For a completely reflected undermoderated core, the ideal beam ports are those oriented tangentially to the core at the mid-height. The radial beam ports of MITR-I are permanent features and cannot be re-oriented. In order to extract reflector maximum thermal neutron fluxes for experiments, with reduced fast neutron and gamma radiation background, the reflector maximum thermal neutron flux region must be forced to appear underneath the core. The MITR radial beam ports would then be made re-entrant to extract neutron beam from underneath the core.

The ability of control rods to influence significantly the thermal neutron flux distribution in a thermal reactor has been suggested (49). The effects of poisoning the upper half core with neutron absorbers in order to force the reflector thermal flux region to appear underneath the core are examined below.

4.2.1 Calculational Model

The thirteen region reactor model used for the calculations is shown in Figure 4.4. The core, region one, was chosen to be a homogeneous model of material composition equivalent to the homogenized composition of present MITR fuel elements given in Table 4.1. The core height of 24 inches was used, and a diameter of 17 inches. Two rings of

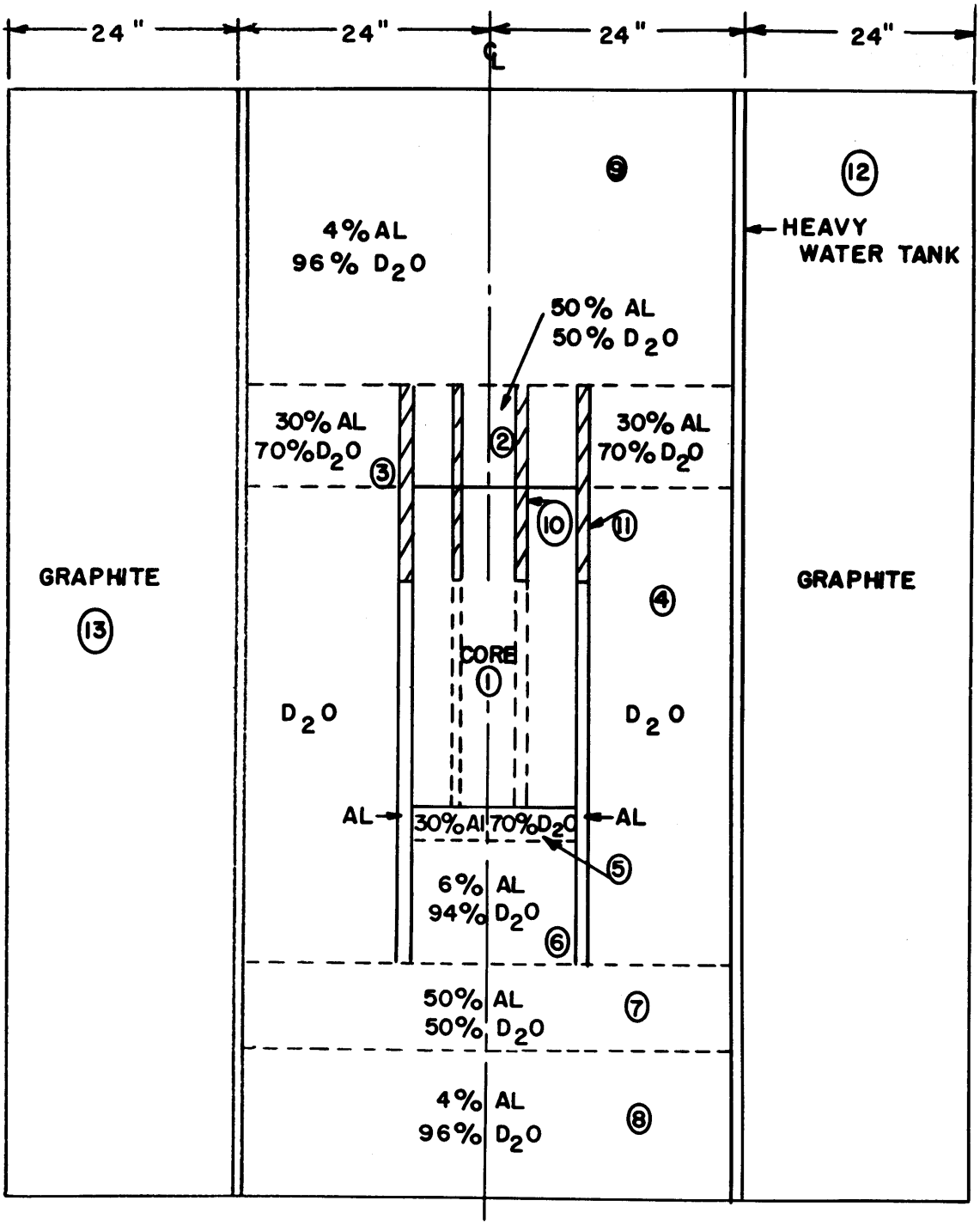

FIG. 4.4 D_2O COOLED AND REFLECTED WITH THE UPPER HALF POISONED CORE MODEL

natural boron absorbers were included in the top eight inches of the core. The inner ring was of an internal diameter of 4 1/2 inches while the outer ring was 17 inches in internal diameter. Each absorber ring was homogenized with aluminum over a total thickness of 0.25 inches, this much aluminum being considered adequate to account for the total aluminum necessary to provide cladding and structural support for the 0.040 inch-thick absorbers. The regions directly under the absorbers were filled with aluminum. For the outer ring, the aluminum beneath the absorber indeed represented the reactor core tank.

The core was surrounded by heavy water reflector, contained in an aluminum tank. The thickness of the heavy water tank, region 12, was 0.50 inches thick with an ID of 4 feet. In order to obtain the net effect of the structural materials on the thermal flux distribution, the heavy water reflector was divided into eight regions, regions two through nine of Fig. 4.4, and aluminum added in these regions in volume functions corresponding to the actual structural material that would be in those regions.

For instance, as it was necessary to reduce structural materials as much as feasible in the region underneath the core to enhance the thermal flux there, fuel element design that had a long lower adapter compared with that in the present MITR, was considered. Region six represents the homogenized lower adapters while region seven represents

the plenum head together with associated structural support. Region five represented a high aluminum concentration region occupied by the joint between a fuel element and the corresponding lower adaptor.

Three neutron energy groups, two dimensional RZ cylindrical calculation was made, with the EXTERMINATOR-II code. The calculated fluxes were normalized to five megawatts.

4.2.2 Thermal Neutron Flux Distribution

The results of the calculations are summarized in Fig. 4.5 in the form of thermal flux distribution. A comparison of the lower K_{eff} in this system with those obtained for the slightly smaller cores described in section 4.1 (Figs. 4.2 and 4.3) gives an indication of the large penalty in reactivity incurred by using this core configuration. A comparison of the $1.0X10^{14}$ thermal neutron flux contour line also gives an indication of the effect of the slight increase in core diameter as well as the presence of the large amounts of structural materials in the core on the reflector maximum thermal neutron flux.

The $1.0X10^{14}$ thermal neutron flux contour line also shows the effect of the absorbers in the upper half of the core on the location of the reflector maximum thermal flux region. The reflector maximum thermal flux region is forced to appear near the bottom of the core. Tips of beam ports

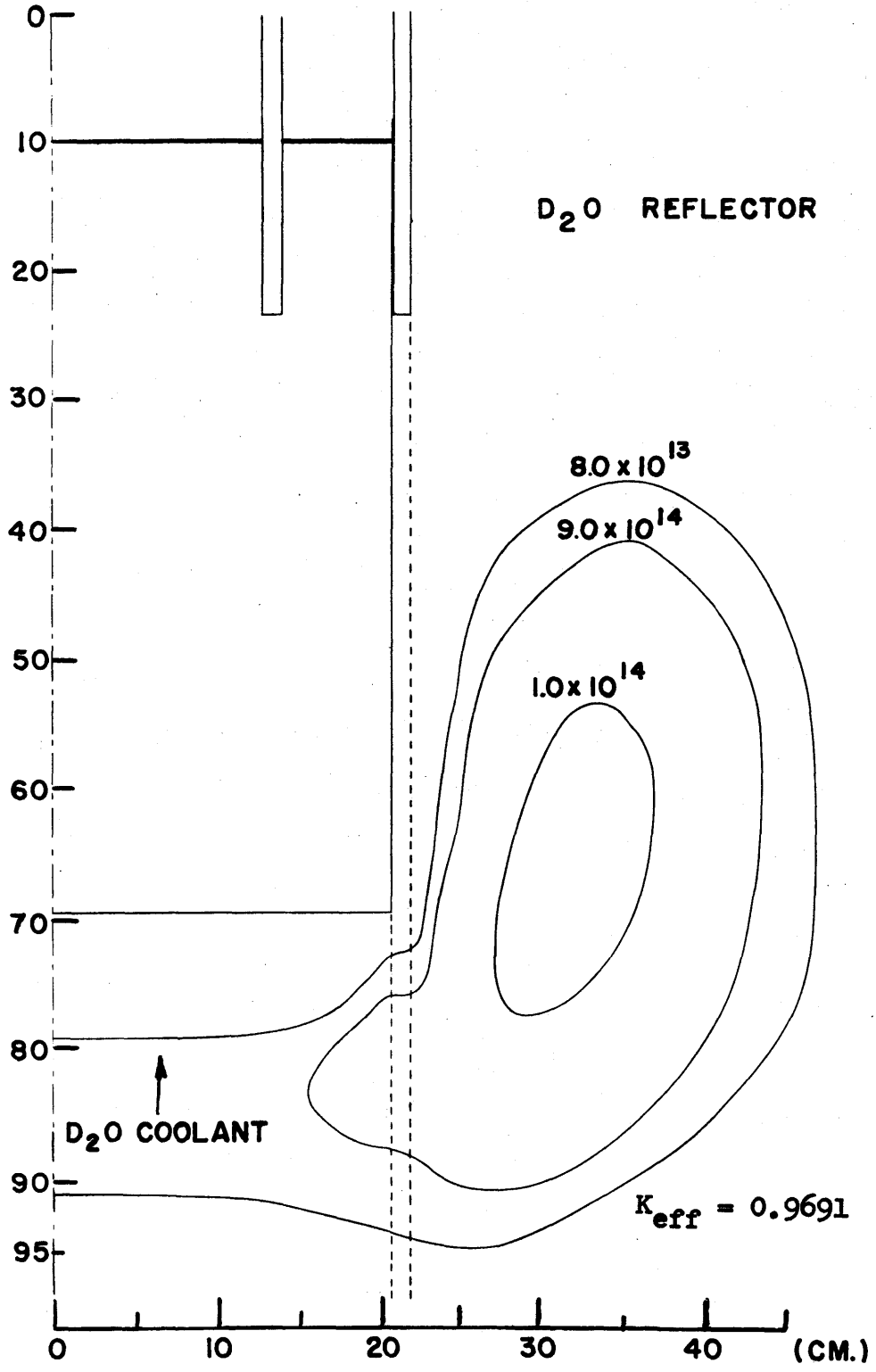

FIG. 4.5 D_2O COOLED AND REFLECTED CORE WITH THE UPPER HALF POISONED

made re-entrant to a circle of about 30 inches diameter would be exposed to unperturbed thermal neutron fluxes of about $1.0X10^{14}$ n/cm^2-sec, relatively free of fast neutron and gamma radiation background.

There are three important features of this core configuration. First, the most serious safety consideration is the large reactivity worth of the absorber rings. A thorough examination of this problem has shown that a good mechanical design of outer (control) ring as well as the inner (fixed absorber) ring can assure the safe operation of the core. A fail-safe control rod mechanism, designed by E. Barnet (2), has weight distribution which assures that under all conceivable conditions of operation, the control rods would always fall into the fully inserted position. The inner control ring, which will be fixed in position, is designed such that it would be accessible only after the reactor as well as coolant pumps have been shut down.

Secondly, the double core arrangement is an advantage from the point of view of fuel element utilization. As the lower part of the elements are subjected to high power densities and hence high burn-up rates, when the lower end of an element is burned up it can be removed and flipped over, putting the fresher upper end into the high flux region.

Thirdly, studies showed that the reflector maximum thermal flux region which has been forced to appear near the bottom of the core is not very stable. The accumulation

of stable fission products or xenon and the burn-up of the lower tips of the control rings as well as the lower end of the core tend to cause the reflector maximum thermal flux region to move away from the bottom of the core, resulting in a decrease of the thermal neutron flux seen by the tips of the re-entrant beam ports.

4.2.3 Effects of Making Bottom End of the Core Spherical

The ability to force the reflector maximum thermal neutron flux region to appear underneath the core is highly dependent on the insertion of the neutron absorber rings. However, a reactivity loss accompanies the insertion of the absorbers and some of the conditions which cause the need to insert the absorbers, such as the burn-up of the lower tips of the fuel elements or the accumulation of xenon, occur when the reactivity in the system is already low. Thus, the method of forcing the maximum reflector thermal neutron flux region to appear underneath the core with the neutron absorbers is not always feasible. The effects of making the bottom end of the core nearly spherical were examined.

A sphere has the smallest surface area to volume ratio. By making the bottom end of the core spherical, leakage of fast neutrons in this region would be increased, resulting in a reflector thermal neutron flux peak along the entire core bottom.

The core model used to study this effect is identical to that shown in Fig. 4.4, except for one change. The lower adoptors, region six of Fig. 4.4, were made of different lengths for each of the three rings of elements in the core. The first ring of elements are those enclosed by the inner absorber ring; the second and third rings occupy the space between the inner and outer absorber rings, with the second ring of elements next to the inner absorber ring. The lower adoptors for the first ring of elements were unchanged relative to those shown in Fig. 4.4; those for the second and third rings of elements were progressively made longer, so that the shape of the bottom end of the core was a stepped sphere. The core as well as the thermal neutron flux distribution around it obtained with the EXTERMINATOR-II code, is shown in Fig. 4.6.

The thermal flux distribution underneath this core spreads out more uniformly. However, calculations showed that this high flux underneath the core tends to move towards the core mid-height as the control rod tip is moved up.

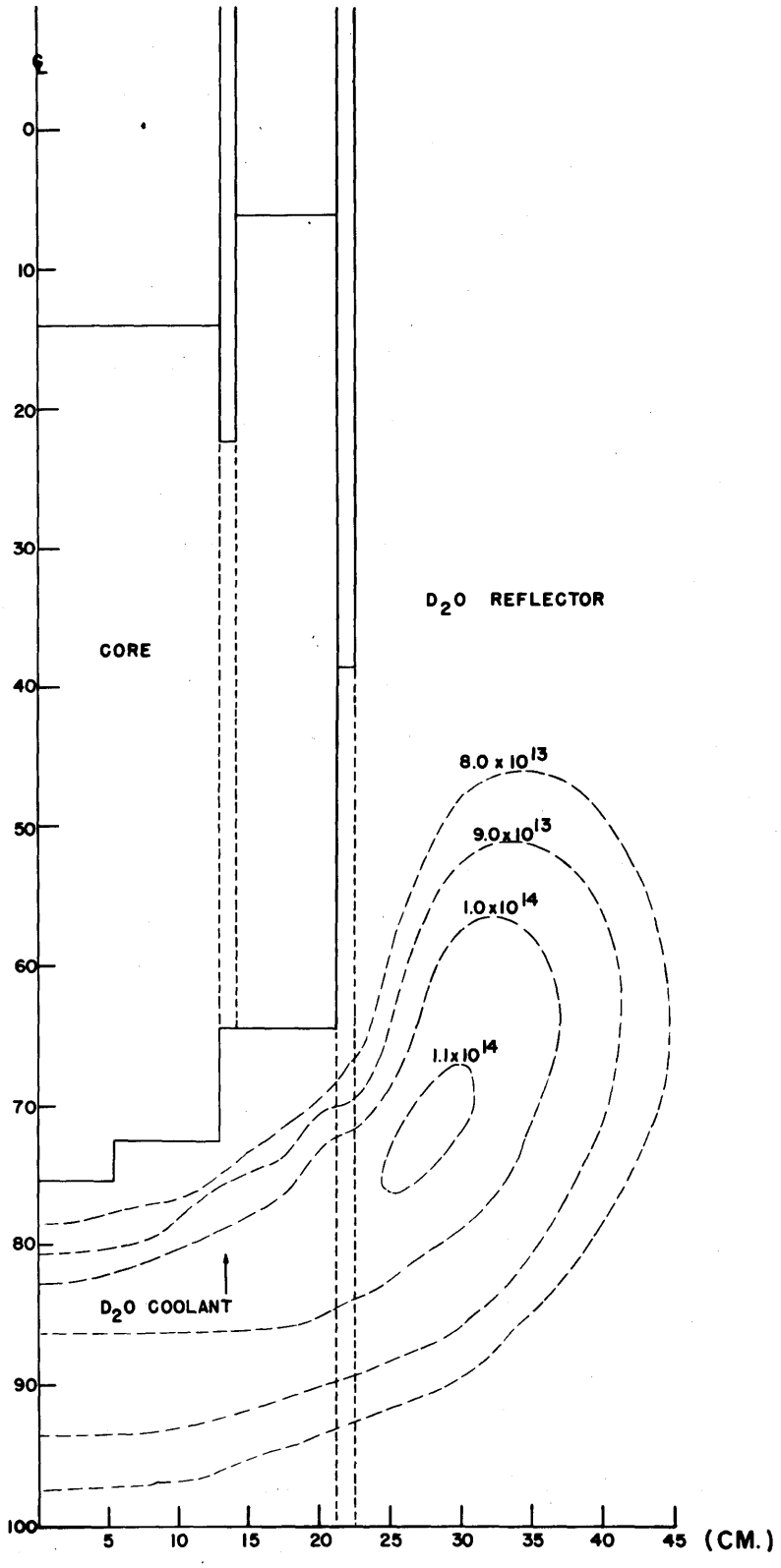

FIG. 4.6 THERMAL FLUX PROFILES AROUND THE SPHERICAL BOTTOM CORE

CHAPTER V

CORES REFLECTED BY HEAVY WATER AND COOLED BY LIGHT WATER AND HEAVY WATER MIXTURES

The work discussed in the previous chapter shows that an undermoderated core, cooled and reflected by heavy water with the upper half core poisoned, can be designed so that radial beam ports could be made re-entrant to extract thermal neutron beams from underneath the core. These beams would be relatively free of fast neutron and gamma radiation background. The reflector thermal neutron flux level underneath the core is dependent on many factors. Some of the factors affecting the reflector maximum thermal neutron flux underneath the core are explored in this chapter.

In particular, the advantages of cores reflected by heavy water and cooled by light water and heavy water mixtures are examined.

5.1 FACTORS AFFECTING REFLECTOR MAXIMUM THERMAL NEUTRON FLUX

An undermoderated core is a sink for the thermal neutrons and a source of fast neutrons, while the reflector is a sink for the fast neutrons and a source of thermal neutrons. The reflector thermal neutron flux peak, therefore, depends on the number of neutrons leaking from the core into the reflector. This number of fast neutrons leaking into the reflector

Fig. 5.1 FACTORS AFFECTING THE REFLECTOR MAXIMUM THERMAL NEUTRON FLUX

1. Fixed reactor power level of five megawatts
2. Fuel meat alloy
3. Uranium density in fuel meat
4. Heat transfer rate
5. Core diameter
6. Reflector design
7. Moderation in the core
8. Power peaking factor

depends not only on the total number of fast neutrons produced in the core per unit time, in other words the reactor power level, but also on many other factors. Eight of these important factors are listed in Fig. 5.1.

5.2 FACTORS WHICH IMPOSED CONSTRAINTS ON THE PROBLEM

The first four of the factors which affect the reflector maximum thermal neutron flux, listed in Fig. 5.1, imposed constraints on the problem because of their values chosen for the present reactor. The reactor power level was limited to the five megawatts chosen for the present MITR. The plate-type fuel element design, using the aluminum-uranium fuel meat technology was retained. Mechanical design considerations ruled out pressurizing the present primary coolant loop system in order to raise the maximum permissible surface temperature of the fuel plate. Thus, the modifications needed in the other features of the present reactor to fully benefit from a more advanced fuel plate design were far more extensive than envisaged. However, advantage was taken of the advances in the aluminum-uranium fuel meat technology; as the weight percentage of uranium in the fuel meat up to about thirty-nine is currently being successfully manufactured (55), the uranium weight percentage in the fuel meat was increased considerably above the present value of 18 per cent.

5.2.1 Heat Transfer Rate

Heat transfer rate from the core is the most important factor that limits the reflector maximum thermal flux. In a small undermoderated core, the reflector maximum thermal neutron flux depends on the power densities in the power peak region at the core-reflector interface; and the heat transfer rate limits power densities in the core such that no type of boiling can be allowed for the safe operation of the reactor.

The influence of the power density on the reflector peak thermal neutron flux has already been pointed out in section 3.3. The maximum reflector thermal neutron flux occurs at a distance from the core equal to about the square root of the age of thermal neutrons in the reflector. The fast neutrons born near the core-reflector interface contribute most significantly to the rate of slowing down into the thermal energy group in this region of the reflector. The degree of undermoderation also plays a role. The higher the degree of undermoderation in the core, the greater is the probability that neutrons born inside the core leak into the reflector. Work discussed below shows that the greater the undermoderation in the core, the greater the power densities at the core-reflector interface, resulting in a higher reflector thermal flux peak. The core, therefore, must be designed to operate at the maximum permissible power

densities in order to produce the maximum reflector thermal neutron flux.

The maximum permissible power density in the core is determined by the limiting fuel plate surface temperature as well as the heat transfer rate in the core. The safety limit on the fuel plate surface temperature which will ensure the structural integrity of the fuel elements has been set at 450°C in the Technical Specifications for the present MITR (50); the onset of incipient boiling of the coolant under operating conditions is the conservative operating limit set on the fuel plate surface temperature to establish stable operating condition with fuel plate temperatures well below the safety limit.

The fuel plate surface temperature at axial position Z from the hottest coolant channel inlet, $T_W(Z)$, is made up of three components as

$$T_W(Z) = T_o + T_B(Z) + T_F(Z) \qquad \ldots 5.2.1.$$

where T_o equals the nominal bulk inlet coolant temperature, $T_B(Z)$ equals the bulk coolant temperature rise up to the axial position Z, and $T_F(Z)$ equals the film temperature rise at the axial position Z.

For the present MITR operating at five megawatts, the maximum operating limit of $T_W(Z)$ is about 100°C, the saturation temperature of the coolant; T_o is limited to about 46°C while $T_B(Z)$ has a maximum value of about 9°C (51). Thus, $T_F(Z)$ is the dominant variable term of the fuel

plate surface temperature and can be expressed directly in terms of the maximum permissible power density as

$$T_F(Z) = K_c F_d PD(Z)/Ah \qquad \ldots 5.2.2.$$

where K_c = a conversion factor

F_d = fraction of fission energy deposited directly at the site of fission

$PD(Z)$ = the maximum permissible power density at the hottest channel axial position Z

A = channel heat transfer area

h = heat transfer coefficient

For a given limiting fuel plate surface temperature, power densities in the core can be increased only if the product of the channel heat transfer area and the heat transfer coefficient, Ah, is increased.

The modified Colburn heat transfer correlation is (52)

$$\frac{hD_e}{K_f} = 0.023\left[\frac{D_e VP}{\mu}\right]^{0.8}\left[\frac{C_p \mu}{K}\right]^{0.3} \qquad \ldots 5.2.3.$$

where, h = heat transfer coefficient

D_e = coolant channel equivalent diameter

K_f = thermal conductivity of coolant

V = coolant velocity

P = coolant density

μ = coolant viscosity

C_p = specific heat

The heat transfer coefficient is observed to be proportional to the four-fifths power of the velocity, if only the velocity

term in equation 5.2.3 is changed. Although the plate-type fuel element has been successfully operated at water velocity in coolant channel at about 35 ft/sec. (7), the corresponding velocity in the present MITR is only 3.5 ft/sec. Thus, nearly a factor of six increase in the heat transfer coefficient, h, can be realized by increasing the water velocity in the MITR coolant channels. Preliminary calculations showed that to increase the total mass flow rate through the core by fifty per cent would require at least one additional heat exchanger and the necessary equipment modifications were too extensive.

The alternative means considered for augmenting the heat transfer rate in the core are discussed by Spurgeon (51). Fuel plate finning as a means of increasing the product Ah was the technique adopted (51). On the basis that a factor of 1.8 increase in Ah could be realized by fuel plate finning and that if the core size is decreased such that the decrease in the core size alone would lead to a factor of 2.1 increase in the water velocity in the coolant channels, the maximum permissible power densities in the homogenized core were limited to about 1.0×10^{13} fission/cm^3-sec.

5.3 FACTORS WHICH WERE OPTIMIZED

The last four of the factors which affect the reflector

maximum thermal neutron flux, listed in Fig. 5.1, were selected in order to enhance the reflector maximum thermal neutron flux underneath the core.

The core diameter had two important effects. It was found that the smaller the effective diameter of a small undermoderated core of fixed power level and height, the higher are both the reflector thermal neutron flux peak and the maximum power density at the core-reflector interface. The smallest core diameter was chosen such that power densities did not exceed the maximum permissible level. For the heavy water cooled and moderated cores, a core diameter of about 18 inches was found to be a good limiting value.

Two properties of the reflector material were found to be most important. The shorter the effective slowing down length of fission neutrons in the reflector, the more rapidly the thermal neutron flux peaks close to the core. On the other hand the longer the thermal neutron diffusion length in the reflector, the less steeply the reflector thermal neutron flux falls off with increasing distance away from the core after reaching the peak value. The very short effective slowing down length of fission neutrons in light water makes it excellent from the point of view of the first consideration; however, the very short diffusion length of thermal neutrons in this reflector causes the reflector thermal neutron flux to fall off too rapidly. A composite

heavy water reflector design has been used. This composite reflector had a restricted amount of light water underneath the core, between the core and the reflector. The thin layer of light water suffices to moderate most of the fission neutrons leaking from the core to the point where they are rapdily thermalized in the heavy water reflector. This reflector design is discussed in section 6.4.3.

Moderation in the core and power peaking affected both the reflector thermal neutron flux peak and the power densities in the core. The effects of using light water and heavy water mixture as the core coolant to effect changes in moderation in the core are discussed below.

5.4 EFFECTS OF MODERATION IN THE CORE

Since the degree of neutron moderation in the core affects the reflector maximum thermal neutron flux peak as well as the power peaking difficulties at the core-reflector interface, it was necessary to study variations in the neutron moderation in the core. In addition, there were two equally important reasons for examining the effects of moderation in the core. First, fuel plate finning was considered as a means of augmenting the heat transfer rate in the core and as this involves replacing heavy water coolant with aluminum, it was necessary to know the effects of the resulting decreased moderation in the core. Secondly,

reducing the spacing between the fuel plates was comtemplated as a means of increasing the uranium loading in the core as well as the total core heat transfer area.

5.4.1 Calculational Model

The calculational model used is the same as that described in section 4.2.1 and shown in Fig. 4.4. The inner absorber ring was withdrawn to the top of the core while the outer absorber ring insertion was eight inches. The core height was 24 inches and a diameter of 18 inches.

5.4.2 Effects of Replacing D_2C Coolant with Aluminum

The effects of replacing heavy water coolant with aluminum were examined. A standard fuel element of MITR-I with coolant channel width of 0.116 inches and fuel plate thickness of 0.050 inches was homogenized. The fuel plate consisted of a 0.020 inch thick fuel meat clad on both sides with 0.015 inch thick aluminum. The homogenized core composition was taken to be the same as the homogenized fuel element composition. The equivalent uranium-235 loading of the "double" core was 9.10 Kg. A three-group two dimensional R-Z cylindrical geometry calculation was performed using the EXTERMINATOR-II code.

The procedure was repeated using the same standard fuel element with only one change being made; the pitch between fuel meat remained unchanged but the cladding thickness was increased in two steps from 0.015 inches to 0.028 inches with the corresponding decrease in the coolant channel width from 0.116 inches to 0.090 inches. The uranium-235 loading in the core, therefore, remained constant at 9.10 Kg, corresponding to core volume fraction of 0.575 per cent.

The results of the calculations are summarized in the form of effective multiplication as well as maximum power density in the core, and the reflector maximum thermal neutron flux 2.5 inches underneath the core versus percentage volume fraction of aluminum in the core curves, given in Figs. 5.2A and 5.2B. The thermal neutron flux at axial distance mid-way between the lower tip of the outer absorber ring and the core bottom (active core mid-height) is also given in Fig. 5.3 for the two cases corresponding to the 0.116 inches and 0.090 inches coolant channel widths.

From Figs. 5.2A and 5.2B it is clear that the undermoderation in the core resulting from the replacement of the heavy water coolant with aluminum causes the leakage flux underneath the core to increase, though the maximum power density in the core increases and the effective multiplication in the system decreases as well. The decrease in the effective multiplication in the system is due to the higher leakage rate of the fission neutrons into the reflector as

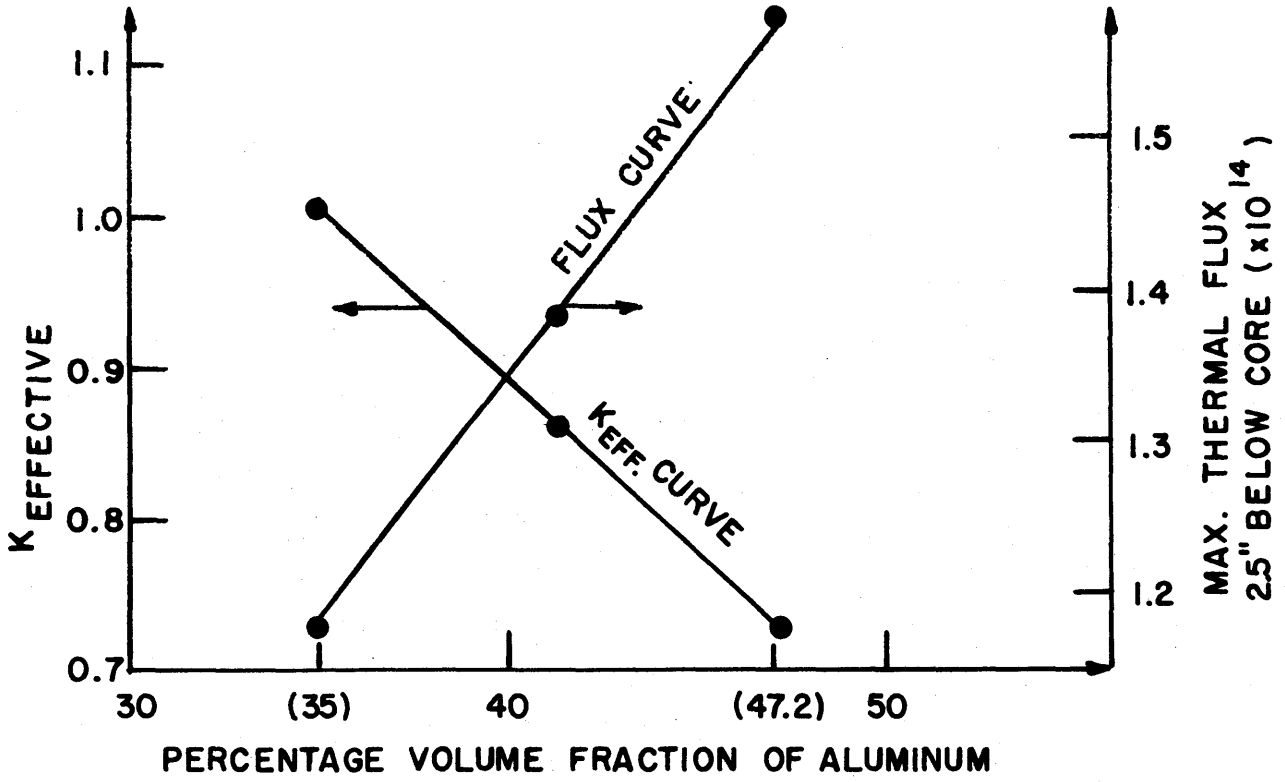

FIG. 5.2A EFFECT OF REPLACING COOLANT WITH ALUMINUM ON $K_{EFF.}$ AND REACTOR FLUX

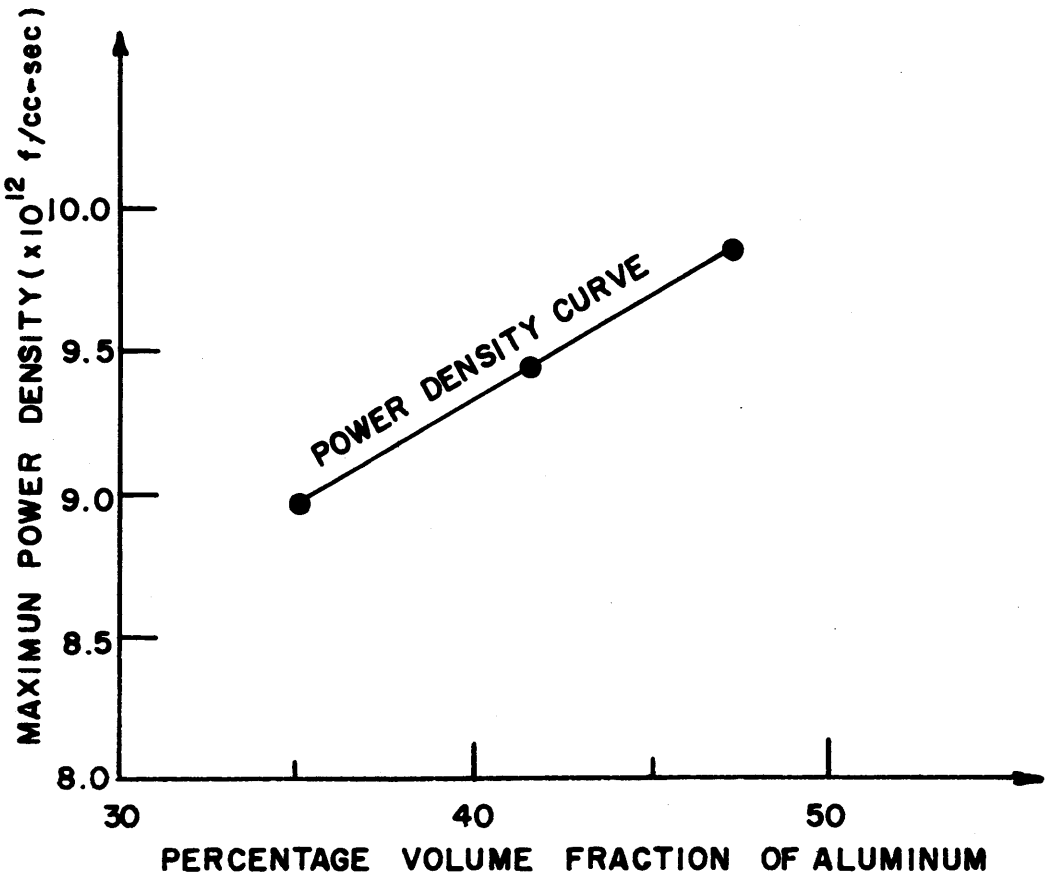

FIG. 5.2B THE EFFECT OF REPLACING COOLANT WITH ALUMINUM ON POWER DENSITY

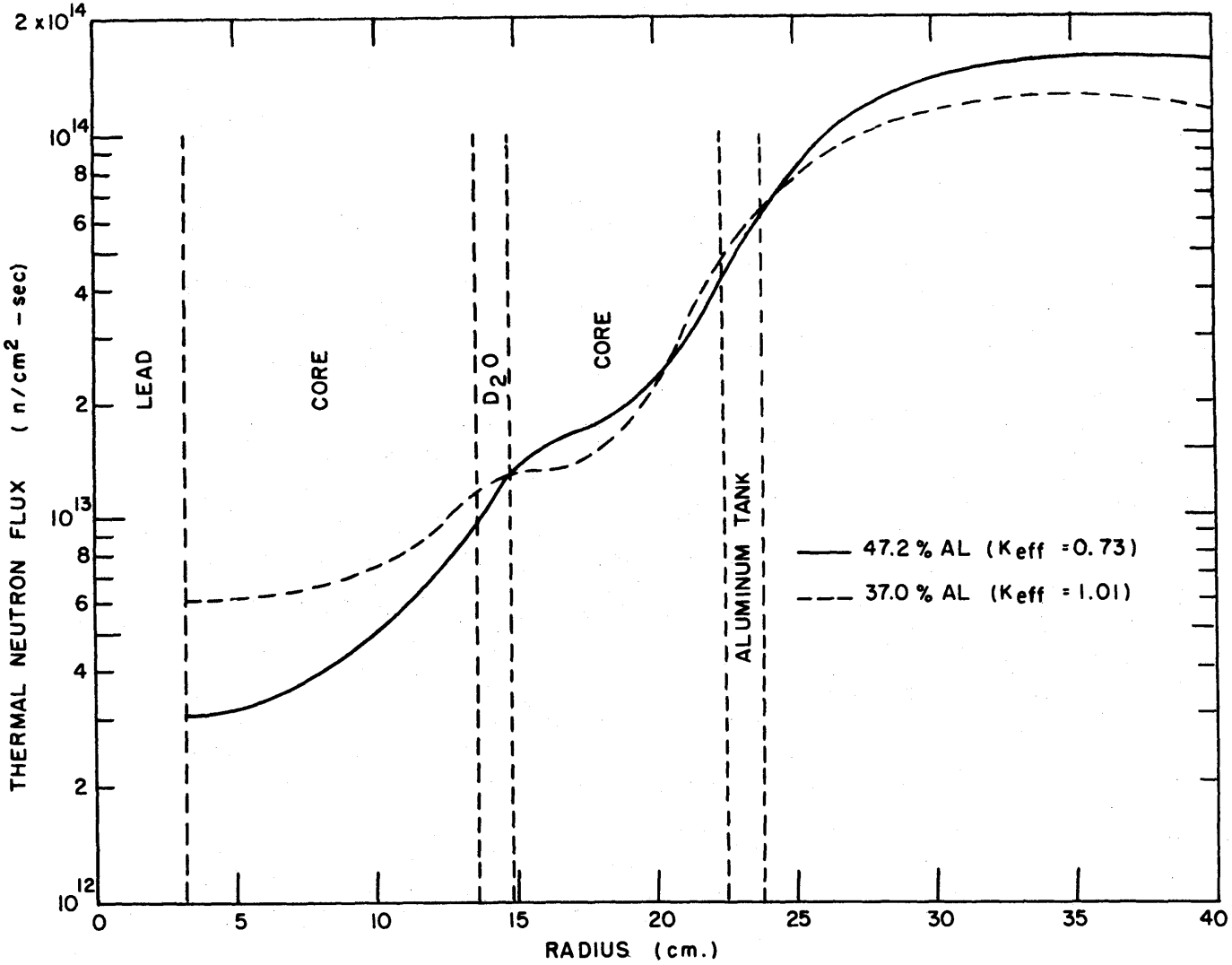

FIG. 5.3 EFFECTS OF REPLACING COOLANT WITH ALUMINUM ON THE THERMAL FLUX AT THE CORE MID-HEIGHT

well as the hardened thermal neutron spectrum in the core as can be seen from the distribution of the thermal neutron flux at the active core mid-height shown in Fig. 5.3.

5.4.3 Effects of Adding H_2O to the D_2O Coolant

As fuel plate finning was considered as a means of augmenting the heat transfer rate in the core, it was necessary to increase the moderation in the core with high volume fraction of aluminum in order to obtain sufficient reactivity to operate it.

The effects of adding light water to the heavy water coolant to increase the moderation in the core were studied. The reactor model used was the same as that described in section 5.4.1 and the core composition corresponding to that of the fuel element with 0.090 inches-wide coolant channels described in section 5.4.2. The results of the calculations are summarized in Figs. 5.4A and 5.4B in the form of effective multiplication as well as maximum power density in the core, and the reflector maximum thermal neutron flux at 2.5 inches below the core versus percentage of light water in the heavy water coolant curves. The radial thermal neutron flux distribution at the active core mid-height is shown in Fig. 5.5 for two cases--namely when there is no light water and when there is twenty per cent light water in the heavy water coolant.

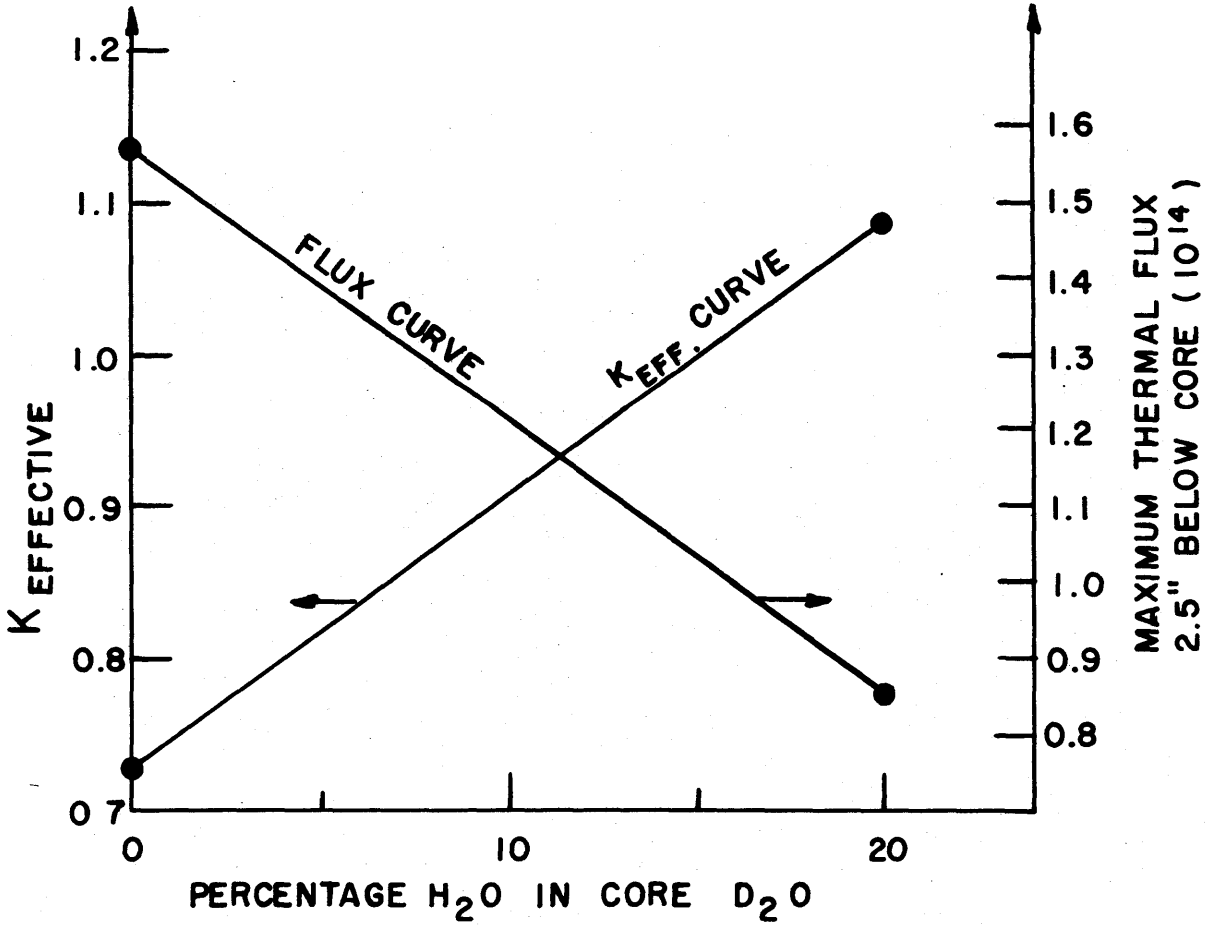

FIG. 5.4A EFFECTS OF INCREASING MODERATION IN THE CORE ON $K_{EFF.}$ AND REFLECTOR FLUX

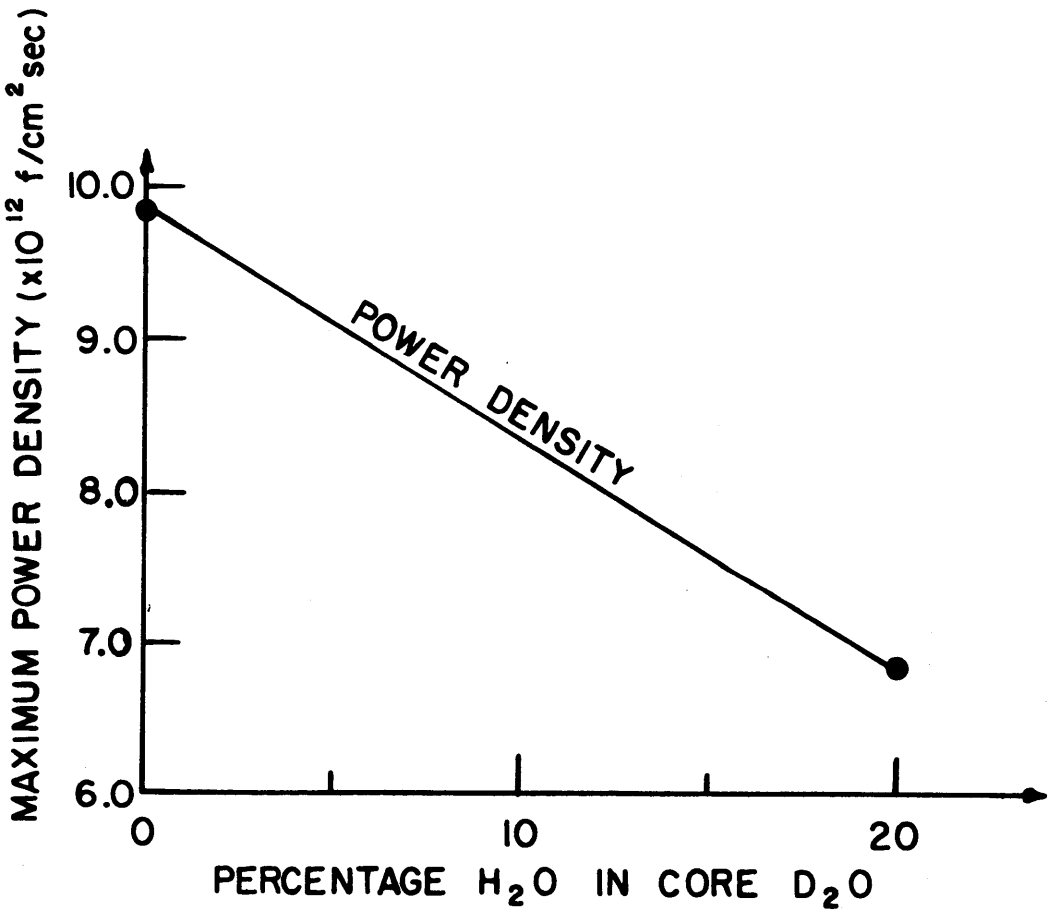

FIG. 5.4B THE EFFECT OF INCREASING MODERATION IN THE CORE ON POWER DENSITY

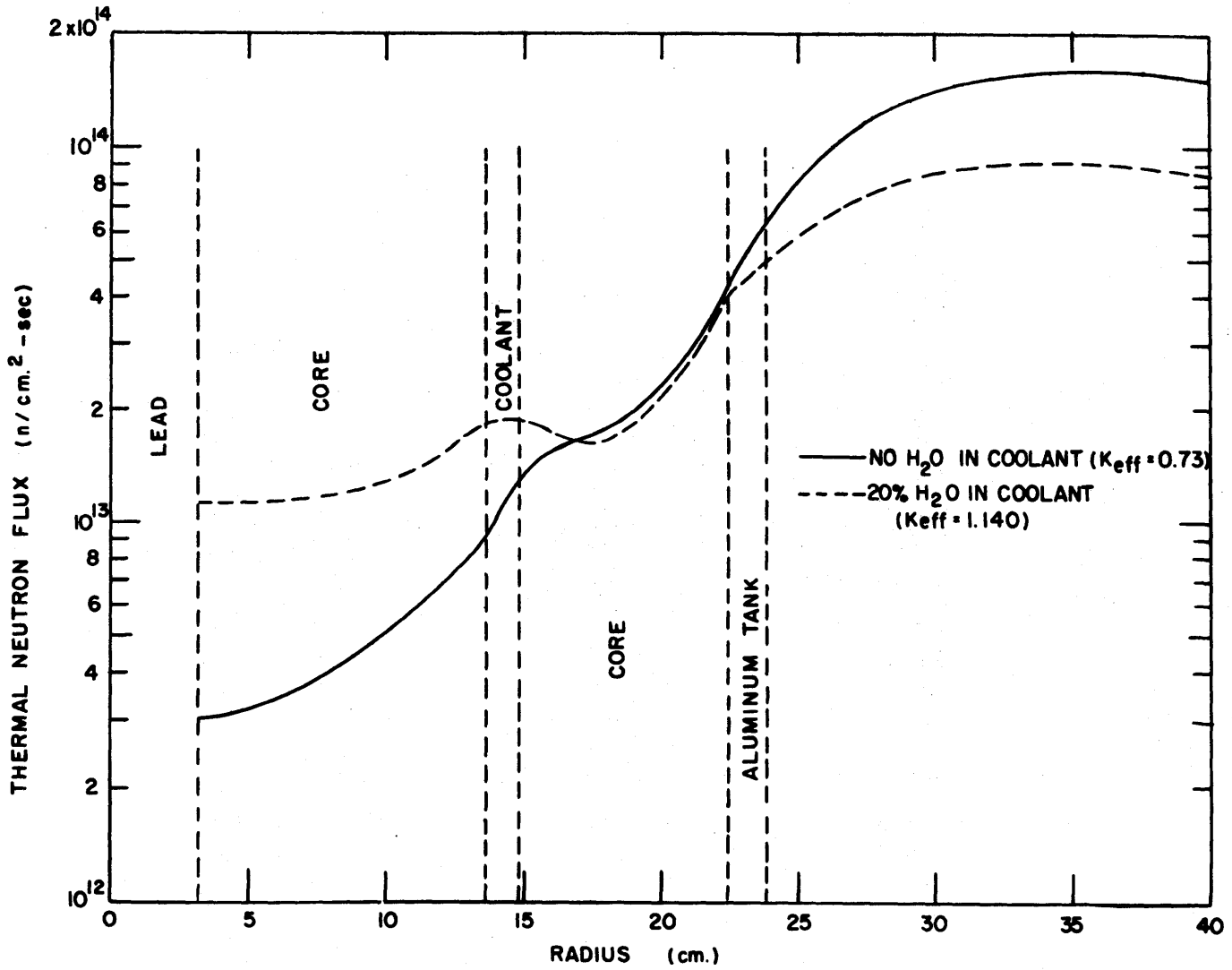

FIG. 5.5 EFFECTS OF REPLACING COOLANT WITH H_2O ON THE THERMAL FLUX AT THE CORE MID-HEIGHT

It is observed from Figs. 5.4A and 5.4B that as the volume percentage of light water in the core increases, the effective multiplication increases, though the reflector thermal neutron flux decreases. As will be seen from Fig. 5.5, the increased moderation in the core causes the power density distribution in the core to flatten. The reduced leakage flux into the reflector is due to the fact that the resulting larger fraction of the fission neutrons born at the center of the core have a lower probability of leaking out of the core. The fact that the increased moderation in the core flattens the power density distribution in the core is borne out by the maximum power density curve shown in Fig. 5.4B; the average power density in the cores is constant and so the maximum power density is directly proportional to the power peaking factor.

5.4.4 Design Core Cooled by H_2O-D_2O Mixture.

On the basis of the work described above, it is clear that the volume fraction of aluminum in the core can be increased as required from heat transfer considerations and light water added to the heavy water coolant to increase moderation in the core. The volume percentage of added light water should be kept to the minimum to provide adequate reactivity in the system.

A design core that was chosen had composition corresponding to a homogenized MITR-I standard fuel element with all

eighteen plates active. The fuel meat width was retained at 0.020 inches, the effective thickness of the finned cladding was taken to be 0.022 inches, and coolant channel width was 0.077 inches. The homogenized core had a diameter of 17.5 inches and a height of 24.0 inches. The homogenized material volume fractions in the core were: 0.667% uranium, 46.5% aluminum and 52.8% coolant. The coolant contained ten per cent of light water, the rest being heavy water.

Some EXTERMINATOR-II runs were made using these core compositions and are summarized in Fig. 5.6. A few characteristics of this design core are summarized under case one of Fig. 5.6. Cases two through five summarize the effects of making some changes to this design core.

Cases one, two and three show that an annular region of 2.5 inches radial width, placed either at the edge of the core or inside the heavy water tank results in a loss of reactivity as well as reflector thermal neutron flux, though the maximum power density decreases slightly. As MITR coolant flows up through the core and then returns to the bottom of the core, where the main coolant outlet pipes are situated, the coolant return path from the top to the bottom of the core must be as far away from the core as possible if the coolant contains a large volume fraction of light water.

Cases one and four summarize the effects of moving the inner absorber ring from the core top to a six-and-a-half inch insertion position, while cases four and five summarize

FIG. 5.6 Cores Cooled by Mixtures of H_2O and D_2O Coolant

Case	$\%H_2O$ in Coolant	Special Conditions	U^{235} Loading (KG)	K_{eff}	Core Dia. (in)	Outer Ring Insertion (in)	Inner Ring Insertion (in)	Max. Power Density ($X10^{12}$ F/cm^3-S)	Max. Thermal Flux 2.5" Below Core ($X10^{13}$ n/cm^2-S)
1	10	Al Follower	10.58	1.133	17.5	8	0	7.87	8.63
2	10	Al Follower 2.5" Annular Region of Coolant Outside Core Tank	10.58	1.121	17.5	8	0	7.77	8.49
3	10	Al Follower; 2.5" Annular Region of Coolant inside Heavy Water Tank	10.58	1.123	17.5	8	0	7.74	8.37
4	10	Al Follower	10.58	1.059	17.5	8	6 1/2	9.32	10.60
5	10	Al Follower Equillibrim Xenon	10.58	1.035	17.5	8	6 1/2	9.34	10.67

the effects of equilibrium xenon.

5.4.5 Advantages of H_2O-D_2O Mixtures as Coolant

The principal advantage of the mixtures of H_2O -D_2O as the reactor coolant is flexibility. Moderation in the core, which influences significantly the reactivity in the system, the fraction of the fission neutrons leaking into the reflector and hence the reflector thermal neutron flux peak, and power peaking difficulties, can be controlled by altering the percentage of light water in the heavy water coolant.

The principal disadvantages of this coolant are economic. Two containment systems will be required, one for the heavy water reflector and the other for the coolant, and this can be a large capital cost. The degradation of the expensive heavy water with light water can also be a serious economic question.

CHAPTER VI

CORES REFLECTED BY HEAVY WATER AND COOLED BY LIGHT WATER

The principal disadvantage of the cores reflected by heavy water and cooled by mixtures of light water and heavy water is economic and results from the degradation of the heavy water. In this chapter, the effects of replacing the mixtures of light water and heavy water coolant with a very much cheaper coolant, pure light water, are examined.

6.1 ADVANTAGES OF CORES COOLED BY LIGHT WATER

The pure light water coolant was considered as a limiting case of the coolant of light water and heavy water mixtures. The reactor model used in the calculations is the design core described in section 5.4.4. A series of EXTERMINATOR-II runs were made in which one of three factors were changed at a time. These three factors are the core diameter, the insertions of the inner and outer absorber rings, and the total uranium weight percentage in the fuel meat alloy. Selected results of the calculations are summarized in Fig. 6.1.

Cases one and two are included in the table shown in Fig. 6.1 for comparison, and they illustrate a typical pure heavy water cooled core and the effects of adding ten

FIG 6.1 Cores Cooled by H_2O

Case	% H_2O in Coolant	Uranium Wt. % in Meat Alloy	K_{eff}	U-235 Loading (KG)	% By Volume of Aluminum in Core	Core Diameter (in)	Core Height (in)	Inner Absorber Ring Insertion (in)	Outer Absorber Ring Insertion (in)	Max. Reflector Thermal Neutron Flux (10^{13})	Max. Reflector Thermal Flux at Effective Core Mid-Height (10^{13})	Max. Reflector Thermal Flux 2.5 in. Below Core (10^{13})	Max. Core Power Density (10^{12} flu-sec)
1	0.0	32.0	1.007	9.10	37.2	18.0	24.0	0.0	8.0	12.80	12.20	11.86	8.98
2	10.0	32.0	1.070	9.10	37.2	18.0	24.0	0.0	8.0	11.00	10.60	10.05	6.77
3	10.0	32.0	1.049	10.58	46.5	17.5	24.0	6.5	8.0	11.37	10.82	10.60	9.32
4	100.0	32.0	1.286	6.14	46.5	13.5	24.0	6.5	8.0	7.01	6.65	6.37	7.14
5	100.0	28.0	1.162	2.81	46.5	12.5	17.0	1.5	1.5	12.92	12.77	10.29	11.30
6	100.0	28.0	1.121	2.81	46.5	12.5	17.0	3.0	3.0	13.50	13.50	11.87	14.04

per cent of light water to the heavy water coolant respectively. Case three is the design core described in section 5.4.4.

Case four shows that changing the coolant of case three to pure light water and reducing the core diameter from 17.5 to 13.5 inches, results in an increase in the system effective multiplication from 1.049 to 1.286. Case five shows that reducing the core diameter of case four further from 13.5 to 12.5 inches as well as the uranium weight percentage in the fuel meat alloy from 32 to 28 causes a reduction in the effective multiplication from 1.286 to only 1.162. Case six shows that reducing the effective core height from 15.5 to 14.0 inches results in the decrease of the effective multiplication from 1.162 to 1.121 with the corresponding increase in both the reflector maximum thermal flux and the core maximum power density. An examination of the last four columns of Fig. 6.1 for cases four through six shows that, generally, as the system effective multiplication decreases, both the reflector leakage flux as well as the maximum core power density increases.

By comparing cores reflected by heavy water and cooled by

(a) pure heavy water, such as case one

(b) heavy water-light water mixture, such as case three

(c) pure light water, such as case six

it is clear that a core cooled by light water would yield

reflector maximum thermal neutron flux comparable to that available from a core cooled by any of the other two coolants. The light water cooled core, however, possessed a number of significant advantages, of which four are discussed below.

The first advantage of this coolant is the significant reduction in the core diameter; a reduction of about 17.5 to 12.0 inches still gives a higher effective multiplication in the light water cooled system. The first effect of this decreased core size is that the core uranium loading is decreased by a factor approaching two. The second effect of this decreased core size is heat transfer rate from the core. As pointed out in section 4.4, the permanent features chosen for the present MITR limit the total flow rate through the core, but there is some flexibility left in the system pressure drop. For the given total flow rate in the core, the actual velocity in the coolant channels is increased by a factor of nearly two as a result of the decreased core diameter. A factor of 1.8 increase in the heat transfer rate in the core can be realized from the increased velocity through the coolant channels alone. The maximum permissible power density in the light water cooled core, therefore, is about 1.8 times the corresponding number in the cores cooled by any of the other two types of coolant.

The second advantage of the light water coolant is the fact that the uranium weight percentage in the fuel meat can

also be reduced and still have a reasonable value of K_{eff} with the smaller core diameter. This is an additional flexibility in the light water system; future core loadings can have a higher uranium weight percentage in the fuel meat, between twenty-seven and the present limit of thirty-nine, if necessary.

The third advantage is that the aluminum volume percentage in the core can be increased from 37.2 as in the heavy water cooled cores to about 56.6 and still maintain a higher effective multiplication in the light water system. This increased aluminum volume percentage in the core would conveniently permit fuel plate finning, which has been considered as the means of augmenting the heat transfer rate in the core.

The fourth advantage of the light water coolant is economic. The system would be cheaper to construct as well as operate and maintain. In addition, the problem of tritium leakage from the primary to the secondary coolant system, which is a minor health hazard, would also be reduced.

The high moderation effect of light water, which leads to a small core size, made additional core configurations worthy of consideration. The three light water cooled core configurations examined are the off-set core, the split core, and the core with poisoned upper half discussed previously. These three cores are discussed briefly below and compared.

6.2 THE OFF-SET CORE CONFIGURATION

The off-set core is shown in cross-section in Fig. 6.2. The principal difference between this core arrangement and that described in section 5.4.4 is that the vertical axis of the off-set core does not coincide with the corresponding axis of the heavy water tank. Instead, the off-set core is positioned such that its vertical axis is nine inches away from the heavy water tank center on the thermal column centerline. It was found that such an off-set core of about twelve inches diameter would permit all the radial beam ports to be made re-entrant tangentially to the core to extract neutron beam at the mid-height, clean of fast neutron and gamma radiation background. The exception was the 12SH1 beam port which is directly opposite the thermal column as shown in Fig. 6.2. This beam port would view the core directly.

The thermal neutron flux distribution around such an off-set core was examined, using two dimensional cylindrical R-Z calculational model. The reactor model is shown in Fig. 6.3. In order to prevent rapid rise in the thermal neutron flux at the top and bottom ends of the core, neutron absorbers were placed in these regions of the core.

The thermal neutron flux distribution around this core, obtained with the EXTERMINATOR-II code, is shown in Fig. 6.4. The $1.2X10^{14}$ thermal neutron flux contour line shows that the maximum reflector flux region extends not more than 2.5 inches away from the core. Only the two beam ports

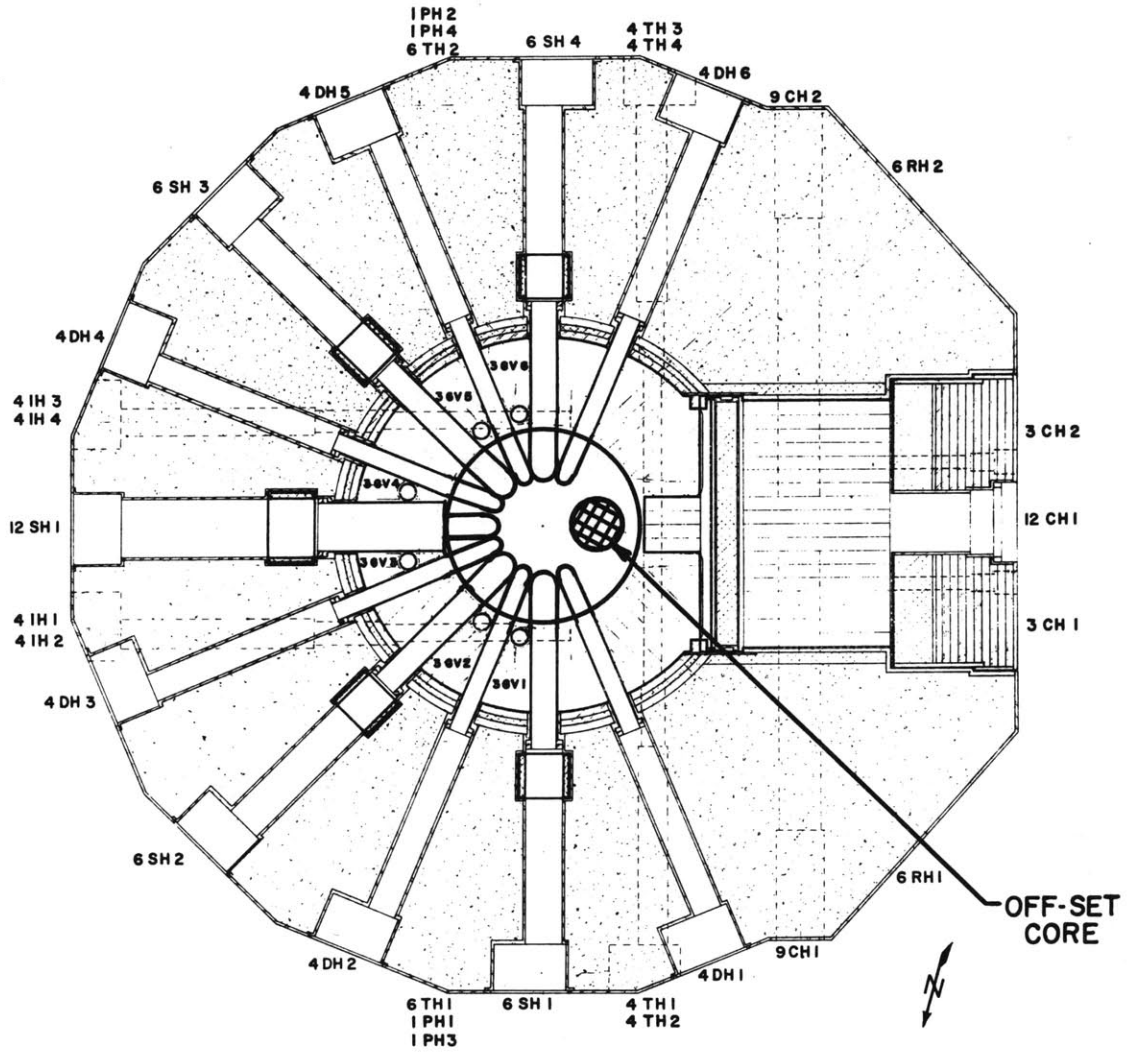

FIG. 6.2 HORIZONTAL SECTION OF THE OFF-SET CORE ARRANGEMENT

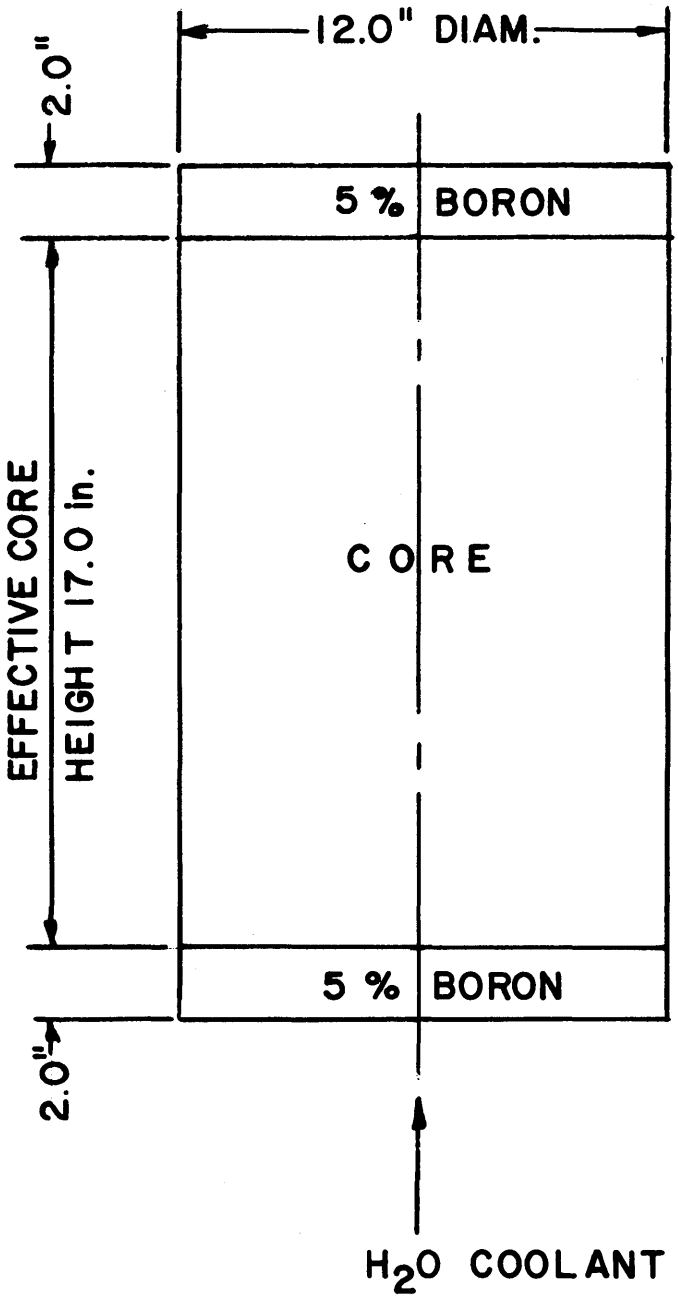

FIG. 6.3 THE OFF-SET CORE MODEL

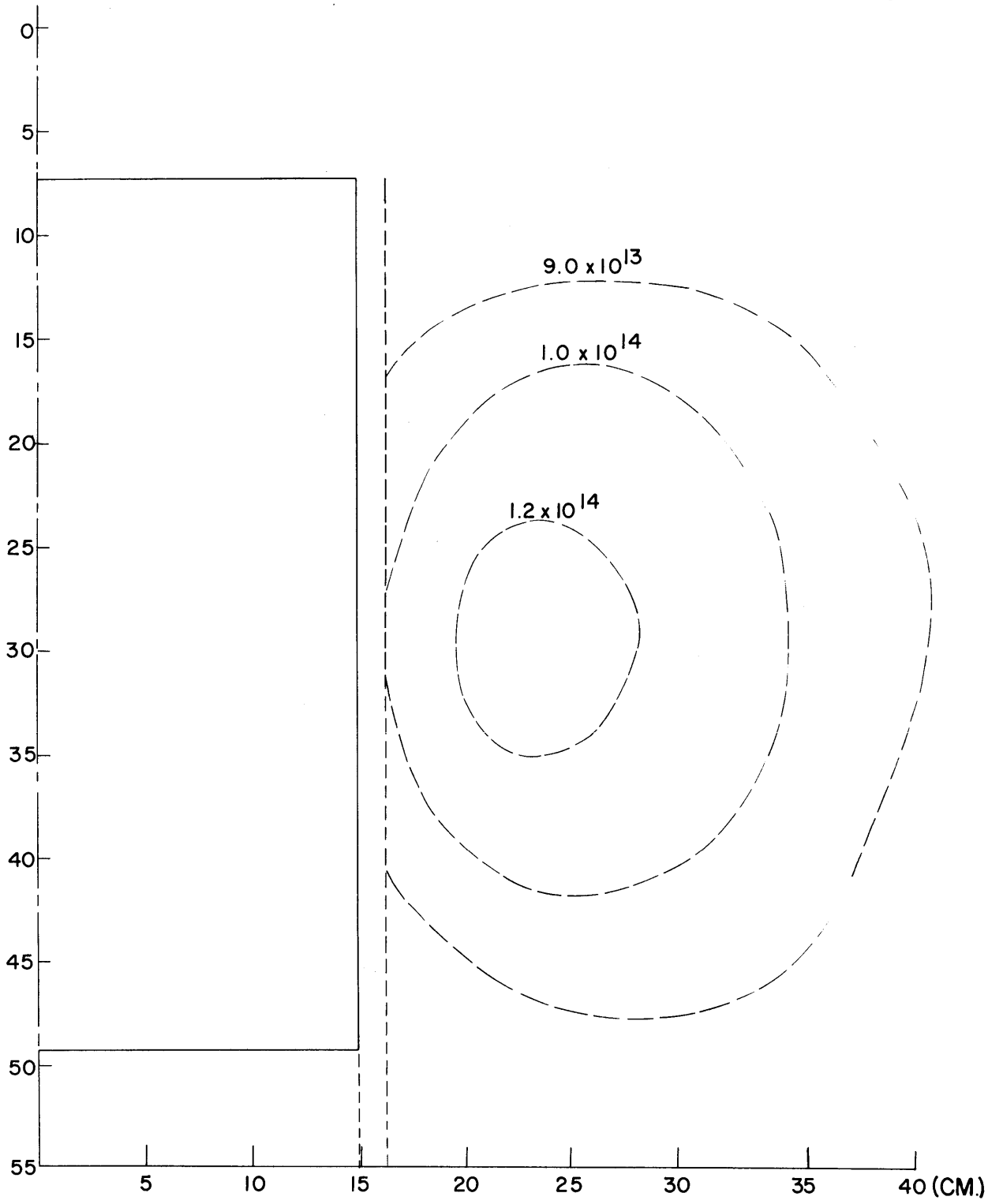

FIG. 6.4 THERMAL FLUX DISTRIBUTIONS AROUND THE OFF-SET CORE

adjacent to the thermal column could be made re-entrant to this region. However, the $1.0X10^{14}$ flux contour line shows that a flux of $1.0X10^{14}$ extends about 8.0 inches from the core and this region can be reached by re-entrant beam ports.

The principal disadvantage of this core configuration is asymmetry. The mechanical design of the light water coolant containment system is complicated by the asymmetry. The calculation of the detail thermal neutron flux distribution in the region where the tips of beam ports would be placed was not possible, except in a three dimensional R-θ-Z geometry. Finally, the detail theoretical study of the effects of the re-entrant beam ports in the proposed location of the beam ports as well as the beam port thermal neutron current to be expected could not be carried out without considerable difficulties.

6.3 THE SPLIT CORE CONFIGURATION

The split core is shown in vertical cross-section in Fig. 6.5. The principal difference between this core and the design core described in section 5.5.5 is that the fuel elements have split fuel plates with no fuel in the middle three-inch gap. The middle three-inch gap of the split core, therefore, consists of only coolant and aluminum. Because of the high moderation effect of light water, the neutron flux in this middle gap is highly thermal and radial beam

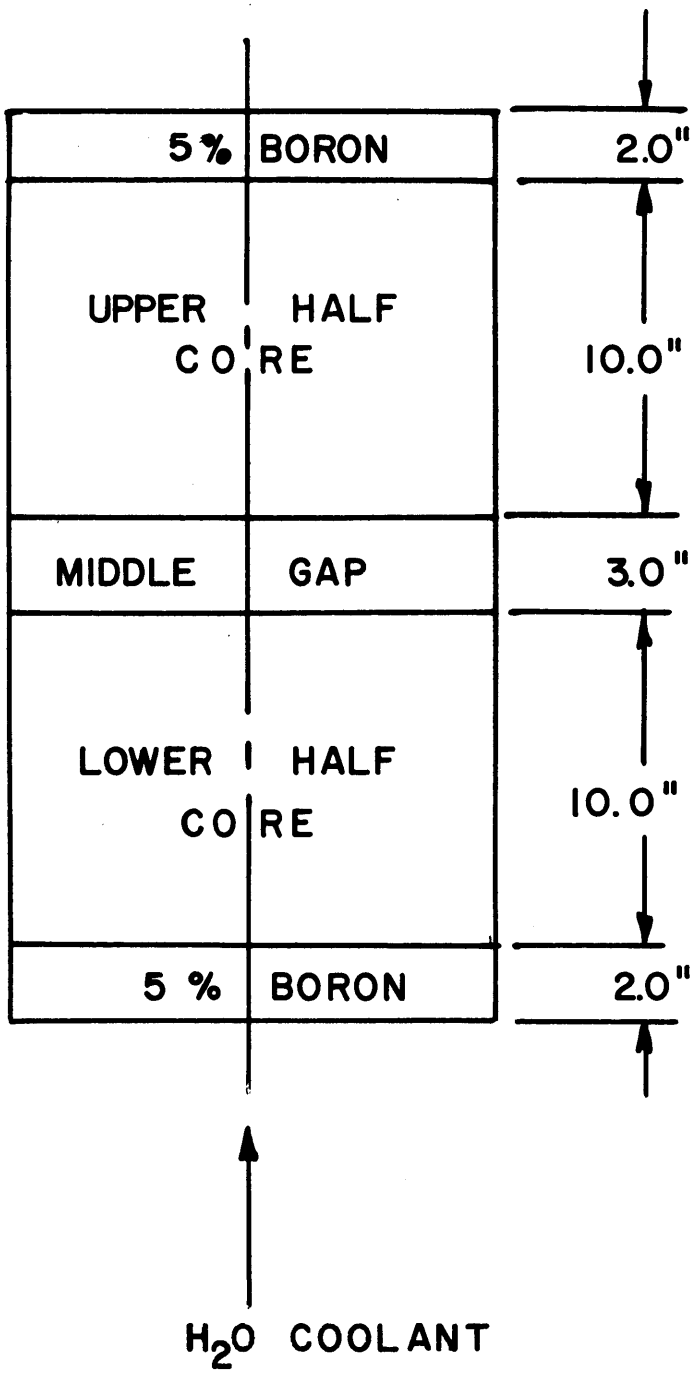

FIG. 6.5 THE SPLIT CORE MODEL

ports can be made re-entrant to extract thermal neutron beam there, relatively low in fast neutron and gamma radiation background.

The axial thermal flux distribution at the center of the core obtained with EXTERMINATOR-II code, is shown in Fig. 6.6; the radial thermal neutron flux distribution at the center of the middle gap is also shown in Fig. 6.7. Figure 6.6 illustrates the very sharp rise in the thermal flux at the middle gap; Fig. 6.7 also shows that radial beam ports made re-entrant to about 25 cm radius would be exposed to thermal neutron fluxes greater than $1.0X10^{14}$ n/cm^2-sec.

The axial power peaking difficulties at the core-middle gap interface are quite severe and this is the principal disadvantage of this core configuration. The mechanical design of suitable control rods for this core is an additional complication.

6.4 THE CORE WITH POISONED UPPER HALF

The poisoned upper half core configuration is that described in section 4.2 and shown in Fig. 4.4. The very high absorption cross-section of light water for thermal neutrons was found to adversely affect the reflector thermal neutron flux underneath the core.

6.4.1 Thermal Flux Distribution Around the H_2O Core with the Upper Half Poisoned

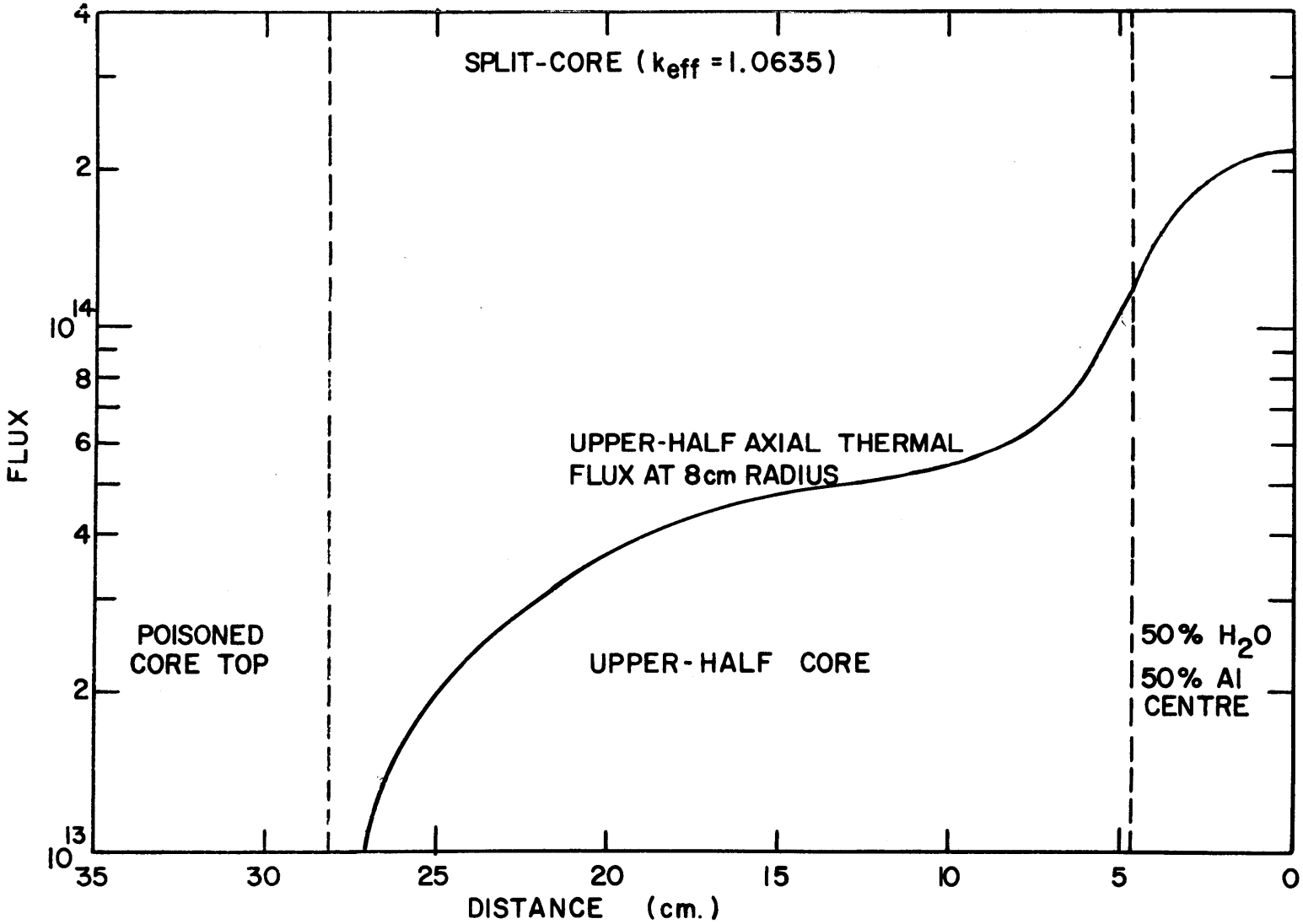

FIG. 6.6 AXIAL THERMAL FLUX DISTRIBUTION FOR A SPLIT-CORE MODEL

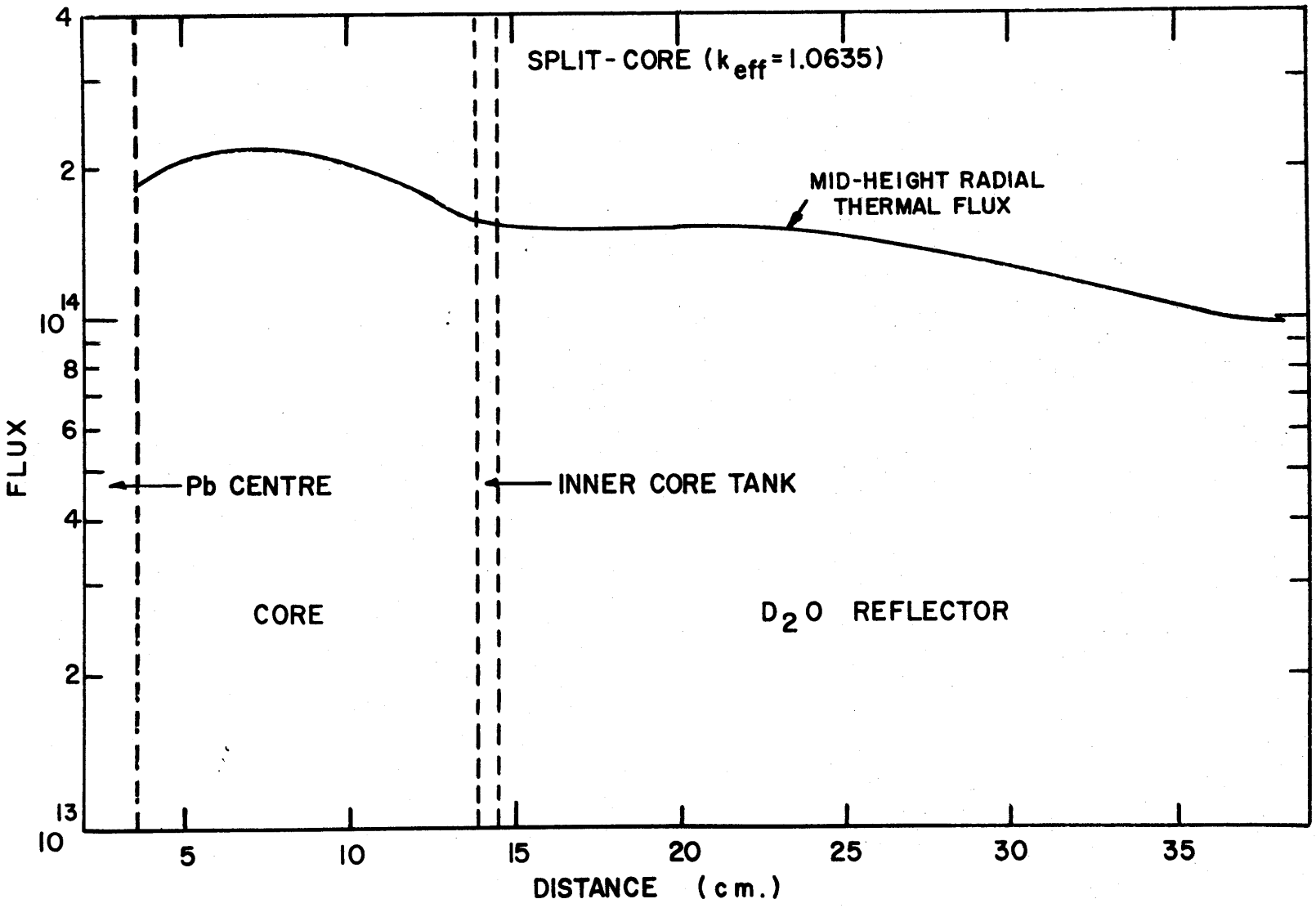

FIG. 6.7 RADIAL THERMAL FLUX DISTRIBUTION FOR A SPLIT-CORE MODEL

A typical thermal flux distribution around a light water cooled core with the upper half poisoned, obtained with the EXTERMINATOR -II code, is shown in Fig. 6.8. This core is similar to that described in case six of Fig. 6.1, except that the uranium-235 weight percentage in the fuel meat has been reduced from twenty-eight to twenty-five.

Referring to Fig. 6.8, it is observed that the thermal neutron flux distribution exhibits two flux peak regions. There is a high flux region on the side of the core which is similar to that found with the heavy water cooled core discussed in section 4.2 and shown in Fig. 4.5. The second flux peak region occurs underneath the core. Because of the high moderation effect of light water, the thermal neutron flux in this region rises very steeply at the bottom core-reflector interface, resulting in a maximum flux in the light water about twice that in the other high flux region which occurs in the heavy water reflector. However, the very short diffusion length of the thermal neutrons in the light water causes the flux to fall off very rapidly.

6.4.2 Advantages of the Poisoned Upper Half Core Configuration

The main disadvantage of this core configuration is that the very short diffusion length of thermal neutrons in light water causes the very high thermal neutron flux peak, which occurs near the core-light water interface underneath the core, to fall off too rapidly such that the thermal neutron

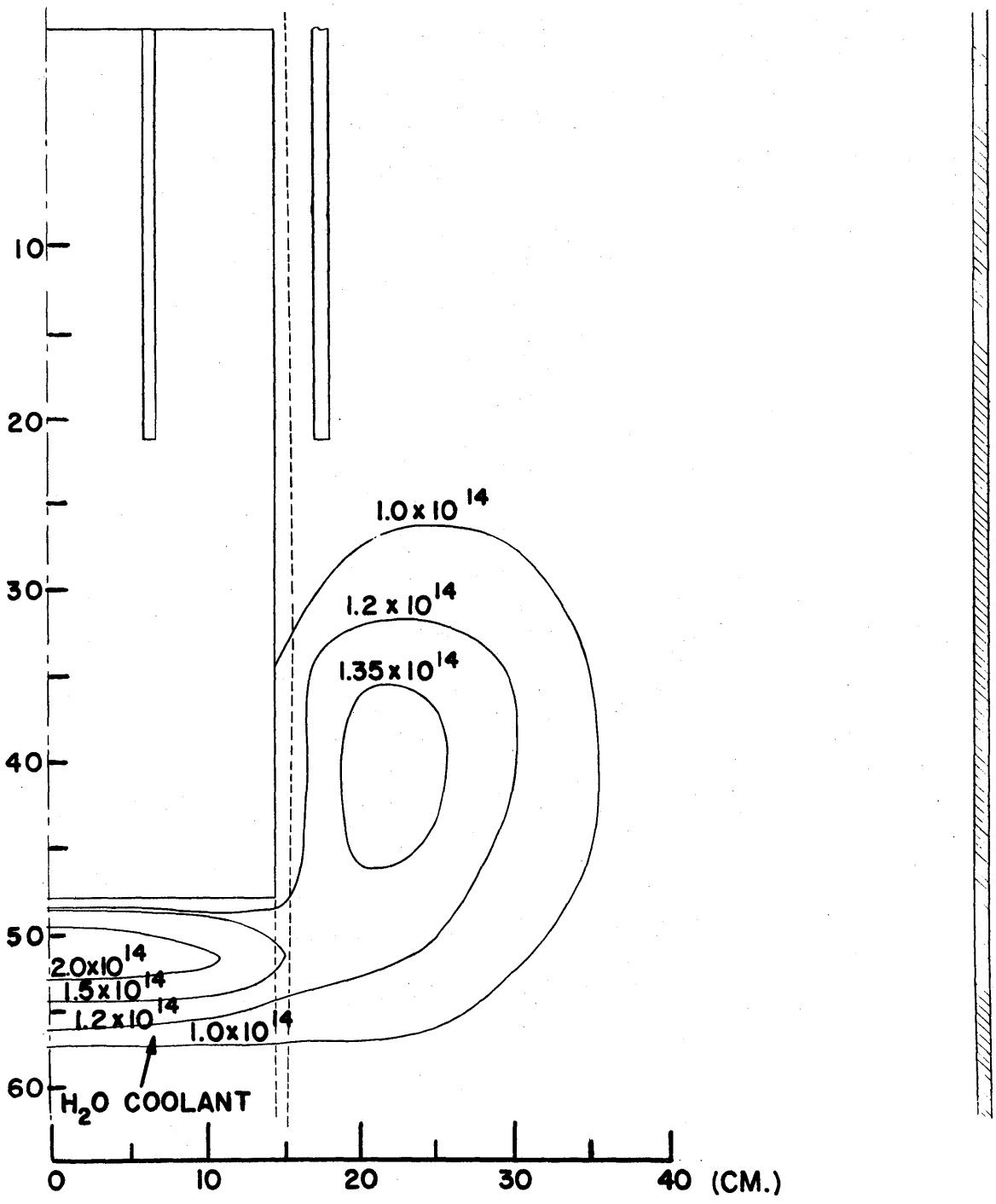

FIG. 6.8 H_2O COOLED CORE WITH THE UPPER HALF POISONED

flux level in the reflector where re-entrant beam port tips would be located, is low compared with the peak value.

Nevertheless, the unperturbed thermal neutron flux level at the proposed beam port tip location for this core configuration is comparable to that available from the other two core configurations. In addition, it has two important advantages. First, this core configuration is quite symmetrical and, therefore, free of the problems of asymmetry inherent in the off-set core configuration. Secondly, the maximum power densities in this core configuration occur at the bottom end of the core compared with the core mid-height for the other two core configurations, and this has economic as well as heat transfer advantages.

The economic advantage is derived from fuel element utilization. When the lower tip of an element is burned up, it can be rotated, putting the fresher upper tip in the high power density region. This procedure will result in a higher and more uniform final burn up of an element compared with the corresponding situation in which the maximum power densities occur at the center of the fuel element.

The heat transfer advantage has two aspects. First, for a given maximum permissible fuel plate surface temperature, the corresponding maximum permissible power density is slightly higher at the bottom than at the mid-height of the core. Referring to equation 5.2.1 of section 5.2 for the fuel plate surface temperature, the film temperature rise,

$T_F(Z)$, has its maximum value at the coolant channel inlet where the bulk coolant temperature rise, $T_B(Z)$, is zero. As the local power density is directly proportional to the film temperature rise, shown by equation 5.2.2 of section 5.2, the local power density also has its maximum value at the bottom of the core. Secondly, the heat transfer coefficient cannot be augmented at the coolant channel mid-height by vortex flow because of the difficulty of generating vortices in this region for channels of the dimensions expected in the fuel element coolant channels (53) (54); however, vortex flow can be maintained over a short distance at the coolant channel inlet region by a suitable design of the inlet plenum. Thus, the heat transfer coefficient can be increased slightly at the bottom rather than at the mid-height of the core.

6.4.3 Composite H_2O-D_2O Reflector Design Underneath the Core

As the poisoned upper half core configuration has some advantages compared with the other two alternative core configurations, it was necessary to improve the reflector design underneath the core to permit neutron beam to be removed from this region.

A series of EXTERMINATOR-II calculations were made in which the effects of restricting the amount of light water underneath the core were examined. The thermal neutron flux distributions underneath the core for a selected number

of these runs are given in Figs. 6.9 through 6.12. The core had an effective height of 12.0 inches and a diameter of 12.0 inches. The uranium-235 weight percentage in the fuel meat was 25 percent.

Figure 6.9 shows the thermal neutron flux distribution around the core with light water bottom plenum of approximately a hemispherical shape. The maximum depth of the light water plenum was about 9.0 cm. A plenum of this size had the volume as well as the suitable spatial distribution of light water underneath the core such that nearly all the fission neutrons leaking from the core into this region of the reflector are moderated to the point where they are rapidly thermalized in the heavy water reflector. The very long diffusion length of the thermal neutrons in the heavy water reflector permit this high flux region to spread to the proposed location for the tips of re-entrant experimental beam ports.

A comparison of Figs. 6.8 and 6.9 shows three features: the maximum thermal neutron flux in the reflector light water is about the same and equals about $2.3X10^{14}$ n/cm^2-sec; the $1.2X10^{14}$ n/cm^2-sec contour line shows that the reflector thermal flux peak region spreads further into the heavy water reflector when the light water underneath the core is restricted; finally, only a single reflector thermal flux peak region occurs with the bottom light water plenum design. Thus, the neutron absorbers in the upper half core as well as the bottom light water plenum force the maximum

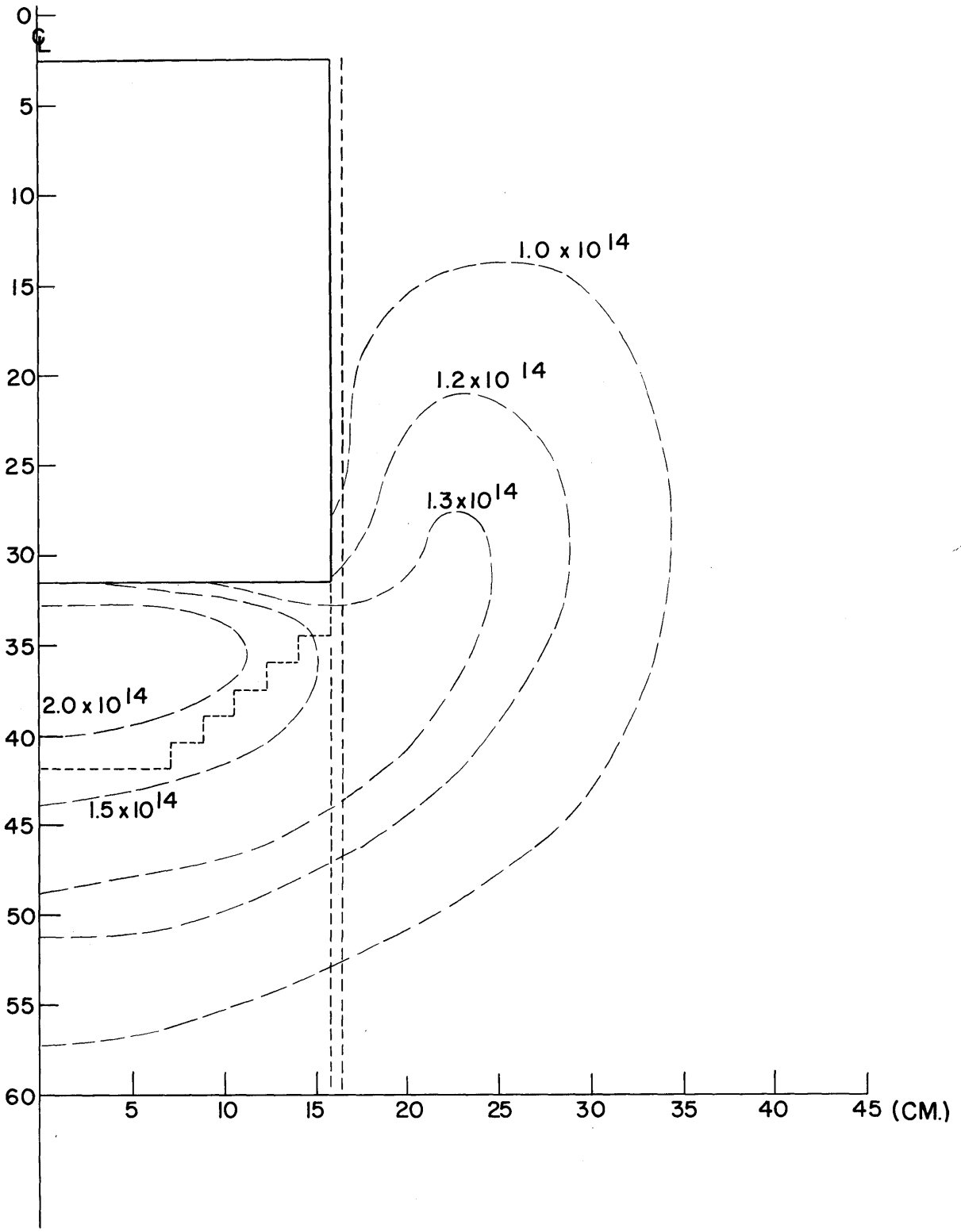

FIG. 6.9 ′ FLUX DISTRIBUTIONS AROUND THE BOTTOM SPHERICAL H_2O PLENUM

reflector thermal neutron flux region to appear underneath the core.

The size as well as the shape of the light water bottom plenum are important. Increasing the depth of the plenum results in a more rapid fall-off of the thermal neutron flux peak, due to the very short diffusion length of the thermal neutrons in the light water. Decreasing the depth of the plenum results in reduced moderation of the fission neutrons leaking from the core; these neutrons, therefore, are not rapidly thermalized by the heavy water and result in the reduction of the heavy water reflector peak flux. Reducing the size of the bottom plenum also poses mechanical design problem of directing the high velocity coolant through it and distributing the flow uniformly in the fuel elements.

Figure 6.10 shows the effect of altering the bottom shape. From fluid flow point of view, this bottom plenum shape is preferable to the hemisphere of Fig. 6.9; coolant entering the bottom plenum either down the side or tangentially to the bottom of the core will distribute more uniformly through the fuel elements with the latter bottom plenum shape. However, a comparison of the $1.3X10^{14}$ n/cm^2-sec flux contour line on Figs. 6.9 and 6.10 shows that the hemispherical plenum shape is better from the point of view of the thermal neutron flux available at the region where thermal neutron beam would be removed for experiments. Ideally, the shape of the light water plenum should be

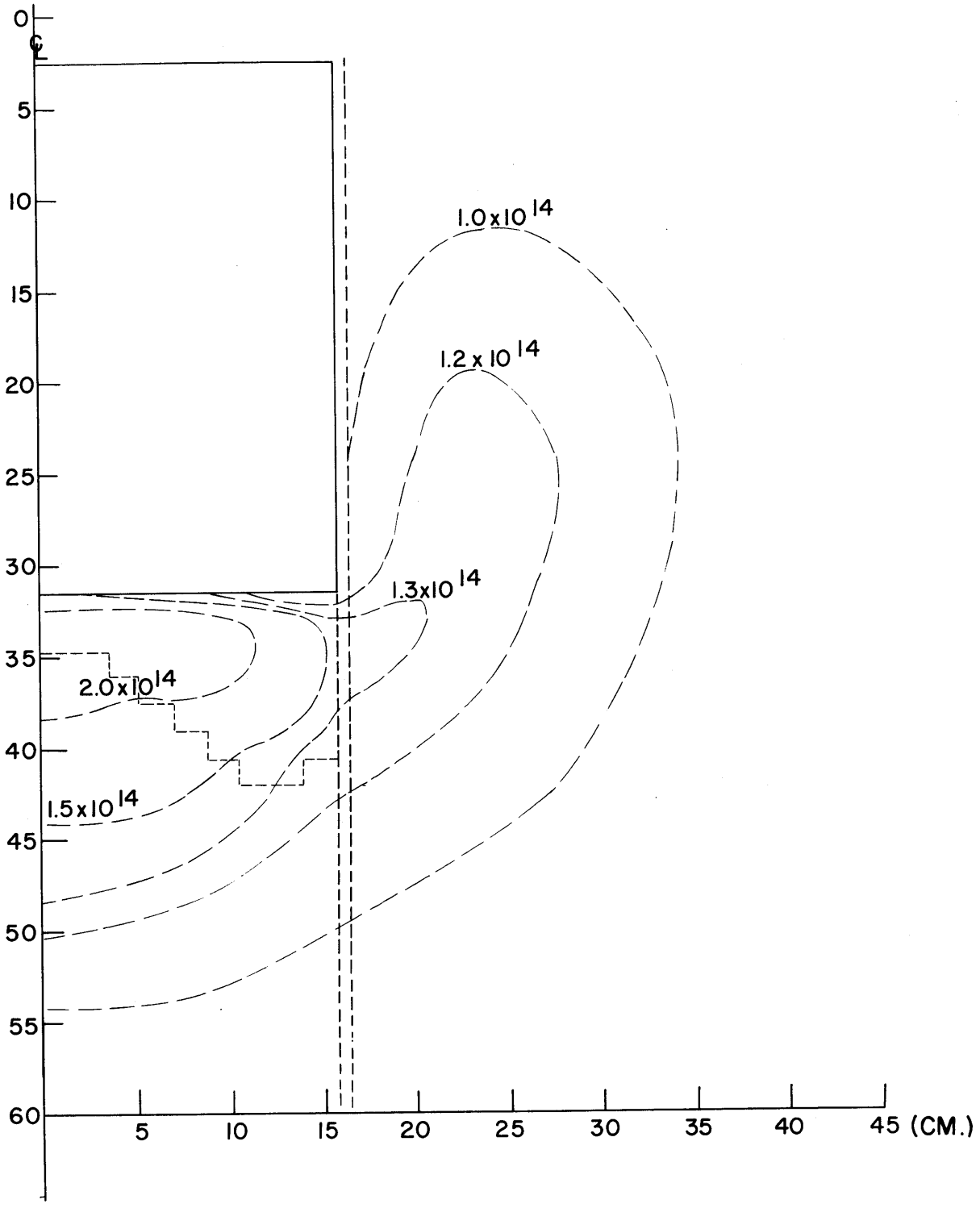

FIG. 6.10 EFFECT OF CHANGING THE SHAPE OF THE BOTTOM H_2O PLENUM

such that most of the neutrons reaching the heavy water region where neutron beam would be extracted for experiments, are either just thermalized or moderated to the point where they are rapidly thermalized in the heavy water reflector. Although the second plenum shape of Fig. 6.10 is better from fluid flow point of view, the distribution of the light water underneath the core is such that most of the neutrons are thermalized and absorbed in the light water and so never reach the heavy water reflector region where neutron beam would be removed for experiments.

A number of alternative methods of directing the coolant into the core were considered. For example, the coolant could flow down the central region of the core into the bottom plenum and then flow up in the outer region of the core. This central core region could either contain fuel or no fuel. In either case the mechanical design of the top part of the core would be a very difficult task because of the lack of adequate space in this region. In addition, if this central region contains no fuel, then the power peaking difficulties at the interface between this central region and the surrounding core would be quite severe due to the high moderation effect of the light water. If the central region contains fuel, then in the event of a transient, boiling or flow instability which is likely to occur at the bottom of the core, would completely cut off coolant flow to the outer core regions.

Figure 6.11 shows another example of a method of directing the coolant into the core by a single 6-inch verti-

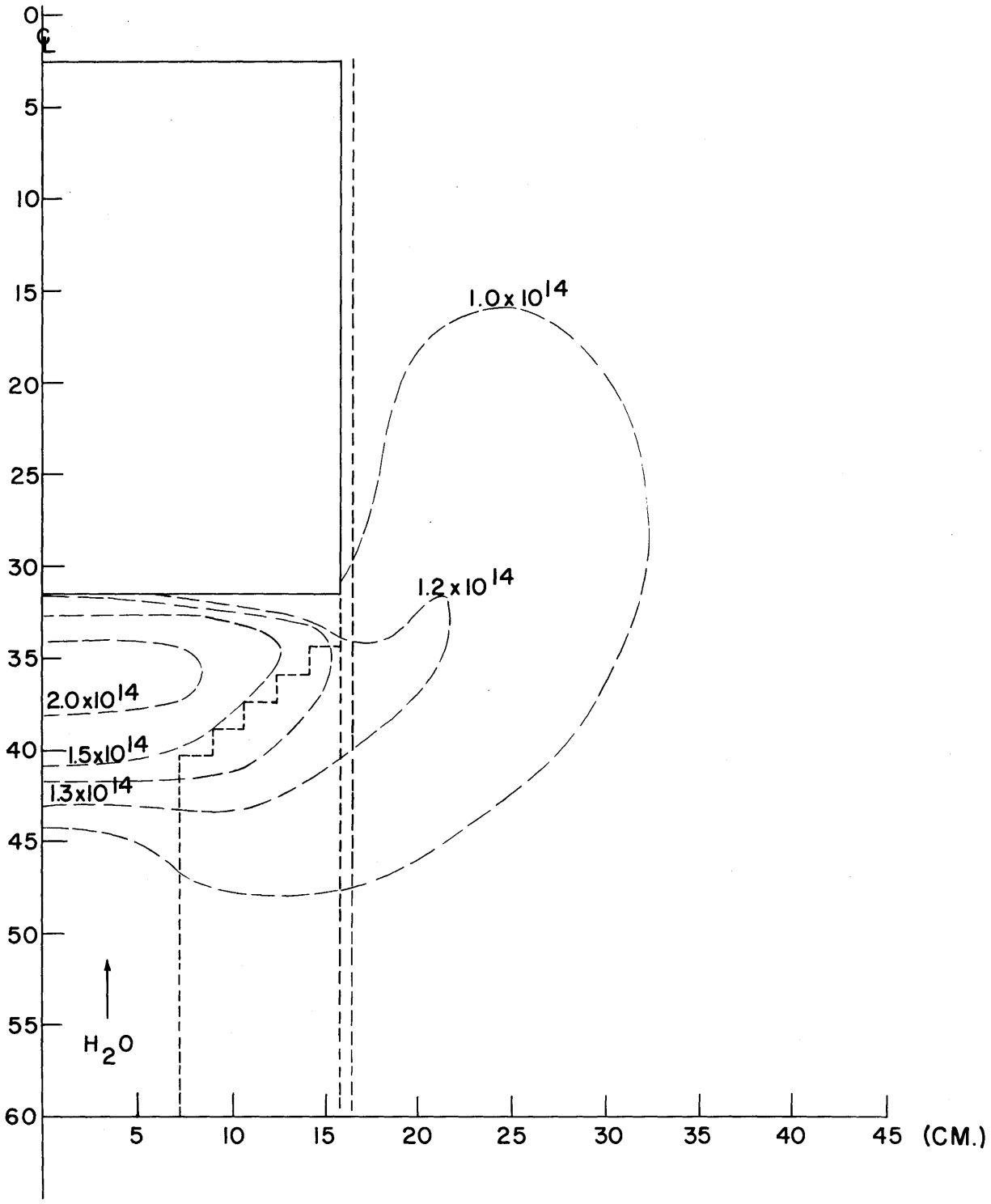

FIG. 6.11 EFFECT OF A SINGLE COOLANT INLET PIPE BELOW THE CORE ON THE THERMAL FLUX DISTRIBUTION

cal pipe underneath the core. A comparison of the $1.3X10^{13}$ n/cm^2-sec flux contour line in Figs. 6.9 and 6.11 shows the large reduction in the thermal neutron flux underneath the core that results. Calculations showed that a similar decrease in the thermal neutron flux underneath the core results by directing the flow into the core by radial pipe(s), oriented tangentially to the core bottom.

Figure 6.12 shows a method of directing the coolant into the core by rectangular pipes, inclined at an angle of about forty-five degrees. A comparison of the $1.3X10^{13}$ n/cm^2-sec contour line on Figs. 6.9 and 6.12 shows that this method does not affect the thermal flux distribution underneath the core significantly, though the mechanical design of the system of rectangular pipes is complex.

An equally good method is to let the coolant flow down the side of the core into the bottom plenum and then flow up through the core. Owing to the high moderating effect of the light water, power peaking on the side of the core adjacent to the light water is quite severe. Calculations showed that this severe power peaking can be reduced significantly by placing about one and a half inch-thick aluminum between the core side and the light water, though at the expense of loss of reactivity in the system. In addition, the aluminum was found to be advantageous from mechanical design point of view: it would provide structural support for the core as well as guides for the control

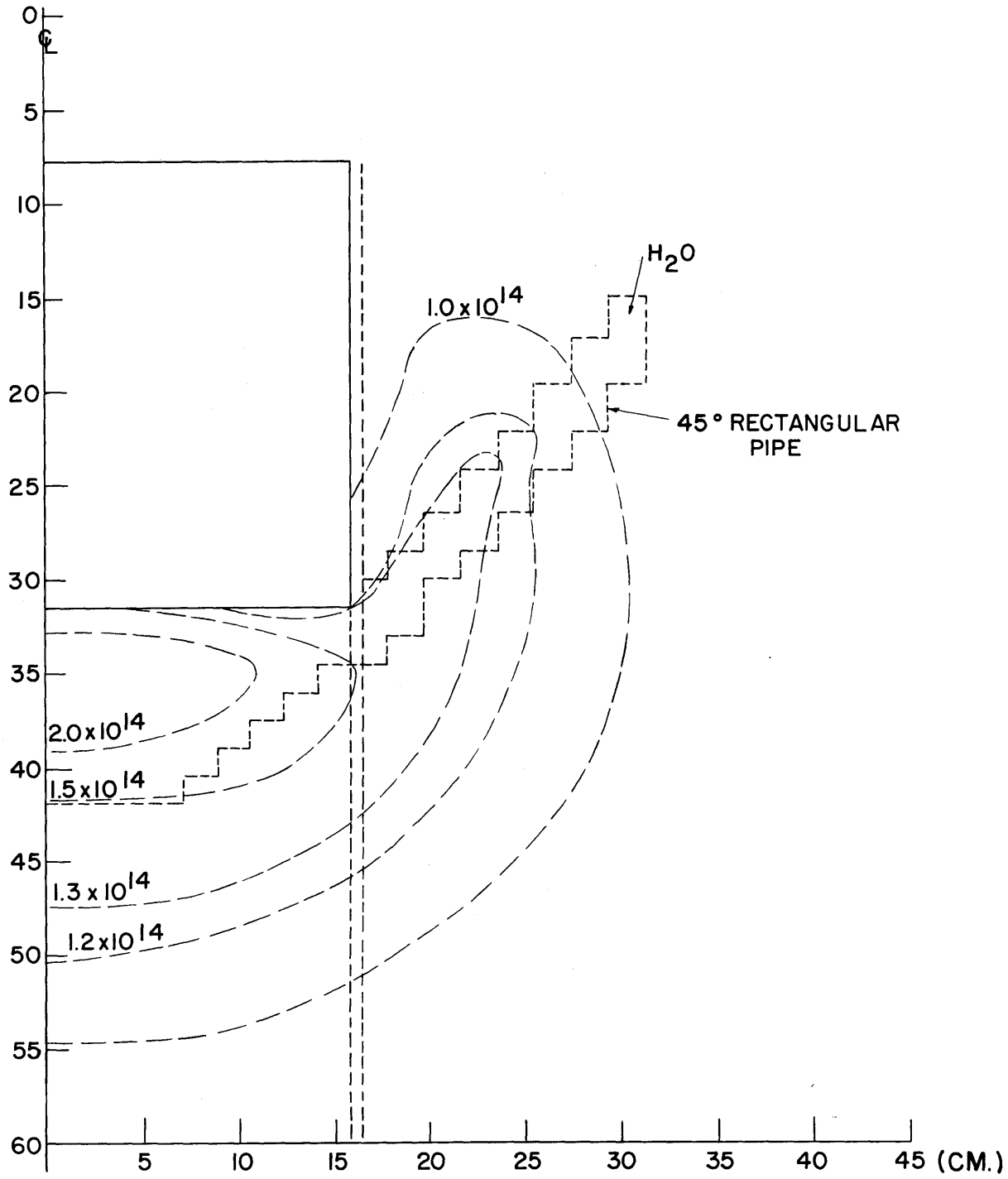

FIG. 6.12 EFFECT OF 45-DEGREE RECTANGULAR COOLANT PIPES ON THE FLUX DISTRIBUTION BELOW THE CORE

rods. This method was thus used in the final design described in the next chapter.

CHAPTER VII

DESIGN BASE MITR-II CORE

On the basis of the calculations described in Chapters 3 through 6, the poisoned upper half core configuration with light water coolant and a heavy water reflector has been chosen as the design base of the MITR-II core. A description of the arrangement of this core as well as its principal characteristics is given in this chapter. Detailed design of the latest MITR-II is given in Chapter 8.

7.1 ARRANGEMENT OF THE DESIGN BASE MITR-II CORE INSIDE THE HEAVY WATER TANK

The arrangement of the core inside the heavy water tank is shown in Fig. 7.1. The compact core is about 14.0 inches in diameter and 24.0 inches high. There is a fixed inner absorber ring as well as an outer movable neutron absorber ring in the top half of the core. The inner fixed absorber ring is 0.040-inch thick cadmium, clad on both sides with aluminum, and has an inside diameter of 4.5 inches. The outer movable absorber ring, which is also the control rod bank for the active part of the core is 0.040-inch thick cadmium, clad on both sides with aluminum.

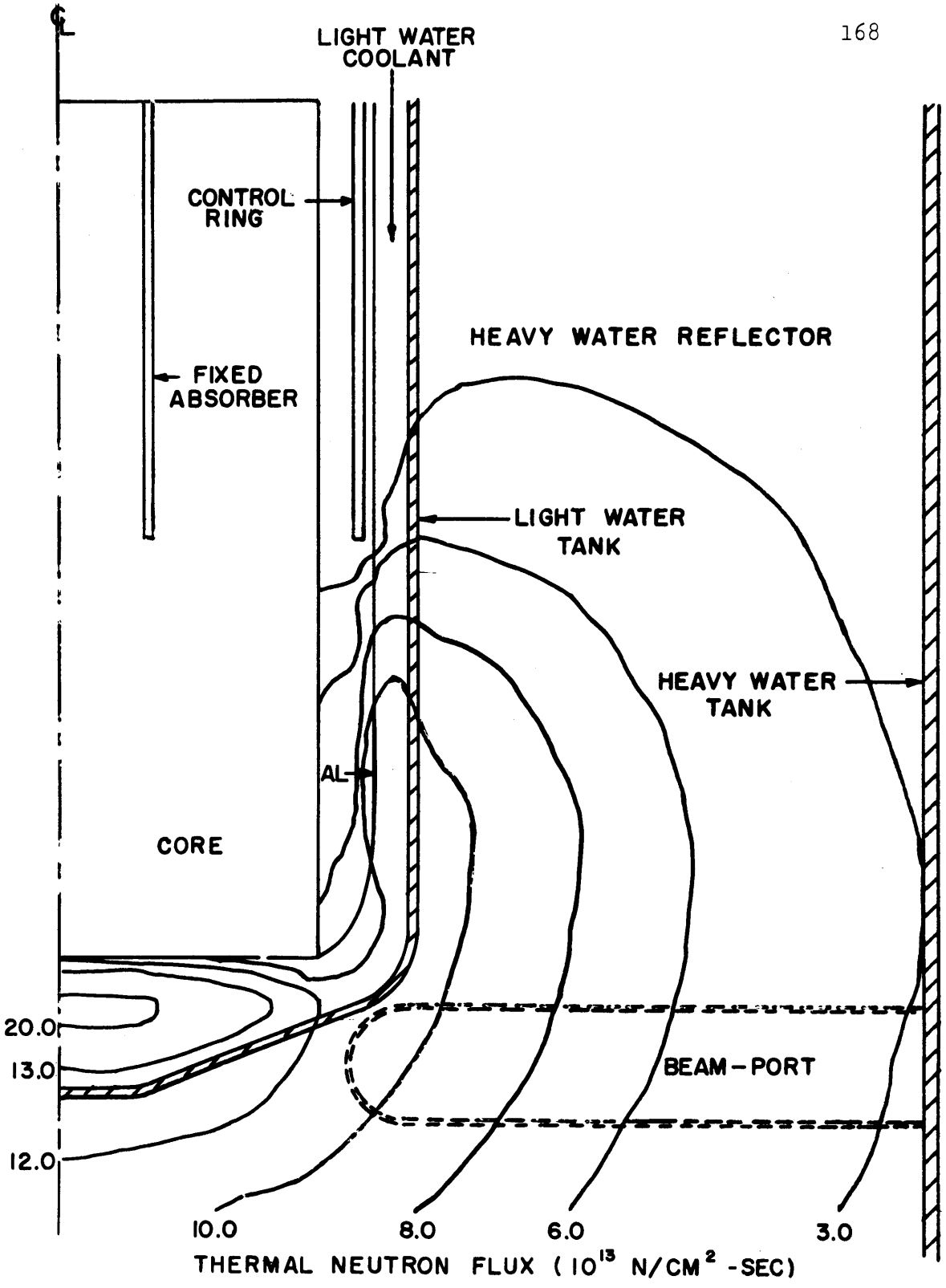

FIG. 7.1 VERTICAL SECTION OF REDESIGNED MITR-II CORE

There is a 1.0-inch-thick annular aluminum layer between the core-edge and the outer movable control ring.

An annular region of effective radial width of about 1.0 inches exists between the outer movable absorber ring and the light water tank. The light water coolant flows down the side of the core through this annular region into the bottom light water plenum and then flows up through the core. As discussed in section 6.4.3, the shape and size of the lower light water plenum have been chosen in order to enhance the thermal neutron flux underneath the core. In addition, the flow of the coolant down the side of the core is a method of directing the light water into the bottom plenum with a minimum perturbation on the thermal neutron flux underneath the core. The 1.0-inch-thick aluminum between the core-edge and the outer movable absorber ring cuts down on the severe power peaking difficulties that would result on the side of the core due to the high moderation effect of light water.

The radial heavy water reflector occupies the annular region of about 17.0 inches in radial width between the light water tank and the graphite reflector. There is also a bottom heavy water reflector of about 24.0 inches minimum depth below the light water plenum. Radial beam ports have been made re-entrant into the heavy water tank to extract thermal neutron beams from underneath the core. There is also a cryostat of about 2.5 inches diameter positioned at the core center.

7.2 THERMAL FLUX DISTRIBUTION INSIDE THE HEAVY WATER TANK

Figure 7.1 also shows the thermal neutron flux distribution in the redesigned reactor operating at 5 megawatts. The fixed inner neutron absorbers as well as the control rod bank which will be inserted in the top half of the core during normal operation of the reactor, are shown at the 12.0 inch insertion position. In this calculation, lead has been used in place of the central cryostat. The effects of the beam port on the thermal neutron flux distribution have not been included in this calculation.

The $3.0X10^{13}$ n/cm^2-sec flux contour line shows that fluxes near the wall of the heavy water tank are not predicted to be very different from the value in the present reactor of about $2.2X10^{13}$ n/cm^2-sec. The advantage of the new design is derived from making the beam ports re-entrant into the heavy water tank. The tips of beam ports will be able to see thermal neutron fluxes of about $1.1X10^{14}$ instead of $2.2X10^{13}$ as it is in the MITR-I. Beam port optimization studies done by Kennedy (4) showed that the re-entrant beam ports in this final design will introduce a perturbation of about 25% in the calculated fluxes.

An important factor is the quality of the thermal neutron fluxes available at the tips of the beam ports. As pointed out in section 1.2.2, the compact core arrangement results in the maximum fast flux region occuring at the center of the core, separated from the maximum thermal

flux region that occurs in the reflector. Consequently, in the reflector where neutron beam is normally removed for experiments, the ratio of the thermal to fast neutron flux improves. A comparison of the thermal flux distribution in MITR-I and MITR-II cores discussed in section 10.3, shows that the ratio of thermal to fast neutron flux at the tips of re-entrant beam ports of MITR-II is 10.0 compared with a corresponding figure at the tips of MITR-I beam ports of 9.6 to 40.9.

The fast neutron as well as the gamma radiation background is further reduced by removing the thermal neutron beam from underneath the core. The neutron absorbers in the top half of the core and the bottom light water plenum are two features in the redesign that assist in maintaining the maximum thermal flux region underneath the core.

7.3 POWER DENSITY DISTRIBUTION

The power density distribution in MITR-II core corresponding to the thermal neutron flux distribution discussed in section 7.2 is shown in Fig. 7.2. The $9.0X10^{12}$ fissions/cm^3-sec power density contour line shows that only the very lower tip of the fuel elements is subjected to power densities of about $1.0X10^{13}$ fissions/cm^3-sec.

The most important point on this figure is the effect of the neutron absorbers in the upper half core on the axial power density distribution. Generally, the maximum power densities occur at the bottom of the core and decrease by

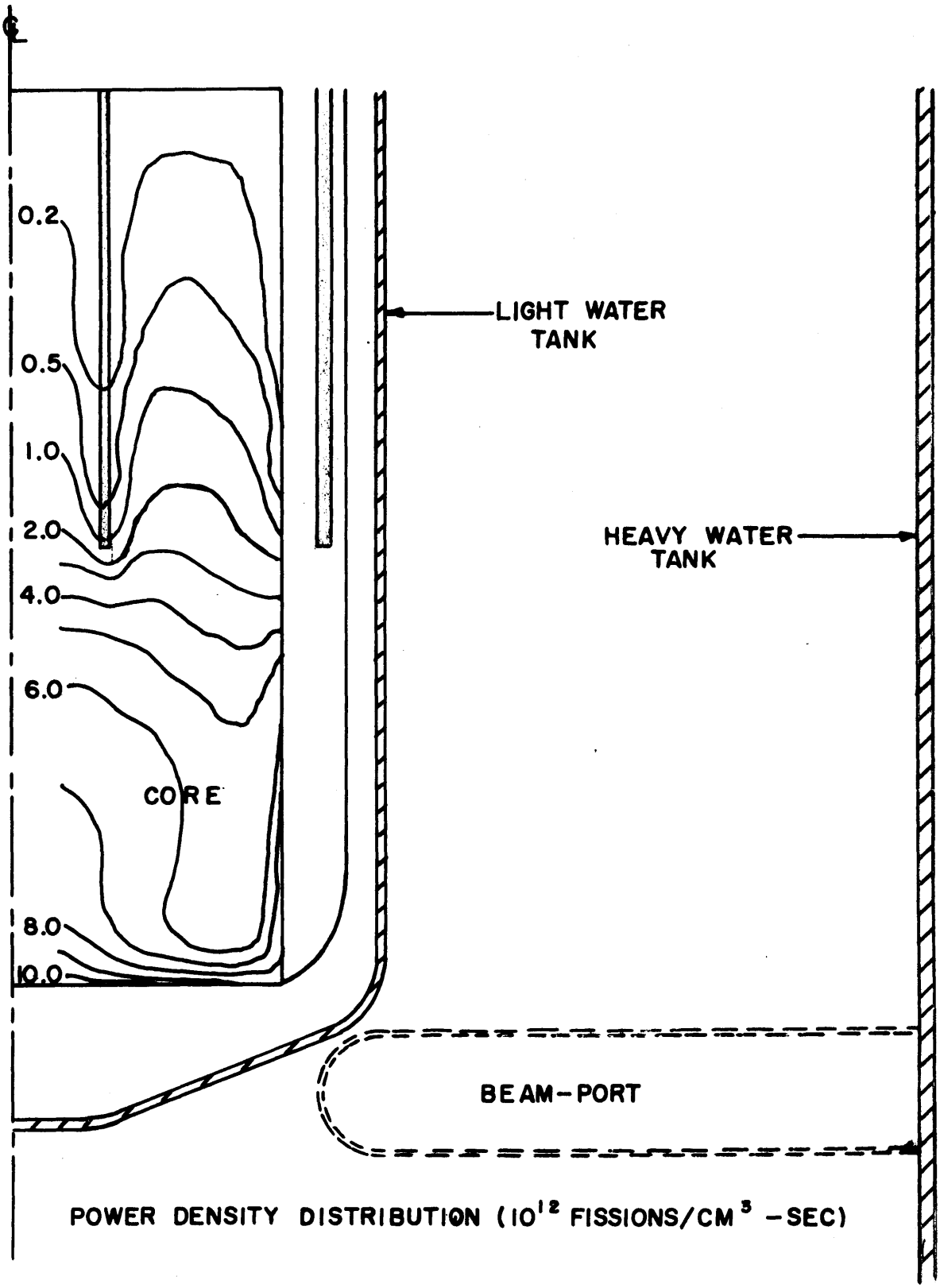

FIG. 7.2 VERTICAL SECTION OF REDESIGNED MIT-R-II CORE

a factor of about 3 at the top of the active part of the core. The initial burn up rate at the lower tip of a fresh fuel element, therefore, is about a factor of 3 greater than that at the axial center. The economic advantage of this core configuration mentioned in section 6.4.4 is derived from making use of this axial power density distribution. After the lower portion of a fuel element has been used up, it can be removed and rotated putting the fresher top portion in the high power density region and thus giving a good fuel element utilization. The fuel elements will also be made less than twice the active core height. In this way, the middle portion, which normally sees the lowest power densities, will be used twice, resulting in a more uniform final burn up of the fuel element.

7.4 DESIGN OF THE NEUTRON ABSORBERS IN THE UPPER HALF CORE

It is desirable to design the neutron absorbers so as to reduce the power generated in the upper half core, as this power does not contribute to the thermal neutron flux underneath the core, where neutron beam is removed for experiments.

Perturbation calculations done using EXTERMINATOR-II (43) showed that the reflector neutrons have their maximum importance at about 1.5 inches from the core face. The movable control rod bank, therefore, has been placed in this region of the reflector (see Fig. 7.1), where the rods have their maximum reactivity worth. The core has three rings

of elements as explained in section 4.2.3. In the core model described in section 7.1, the inner fixed absorber ring has been placed at the interface between the first and second ring of elements. The power density distribution for this core configuration, given in Fig. 7.2, shows that the power density rises significantly at midway between the absorber rings. This results in about 11.6% of the total core power generated in the upper half core.

Two methods for reducing the power generated in the upper half core were examined. First, it was found that placing the movable outer absorber ring next to the core face resulted in significant reduction in the power density distribution only in the core outer annular region of about 0.5-inch radial thickness. The probably mechanical problems of placing the movable outer absorber ring inside the core, therefore, outweighed the slight reduction in the power generated in the upper half core. Secondly, it was found that placing a second fixed absorber ring at the interface between the second and the third rings of fuel elements reduced the power generated in the upper half core from 11.6% to 4.5%. However, the reactivity loss due to the additional aluminum in the active part of the core as well as the resulting mechanical design complexity ruled out this approach.

On the basis that it will not be necessary to increase the core diameter very much above 14.0 inches, the two

absorber rings design described in section 7.1 has been retained. The 11.6% of the core power generated in the upper half core will be further reduced by the method of flipping the fuel elements described above in conjunction with fuel management discussed in section 7.4 below.

7.5 THE CORE RADIAL SECTION

The calculations discussed in Chapter 3 show that the cylindrical core radial section has advantages compared with other geometrical arrangements. Cylindrical core, therefore, has been used in the reactor models discussed so far. A plate-type fuel element design was sought such that a number of these could be loaded to form a core radial section as close to a cylinder as possible.

7.5.1 The ATR Type Sector Fuel Elements

A plate-type fuel element design that can be loaded to form a cylindrical core is the sector fuel element already being used in ATR (57). A typical arrangement of these elements to form a 25-element cylindrical core for MITR-II is shown in Fig. 7.3. This consists of 12 identical fuel elements in the outer ring of elements, another 12 identical fuel elements in the intermediate ring of elements, and inside the inner fixed absorber ring is a single central fuel element with cryostat position in the center.

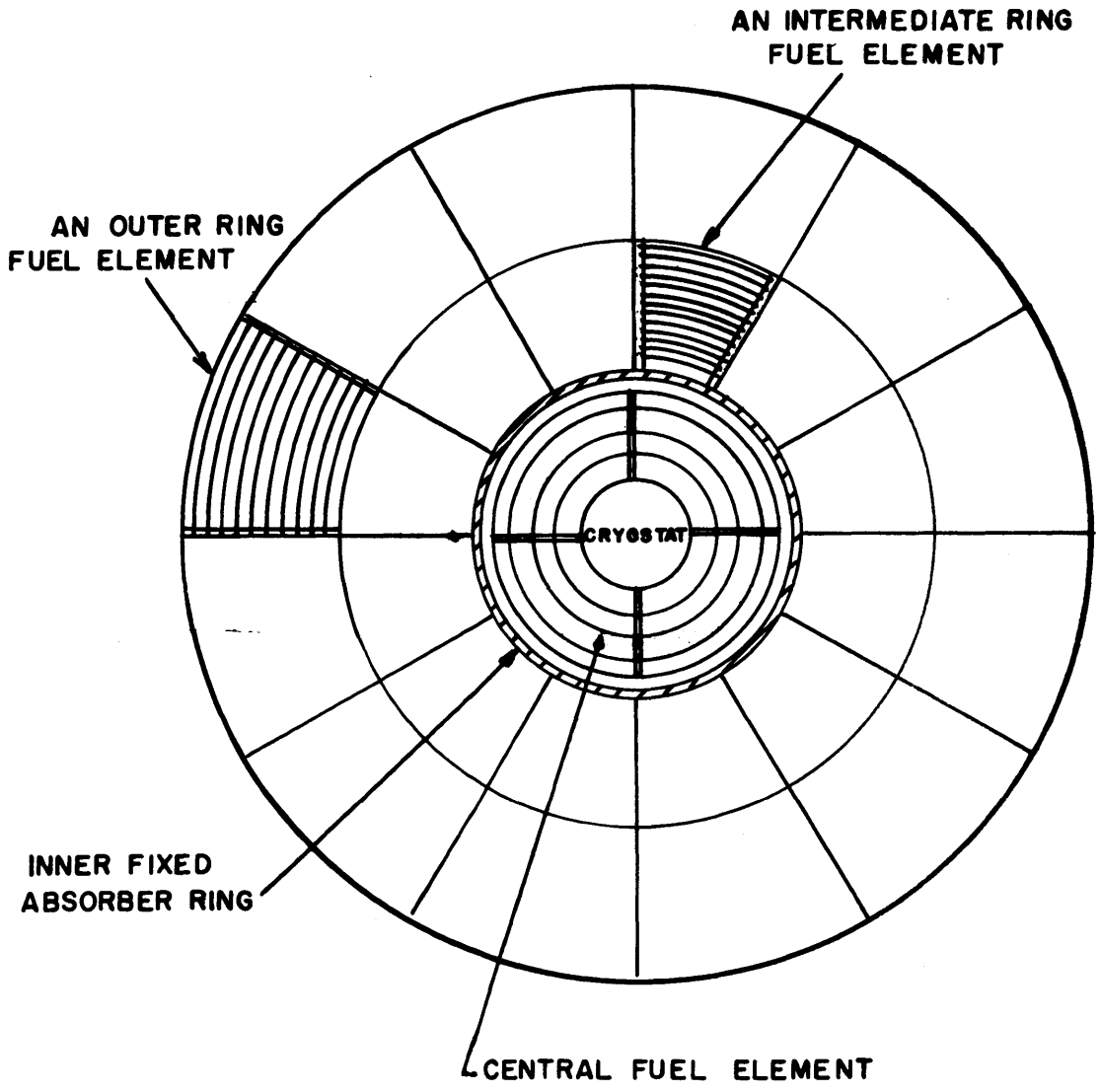

FIG. 7.3 CYLINDRICAL CORE WITH ATR TYPE FUEL ELEMENTS

A detailed layout of these elements for MITR-II core by E. Barnet (2) revealed that each of the fuel elements in the outer and intermediate rings of elements will have to be made up of about 18 fuel plates each of different lengths. The fabrication of these fuel elements will be much more expensive than fuel elements of the same 18 fuel plates but equal length. The fact that fuel elements are neither interchangeable between the outer and intermediate ring of elements nor can be rotated on their own vertical axis through 180 degrees is a further limitation on the flexibility of changing fuel element position for fuel management purposes.

Another important limitation on this fuel element design is the apparent need to grade plate by plate the fuel loading in the first few longest plates of the fuel elements in the outer ring. The power density distribution given in Fig. 7.2 shows the very rapid rise in the power densities towards the core-reflector interface. The diffusion calculations underestimate the sizable variations in the power distribution towards the core face due to the very soft spectrum of re-entrant flux of thermal neutrons. Unless fuel loading variations plate by plate are sizable over the first few outermost fuel plates, the power peaking difficulty in the outermost coolant channels can be severe.

7.5.2 Rhomboidal Fuel Element Design

The fuel elements used in the design base are rhomboidal in sectional shape and have 15 fuel plates each of the same length. The hexagonal core radial sectional shape that results by arranging 27 of these elements is shown in Fig. 7.4.

This final core radial sectional shape is not cylindrical, nevertheless, the arrangement has three advantages. First, all 15 fuel plates are of equal length, and hence the fabrication of this fuel element will be cheaper than the ATR type fuel element described in section 7.5.1. Secondly, all the 27 fuel element positions are interchangeable and each element can be rotated on its vertical axis through 180 degrees. This flexibility in fuel element placement is advantageous for fuel management purposes. Thirdly, the typical fuel element shown in Fig.7.4 has its coolant channels breadth along a radial direction compared with the transverse direction for the sector fuel element given in Fig. 7.3. Consequently, the finning effect of the radial fuel plates reduces the importance of the sizable variations in power density towards the core face. It is, therefore, not necessary to grade plate by plate the fuel loading in these elements. Exceptions are the three corner elements marked C_1, C_2 and C_3 in Fig. 7.4. However, the great flexibility of placement of fuel elements will permit fuel management to be used to reduce power peaking difficulties in fuel elements placed in positions C_1, C_2 and C_3. For example,

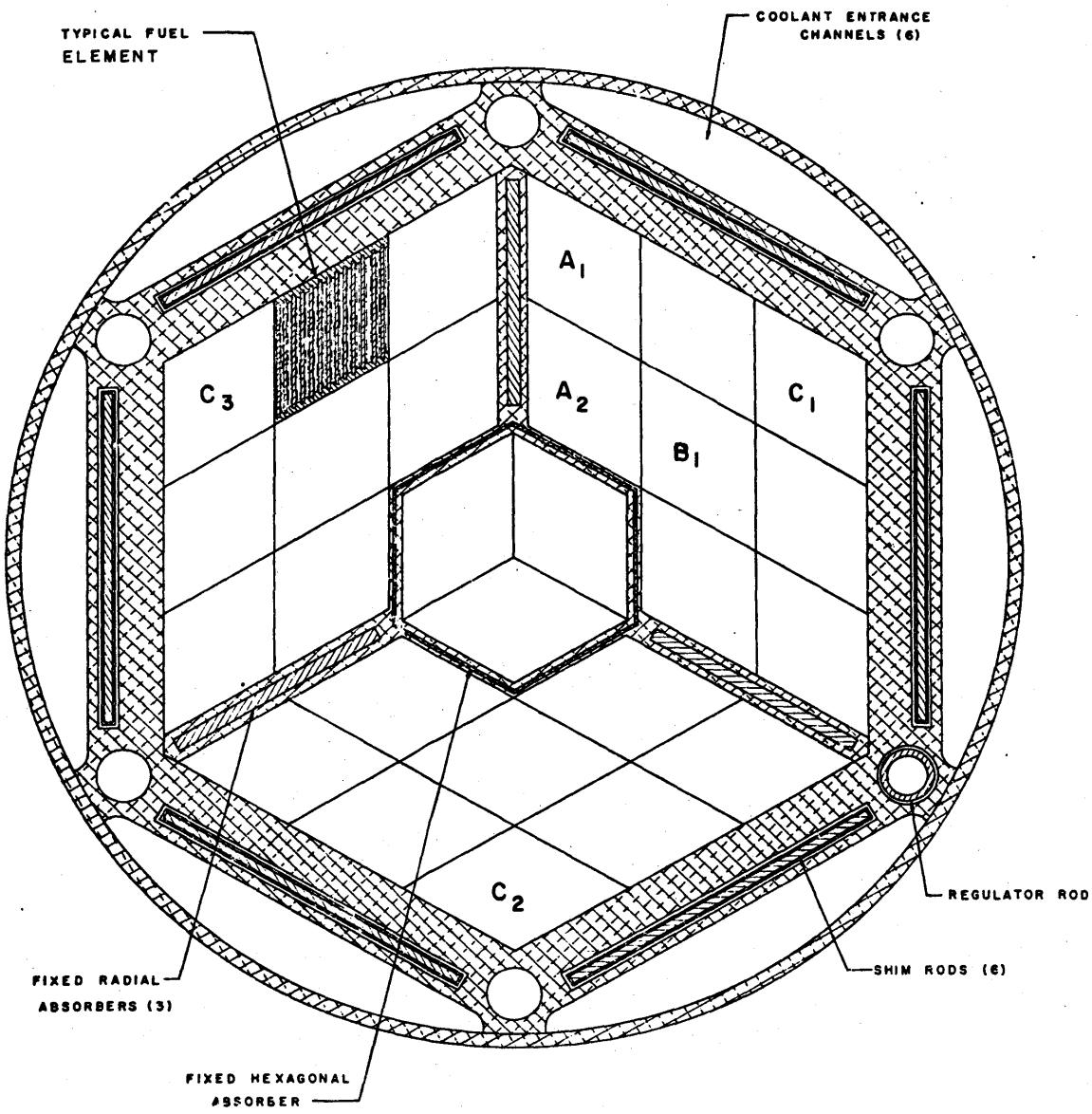

FIG. 7.4 RADIAL SECTION OF MITR-II CORE

a fuel element with moderately burned up lower tips will be placed in these positions, where the hottest channels are likely to occur.

Referring to Fig. 7.4, one of the three fuel element positions in the center will be used as the central cryostat position. The aluminum at the core face to help reduce power peaking difficulties, as mentioned in section 7.1, has been made a larger structure to provide support for the whole core. This structure has central and outer hexagonal sections that are joined together by three radial ribs. In the upper half core, a hexagonal ring of cadmium absorber (the inner fixed absorber described in section 7.1) is inserted in the central hexagonal section. The outer ring of absorber consists of the 6 shim rods shown in Fig. 7.4. These shim rods are guided through the outer hexagonal section.

In the upper half core, 0.040 inch-thick cadmium, clad on both sides with aluminum, is to be inserted in the three radial ribs. These will reduce further the 11.6% of the core power produced in the upper half core. In addition, these will also improve the fuel management scheme to reduce the fraction of the power generated in the upper half core. For example, an element with fresh upper end will be placed in a position such as A_1 or A_2 indicated in Fig. 7.4, where two sides of the element are protected by the cadmium plates. When the element is removed and flipped

over, its burned upper half can be placed in a position such as B_1 in Fig. 7.4. The detailed studies of depletion effects in this core and the optimum fuel management procedure necessary to reduce the power peaking in elements placed in positions C_1, C_2 and C_3 as well as reduce the power generated in the upper half core is the subject of a doctoral thesis to be undertaken by Kadak (58).

7.6 COMPLETE ASSEMBLY OF THE REDESIGNED REACTOR

The complete assembly of the redesigned MIT reactor is shown in Fig. 7.5. A comparison of Fig. 7.5 with Fig. 1.1 shows that the redesign has been confined principally to the region occupied by the heavy water tank as well as the regions above (2) and below (3) the heavy water tank.

7.6.1 The Fail-Safe Control Rod Design

An important safety feature of the mechanical design of the region above the core by E. Barnet (2) is the fail-safe control rod design as mentioned in section 4.2. The six rods consist of 0.040-inch-thick cadmium plates sandwiched in aluminum and guided through the outer hexagonal section of the aluminum core support structure described in section 7.5.2. Each control rod plate is attached to an arm which in turn is attached to a weighted member. A light rod connects the weighted member to a magnet armature

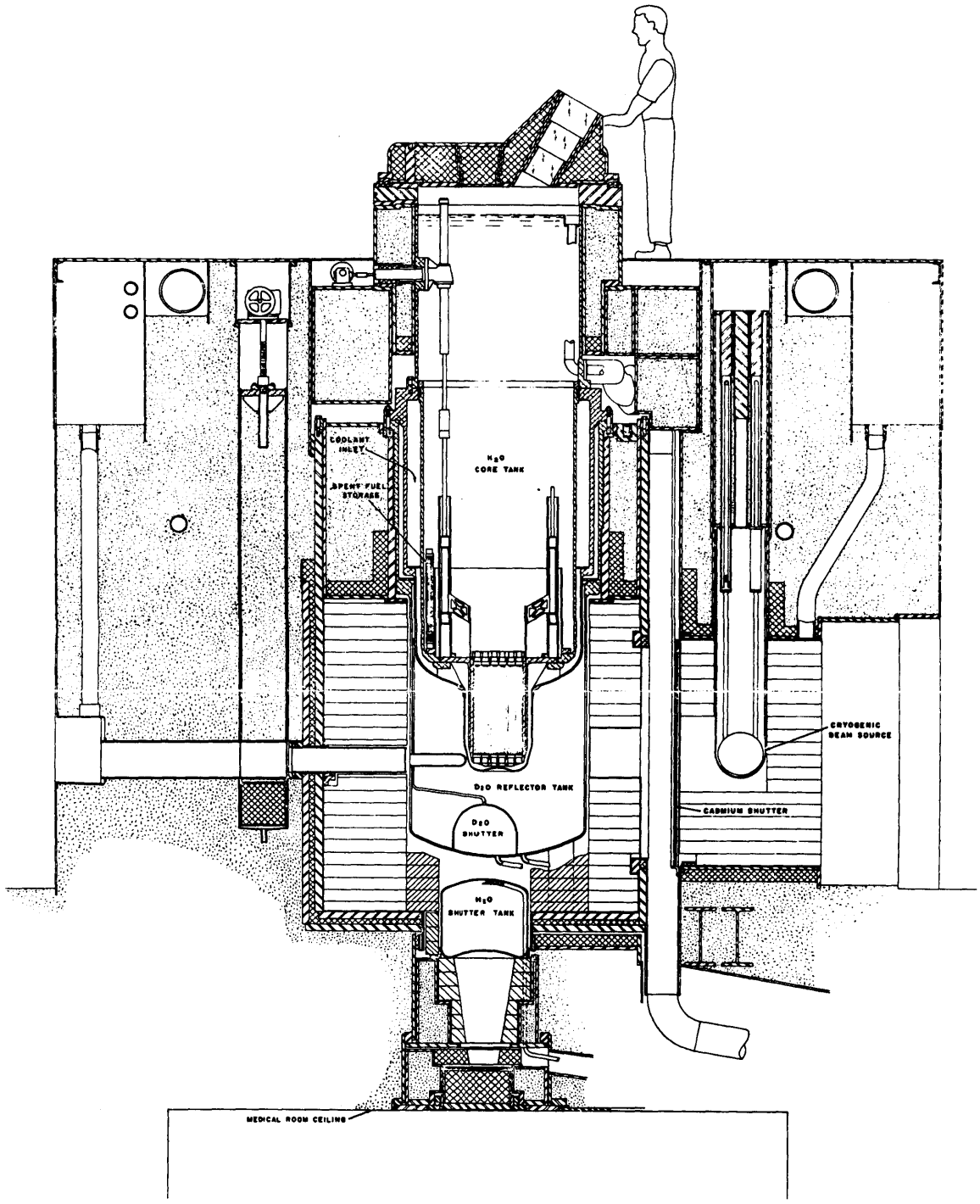

FIG. 7.5 VERTICAL SECTION OF MITR—II

that is near the top of the heavy water tank.

A magnet is lowered from above the heavy water tank, makes contact with the armature and the control rod is lifted from the core as required. The weight distribution of the weighted member is such that under operating conditions no conceivable hydraulic forces can lift the rods from the fully inserted position. On either a scram signal when the magnet current drots to zero or a failure of any of the parts above the weighted member, the massive weight of the weighted member acting under gravity rapidly scrams the system.

7.6.2 Full Scale Flow Mock-up of the Bottom H_2O Plenum

The general light water coolant flow configuration is downward into an upper plenum near the top of the heavy water tank. From this upper plenum, the coolant is uniformly distributed into 6 coolant channels between the light water tank and the aluminum core structure shown in Fig. 7.4. The coolant then flows down the side of the core through the 6 channels. Near the bottom of the core, the 6 coolant channels taper into a cylindrical annular cross-section as shown in Fig. 7.1. At this point, the light water coolant flow is turned sharply through 90 degrees into the bottom plenum, from which the coolant flows up through the core.

In section 6.4.3, it was pointed out that the bottom plenum shape shown in Fig. 6.9 results in a better thermal neutron flux distribution underneath the core, though gives a non-uniform flow distribution through the fuel elements. On the other hand, the bottom plenum shape, shown in Fig. 6.10, which gives a more uniform flow distribution through the fuel elements, results in a poorer thermal neutron flux distribution underneath the core.

A full scale flow mock up of the bottom plenum has been completed by the MIT Reactor Operations Division. The bottom plenum shape used in the tests is that shown in Fig. 6.10. Preliminary tests showed that the corner elements had a low flow relative to the central elements. A change was made in the bottom design and flow diverters added to the corners of the bottom annular cross-section into which the 6 coolant channels taper. The effect of these diverters is to impart a horizontal swirl to the coolant as it begins to flow up through the core. Subsequent flow measurements showed that the flow through the fuel elements was more uniform and followed a predictable pattern.

7.6.3 Design of the Region Underneath the Core

EXTERMINATOR II calculations showed that, because of the long diffusion length of the thermal neutrons in heavy water, a minimum heavy water reflector height of 2 feet was required below the bottom light water plenum. An

increase in the heavy water reflector height above 2 feet did not show significant effect on either the effective multiplication in the system nor the fluxes underneath the core.

The redesign of the medical therapy room below the core for continued research on brain cancer has been guided by two principles: to increase both the ratio of the epithermal to thermal neutron flux (58) and the intensity of the flux available at the medical therapy room.

To provide the flexibility of altering the epithermal flux intensity, a D_2O shutter tank of about one foot high has been placed underneath the bottom of the heavy water tank. When the D_2O shutter tank is emptied, the height of heavy water reflector below the bottom light water plenum is at the minimum of one foot and the ratio of epithermal to thermal neutron flux reaching the medical therapy room is maximum.

Neutrons pass through a 29-inch diameter hole to reach the medical therapy room. The method of optimization of the number of neutrons passing through this hole is discussed by Sanders and Thompson (3). Their design of this hole is shown in Fig. 7.6.

7.7 FLEXIBILITY IN THE MITR-II CORE

Critical experiments to determine the detailed

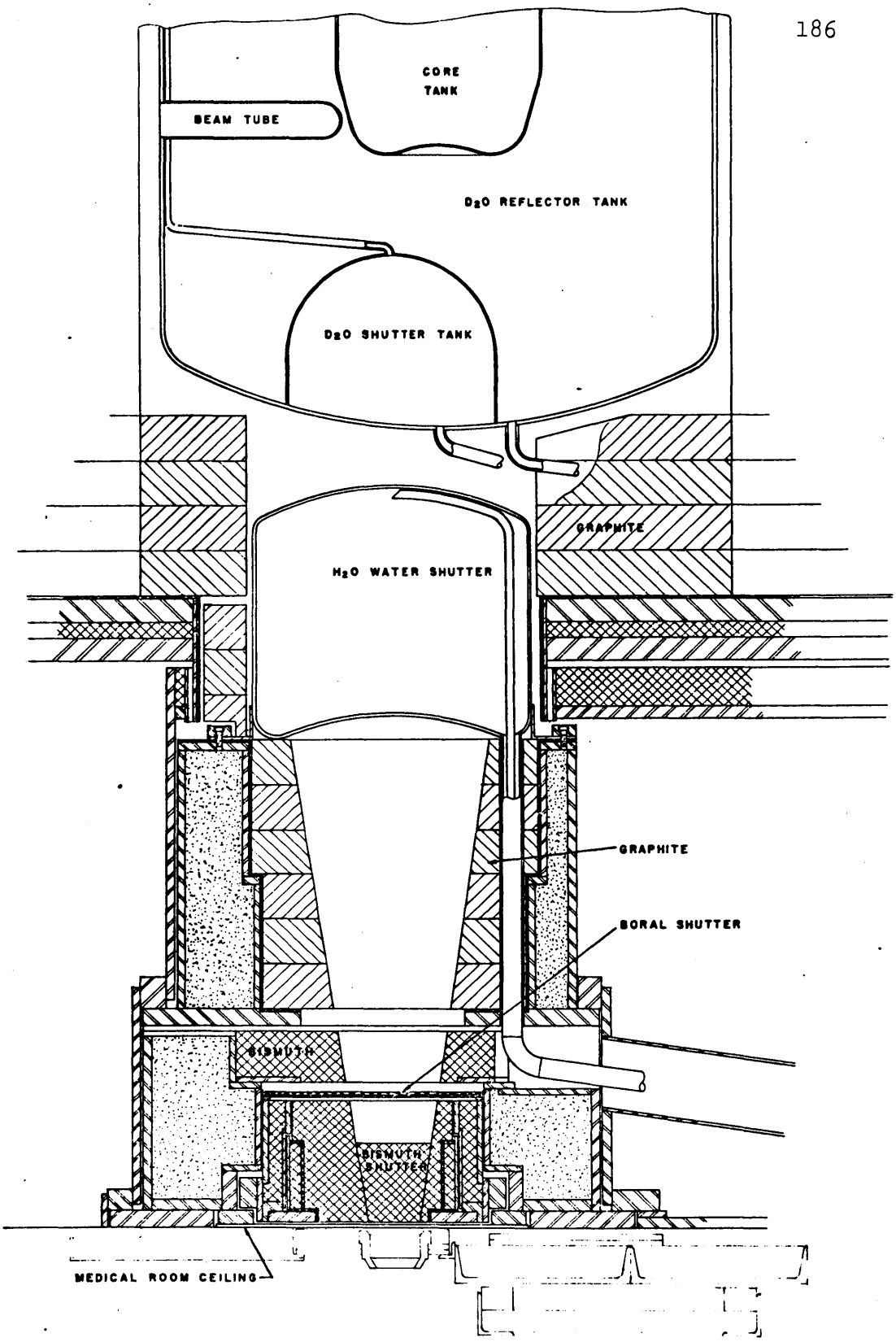

FIG. 7.6 MEDICAL THERAPY ROOM DESIGN

characteristics of MITR-II core are not envisaged prior to the first loading of the core. There is, however, adequate flexibility in the MITR-II core to obtain a useful life out of the first loading as well as to permit future core loadings to be responsive to the experience gained in the operation of the preceeding cores.

7.7.1 Flexibility in the First Core Loading

Adjustment of the effective core height is the means of changing the effective multiplication in the system during the first core loading. If the calculated critical mass for some reason is low, the effective core height can be raised. Figure 7.7 shows the situation in which the effective core height has been increased from 12 to 16 inches. The effective multiplication in the system has increased by about 7% in K_{eff} while the unperturbed thermal neutron flux at the beam port tips has decreased from $1.10X10^{14}$ (Fig. 7.1) to $0.9X10^{14}$ n/cm^2-sec (Fig. 7.7). The effective core height can be increased to a maximum of 24 inches.

The situation in which the calculated critical mass is high is shown in Fig. 7.8, and the effective core height has been decreased from 12 to 8 inches. The effective multiplication in the system has decreased by about 13% in K_{eff} and the thermal neutron flux at the beam port tips has increased from $1.10X10^{14}$ (Fig. 7.1) to $1.3X10^{14}$ n/cm^2-sec (Fig. 7.8). In this case, the limiting core

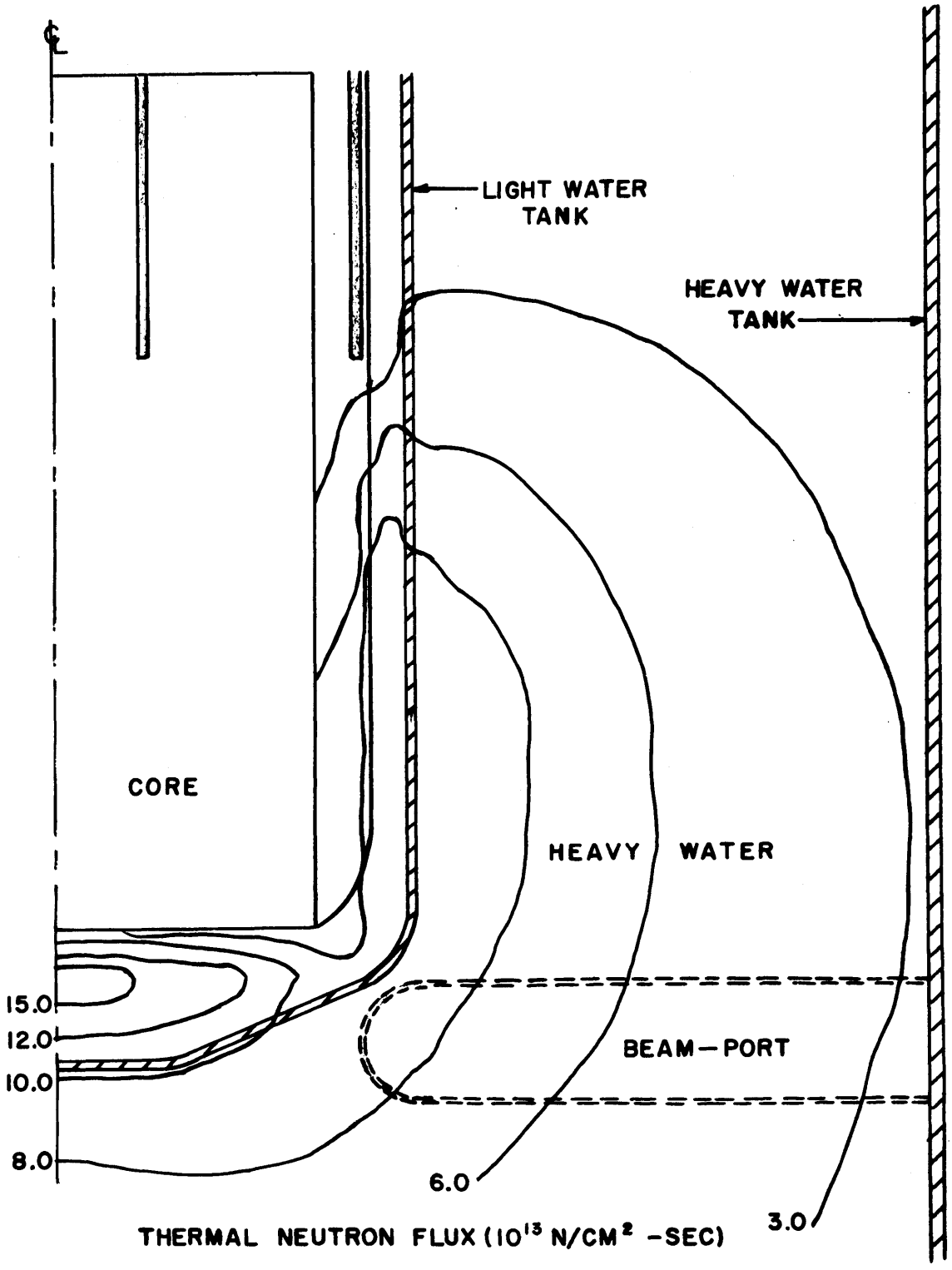

FIG. 7.7 THERMAL FLUX DISTRIBUTION FOR 16-INCH CORE

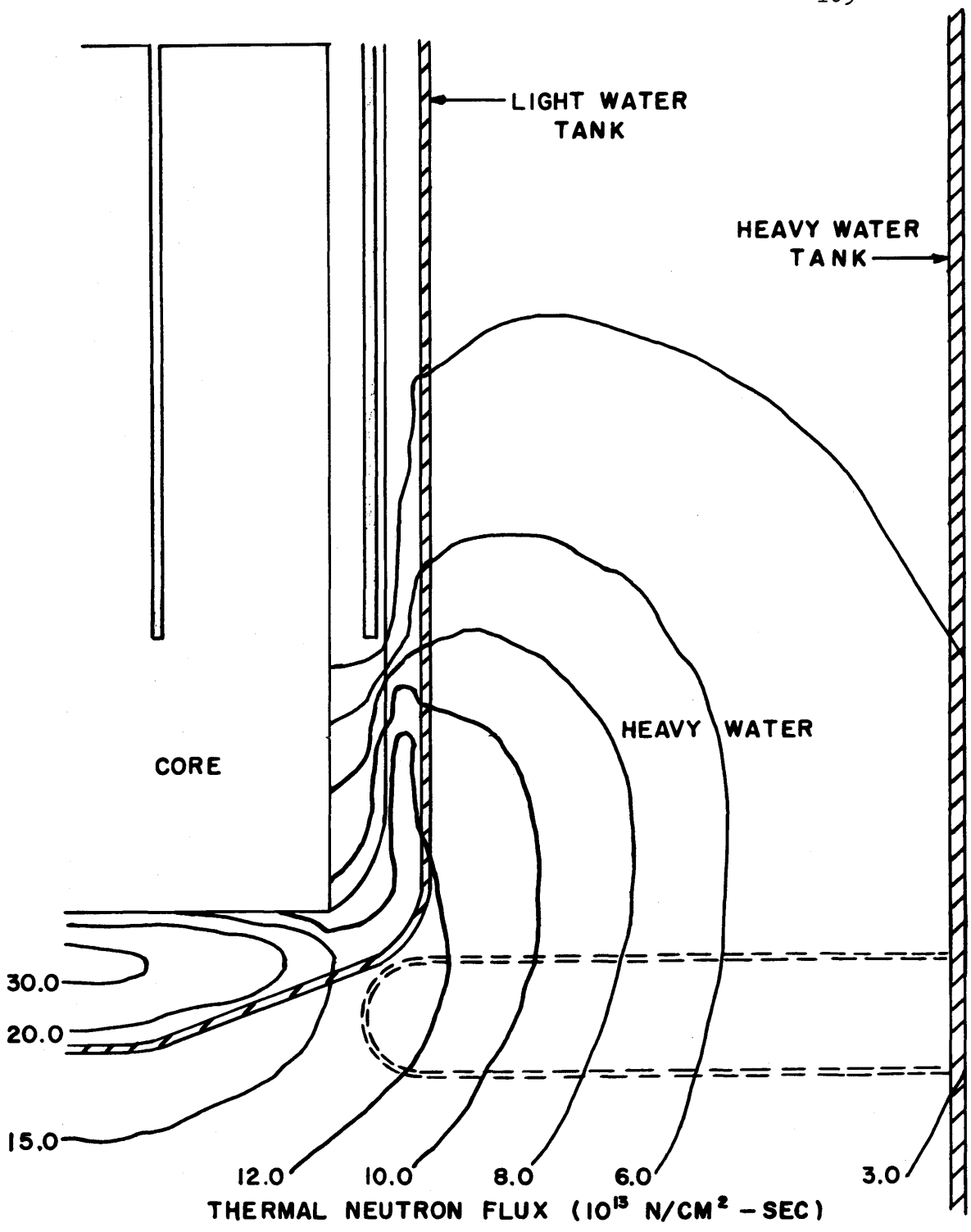

FIG. 7.8 THERMAL FLUX DISTRIBUTION FOR THE 8-INCH CORE

height is determined by heat transfer difficulties in the hottest coolant channel. If necessary, the reactor may be operated at a power level less than 5 megawatts in order to insure that the maximum local fuel plate surface temperature in the core does not exceed the maximum permissible value.

7.7.2 Flexibility in Future MITR-II Core Loadings

In future MITR-II core loadings, the flexibility of changing the effective core height is available. In addition, the uranium weight percentage in the fuel meat as well as the volume fraction of aluminum in the core may be altered without changing the outer dimensions of the fuel elements.

The important effect caused by increasing the uranium weight percentage in the fuel meat is the corresponding increase in the effective multiplication in the system. A calculation of the effective multiplication in the core versus the uranium weight percentage in the fuel meat shows that there is about 1% gain in effective multiplication for 1% increase in the uranium weight percentage in the fuel meat. Presently, the problem of uranium segregation limits the uranium content in the fuel meat to about 33 weight per cent when the aluminum-uranium alloy is used. However, when powder metallurgy technique is used, the uranium weight percentage in the fuel meat may be as

high as about 40%.

Replacing aluminum in a core of fixed size and uranium loading results in higher effective multiplication in the system, though the leakage flux in the reflector decreases. This effect is illustrated by curves of ΔK_{eff} and reflector flux versus the total aluminum volume fraction in the core shown in Fig. 7.9. The fins on MITR-II fuel plates provide additional heat transfer area. Thus, depending on the need for additional heat transfer capability, the aluminum volume fraction in the core may be increased to provide additional heat transfer area as required. On the other hand, if it is found necessary to increase the variable reactivity in the system, the aluminum volume fraction in the core may be decreased.

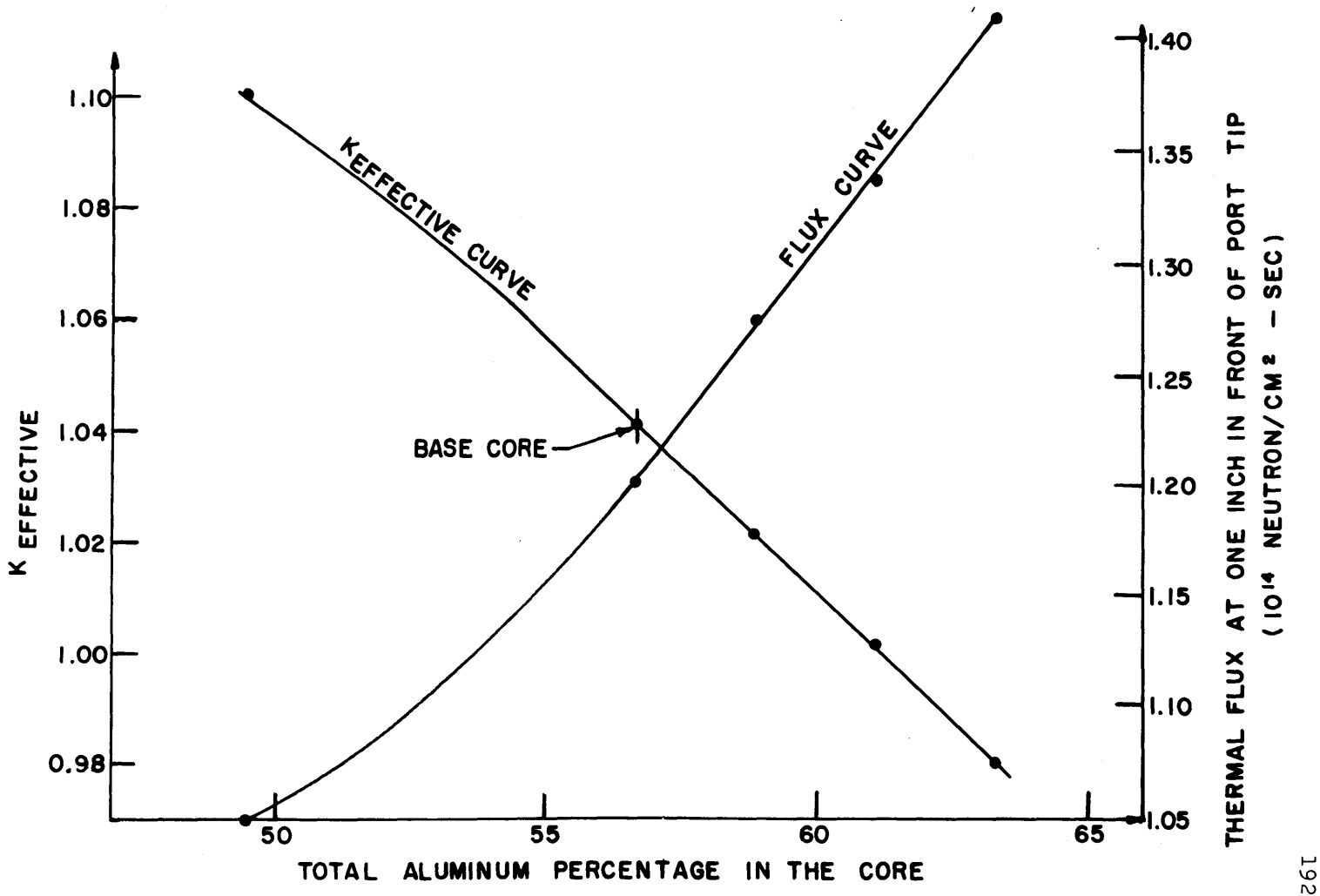

FIG. 7.9 EFFECT OF CHANGING MODERATOR TO ALUMINUM RATIO IN THE BASE CORE, KEEPING TOTAL CORE SIZE AND URANIUM LOADING CONSTANT

CHAPTER VIII

REFINEMENT OF THE THREE-GROUP CROSS-SECTIONS AND GEOMETRICAL DETAILS

As critical assembly experiments are not envisaged prior to the first loading of the MITR-II core, an effort has been made to refine the calculations. The refinement of the three group cross sections has shown that slight changes in the dimensions and composition of the design base of the MITR-II core, described in section 7.1, are necessary. In addition, since the calculations so far have been done in cylindrical geometry, the geometrical effects which could not be treated conveniently in this geometry have been examined. These refinements and a resulting modified MITR-II core are described in this chapter.

8.1 REFINEMENT OF THE THREE-GROUP CROSS-SECTIONS

Using a spherical approximation of the design base of the MITR-II core, described in section 7.1, three-group calculations have been carried out to determine the effects of the thermal cut-off energy and the five thin regions of light water and aluminum outside the core. These three-group calculations have been compared with twenty-three group transport as well as diffusion theory calculations

as described in section 2.2. On the basis of these comparisons, the thermal cut-off energy has been raised from 0.284 eV to 0.40 eV.

The cross section data used has also been improved. The library tape containing scattering kernels and absorption cross section data as the primary input to THERMOS [prepared by the LIBP code (19), (24)] has been changed. The LIBP code described by reference (24) has been rewritten in order to produce the thermal library tape of the LAZER code (24) in a format suitable for input to THERMOS (19), which is available at MIT. As discussed in section 2.3, the LAZER thermal library tape contains the Nelkin scattering kernel (22) for the bound proton in light water as well as Honeck's extension of the Nelkin kernel to heavy water (26) with the transport correction defined by Honeck (23). These kernels have been found to yield satisfactory agreement with measured data (23), (27). THERMOS (19) has also been modified to take account of fuel plate self-shielding effects as described in section 2.3.1.

The initial comparison of fifteen-group AIM-6 (59) diffusion calculations with the Olcott reactors (34) in spherical geometry yielded good agreement. AIM-6 was also used to obtain the initial set of three-group cross sections. A further comparison of both fifteen-group and three-group EXTERMINATOR-II diffusion calculations with

experimental criticality data for homogeneous systems has been carried out in cylindrical geometry as described in section 2.4. These latter calculations revealed that the original EXTERMINATOR-II few group collapsing scheme yielded poor results for the compact MITR-II core. The modified EXTERMINATOR-II few group collapsing scheme is described in section 8.1.1 below. The resulting modified design base of the MITR-II core as well as the flux and power density distributions are described below in sections 8.1.2 and 8.1.4 respectively.

8.1.1 The Modified Few Group Collapsing Scheme

The few group, G, cross-sections for nuclide N calculated by the EXTERMINATOR-II code (42) are as follows:

$$\sigma_i(N,G) = \frac{\sum_M \mathrm{CONC}(M,N)V(M) \sum_{g=g_1}^{g_2} \sigma_i(N,g)\bar{\phi}(M,g)}{\overline{\mathrm{CONC}(N)}\ \overline{\mathrm{PHI}}(G)\ \mathrm{VT}} \qquad \ldots 8.1.1$$

$$\sigma_r(N,G\rightarrow GG) = \frac{\sum_M \mathrm{CONC}(M,N)V(M) \sum_{g=g_1}^{g_2} \bar{\phi}(M,g) \sum_{l=l_1}^{l_2} \sigma_r(N,g\ l)}{\overline{\mathrm{CONC}}(N)\ \overline{\mathrm{PHI}}\ (G)\ \mathrm{VT}} \qquad \ldots 8.1.2$$

where

$$\overline{CONC}(N) = \frac{1}{VT} \sum_{M} CONC\ (M,N)V(M) \qquad ...8.1.3$$

$$\overline{PHI}(G) = \frac{1}{VT} \sum_{M} V(M) \sum_{g=g_1}^{g_2} \bar{\phi}(M,g) \qquad ...8.1.4$$

$$VT = \sum_{M} V(M) \qquad ...8.1.5$$

σ_i represents σ_a,σ_f and ν; g_1 and g_2 define the multigroup boundaries for the few group G; l_1 and l_2 define the multigroup boundaries for the few group G+1; GG=G+1; M is the composition (mixture) index; V(M) is the volume of composition M; $\bar{\phi}(M,g)$ is the average multigroup g flux in composition M; σ_r is the transgroup cross section, and CONC(M,N) is the concentration of nuclide N in composition M.

Although in equations 8.1.4 and 8.1.5 contributions should be included only if the nuclide density, CONC(M,N), is non-zero in composition M, this was found not to be the case. Consequently, the σ_i and σ_r calculated for isotopes in the core region where the region $\overline{PHI}(G)$ (defined by equation 8.1.4) is larger than that for the whole reactor, the calculated σ_i and σ_r were increased by the factor F,

where

$$F = \frac{\overline{PHI}(G)\ core}{\overline{PHI}(G)\ reactor} \qquad ...8.1.8$$

As pointed out in section 2.2.1, the epithermal flux in this kind of core is fairly flat, and hence, F for the epithermal group (few group 2) is only slightly greater than 1.0. However, as the fast flux peaks in the core and drops off rapidly in the reflector, F for this energy group is greater than 1.0. A comparison of few group cross sections calculated by using the original collapsing scheme (equations 8.1.1 through 8.1.5) with those obtained from modified collapsing scheme (equations 8.1.6 through 8.1.7) shows that F is about 2.0 for the few group one.

The ratio of fission neutrons produced to those absorbed is not sensitive to the value of F (section 2.2.3); however, both the transport and transgroup cross sections are sensitive to the value of F. The effect of the value of 2.0 for F in the core for the few group one is to cause an over-estimate of the moderation when these few group cross sections are used.

The difficulty with the few group cross sections has been eliminated by using a modified few groups collapsing scheme for the work described in section 2.4.

The few group, G, cross sections for nuclide N calculated by using the modified few group collapsing scheme may be averaged over the region defined by M=M1 to M2, and are as follows:

$$\sigma_i(N,G) = \frac{\sum_{M=M_1}^{M_2} CONC(M,N)V(M) \sum_{g=g_1}^{g_2} \sigma_i(N,g)\bar{\phi}(M,g)}{\sum_{M=M_1}^{M_2} CONC(M,N)V(M) \sum_{g=g_1}^{g_2} \bar{\phi}(M,g)}$$

$$\sigma_r(N,G \rightarrow GG) = \frac{\sum_{M=M_1}^{M_2} CONC(M,N)V(M) \sum_{g=g_1}^{g_2} \bar{\phi}(M,g) \sum_{l=l_1}^{l_2} \sigma_r(N,g\rightarrow l)}{\sum_{M=M_1}^{M_2} CONC(M,N)V(M) \sum_{g=g_1}^{g_2} \bar{\phi}(M,g)}$$

...8.1.7

The modified methods of calculating the few group transport cross sections as discussed in section 2.2.3 are given in Appendix A.

8.1.2 The Modified Design Base of the MITR-II Core

Since the EXTERMINATOR-II few group constants used in determining the dimensions of the design base of the MITR-II core, described in section 7.1, have been found to be in error, it is necessary to redetermine the optimum dimensions of the core. In particular, as the use of the unmodified few group cross sections resulted in an effective increase in the moderation in the core (see section 8.1.1), when the modified cross sections were used the core reactivity was too low and methods had to be found to increase the reactivity in the core with the minimum loss of the reflector maximum thermal neutron flux.

The effects of increasing the number of fuel plates in the elements of the design base of the MITR-II core, described in section 7.1, have been studied and summarized in Figs. 8.1 and 8.2. The K_{eff} and the effective core diameter are plotted as functions of the number of fuel plates per element in Fig. 8.1, while the corresponding reflector thermal neutron flux at the tips of experimental beam ports and the maximum normalized power density at the core-reflector interface are shown as functions of the number of fuel plates per element in Fig. 8.2.

From Fig. 8.1, it is observed that increasing the number of fuel plates per element from 15 as used in the design base of the MITR-II core described in section 7.1 to 18 results in the increase of the effective diameter of the core from 13.9 to 16.2 inches. The corresponding increase in K_{eff} is from 0.89 to 0.99. From Fig. 8.2, it is observed that the reflector thermal neutron flux at the tip of the beam ports decreases from 10.9 to 6.95X 10^{13} n/cm^2-sec, representing a 36% decrease in the flux. Increasing the core radius without changing the water to metal ratio in the core in order to gain reactivity, therefore, results in too large a reduction in the reflector thermal neutron flux.

The other alternative means of increasing the reactivity in the core with the minimum change in the core radius are either to increase the uranium loading per fuel

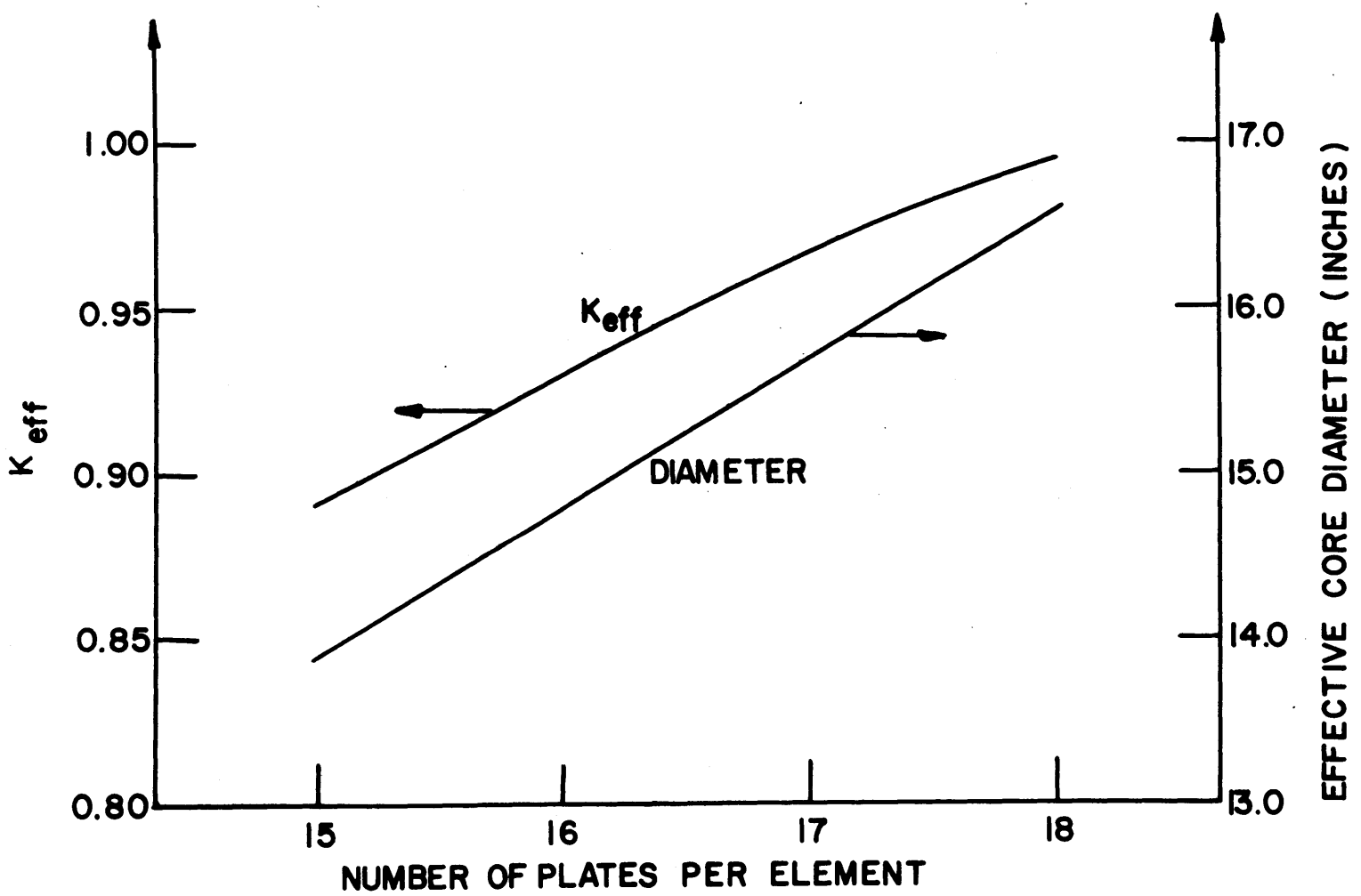

FIG. 8.1 EFFECTIVE MULTIPLICATION AND CORE DIAMETER AS A FUNCTION OF THE NUMBER OF PLATES IN A FUEL ELEMENT

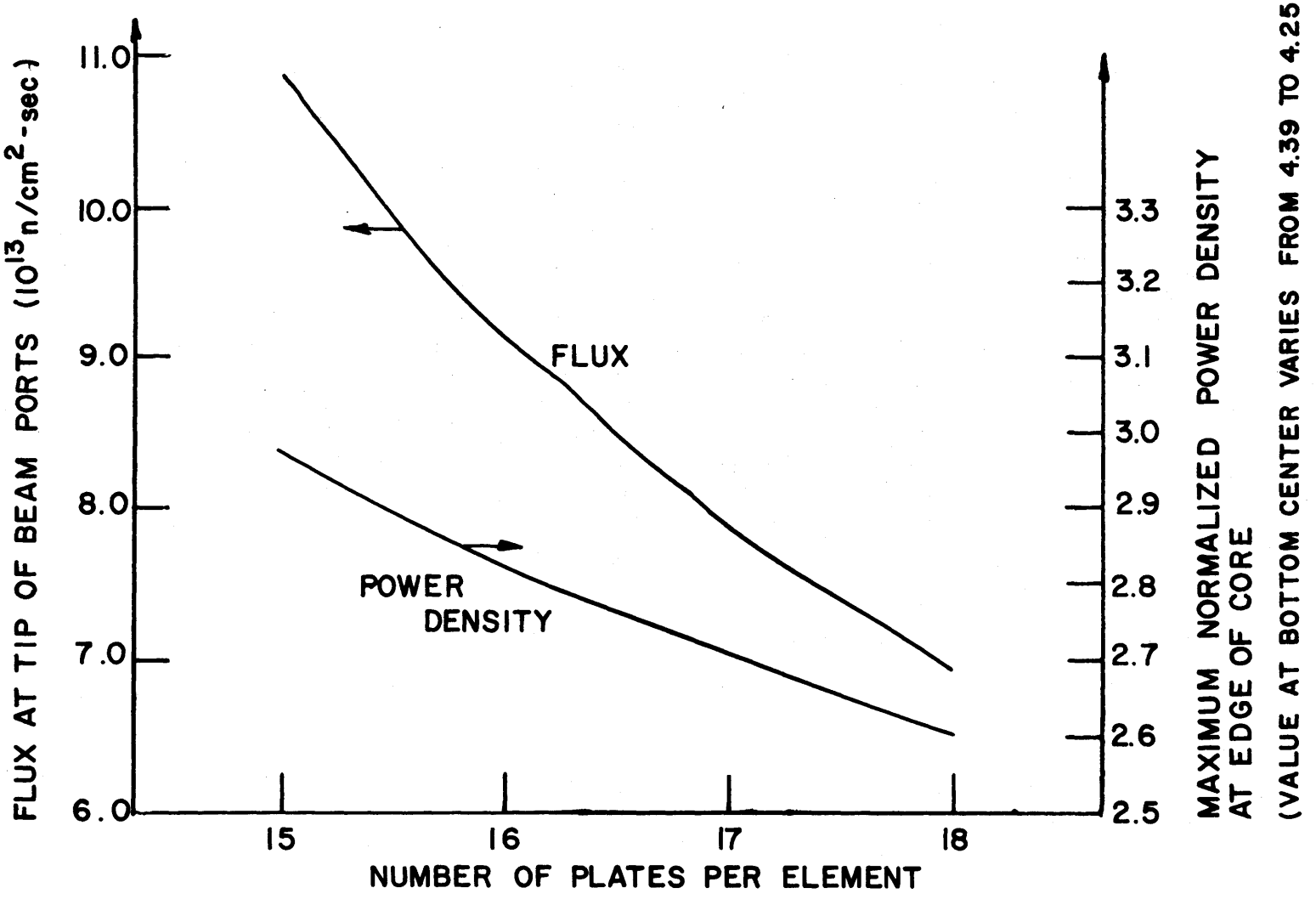

FIG. 8.2 THERMAL FLUX AND POWER DENSITY AS A FUNCTION OF THE NUMBER OF PLATES IN A FUEL ELEMENT

plate as much as possible, or to increase the water to metal ratio in the core, or to increase the core height. The uranium weight percentage in the fuel meat has been increased to 39%.

Calculations performed to study the effects of increasing the water to metal ratio as well as the height of the core are summarized in Table 8.1. Cases one and two are the 15 and 18 fuel plates per element cores described above in Figs. 8.1 and 8.2 and given in Table 8.1 for comparison. The weight percentage of uranium in the fuel meat for cases 3 through 6 is 39% and the effects of fuel plate self-shielding (section 2.3.1) have been included in the calculations for these last 4 cases.

A comparison of the K_{eff}, core diameter, and normalized power density for cases 2 and 3 shows that increasing the fuel loading per plate as well as widening the coolant channel gap in order to increase the water to metal ratio in the core is the method of choice for increasing the reactivity in the core with the minimum loss of the reflector thermal neutron flux. This same conclusion is borne out by comparing cases 3 and 5. Increasing the core height is also shown to be an effective method of adding reactivity to the core. A comparison of either cases 3 and 4 or 5 and 6 shows that increasing the core height results in a large increase in reactivity as well as a reduction in the core maximum normalized power density without changing the water velocity

TABLE 8.1

The Effects of Increasing Both the Height and H_2O% in the Core

Case	Number of Fuel Plates	$\%H_2O$ in an Element	Core Coolant Flow Area (in^2)	Effective Core Diameter	Effective Core Height (in)	K_{eff}	Flux at** Beam Port Tips (10^{13} n/cm^2-sec)	Maximum Normalized Power Density
1	15	43.99	61.72	13.9	12.0	0.891	10.9	4.39
2	18	43.99	91.48	16.6	12.0	0.99	6.95	3.95
3	15	48.75	83.85	15.3	12.0	1.023	7.04	3.77
4	15	48.75	83.85	15.3	15.0	1.072	6.20	3.12
5	16	47.74	87.46	15.9	12.0	1.036	6.62	3.78
6	16	47.74	87.46	15.9	15.0	1.085	5.85	3.13

**perturbed flux including the effect of beam ports (4)

in the coolant channels. Since in the MITR-II core, the total flow rate is fixed, there is a heat transfer advantage to be gained by increasing the core height as much as possible.

The modified design base of the MITR-II core is exactly the same as that described in section 7.1, except for two changes. The uranium weight percentage in the fuel meat has been increased to 39% and the effective coolant channel gap has widened from 0.077 to 0.088 inches. Consequently, the effective core diameter has increased from 13.9 to 15.0 inches. The 15 plates per fuel element design has been retained. The fuel plate effective thickness and the nominal core height have been retained at 0.064 and 12.0 inches respectively. The calculated core data and the atom number densities for this core are summarized in Figs. 8.3 and 8.4 respectively.

8.1.3 Further Comparison of Calculations with Criticality Data of a Partially Reflected Homogeneous Core

The first moment of the spectrum, V, is 1.622 at the center of the modified design base of the MITR-II core described in section 8.1.2 and Fig. 8.3. The spectrum in this core is harder than those described in section 2.5. A further comparison of calculations with experimental criticality data on a partially reflected

Fig. 8.3 Calculated Core Data for the Modified MITR-II

Fuel Element Specifications	
Effective Coolant Channel Gap	0.088 in.
Effective Fuel Plate Thickness	0.064 in.
Slant Side	2.653 in.
Cross Sectional Area	6.096 $in.^2$
Number of Fuel Plates	15.0
Length of Fuel Bearing Region	24.0 in.
Average Volume Fractions in a Fuel Element	
Total Uranium	0.00918
Aluminum	0.49093
Light Water	0.49989
Average Volume Fractions in the Core	
Total Uranium	0.00853
Aluminum	0.52719
Light Water	0.46428
Calculated Uranium-235 Loadings	
Per Fuel Plate	25.5 gm.
Per Fuel Element	382.5 gm.
Per 27-Element Core (Initial)	10.33 Kg.

Fig. 8.4 Calculated Atom Number Densities of the Core Constituents

Central Fuel Region*	
U-235	4.0935×10^{20}
U-238	8.0811×10^{19}
Aluminum	2.9569×10^{22}
Light Water	1.6536×10^{22}
Outer Fuel Region**	
U-235	3.8823×10^{20}
U-238	2.9222×10^{19}
Aluminum	3.1151×10^{22}
Light Water	1.5683×10^{22}

* The central fuel region consists of the 3 inner fuel elements.

** The outer fuel region consists of the remaining 24 fuel elements together with the 3 radial ribs (see section 7.4).

homogeneous core has been carried out to determine whether the hardened thermal neutron spectrum would affect the accuracy of the calculational procedures used and described in section 2.3.

The homogeneous core is a solution of uranyl-fluoride (UO_2F_2) in light water contained in an aluminum cylinder and partially reflected by light water. The light water reflector is effectively infinite at the bottom as well as the sides of the core up to a height equal to that of the fissile solution. This core had a H/U-235 atomic ratio of 74.6, a height of 12.0 cm., a diameter of 38.1 cm., and a critical mass of 4.5 Kg of uranium-235. The uranium enrichment was 93.2 weight per cent uranium-235. The first moment of the spectrum (defined by equation 2.3.13) at the center of this homogeneous core is 1.681 compared with 1.622 for the modified design base of the MITR-II core. This partially reflected homogeneous core is described in Table 5.12b of reference (32) as well as in Table 3.58 of reference (60)

The K_{eff} obtained for the fifteen group EXTERMINATOR-II diffusion calculation is 0.9845; while the corresponding three-group result is 1.0035. About 81% of the fissions occur in the energy range below 0.4 eV compared with the corresponding figure of about 89% for the first homogeneous core described in section 2.5. These results are consistent with those obtained for section 2.5 and show that the hardened spectrum would not affect the accuracy of the

calculational method.

8.1.4 Thermal Neutron Flux and Power Density Distributions in the Modified MITR-II Core

The neutron flux as well as the power density distributions in the modified MITR-II core have been determined by using EXTERMINATOR-II. The details of the light water plenum used in the calculations is given in Fig. 8.5.

The thermal neutron flux distribution around the core operating at 5 megawatts is given in Fig. 8.6. The fixed inner absorber ring as well as the control rod bank (outer movable absorber) are shown at the 12.0 inch insertion position. Lead has been used in place of the central cryostat position and the effects of the beam ports on the thermal flux distribution have not been included in the calculations.

A comparison of the $3.0X10^{13}$ n/cm^2-sec flux contour line on Figs. 7.1 and 8.6 shows that the predicted fluxes near the wall of the heavy water tank have not been affected by the changes in MITR-II core composition and dimensions. Indeed, the predicted thermal neutron flux at the heavy water tank for the MITR-II core is about the same as that flux at the same region for the MITR-I core (see section 10.2). The advantage of the redesign, therefore, is derived from making the beam ports re-entrant into the heavy water tank.

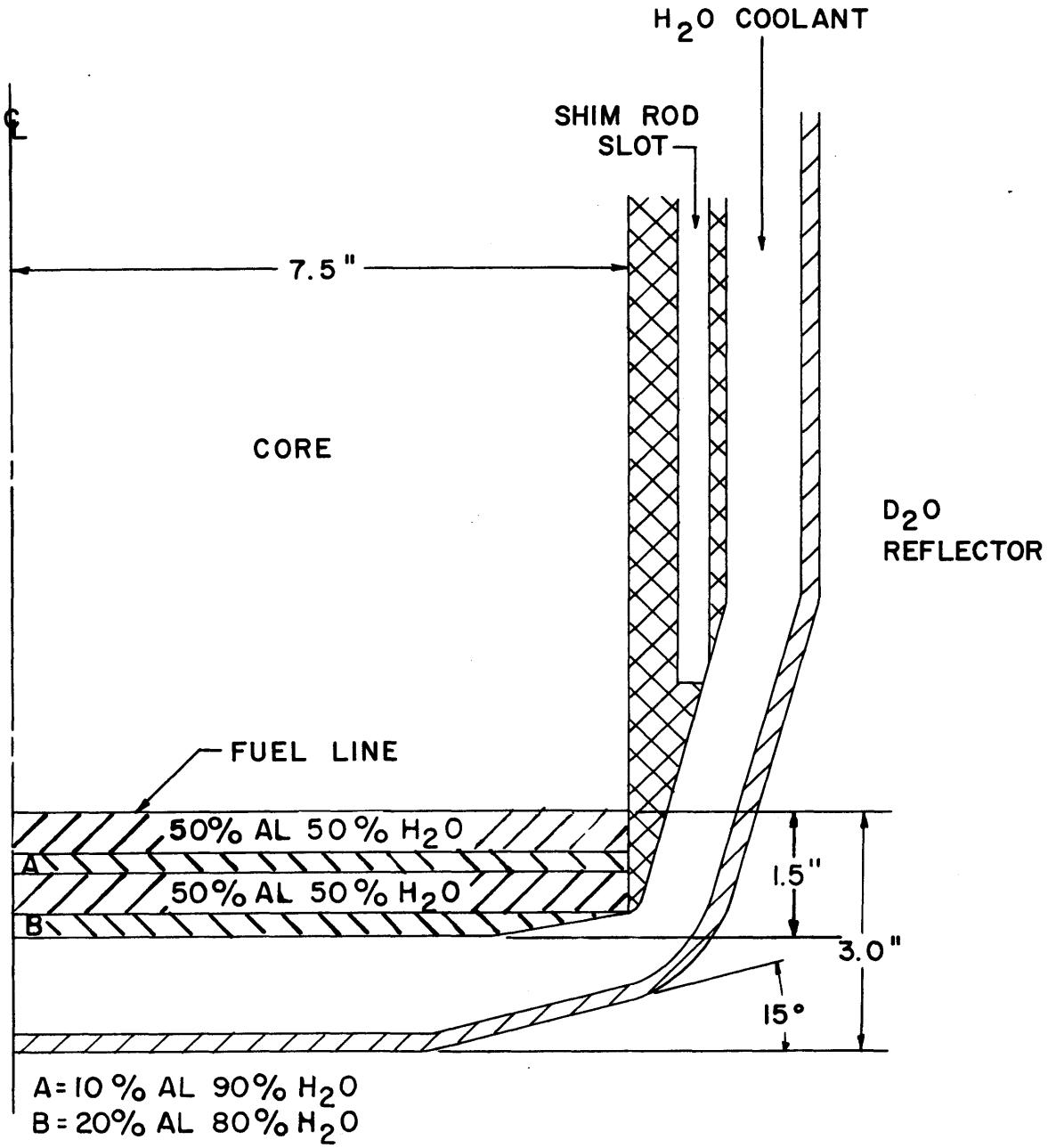

FIG. 8.5 DETAILS OF BOTTOM H_2O PLENUM

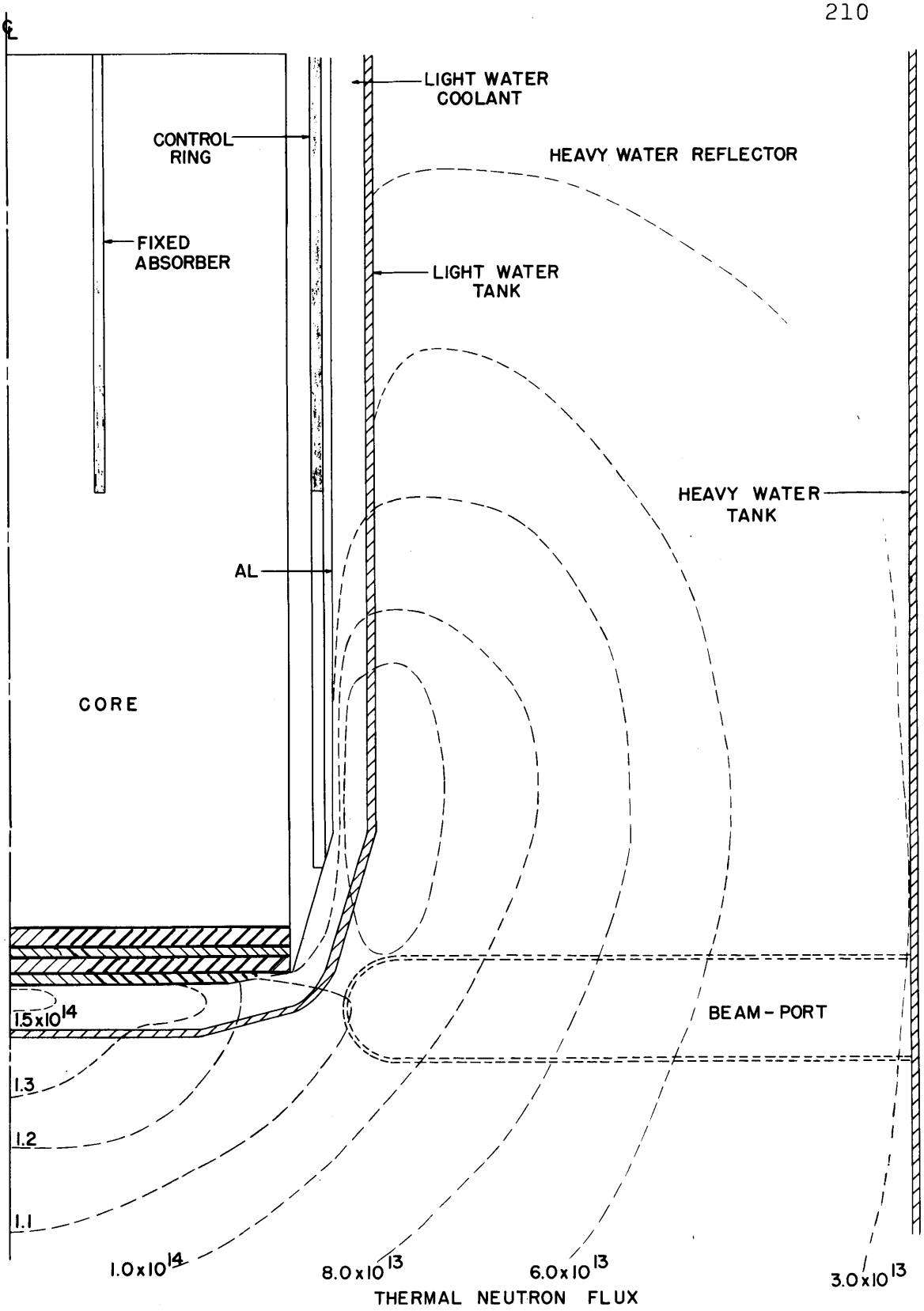

FIG. 8.6 VERTICAL SECTION OF MODIFIED MITR-II CORE

The $1.1X10^{14}$ n/cm^2-sec flux contour line on Fig. 8.6 shows that the predicted unperturbed thermal neutron flux at the tip of the beam ports is about $1.1X10^{14}$ n/cm^2-sec as observed in Fig. 7.1. Beam port optimization studies done by Kennedy (4) showed that the re-entrant beam ports in the design of Fig. 7.1 will introduce a perturbation of about 25% in the calculated fluxes. The long diffusion length of thermal neutrons in the heavy water reflector surrounding the tip of the beam ports suggests that the higher flux regions both above and below the tip of the beam ports position in the design of Fig. 8.6 will help reduce the perturbation caused by the re-entrant beam ports.

The power density distribution in the MITR-II core corresponding to the thermal neutron flux distribution of Fig. 8.6 is shown in Fig. 8.7. Both the $2.0X10^{12}$ and $3.0X10^{12}$ fissions/cm^3-sec power density contour lines on Figs. 7.2 and 8.7 show that the power density distribution at the active core top has not been affected by the changes in both the composition and dimensions of the MITR-II core.

However, a comparison of the $0.5X10^{12}$ fissions/cm^3-sec power density contour lines on Figs. 7.2 and 8.7 shows that there is relatively considerable power generation in the upper half core of Fig. 8.7. Natural boron was the neutron absorber used in the calculations shown in Fig. 7.2 and the fraction of the total core power generated in the

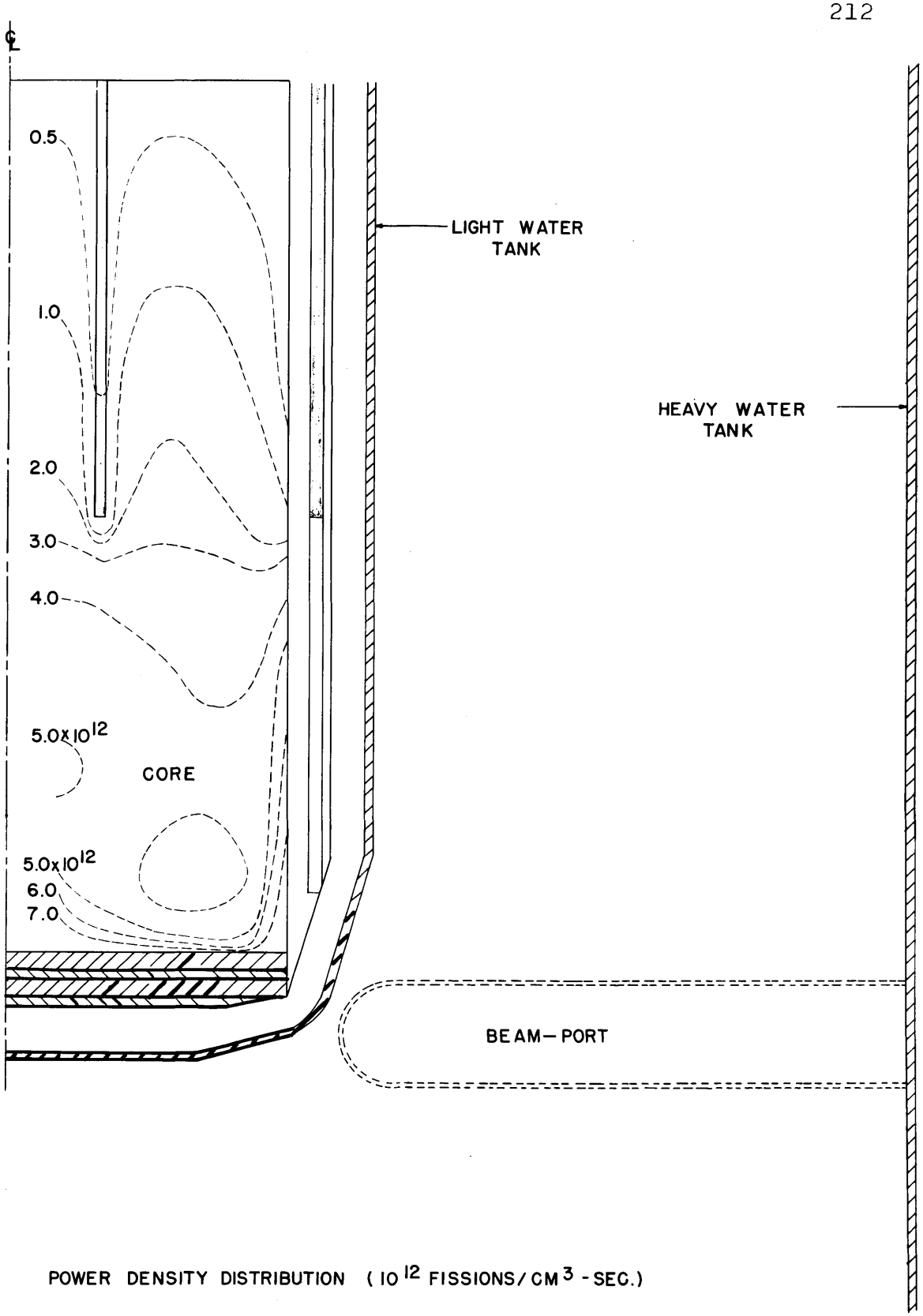

FIG.8.7 VERTICAL SECTION OF MODIFIED MITR-II CORE

upper half core was about 11.6%. In the calculations shown in Fig. 8.7, cadmium was the neutron absorber used and about 18% of the total core power is generated in the upper half. The increase in the fraction of core power generated in the upper half is not due mainly to the reduced epithermal captures in cadmium compared with natural boron. The increased core diameter as well as the higher concentration of uranium in the modified MITR-II core of Fig. 8.7 has largely contributed to the increased power generation in the upper half core. Although the effect of the absorbers in the radial ribs have not been included in these calculations, it appears that as the core diameter is further increased the fraction of the core power degraded in the upper half core will be considerable. A study of methods of reducing this power degraded in the upper half core, such as shortening the fuel loading or the development of a neutron absorber with higher epithermal captures, will be a good area for future development.

A comparison of the $7.0X10^{12}$ contour line on Fig. 8.7 with the $8.0X10^{12}$ fissions/cm^3-sec line on Fig. 7.2 shows that the homogenized power densities in the active part of the modified MITR-II core of Fig. 8.7 are slightly lower. Taking into account the effects of the increased coolant channel gap, the heat transfer difficulties in the modified core are no more severe than those of the core of Fig. 7.2.

8.2 REFINEMENT OF GEOMETRICAL DETAILS

The radial section of the design base of the MITR core, given in Fig. 7.4, is hexagonal. The calculations done so far have been based on a cylindrical approximation of this core radial section. The volumes of regions have been preserved in the cylindrical geometry approximation, and hence, most reactivity effects will be correctly predicted. However, neutron flux as well as power density distributions may be poorly predicted by this approximation. Further, the six shim rods, shown in Fig. 7.4, have been represented in the cylindrical geometry calculations as a single absorber ring. The reactivity worth of the shim rods as well as the power density distribution in the core as a function of the position of the shim rods may be poorly predicted by this approximation.

In order to answer the questions raised above, an effort was made to carry out a few three-dimensional hexagonal geometry calculations, by using the PDQ-7 code (45), (47). This work is described in section 8.2.1 below. A comparison of two-dimensional hexagonal geometry calculations with one-dimensional cylindrical calculations has also been done and is discussed below in section 8.2.2

8.2.1 Three Dimensional Hexagonal Geometry Calculations with PDQ-7

The PDQ-7 code (45), described in section 2.6.5, has three-dimensional hexagonal geometry option that can describe precisely the hexagonal radial section of the core, shown in Fig. 7.4. Three-dimensional PDQ-7 hexagonal geometry calculations, therefore, will enable a more precise determination of the reactivity worth of the shim rods, the flux distribution, and the power density distribution in the core as a function of the shim rods' position.

PDQ-7 was originally written for the CDC-6600 computer (45), (46). Since the IBM system is the principal computational facility at MIT, an effort was made to get the recently converted PDQ-7 for the IBM system 360 (47) operational here. At that time, there was a lack of a report of a conclusively successful operation of the latter version of PDQ-7 in the country. However, with the help of a computer consultant (the person who headed the group that converted the original CDC-6600 PDQ-7 (45) to the IBM version), PDQ-7 was made operational at MIT by December of 1969.

The slightly less than 450,000 bites of core available on the MIT computing facility for users at that time was a handicap. PDQ-7 for the IBM system requires about 420,000 bites of computer core to load the program. In addition, PDQ-7 stores fluxes and coefficients out of the computer core, on auxiliary equipment such as 2314 disc

drives, in the form of files. Thus, depending on the size of the problem, additional computer core storage is required for a few in-core files during iteration processes as well as buffer space to process the out-of-core files. The 3-dimensional calculations, therefore, could not be done with the 450,000 bites of computer core storage space. This problem was resolved when an additional computer core module was added to the IBM system 360/65 at MIT in December of 1969, increasing the computer core space available to users to about 700,000 bites.

The complete radial cross section of the design base of the MITR-II core was found to require at least 34 by 34 mesh points to describe it precisely in the hexagonal geometry. In the 3-dimensional problems, a number of identical planes are stacked together and the composition corresponding to a region is specified at each plane. As a first trial, the core was represented by 3 axial planes with 12 inches equal mesh spacing; a 15-inch thick top light water reflector as well as a 15-inch thick bottom heavy water reflector was added to make a five axial plane reactor problem. This problem required about 30 minutes to successfully complete 3 outer iterations.

The full core problem was set up. It was found from 2-dimensional cylindrical geometry calculations that at least 28 axial planes were needed to obtain a meaningful description of the reactor. This full core problem of

34X34 by 28 axial planes was found to require about 110 minutes to successfully complete one outer iteration. Of the 110 minutes, only 28 minutes were spent on the actual flux iterations, the rest of the time being used on the calculation of coefficients and output information which are done once for a problem.

The full core problem described in the above paragraph was re-run, but in this case allowing sufficient time for 10 outer iterations. The first outer iteration was completed successfully as before; however, the inner iterations of the second outer iteration never converged. A full computer core dump was taken and sent to the computer consultant, but the cause of the difficulty could not be traced.

Suspecting the cause of the difficulty was the IBM machine problem, it was decided to try to run the problem outside MIT on the CDC-660 computer for which PDQ-7 was originally written. The five axial plane reactor problem was repeated on the CDC-660 computer. The K_{eff} agreed with that obtained for the same problem on the IBM machine up to the sixth significant figure, and took about 4 1/2 minutes compared with 30 minutes on the IBM computer.

The full core problem of 34X34 by 28 axial planes was repeated on the CDC-660 computer, allowing sufficient time for about 7 outer iterations. The result was exactly the same as obtained on the IBM computer: the first outer

iteration converged but the inner iterations of the second outer iteration never converged.

At this point, it appeared the difficulty was a basic one with PDQ-7 rather than the computer machine version of it. Some of the writers of PDQ-7 at the Bettis Atomic Power Laboratory were contacted. The difficulty seemed to be with the iteration scheme used in the axial direction. In three dimensional problems, a block Gauss-Seidel procedure is used, each block consisting of a single plane (45). The resulting inner iteration procedure may fail to converge if either there are too many discontinuities in the axial direction or the axial planes are closely spaced and hence tightly coupled.

In order to reduce the discontinuities in the axial direction, the axial mesh points were rearranged and the full core problem repeated on the CDC-6600 machine. The result was even worse: the inner iterations of the first outer iteration never converged.

At this point, it appeared that the very long diffusion length of thermal neutrons in heavy water was causing the axial planes to be tightly coupled. In order to confirm this, a series of 3 axial plane problems were tried in hexagonal geometry. The problems were identical with reflecting boundary conditions at both the top and bottom planes, the only variable being the equal mesh spacing between the planes. The results of the runs, summarized

in Table 8.2, show that with heavy water systems the minimum axial mesh spacing for which the inner iterations will converge is about 6 inches.

With about 6 inches minimum axial mesh spacing, it is not possible to obtain useful answers for the MITR-II core, because of the bottom light water plenum design. However, with the same minimum axial mesh spacing, useful results may be obtained for the MITR-I core. The calculation of the MITR-I core is discussed in section 10.2.

8.2.2 Comparison of Two-Dimensional Hexagonal and One-Dimensional Cylindrical Geometry Calculations

The results discussed in section 8.2.1 show that useful answers cannot be obtained for the MITR-II core by using the version of PDQ-7 presently available. However, useful information on the reactivity worth of the shim rods as well as radial power peaking factors may be obtained by comparing two-dimensional hexagonal and one-dimensional cylindrical geometry calculations. These comparative calculations have been made and discussed below.

In the one-dimensional cylindrical and two-dimensional hexagonal geometry calculations, neutron leakage in the axial direction was accounted for by material and group dependent bucklings. These bucklings have been calculated

TABLE 8.2

3-Axial Plane Reactor Problems in Hexagonal Geometry

Equal Axial Mesh Spacing (inches)	Total Time Run (min.)	Inner Iterations Needed for Convergence								
		1st Outer Iteration			2nd Outer Iteration			3rd Outer Iteration		
		Group 1	Group 2	Group 3	Group 1	Group 2	Group 3	Group 1	Group 2	Group 3
4.0	30	5	5	not converged						
5.0	30	4	4	not converged						
6.0	40	3	3	15	3	3	21	3	3	17
12.0	20	3	3	3	3	3	5	3	3	5

for a 2-cm. thick slab at the active core mid-height by using EXTERMINATOR II. The method used in the calculation of the bucklings is discussed in Appendix A. The flux distributions calculated for a one-dimensional disc by using these bucklings were found to be similar to the corresponding values at the active core mid-height.

The normalized radial power density distribution (radial peaking factors) calculated for the actual hexagonal core radial section and the cylindrical approximation of the core are given in Figs. 8.8 and 8.9 respectively. The symmetry in the actual core hexagonal section (Fig. 7.4) permitted the isolation of a third of the radial section for the detailed calculations as given in Fig. 8.8.

In general, the power density distributions for the actual core (Fig. 8.8) and the cylindrical approximation (Fig. 8.9) are similar to those observed for the spherical approximations to the core (Figs. 2.4 and 2.6) discussed in Chapter 2. The local power density is maximum at the core-reflector interface. This maximum value drops off rapidly as one moves inwards along a radial direction towards the core center. A comparison of Figs. 8.8 and 8.9 shows that the maximum local power density predicted by the cylindrical core model is higher at the center while at the core-reflector interface it is lower than the value in the actual hexagonal core.

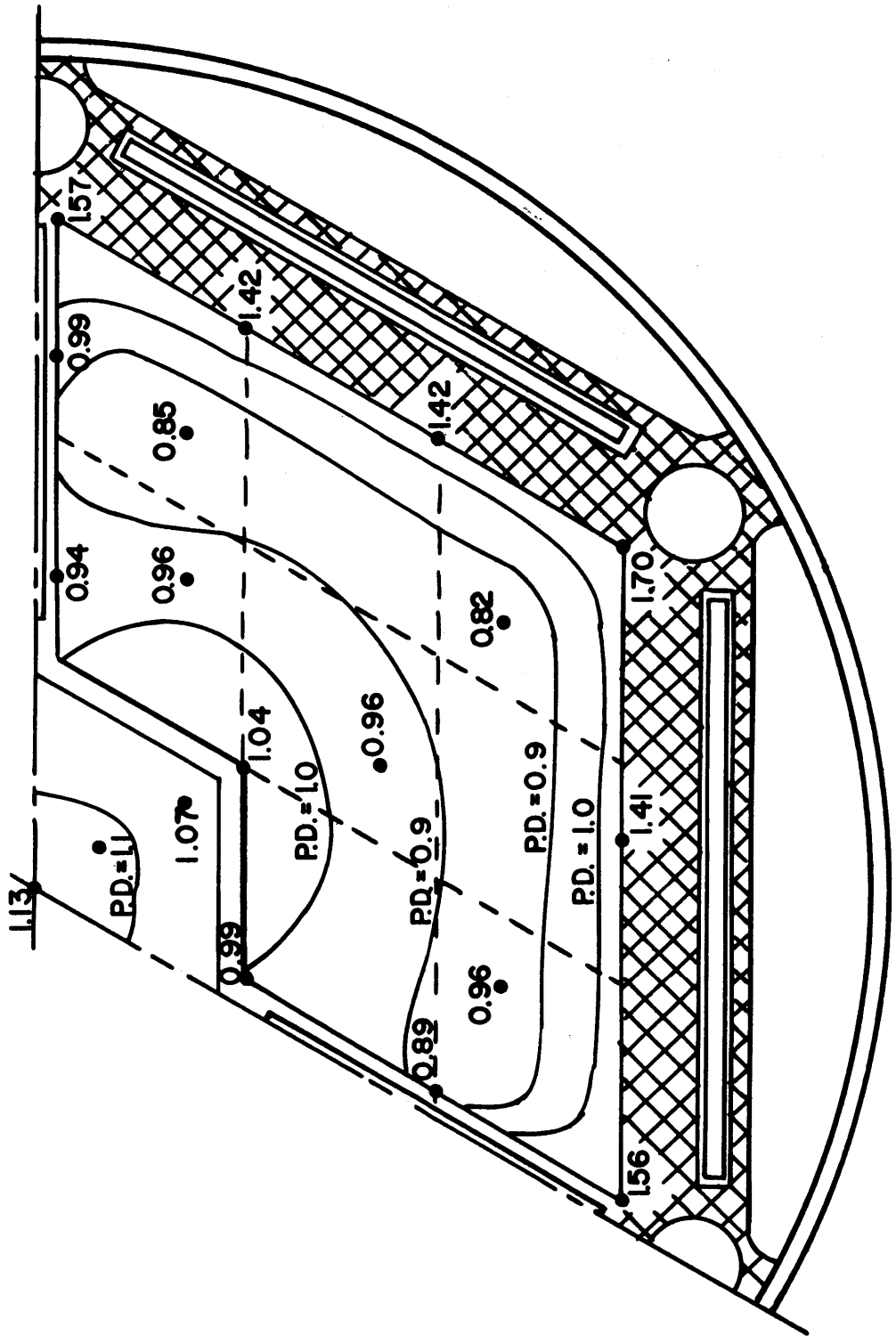

FIG. 8.8 RADIAL NORMALIZED POWER DENSITY DISTRIBUTION IN THE ACTUAL HEXAGONAL CORE MID-HEIGHT

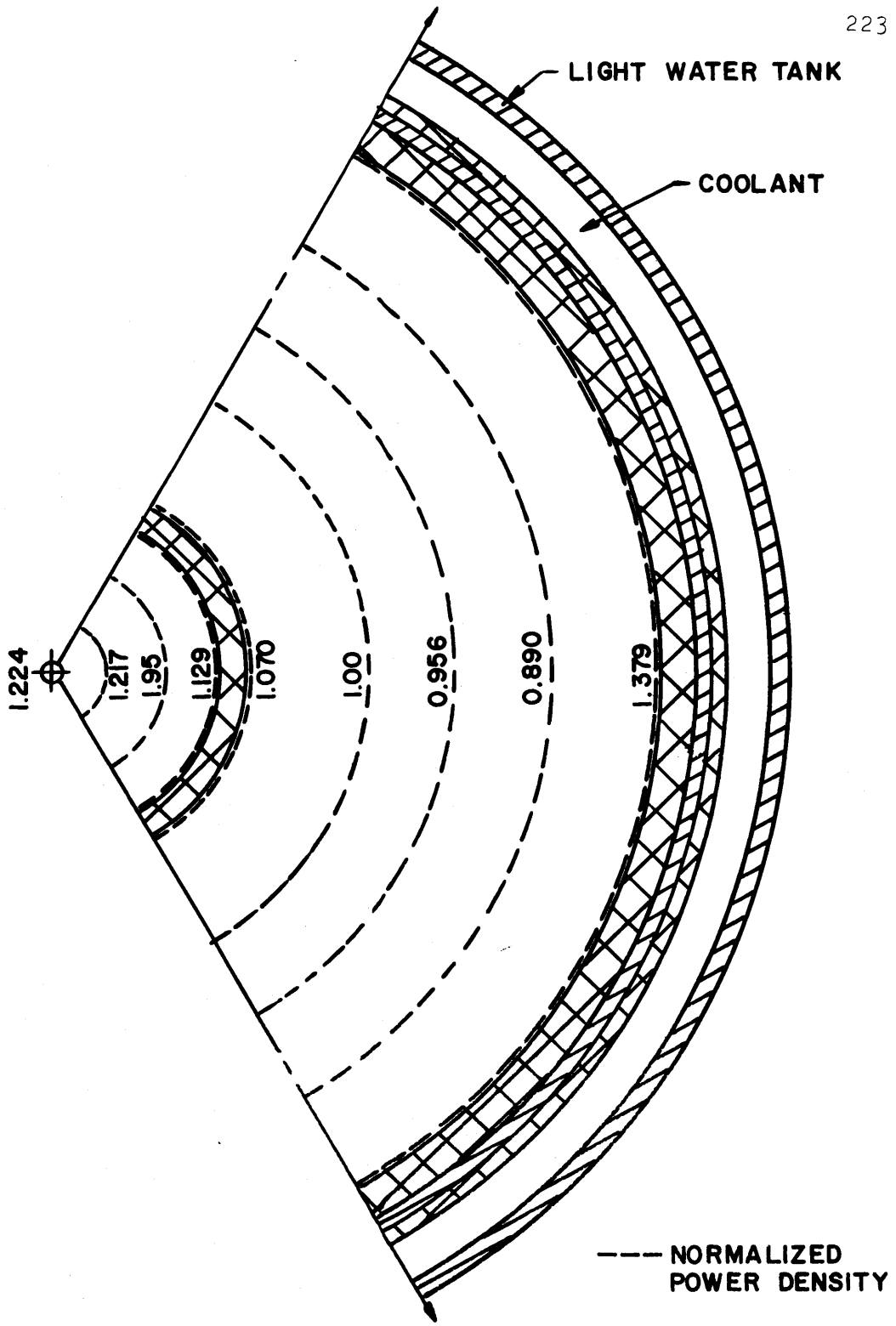

FIG. 8.9 RADIAL NORMALIZED POWER DENSITY DISTRIBUTION IN THE CYLINDRICAL CORE MODEL MID-HEIGHT

The actual positions occupied by fuel elements are shown in dotted lines in Fig. 8.8. It is observed that in the fresh clean core (no burn up as well as stable fission products and xenon effects) the hottest fuel element is clearly the central one. As pointed out in section 7.5.2, the fuel elements are positioned such that the fuel plate breadth lies in a radial direction. The finning effect of these radial plates will reduce the importance of the rapid rise in power density towards the core-reflector interface. An exception is the corner element marked C in Fig. 8.8. One of the outermost fuel plates of this element will always lie next and parallel to the core-reflector interface. The hottest channel, therefore, is that associated with this fuel plate.

Calculations have also been done to compare the reactivity worth of the six shim rods in the actual hexagonal section with that of the outer absorber ring used in the cylindrical model of the core. In the MITR-II core, the region below the shim rods is occupied by light water. In the one-dimensional cylindrical and two-dimensional hexagonal geometry calculations through the active core mid-height, the reactivity change that results from replacing the light water below the absorber with the actual absorber has been determined and summarized in Table 8.3. These results show that the reactivity change in the actual hexagonal geometry is 1.13 times the corresponding

TABLE 8.3

Comparison of 1-D Cylinder and 2-D Hexagon

Reactivity Worth of Shim Rods

Case	Material Occupying Position of Shim Rods	1-D Cylinder		2-D Hexagon	
		K_{eff}	$\rho(\%\Delta K/K)$	K_{eff}	$\rho(\%\Delta K/K)$
1	H_2O	1.0163	1.658	1.0018	0.1805
2	Cadmium	0.8776	-13.9409	0.8521	-17.3641
	$\Delta\rho(\%\ \Delta K/K)$		15.5467		17.5446

$$\frac{(\Delta\rho)HEX}{(\Delta\rho)CYLD} = \frac{17.5446}{15.5467} = 1.13$$

reactivity change in the cylindrical core model. These results indicate that the six shim rods are worth about 1.13 times more in reactivity than the corresponding single absorber ring used in the cylindrical core model.

Assuming that the worth of the six shim rods at each axial plane is 1.13 times the corresponding worth of the outer absorber ring in the cylindrical core model, the total worth of the shim rods from the active core top (12.0 in. level) to the fully inserted position (22.0 in. level) has been derived from the results of the two-dimensional cylindrical core model calculations. The results of the calculations are summarized in Table 8.4 and the derived reactivity worth of the six shim rods is 13.08% $\Delta k/k$.

Calculations have also been performed to compare the reactivity changes that result by placing cadmium in the positions of the following three regions of the hexagonal core separately--namely, the six shim rods, the inner fixed absorber ring, and the three radial ribs. The results of the calculations, summarized in Fig. 8.5, show that the inner fixed absorber and the radial ribs have reactivity worths of 93.5% and 67.9% that of the six shim rods if each is inserted separately. During the normal operation of the MITR-II core, the shim rods, the inner fixed absorber, and the radial ribs will be inserted simultaneously in the upper half core. The resulting interference effects will reduce the fractional reactivity worth of the inner fixed absorber and the radial ribs.

TABLE 8.4

Comparison of 2-D Cylinder and 3-D Hexagon

Reactivity Worth of Shim Rods

	Absorber Lower Tip Position from Core Top	2-D Cylinder		3-D Hexagon	
		K_{eff}	$\rho(\%\Delta k/k)$	K_{eff}	$\rho(\%\Delta k/k)$
1	12.0 in.	1.0510	4.8519	[1.057]	
2	22.0 in.	0.9370	-6.7235		
	$\Delta\rho(\%\Delta k/k)$		11.5754		13.0802

TABLE 8.5

Comparison of Reactivity Worth of the Shim Rods,

Inner Fixed Absorbers and Radial Rib in 2-D Hexagonal Geometry

Case	Region Occupied By Cadmium	K_{eff}	ρ	$\Delta\rho$	$\frac{\Delta\rho}{-17.5446}$
1	None	1.0018	0.1805	0.0	0.0
2	Shim Rods	0.8521	-17.3641	17.5446	1.0
3	Inner Fixed Absorbers	0.8603	-16.2403	16.4208	0.935
4	Radial Ribs	0.8952	-11.7076	11.8881	0.679

CHAPTER IX

REACTIVITY STUDIES

Studies have been carried out to determine the principal reactivity characteristics of the modified MITR-II core described in section 8.1.3. The results of these studies are summarized in this chapter.

9.1 THE EFFECTS OF CHANGING THE EFFECTIVE CORE HEIGHT

The effective height of the MITR-II core may be changed by inserting an inner hexagonal cadmium absorber ring (section 7.4) of the appropriate height, and adjusting the position of the six shim rods. This is the principal flexibility in the first loading of the MITR-II core for changing the reactivity in the system. The effects associated with changing the effective height of the design base of the modified MITR-II core are discussed below.

9.1.1 Calculational Model

The calculational model used is that described in section 10.1. Calculations were done for both the full 27-element core and a 26-element core in which the central fuel element position has been replaced with lead. Three-group two-dimensional R-Z cylindrical geometry calculations have been done by using the PDQ-7 code (45). The reported

reactivity (ρ) has been calculated by PDQ-7 using the formula

$$\rho = (1-\frac{1}{K}) \text{ X100}$$

where K is the effective multiplication in the perturbed system, and ρ is in units of $\%\Delta K/K$.

9.1.2 Reactivity and Reflector Leakage Flux Effects

The predicted reactivity effects are summarized in the form of the effective multiplication (K_{eff}) and reactivity (ρ) in the system versus the effective core height in Figs. 9.1 and 9.2 respectively. It is observed from these figures that both K_{eff} and ρ increase almost linearly with increasing effective core height.

As the effective core height is increased from 12.0 to 15.0 inches, there is about 4.0%K increase in the reactivity in the system. The graph of thermal neutron flux at beam ports tips versus the effective core height, given in Fig. 9.3, shows that the corresponding decrease in the flux at beam ports tips is about 12.0%. Calculations show that an equal gain in reactivity of 4.0%K may be achieved by increasing the core diameter by 1.0 inches, though the corresponding decrease in the thermal neutron flux at beam port tips of about 18.0% is relatively high (see Figs. 8.1 and 8.2). On Fig. 9.3 is also shown the maximum normalized power density in the core as a function

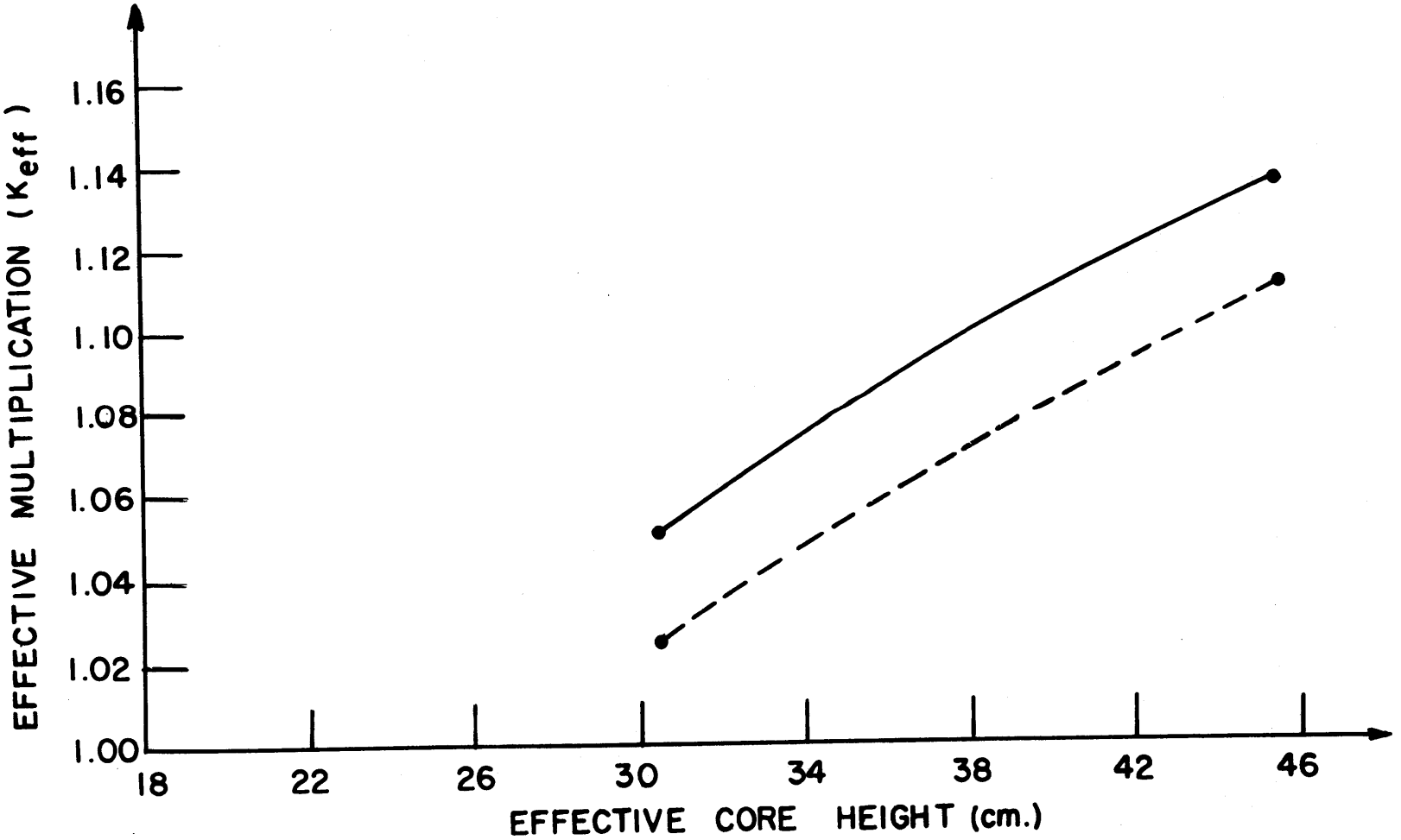

FIG. 9.1 EFFECTIVE MULTIPLICATION IN THE REACTOR AS A FUNCTION OF THE EFFECTIVE CORE HEIGHT

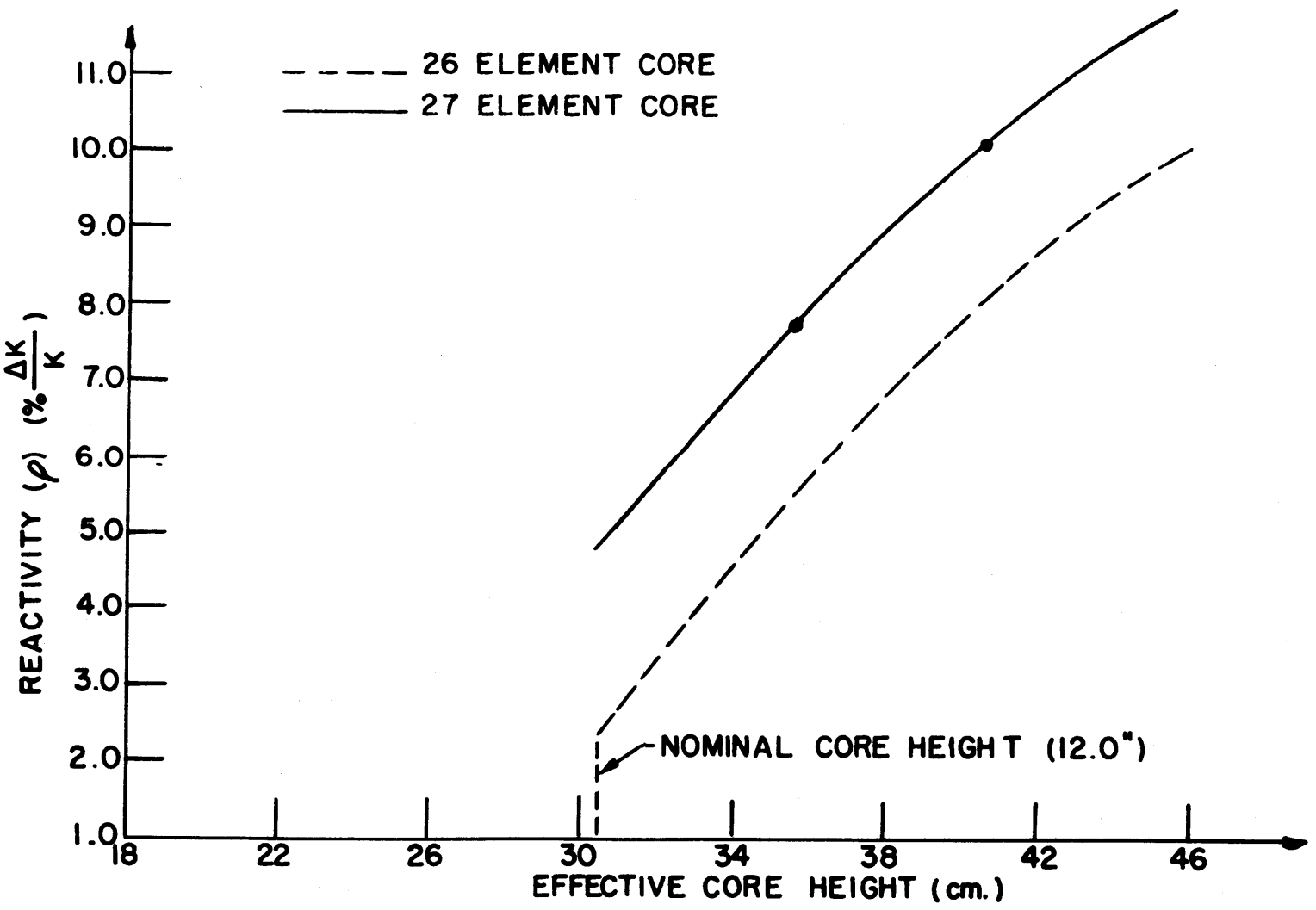

FIG. 9.2 REACTIVITY IN THE REACTOR AS A FUNCTION OF THE EFFECTIVE CORE HEIGHT

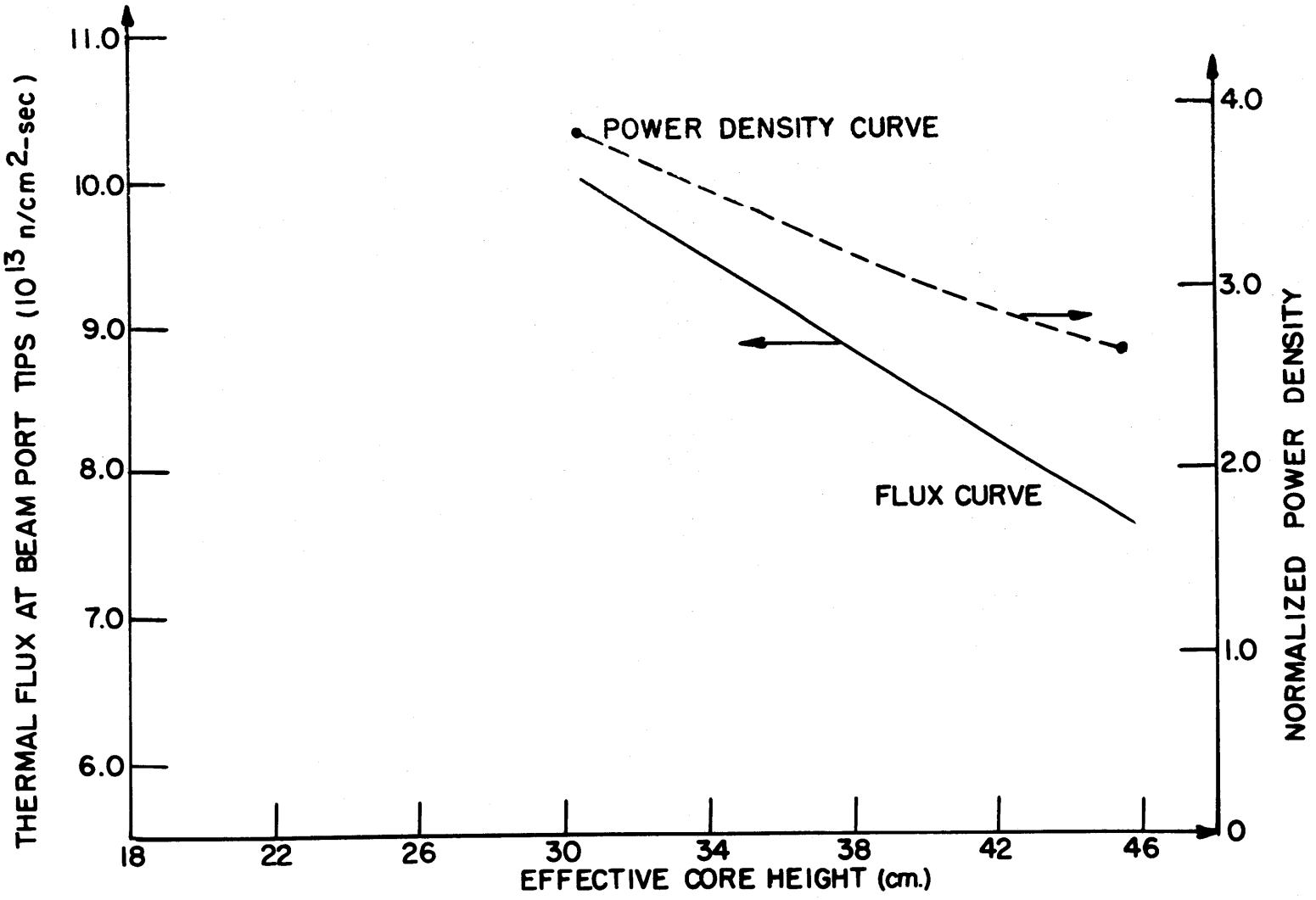

FIG. 9.3 REFLECTOR THERMAL FLUX AT BEAM PORT TIPS AND NORMALIZED POWER DENSITY AS A FUNCTION OF EFFECTIVE CORE HEIGHT

of the effective core height. As the effective core height is increased, the normalized power density decreases. Increasing the core diameter also results in a corresponding decrease in the maximum power density, though in this case the actual velocity in the coolant channels decreases, due to the limited total coolant mass flow rate through the MITR core. This tends to balance the power decrease such that the fuel plate temperatures at the hot spot remain high.

Increasing the effective core height, therefore, results in an increase in the reactivity in the system with the minimum reduction in the reflector thermal neutron flux and reduced heat transfer difficulties.

9.2 REACTIVITY WORTH OF THE CENTRAL FUEL ELEMENT

The effects of replacing the central fuel element with either aluminum, lead, heavy water and light water have been examined. The replacement of the central fuel element with any of the above materials always results in a negative reactivity effect. The results of the calculations, summarized in Table 9.1, show that the moderating power and the absorption cross section are the two properties of a non-fissionable material that determine the magnitude of the negative reactivity change. The larger the moderating power the smaller the negative reactivity

change, whereas the higher the absorption cross section the larger is the negative reactivity change.

From Table 9.1, it is observed that the negative reactivity change is a minimum of -0.6912% ΔK/K when the central fuel element is replaced with light water which has the highest moderating power, and a maximum of -2.8634%ΔK/K when the replacement material is aluminum which has both a low moderating power and high absorption cross section.

The reactivity effect of high moderating power outweighs that of absorptions in the undermoderated core. This conclusion is borne out by the results for heavy water and light water. The reactivity change is -0.6912% ΔK/K when the replacement material is light water which has both high absorption and moderating properties. Despite the negligible absorption cross section of heavy water, the lower moderating power of this coolant results in a larger negative reactivity change of -1.7103%ΔK/K when it is the replacement material.

It may also be observed from the last column of Table 9.1 that a high moderating power of the replacement material raises a heat transfer problem. The maximum normalized power density at the inner core face increases from 3.75 to 5.61 when the replacement material is light water. Boiling, therefore, might occur if the reactor

TABLE 9.1

Reactivity Worth of Replacing the Central Fuel Element with Different Materials

Case	Material in the Central Fuel Position	K_{eff}	Reactivity $-(\rho)$ (%ΔK/K)	$\rho-4.8519$ (%ΔK/K)	Maximum Normalized Power Density at Inner Face
1	Fuel	1.0510	4.8519	0.0	3.75
2	H_2O	1.0434	4.1607	-0.6912	5.61
3	D_2O	1.0360	3.4716	-1.7103	4.26
4	Lead	1.0248	2.4164	-24355	3.53
5	Aluminum	1.0203	1.9885	-2.8634	3.02

is being operated with the maximum fuel plate temperature (hot spot) close to the maximum permissible value and the central fuel element is replaced with a hydrogeneous material.

9.3 REACTIVITY WORTH OF DUMPING THE RADIAL HEAVY WATER REFLECTOR

A secondary shutdown feature of the MITR is the dumping of part of the heavy water reflector. In MITR-II, the radial heavy water in the annular region above the level of the bottom fuel line is the volume that may be dumped. The height of this region is approximately 2 feet.

Since the shim rods also operate in the region between the core and the radial heavy water reflector, the reactivity worth of dumping this radial reflector is dependent on the position of the shim rod bank. The reactivity worths of dumping the radial reflector when the shim rods are at the active core top and in the fully inserted position have been determined for the 27 element core and given in the table below.

Case	Position of Shim Rod Bank	Reactivity Worth
1	Active Core Top (12.0 in. below core top)	12.32%ΔK/K
2	Fully Inserted Position (22.0 in. below core top)	7.49%ΔK/K

These results show that the reactivity worth of dumping the radial heavy water reflector when the shim rod bank is fully inserted is about 30% less than the corresponding value when the shim rod bank is at the active-core top. The positions of the shim rods are, therefore, important in determining the reactivity worth of dumping the radial reflector. It may also be observed that, from safety point of view, this radial heavy water reflector could be pumped up with the shim rods in the fully inserted position to ensure that the reactivity insertion rate is a minimum.

9.4 REACTIVITY WORTH OF SHIM RODS

The reactivity in the 27-element core, with an effective height of 12.0 inches, has been determined as a function of the shim rod bank position. The results of the calculations are summarized in Fig. 9.4 in the form of both the reactivity (ρ) and the effective multiplication in the system (K_{eff}) as functions of the shim rod bank position from the top of the core. The two curves are nearly identical when the reactivity in the system is about $\pm 3.0\% \Delta K/K$.

The results show that when the shim rod bank is fully withdrawn to the core top, the K_{eff} in the system is 1.122, corresponding to a reactivity of $10.5\% \Delta K/K$, while when it

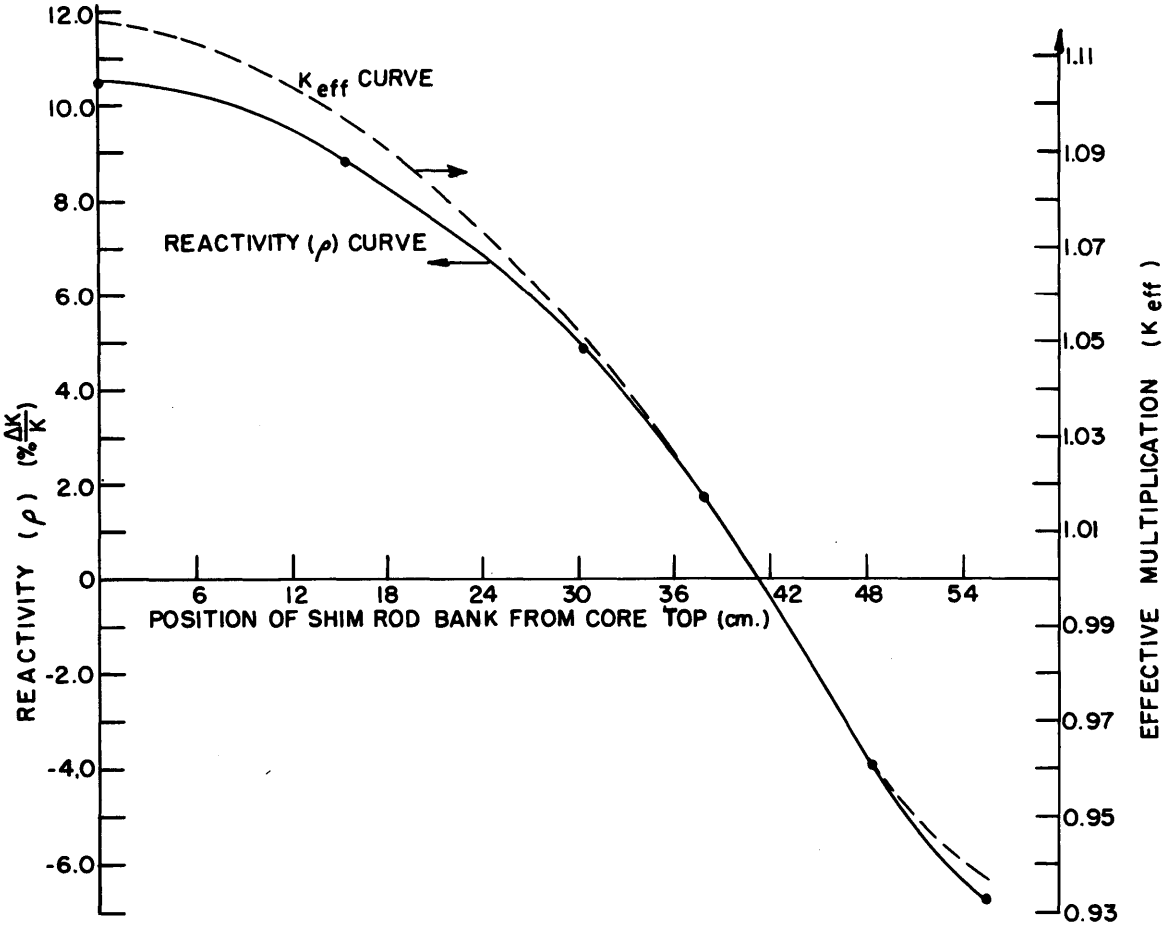

FIG. 9.4 REACTIVITY IN 27 ELEMENT CORE AS A FUNCTION OF SHIM ROD BANK POSITION

is fully inserted the K_{eff} drops to 0.937 corresponding to a reactivity of -6.8%ΔK/K. It may thus be observed that the total reactivity worth of moving the shim rods from the core top to the fully inserted position is 17.3%K. The reactivity worth of dropping the shim rod bank through the first 12.0 inches poisoned upper half core is 5.65%ΔK/K, which is about 30% of the total worth of the shim rods.

By making use of the results of the comparison of the reactivity worth of shim rods in one-dimensional cylinder and two-dimensional hexagon, given in Table 8.4 of section 8.2.2, the reactivity worth of a shim rod has been derived. The results are shown as a curve of reactivity versus a shim rod position from the core top in Fig. 9.5. It is seen from Fig. 9.5 that the total reactivity worth of a shim rod from the core top to the fully inserted position is 3.22%ΔK/K, of which 1.04%ΔK/K is the worth in the first 12.0 inches poisoned upper half core.

9.5 REACTIVITY EFFECTS OF LEAKAGE OF LIGHT WATER INTO THE HEAVY WATER REFLECTOR AND VICE VERSA

The reactivity effects of the leakage of light water into the heavy water reflector as well as the leakage of heavy water into the light water system have been examined. Light water has both higher moderating power and absorption cross section than heavy water. In an undermoderated core

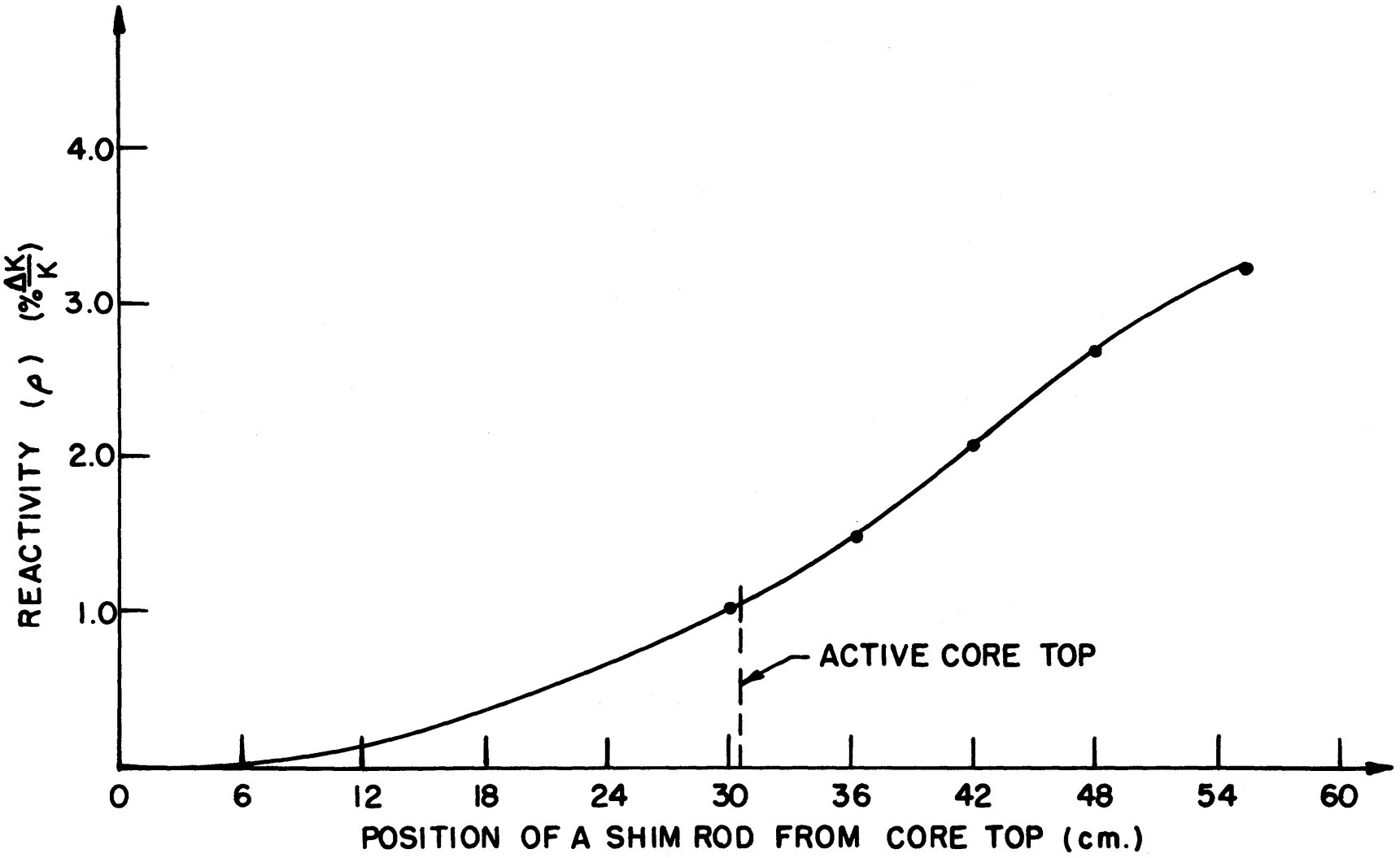

FIG. 9.5 REACTIVITY WORTH OF A SHIM ROD

of hardened neutron energy spectrum, the effect of the high moderating power of light water outweighs its absorptions and consequently replacing this coolant in the core with heavy water has been found to result in a negative reactivity effect. However, in the reflector of relatively softer neutron energy spectrum, the absorptions by light water outweigh the effect of its high moderating power, and it has been found that both replacing the light water in the reflector with heavy water initially results in a positive reactivity effect, and replacing the heavy water in the reflector with light water always results in a negative reactivity effect.

The effect of the leakage of light water into the heavy water reflector is shown in Fig. 9.6. The negative reactivity change increases approximately linearly with the percentage of light water contaminant in the heavy water reflector. Ten per cent light water contaminant results in a reactivity change of -1.27%ΔK/K.

The effects of the leakage of heavy water into the light water system are shown in Fig. 9.7. It is observed from Fig. 9.7 that the leakage of heavy water into either the light water reflector above the top of the core or the light water reflector below the top of the core is positive. However, the leakage of heavy water into the light water in the core results in a strong negative reactivity effect. The leakage of heavy water into the

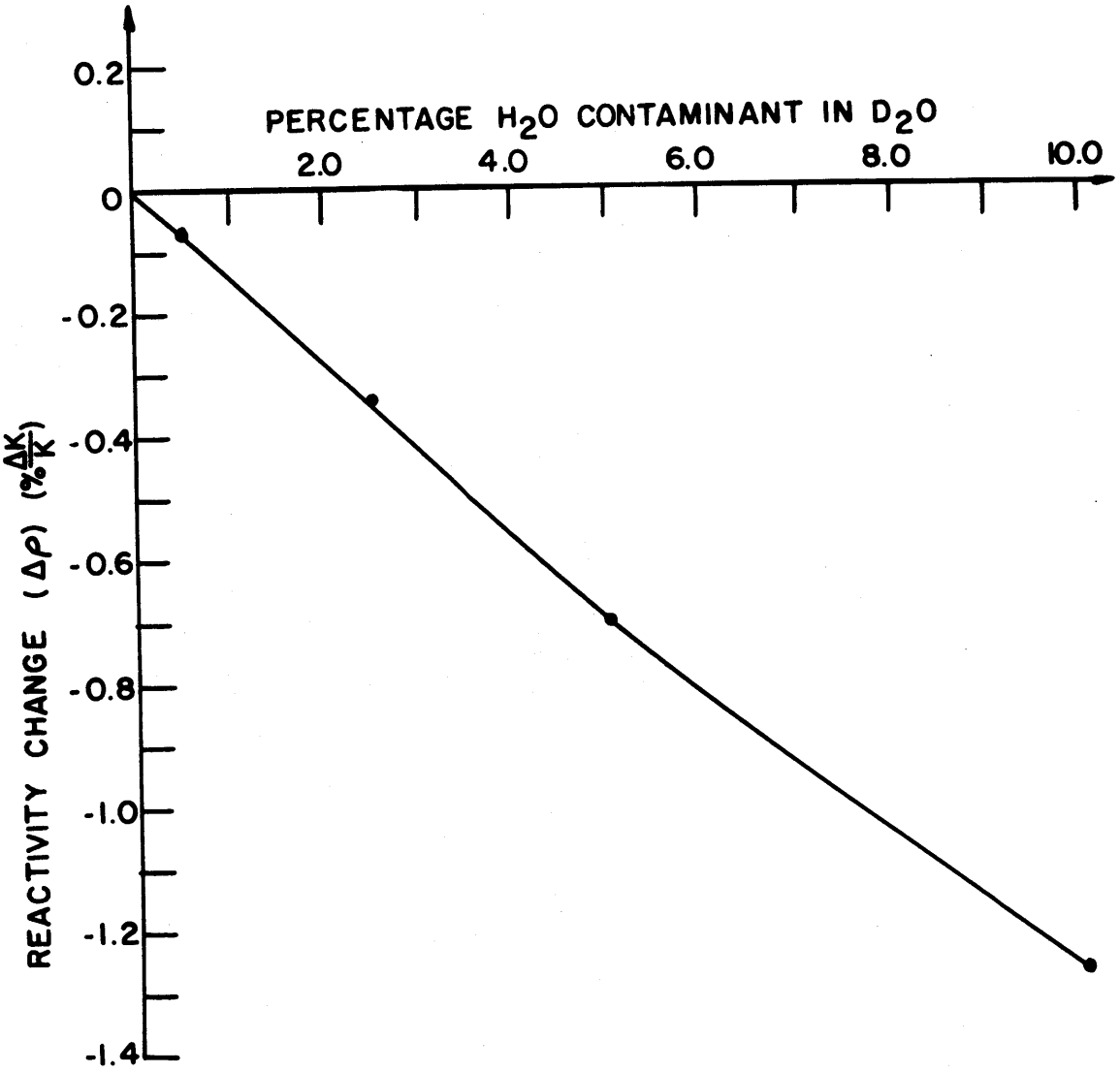

FIG. 9.6 EFFECT OF LEAKAGE OF H_2O INTO THE D_2O REFLECTOR

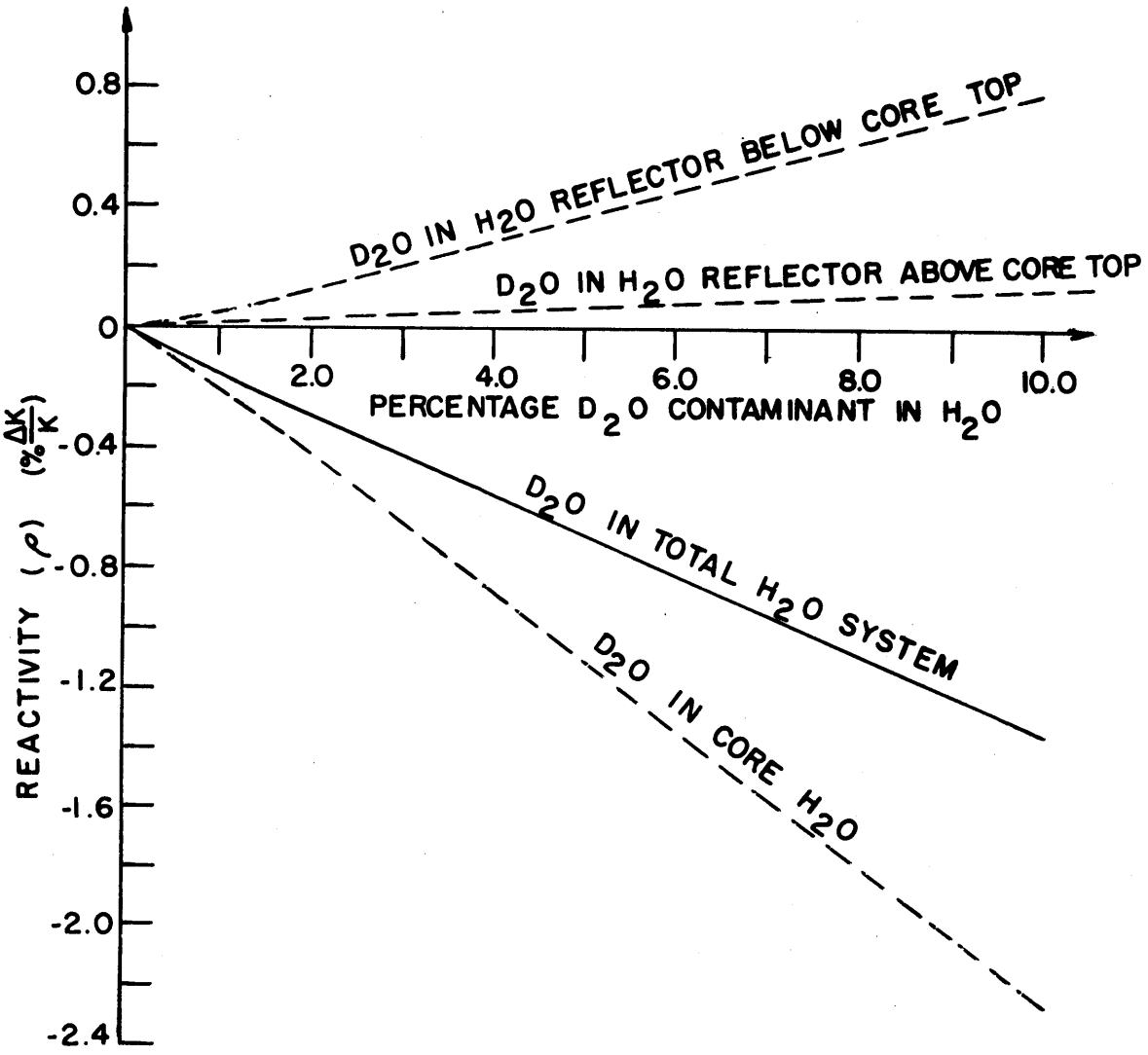

FIG. 9.7 EFFECTS OF LEAKAGE OF D_2O INTO THE H_2O SYSTEM

entire light water system is observed to be also strongly negative. Ten per cent heavy water contaminant in the entire light water system results in a negative reactivity effect of -1.18%ΔK/K.

9.6 TEMPERATURE AND VOID COEFFICIENTS OF REACTIVITY

Calculations have been made in which the density of both heavy water and light water in the core and reflector have been changed by small amounts. The changes in density considered are small such as to be useful in considering the range of variations that one might expect due to changes in temperature during the normal operation of the reactor.

The results of the calculations, summarized in Fig. 9.8 , show that a decrease in density of either the heavy water reflector separately, or the light water in the core separately, or the total water in the core results in negative reactivity changes. A reduction of 1.5% in density of the heavy water reflector and the light water in the core result in reactivity changes of -0.07%ΔK/K and -0.570%ΔK/K respectively. The reactivity changes are also observed to increase almost linearly with increasing percentage reduction in water density.

A good first approximation to the temperature coefficient of reactivity can be made by considering the effect

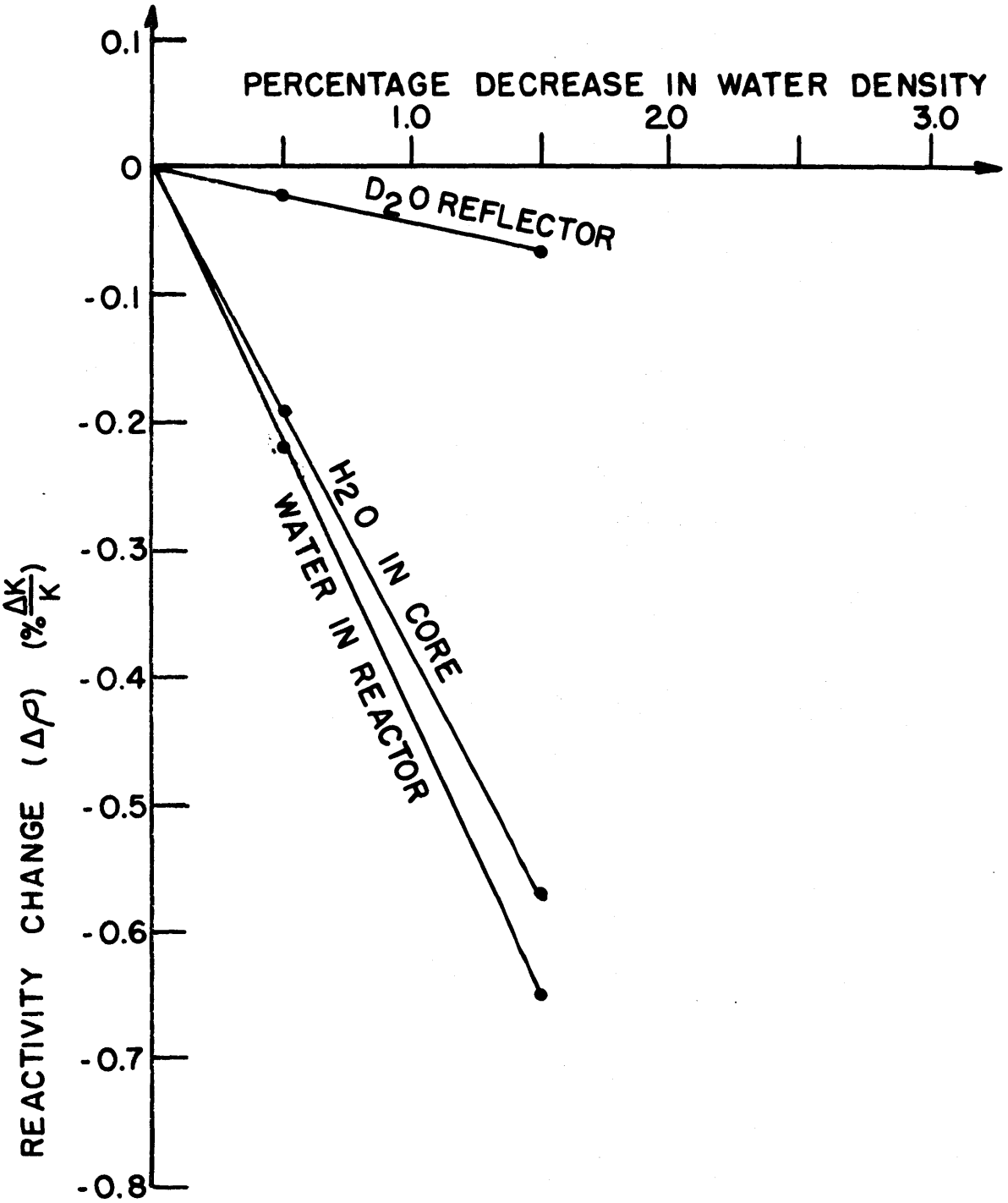

FIG. 9.8 EFFECTS OF DECREASING WATER DENSITY

of changes in the water density. The temperature coefficient of reactivity is then given by

$$\frac{1}{K}\frac{\partial K}{\partial T} = -\alpha \frac{\rho}{K}\frac{\partial K}{\partial \rho} \qquad \ldots 9.6.1$$

where α is the volume coefficient of expansion of the water and ρ is water density. The average water coefficient of expansion in the temperature range of MITR during normal operation has been taken as 4.11×10^{-4}/°C, and the calculated temperature coefficients of reactivity are summarized below

Region	Temperature Coefficient of Reactivity $(\frac{1}{K}\frac{\partial K}{\partial T})$
D_2O Reflector	-1.8×10^{-5} %Δ K/K per °C
Core	-1.58×10^{-4} %Δ K/K per °C

The major effect omitted by this approximation to the temperature coefficient of reactivity is that of the thermal neutron spectrum changes.

The effects of voiding the whole core and also locally in the bottom 2.0 inches fuel region of the core have been examined by considering the changes in water density alone, without including thermal neutron spectrum changes. Calculations have shown that both local and homogeneous voids in the core result in negative reactivity changes. Fifty

per cent void fraction in the bottom 2.0 inches fuel region results in a reactivity change of -2.15%ΔK/K, while a 20% void fraction in the whole core causes a reactivity change of -8.82%ΔK/K. These negative reactivity changes were also observed to increase linearly with increasing void fraction. The void coefficient of reactivity for homogeneous voids in the whole core has been determined to be -7.04×10^{-4} %ΔK/K per cm^3 void.

9.7 REACTIVITY WORTH OF EQUILLIBRIM XENON

The reactivity worth of equillibrim xenon has been determined by using EXTERMINATOR-II (45). The calculated value is 2.55%K.

CHAPTER X

COMPARISON OF MITR-I AND MITR-II CORES

The purpose of redesigning the MITR is to improve the intensity of the thermal neutron flux available at the tip of experimental beam ports with a minimum fast neutron and gamma radiation background. Discussed in this chapter are calculations carried out to compare the intensity and the ratio of the thermal to fast flux available at the tip of experimental beam ports in the clean cold MITR-II and MITR-I cores. These calculations, given in sections 10.1 and 10.2 respectively, have not included the effects of beam ports, burn up, equillibrim xenon, and stable fission products. A comparison of selected characteristics of the MITR-II and MITR-I cores constitutes the material for section 10.3. A brief discussion of the effects of the principal constraints imposed by the permanent features of the MITR is made in section 10.4

10.1 TWO-DIMENSIONAL R-Z CALCULATION OF MITR-II

Three group fluxes in MITR-II operating at 5 megawatts and with the effective multiplication (K_{eff}) in the system near unity, have been calculated in 2-dimensional R-Z cylindrical geometry by using the PDQ-7 code (45).

As the calculated K_{eff} in the system was only 0.1% $\Delta K/K$ supercritical, the resulting fluxes would not be much distorted from those that would be measured during low power criticality tests.

The bottom light water plenum shape used is that given in Fig. 8.1. The central fuel element position was replaced with lead and the effective core height was 12.0 inches. The shim rod bank (outer absorber ring) was inserted 2.0 inches below the active core top position in order to reduce the reactivity to the 0.1%$\Delta K/K$ mentioned above.

The actual 30-region R-Z cylindrical core model used in the calculations is given in Fig. C.1 of Appendix C. In this core model, the heavy water has been assumed to contain 0.5% light water. The effects of voids and aluminum in the radial graphite reflector (29) have been included in the 23.75-inch high region below the active core top. Referring to Fig. C.1, region 25 is the 1.0 inch helium-filled gap immediately outside the heavy water tank (region 15). Region 28 is the inner 8.0 inches of the radial graphite reflector containing 15.74% by volume in voids and 2.0% of aluminum. The remaining radial graphite reflector, region 29, contains 1.0% aluminum.

The details of the materials (mixtures) corresponding to each of the 30 regions of Fig. C.1 are given in Table C.1. Although it is observed from Table C.1 that the

material corresponding to region 30 is heavy water, this region also represents the location of the re-entrant portion of a beam port, whose horizontal centerline coincides with mesh point 32 on the Z axis.

The calculated 2-group fluxes are given in Appendix C.1. The fast and thermal flux distributions along the centerline of a beam port are shown plotted in Fig. 10.1. The thermal to fast flux ratio at the proposed location of the beam ports tips is about 5.5. This ratio can be improved to the value of 10.5 if the beam ports are withdrawn radially by 2.0 inches. This 2.0 inch movement will result in only a 1% reduction of the unperturbed thermal flux available at the beam port tip.

10.2 THREE-DIMENSIONAL XYZ CALCULATION OF MITR-I

Three-group fluxes in the MITR-I, operating at 5 megawatts, have been calculated in 3-dimensional XYZ geometry, by using PDQ-7. The minimum mesh spacing between planes in the axial direction has been made about 6.0 inches since the problem may not converge for heavy water systems if the axial mesh spacing is much smaller than about 6.0 inches (see section 8.2.1).

With a minimum axial mesh spacing of about 6.0 inches, it has not been possible to duplicate exactly some of the criticality data measured during the initial low power tests of MITR-I in 1958. However, during the initial

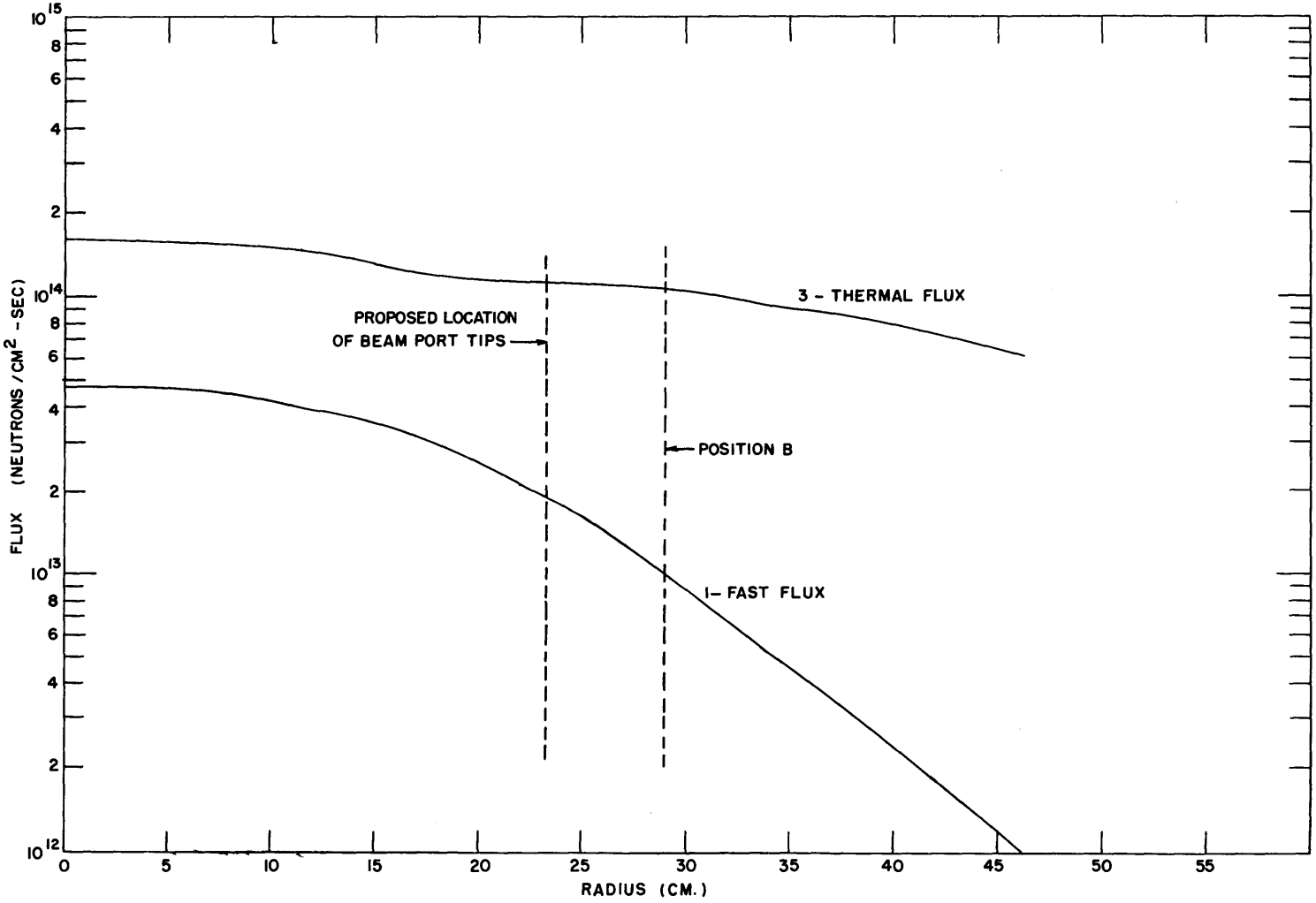

FIG. 10.1 FAST AND THERMAL FLUX DISTRIBUTIONS ALONG A BEAM PORT CENTERLINE IN MITR-II

criticality tests measurements of reactivity effects were measured and these measured values have been used to estimate the reactivity differences between the critical experiment and the calculational model that has been used. The calculational model is discussed below.

10.2.1 Calculational Model for MITR-I

The arrangement of fuel elements, six shim rods, and a regulating rod inside the heavy water tank of MITR-I has been described in section 1.1.1. The details of the arrangement of fuel elements inside the core tank are given in Fig. 10.2.

The MITR-I core configuration from which the calculational model was derived is the 19-element core used for the low power starup experiments on October 21, 1958 (29), (30). The core consisted of nine 105 gm fuel elements in positions 1 through 8 and in position 14; ten 160 gm fuel elements occupied the remaining first 19 fuel positions. The shim rod bank and the regulating rod had been raised above the fuel centerline by 6.75 inches and 13.0 inches respectively. The reactor stable period was 14.7 seconds corresponding to an excess reactivity of 90 mβ.

The active fuel bearing region of a fuel element of this core configuration is 23.375 inches and the material

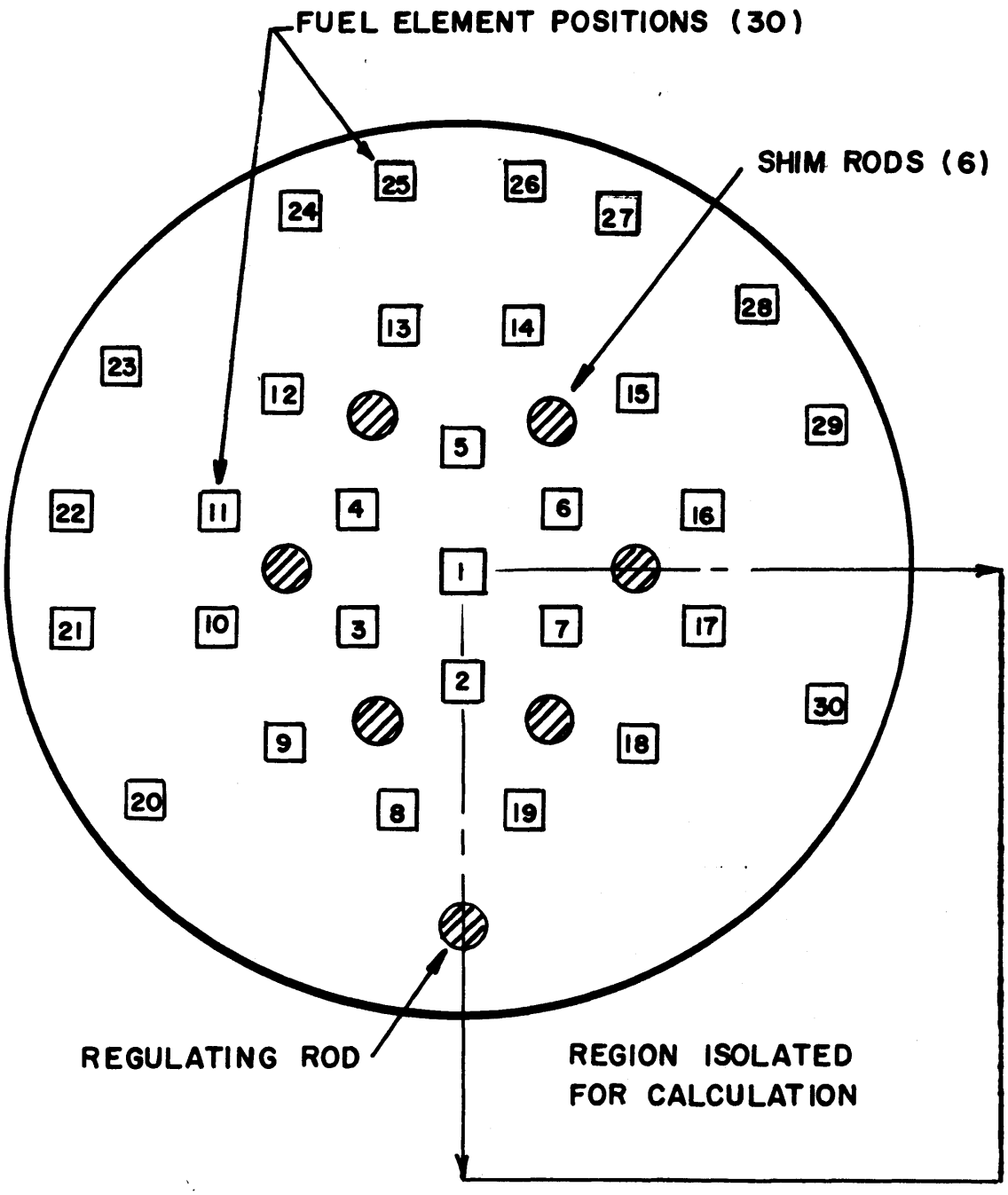

FIG. 10.2 ARRANGEMENT OF FUEL ELEMENTS INSIDE THE HEAVY WATER TANK

distribution above and below this fuel region is discussed by Larson (29). The details of the dimensions and calculated percentages by volume of the axial distribution of materials in a fuel element are given in Fig. 10.3.

The calculational model was derived from the above core configuration by re-homogenizing the material distribution such that material discontinuities in the axial direction may be described by planes with minimum mesh spacing not much smaller than 6.0 inches. The dimensions and percentages by volume of materials in a resulting 11 axial plane core model are shown in Fig. 10.4.

A quadrant of the core isolated for the calculations is shown in Fig. 10.2. The circular heavy water tank and the two zone radial graphite reflector boundaries were represented in X-Y geometry as shown in Fig. 10.5. The heavy water tank wall was homogenized with heavy water in order to reduce the number of mesh points necessary to describe it.

Five changes have been made between the 19-element core discussed above and the calculational model. First, in the calculational model the shim rods are at the level of plane 4 and this represents an insertion of 0.906 inches more than shim position in the critical experiment. Secondly, the regulating rod is at the level of plane 3, and this also represents a further insertion of 1.312 inches. Thirdly, the 105 gram fuel elements in positions

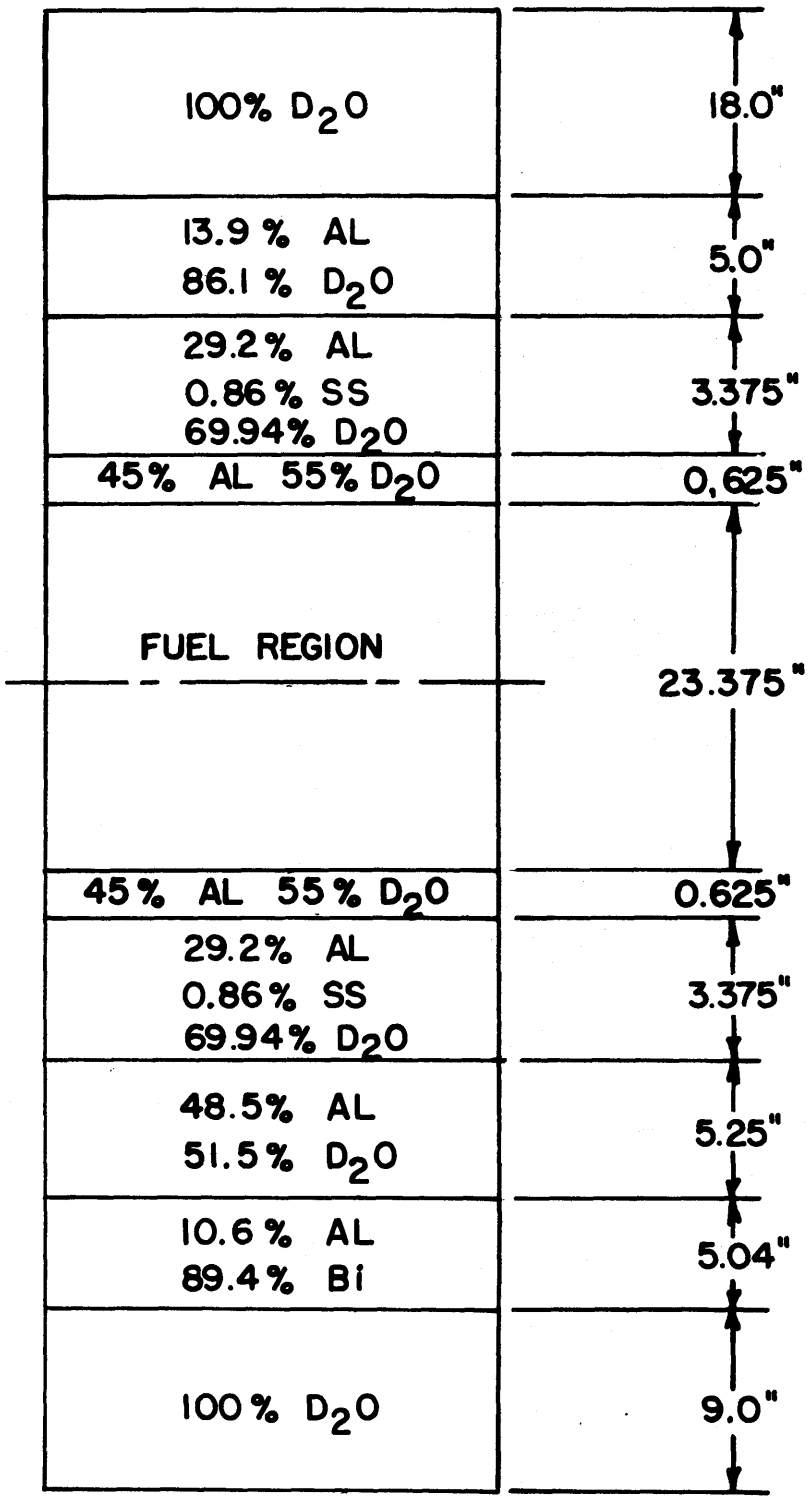

FIG. 10.3 ACTUAL AXIAL MATERIAL DISTRIBUTION IN A FUEL ELEMENT POSITION

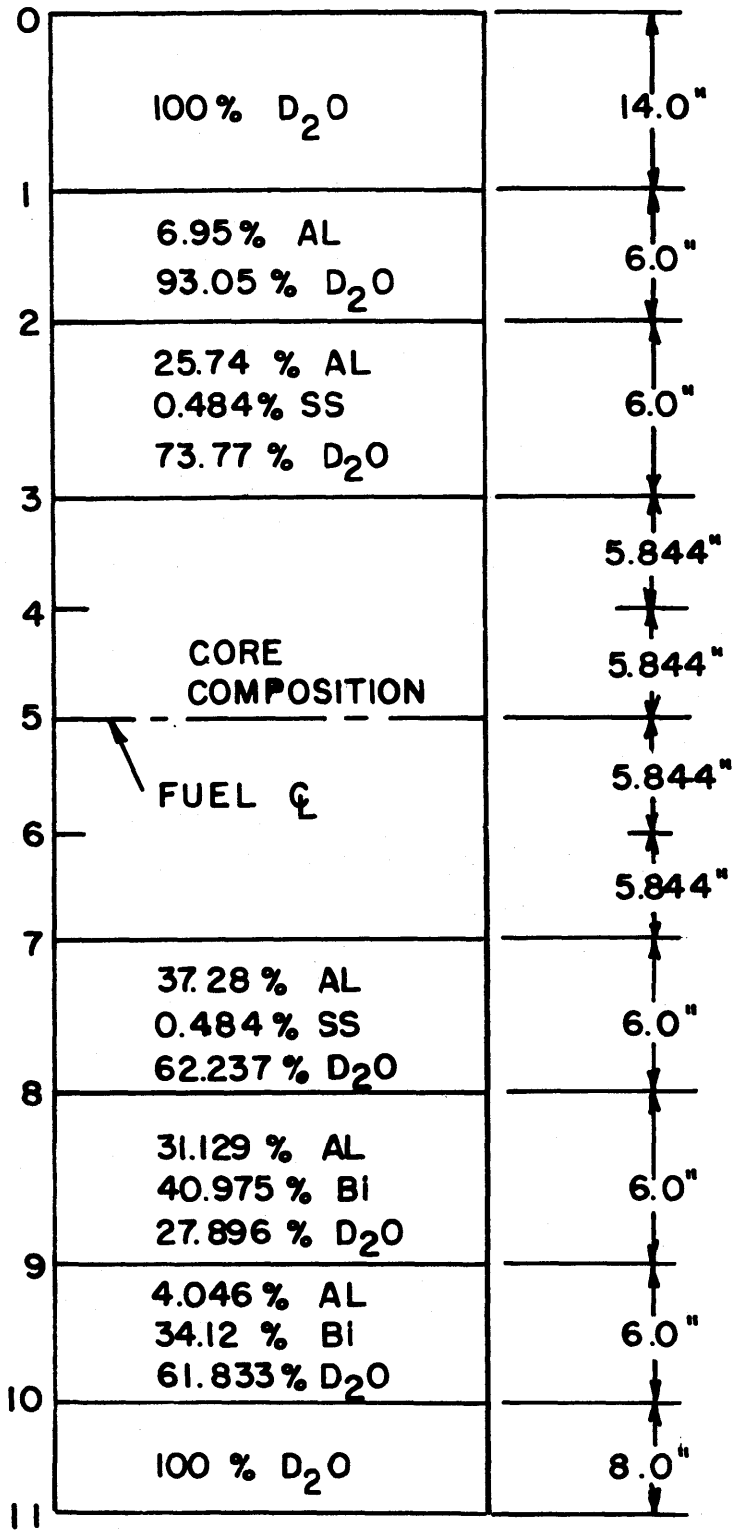

FIG. 10.4 A FUEL ELEMENT OF AN ELEVEN AXIAL PLANE CORE MODEL

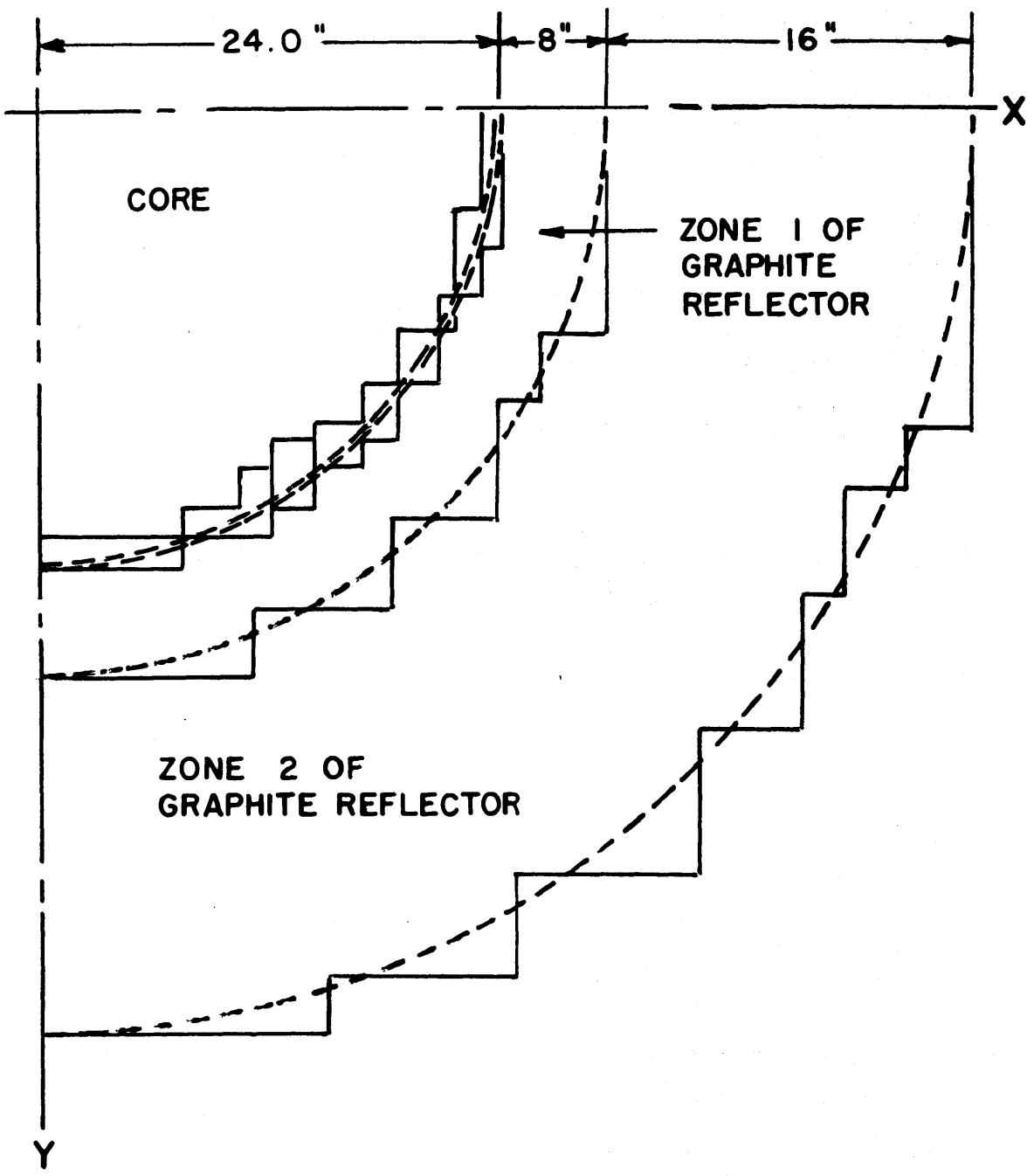

FIG. 10.5 X, Y, GEOMETRY REPRESENTATION OF THE CORE TANK AND THE TWO ZONE GRAPHITE RADIAL REFLECTOR

8 and 14 have been replaced with 160 gram elements. Fourthly, an additional 105 gram fuel element has been placed in position 30 of Fig. 10.2. As MITR-I is normally operated at power with more than 19 fuel elements, the presence of this additional fuel element will result in a more realistic ratio of thermal to fast flux in the region of the reflector where neutron beam is normally removed for experiments. Finally, the symmetry in Fig. 10.2 requires a second regulating rod be placed in the corresponding mirror image position in the core.

The effects of these changes have been estimated, by using the measured results reported by Larson (29), and are summarized in Table 10.1. The effect of natural boron in the braze material used in the initial 105 gram fuel elements has been included in the calculation. Based on the results of the critical experiments, the estimated reactivity in the calculational core model is 5208 mβ (4.39%ΔK/K) corresponding to an effective multiplication of 1.047.

10.2.2 Calculated Three-Group Fluxes

Quarter core symmetry was used for the calculation. The radial detail of the calculational model, shown in Fig. 10.2, was represented by a 30-region model, and is given in Fig. C.2 of Appendix C. The material corresponding to a planar region was specified at each of the 11

TABLE 10.1

Reactivity Effects of Changes Made to

the 19-Element Core Configuration

Change	Associated Reactivity Change (mβ)
1. Lower Shims From 16.75" to 15.844" Position	-1350 (1200)
2. Lower Reg. Rod From 26.0" to 24.69" Position	-25
3. 105 gm Elements in Position 8 and 14 Replaced by 160 gm Elements	+1708±34
4. Additional 105 gm Element in Position 30 plus Other Required by the Quadrant Symmetry	+3016
5. Additional Mirror Image Regulating Rod	-43
6. Reactivity Worth of Boron in 105 Braze	+2412
7. 147 Second Initial Period	+90
Total	5208 (4.385%ΔK/K)

axial planes of Fig. 10.4. In the fuel element positions, the axial material specification was similar to that shown in Fig. 10.4.

The three group cross section data used as input to the 3-dimensional XYZ PDQ-7 calculations were derived from THERMOS and EXTERMINATOR-II codes. THERMOS was used to obtain the homogenized cross sections in the energy range below 1.0 eV by the procedure described in section 2.3. The homogenized atom number densities for the 105 and 160 gram fuel elements are given in Table 10.2. A fifteen group EXTERMINATOR-II R-Z cell calculation was made for the 105 and 160 gram fuel elements. The entire fuel element model, shown in Fig. 10.4, was surrounded with a heavy water reflector and a 2-dimensional cell calculation performed to obtain region averaged 3 group constants. The moderator to fuel region volume ratio used for the 105 gram elements in the central positions 1 through 7 was 3.0 while a ratio of 4.0 was used for the others.

The calculated three group fluxes for planes 5 and 6 are given in Appendix C.2. The materials corresponding to each region of Fig. C.2 are also given in Table C.2 of Appendix C.2. The fast and thermal flux distributions in the axial plane 6 and along the two horizontal axes of symmetry (XX and YY) are shown plotted in Figs. 10.6 and 10.7 respectively. It may be observed from Fig. C.2 of Appendix C that the additional 105 gram fuel element placed in the outermost ring (region 14 on Fig. C.2)

TABLE 10.2

Atom Number Densities in Homogenized Fuel Elements

Isotope	105 Gram Element	160 Gram Element
U-235	7.4878×10^{19}	1.1454×10^{20}
U-238	5.6369×10^{18}	2.44×10^{18}
Aluminum	2.5513×10^{22}	2.5459×10^{22}
D_2O	1.9012×10^{22}	1.9012×10^{22}

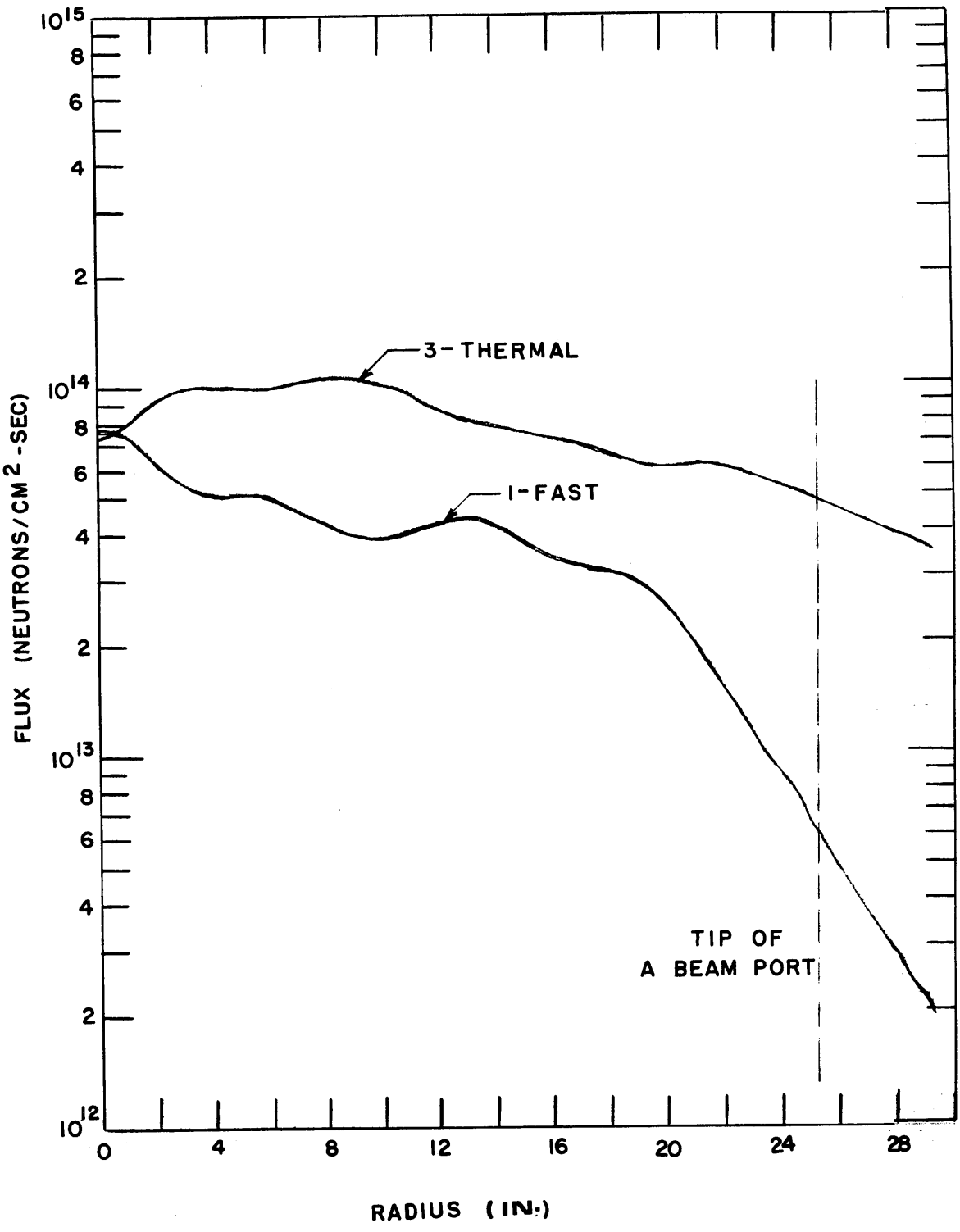

FIG. 10.6 FAST AND THERMAL FLUX DISTRIBUTIONS IN THE AXIAL PLANE 6 ALONG THE X,X AXIS FOR MITR-I

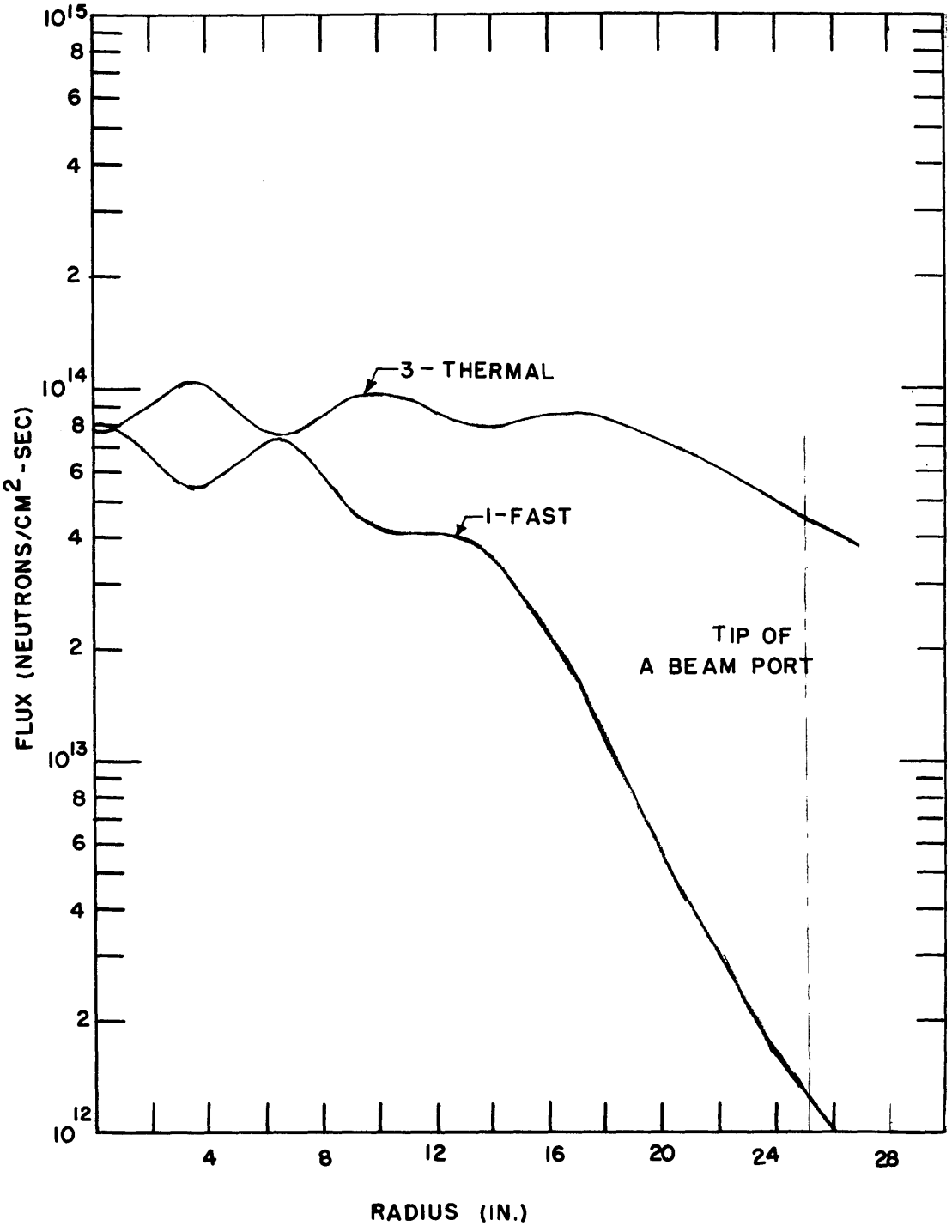

FIG. 10.7 FAST AND THERMAL FLUX DISTRIBUTIONS IN THE AXIAL PLANE 6 ALONG THE Y,Y AXIS FOR MITR-I

is near the XX axes. The effect of this element on the thermal to fast flux ratio in the reflector region where neutron beam is normally removed for experiments is revealed by comparing the calculated thermal to fast flux ratios obtained on the XX and YY axes respectively.

It is observed from Fig. 10.6 that the thermal to fast flux ratio at the wall of the heavy water tank near the additional 105 gram element is 9.6. From Fig. 10.7, it is also seen that the corresponding ratio at the heavy water tank far from the additional 105 gram element is 40.9. It is observed from Fig. 10.2, that the fuel element configuration calculated corresponds to four elements in the outer ring in positions 29 and 30 together with the two mirror image elements near positions 20 and 23. When MITR-I is operated with more than 4 fuel elements in the outer ring, therefore, the best flux ratio available at any of the beam ports will be less than the calculated value of 40.9 and the worst ratio will also be less than the calculated value of 9.6.

The three group fluxes calculated for MITR-II and given in Appendix C, show that the thermal to fast flux ratio at the wall of the heavy water tank is about 165 which is much larger than the maximum ratio of 41 available at the same region in MITR-I. The fast and thermal group fluxes plotted on Fig. 10.1 show that by making the beam ports re-entrant to within 2.0 inches of the light water

tank of MITR-II, the thermal to fast flux ratio may be reduced to below 10. However, by removing the thermal neutron beams from underneath the MITR-II core, the fast neutron streaming effects as well as the gamma radiation background will be significantly reduced, resulting in an improved quality of the flux available at the MITR-II experimental beam ports.

Both the core configuration and the approximations made in the MITR-I calculational model are factors to be taken into account when comparing the calculated fluxes with those available in the operating MITR-I core. The measured thermal neutron flux at the tips of beam ports is about $2.2X10^{13}$ n/cm^2-sec (56); the corresponding calculated values are $4.84X10^{13}$ on the XX axis and $4.28X10^{13}$ on the YY axis.

The MITR-I core is normally operated with only 160 gram fuel elements. The replacement of the seven inner 160 grams with the 105 elements as in the calculational model will cause a reduction in the thermal fluxes near the core center while those near the wall of the core tank will increase. The calculated thermal flux at the wall tank is $4.84X10^{13}$ n/cm^2-sec near the additional 105 gram element while that value far from this element is $4.28X10^{13}$ n/cm^2-sec. The measured MITR-I thermal neutron

flux, given in Fig. 1.3, shows a flux of about $3.1X10^{13}$ n/cm^2-sec at the wall tank. The core configuration measured had 19 fuel elements, with eleven 105 gram elements in positions 1 through 7 and in positions 8, 11, 14, and 17. Placing relatively more fuel in the outer core region will cause an increase in the thermal neutron flux at the wall of the core tank. The effective height of the calculational model is also shorter than that at which MITR-I is normally operated.

The geometrical approximations used in the representation of the cylindrical boundaries in the XY geometry (see Fig. 10.5) together with the material homogenization over large distances in the axial direction in order to achieve mesh spacing of about 6.0 inches are further reasons to expect disagreement between the calculated and measured flux distributions. There is a 1-inch thick helium-filled gap outside the heavy water tank, but this region was not included in the calculational model. The long transport mean free path of the neutrons in this region would have resulted in a minimum axial mesh spacing much larger than 6.0 inches for the iterations to converge.

The calculated effective multiplication is 1.0722, corresponding to a reactivity of 6.729%ΔK/K; the predicted reactivity (Table 10.1. of section 10.2.1) is 4.385 %ΔK/K. The reactivity of 2.444%ΔK/K over-predicted by the calculational model is considered satisfactory within the approximations of this model.

10.3 COMPARISON OF SELECTED CHARACTERISTICS OF THE MITR-II AND MITR-I CORES

Some selected characteristics of the MITR-II and MITR-I cores are summarized in Table 10.3 for comparison. Referring to Table 10.3, it is observed that the core temperature coefficient of reactivity is $-1.6X10^{-4}$%ΔK/K per °C in MITR-II compared with $-4.5X10^{-4}$%ΔK/K per °C in MITR-I. Although the value in MITR-II is just under one half, but still strongly negative as in the MITR-I, the calculated and the measured void coefficients of reactivity in the two cores respectively are both negative. In addition, the leakage of light water into the heavy water system and vice versa has been found to lead to negative reactivity effects. Reactivity disturbances, therefore, will in general be negative in the MITR-II core as the experience has been with the MITR-I core.

The reactivity worth of a shim rod in the active part of the MITR-II core is 2.0%ΔK/K compared with 4.02% ΔK/K in the MITR-I core. The equillibrim xenon reactivity worth has reduced from 2.75%ΔK/K in MITR-I to 2.55%ΔK/K in MITR-II. The reduced reactivity worth of the equil-librim xenon in the MITR-II core is due to the harder thermal neutron spectrum.

The unperturbed thermal neutron flux at tips of beam ports in MITR-II is $1.1X10^{14}$ n/cm^2-sec compared with $2.2X10^{13}$

TAPLE 10.3

Comparison of Selected Characteristics of the

MITR-II and MITR-I Cores

Property	MITR-II Core	MITR-I Core
1. Core Temperature Coefficient (Percentage ΔK/K per Deg. C)	-1.6E-4	-4.5E-4
2. A Shim Rod Worth (Percentage ΔK/K)	2.0	4.02
3. Equillibrim Xenon Worth	2.55	2.75
4. Maximum Unperturbed Thermal Flux at Beam Ports Tip in the Cold Clean Core (10^{13} n/cm^3-sec)	11.0	2.2
5. Average **Thermal to Fast** Flux Ratio at Beam Ports Tip	5.5	9.6 to 41

n/cm^2-sec in MITR-I. However, the corresponding thermal to fast flux ratios are 5.5 in MITR-II and between 9.6 and 41 in MITR-I. The fluxes plotted in Fig. 10.1 show that the thermal to fast flux ratio in MITR-II may be increased to over 10 by moving the beam ports radially by about 2.0 inches and still maintain the flux at the beam ports about $1.0X10^{14}$. The quality of the thermal neutron flux available to the experimenter is improved due to the reduced fast neutron streaming effects as well as gamma radiation background resulting from removing neutron beams below the MITR-II core.

10.4 EFFECTS OF THE PRINCIPAL CONSTRAINTS IMPOSED BY THE PERMANENT FEATURES OF THE MITR

The two most important constraints, which have influenced the optimization of the maximum thermal neutron flux available at the tips of experimental beam ports, are the radial beam ports and the low average power density in the core. These two constraints have been imposed by the permanent features of the MITR.

10.4.1 Constraint on the Location of Beam Ports

The radial beam ports of the MITR are permanent features and cannot be changed. However, the reflector thermal neutron fluxes available at the wall of the heavy water tank (the present location of beam port tips in the MITR-I) has not changed significantly by the redesign. The advantages of the re-design, therefore, are derived from making the beam ports re-entrant into the heavy water tank to extract neutron beams from the maximum reflector **thermal flux region** which normally occurs at the active core mid-height (see section 4.1). In the MITR-II, the reflector maximum thermal flux region has been forced to appear below the core, where re-entrant radial beam ports can extract thermal neutron beams with reduced fast neutron and gamma radiation background. The corresponding re-entrant

beam ports oriented tangentially to the core would have a greater flexibility of placement in the axial plane, resulting in a design of an improved thermal neutron flux at beam ports tips.

10.4.2 Constraints Imposed on the Average Power Density in the MITR-II Core

The constraints imposed by the permanent features of the MITR have limited the average power density in the MITR-II core to a value well below that in reactors of a similar core concept (7), (62).

Summarized in Table 10.4 are selected core properties of the MITR-II, the Brookhaven High Flux Beam Reactor (BHFBR), and the Argonne Advanced Research Reactor (AARR). It is observed from Table 10.4 that the average power density in the MITR-II core is factors of 4.5 and 12.0 less than the corresponding values in the BHFBR and AARR, respectively. The low operating primary coolant pressure and the low water velocity in the coolant channel are the two features of the MITR-II that limit the average power density in the core.

By making use of equations 5.2.1 and 5.2.2, the maximum permissible power density at the hottest coolant channel axial position Z, PD(Z), can be expressed directly in terms of the heat transfer coefficient, h, and the fuel plate surface temperature, T_w (Z) as

TABLE 10.4

Selected Core Properties

Property	MITR-II	BHFBR	AARR
1. Power Level (Megawatts)	5.0	40.0	100.0
2. Average Power Density (Mw/litre)	0.108*	0.453	1.30
3. Normal Operational Pressure	Atmospheric	200 psig	750 psig
4. Maximum Fuel Plate-Water Interface Temperature (°F)	226.8	359.0	378.0
5. Water Velocity in Coolant Channels (ft/sec)	7.8	35.0	45.0
6. Reflector Maximum Unperturbed Thermal Flux at Beam Port Tips (10^{14} n/cm^2-sec)	1.1	7.0	13.5**

*The lower 12.0 inches high active core part only.

**The predicted maximum thermal flux in the H_2O internal column was $1.35X10^{15}$ while that in the beryllium reflector was $1.0X10^{15}$ n/cm^2-sec.

$$PD(Z) = \frac{K_c \cdot F_d}{A} \cdot h[T_w(Z)-T_o-T_B(Z) \qquad \ldots 10.4.1$$

where the terms in the equation have been defined in section 5.2. PD(Z) is, thus, observed to increase with increasing value of the product h X $T_w(Z)$.

The fourth row of Table 10.4 shows that increasing the operating pressure of the primary coolant raises the maximum allowable fuel plate-water interface temperature, $T_w(Z)$. Furthermore, equation 5.2.3 shows that the heat transfer coefficient, h, is proportional to the four-fifths power of the water velocity in the coolant channels.

In the absence of the permanent features of the MITR, which impose a limit on the primary coolant operating pressure (see section 5.2) as well as the water velocity in the coolant channels (see section 5.2.1), presently available technology would permit an increase of a factor between 4.5 and 12.0 in the maximum power density in the MITR-II core. Such an increase in the water velocity in the coolant channel would also permit the aluminum fins in MITR-II to be eliminated from the design. Both the diameter and the effective height of the core could be reduced well below 15.0 and 12.0 inches respectively and a resulting much smaller core would produce more intense reflector maximum thermal neutron flux.

The last row of Table 10.4 shows that, despite the constraints imposed by the permanent features of the

MITR, the calculated value of the unperturbed reflector maximum thermal neutron flux per unit power of $2.2X10^{13}$ n/cm^2-sec per Mwt for MITR-II is competitive with the corresponding values of $1.8X10^{13}$ and $1.35X10^{13}$ n/cm^2-sec per Mwt available in the BHFBR and AARR respectively.

CHAPTER XI

CONCLUSIONS AND RECOMMENDATIONS

11.1 CONCLUSIONS

The reactor physics studies show that the redesigned MITR-II core will permit an increase in the unperturbed thermal neutron flux available at the tips of the MITR experimental beam ports by a factor of about three or better, without altering the operating power level.

The comparison of the water velocity in the MITR-II coolant channels and the operating pressure in the primary coolant loop with the corresponding properties in reactors employing a similar core concept show that the permanent features of the MITR limit the maximum power densities in MITR-II core to a factor between 4.5 and 12 of that achievable with presently available technology. Nevertheless, the unperturbed reflector thermal flux available at the tips of experimental beam ports per unit power is competitive with corresponding values available in reactors of its type.

Calculations show that the re-entrant beam port design in the MITR-II will result in only a slight reduction in the thermal to fast flux ratio available at the tips of experimental beam ports. However, both the fast neutron streaming effects as well as the gamma radiation background will be significantly reduced by removing neutron beams for

experiments below the MITR-II core.

The change from heavy water to light water coolant will result in a simpler operation as well as cheaper maintenance of the redesigned reactor. The problem of tritium leakage into the secondary coolant system, a minor health hazard, will be reduced. The double core arrangement will result in a better utilization of the fuel elements as well as increase the flexibility of changing the reactivity in the system. Future core loadings can be made to be responsive to changes observed during the operation of the preceeding cores.

The self-regulating characteristics as well as the safety features of the redesigned MITR-II core are generally similar to the present MITR-I core which has been successfully operated for ten years. The operation of the redesigned reactor is expected to be similar to the past experience with an enhanced utility of the reactor.

11.2 RECOMMENDATIONS FOR FUTURE WORK

The studies which might be done as a continuation of this work fall into two groups. The first group, discussed in sections 11.2.1.1 through 11.2.1.7, are logically desirable in order to answer questions raised in the present work. The other group, discussed in section 11.2.2.1 through 11.2.2.4, are detailed engineering studies that might be useful before the first loading of the MITR-II Core.

11.2.1.1 Bottom H_2O Plenum Shape

Flow diverters were necessary in order to achieve a uniform flow through a plenum shape similar to that shown in Fig. 6.10 (see section 7.6.2). It is clear that the flow through a plenum shape similar to that shown in Fig. 6.9 will be non-uniform, unless the fuel elements are orificed. This latter plenum shape has been used in the calculations as it predicts higher reflector thermal neutron flux in the region where beam port tips are located. Further hydraulic and nuclear studies are necessary to decide on a final H_2O plenum shape that predicts high fluxes as well as permits a uniform flow distribution through the fuel elements.

11.2.1.2 Few Group Scheme

The advantage of the few group scheme used compared with the standard procedures such as the MUFT-THERMOS scheme is that spatial dependence of the thermal group constants as well as both the fast and epithermal transgroup and transport constants may be retained. Epithermal resonance absorption, though not a very serious problem in this core due to the low concentration of uranium-238, is difficult to account for accurately by the scheme used. A comparison of the method used with the standard procedure to determine the spatially dependent effects in the fast and thermal groups will be useful.

11.2.1.3 Experimental Criticality Data on a Heterogeneous H_2O Compact Core

The calculational method used has yielded good agreement with D_2O or H_2O homogeneous systems as well as MITR-I D_2O heterogeneous core. A further test of the procedure against an H_2O heterogeneous compact core is desirable.

11.2.1.4 Three-Dimensional Axial Power Distribution in the Hottest Coolant Channel

Useful three-dimensional hexagonal geometry calculations for the MITR-II core are not feasible with the

presently available PDQ-7 version. However, the 1-dimensional cylindrical and 2-dimensional hexagonal geometry comparative calculations, discussed in section 8.2.2, might be extended to synthesize the 2-dimensional hexagonal calculations to produce a full 3-dimension power density distribution.

11.2.1.5 Effects of Cadmium in the Upper Half of the Three Radial Ribs

The radial ribs contain cadmium in the upper half core. The shim rods reactivity worth as well as the power density distributions in both the upper and lower active halves of the core are affected by these neutron absorbers. The development of a method to estimate their effects will be useful, and perhaps, necessary for the detailed fuel management studies.

11.2.1.6 The Leakage of D_2O into the H_2O System

The work discussed in section 9.5 shows that the leakage of D_2O into the entire H_2O system initially results in a negative reactivity effect, though the contribution from the H_2O reflector region is a positive reactivity effect. The location of the D_2O reflector relative to the H_2O system is such that any leakage into the latter system will most likely begin in the H_2O reflector. Studies of the

worst situation that could arise during the first few moments a leak is initiated as well as after amounts of D_2O contaminant in excess of the 10% investigated in section 9.5, will be desirable.

11.2.1.7 Coefficients of Reactivity Including Effects of Spectrum Changes and Equillibrim Xenon

Further hardening of the thermal neutron spectrum in the undermoderated core due to temperature effects will cause a reduction of absorption in the core, including the parasitic absorbers such as xenon and shim rods. The reduction in the absorptions of these parasitic absorbers will lead to a positive reactivity effect. Coefficients of reactivity studies including the effects of spectrum changes will be desirable

11.2.2.1 Further Reactivity Studies

There are a number of reactivity studies which have been considered outside the scope of the present work, though desirable as a part of the detailed engineering studies. These reactivity effects include the worth of flooding either the beam ports, the D_2O shutter tank, or the H_2O shutter underneath the core (see Fig. 7.6).. A more detailed study of the reactivity worth of dumping the radial D_2O reflector with the shim rod bank at different

positions, including the reactivity insertion rate as this reflector is pumped up, is desirable. The reactivity effects of removing single fuel plates and the effects of the vibrations of shim rods are useful additions to the list.

11.2.2.2 Sensitivity Studies

Calculations have shown that the reactivity in the system is sensitive to slight changes in the fuel element specification. Studies to investigate how sensitive the reactor characteristics are to changes in the core components' dimensions will be useful. The effects of the little gaps between fuel elements in the compact core, not included in the calculations so far, might also be examined.

11.2.2.3 Asymmetry Effects

In the calculations done so far the effects of non-symmetrical distribution of material around the core have been ignored. The beam ports are not symmetrically distributed around the core; the vertical axis of the medical therapy room hole is off-set about 9 inches from the core vertical axis; and the thermal column is non-symmetrically situated with respect to the core. The study of the effects caused by the asymmetry on the core is desirable.

11.2.2.4 Fuel Management

In the MITR-II core, the fuel management is part of the optimization of the reflector thermal neutron flux. The total fuel loading height will have to be determined from burn up studies. The fuel programming scheme will determine the net fraction of the core power that will be degraded in the upper half core.

REFERENCES

1. "Operating Manual for the MIT Reactor," prepared by the MIT Staff, November, 1965.
2. T. J. Thompson and E. J. Barnett, "MIT Reactor Core Modifications," Trans. Am. Nucl. Soc., 12, 2, pp. 749 (November, 1969).
3. R. C. Sanders and T. J. Thompson, "Optimization of the MIT Reactor Medical Facility," Trans. Am Nucl. Soc., 12, 2, pp. 795 (November, 1969).
4. D. J. Kennedy, "Beam-Port Optimization for the Proposed High-Flux MITR," Sc. D. Thesis, M.I.T. Nucl. Eng. Dept. (August, 1969).
5. T. J. Thompson and D. R. Spurgeon, "Flat-Plate Heat Transfer Augmentation, Trans. Am Nucl. Soc., 12, pp.808 (November, 1969).
6. B. Luxford, "Process System Safety Limits of the MITR-II," S. M. Thesis, M.I.T. Nucl. Eng. Dept. (June, 1970).
7. J. M Hendrie, "Final Safety Analysis Report on the Brookhaven High Flux Beam Research Reactor," BNL 7661 (April, 1964).
8. C. Sastre, "HFBR First Loading," BNL Memorandum (January 17, 1967).
9. "Reactor Physics Division Annual Report," ANL-7010 pp. 54-69 (July, 1964 - June, 1965).

10. "Reactor Physics Division Annual Report," ANL-7110 pp. 42-76 (July, 1964 - June, 1965).
11. "Reactor Physics Division Annual Report," ANL-7210 pp. 47-109 (July, 1965 - June, 1966).
12. "Reactor Physics Division Annual Report," ANL-7310 pp. 45-135 (July, 1966 - 1967).
13. "Reactor Physics Division Annual Report," ANL-7410 pp. (July, 1967 - 1968).
14. G. E. Hansen and W. H Roach, "Six and Sixteen Group for Fast and Intermediate Critical Assemblies," LAMS-2543.
15. Cross sections Library of the ANISN code (37).
16. L. P. Abagyan, N. D. Bazazyants, I. I Bondarenko, and M. N. Nikolaev, "Group Constants for Nuclear Reactor Calculations."
17. Sandy-II, Cross section Library Tape.
18. H. C. Honeck, "THERMOS, A Thermalization Transport Theory Code for Reactor Lattice Calculations," BNL-5826 (1961).
19. B. Toppel and I.Baksys, "The Argonne Revised Thermos Code," ANL-7023 (March, 1965).
20. R. L. Hellens, "Few-Group Approximations," Naval Reactors Physics Handbook, Volume 1 (1964).
21. R. S. Wick, "Homogenization Techniques," Naval Reactors Physics Handbook, Volume 1 (1964).

22. M. Nelkin, "The Scattering of Slow Neutrons by Water," Physical Review: 119, 741 (1960).

23. H. C. Honeck, "The Calculation of the Thermal Utilization and Disadvantage Factors in Uranium Water Lattices," Nuclear Science and Engineering: 18, 49 (1964).

24. C. G. Poncelet, "LAZER--A Depletion Program for Lattice Calculations Based on MUFT and THERMOS," WCAP-6073 (1966).

25. H. Brown and D. St. John, "Neutron Energy, Spectrum in D_2O," DP-33 (1954).

26. H. C. Honeck, "An Incoherent Thermal Scattering Model Heavy Water," Transactions of the American Nuclear Society, 5, 1, 47 (1962)

27. C. G. Poncelet, "Burnup Physics of Heterogeneous Reactor Lattices," WCAP-6069 (1965).

28. R. L. Mathews, "Flux Distributions in the MIT Reactor," Sc.D. Thesis, MIT Dept. Nucl. Eng. (1964).

29. C.L. Larson, "Reactivity Studies of a Heavy Water Moderated Highly Enriched Uranium Reactor," Sc.D. Thesis, MIT Dept Nucl. Eng. (1959).

30. "MIT Reactor Operations Log Book," MIT Nucl. Eng. Dept. (1956).

31. H. C. Paxton, et al., "Critical Dimensions of Systems Containing U-235, PU-239, and U-233," TID-7028 (1964).

32. F. Abbey, et al., "Handbook of Experimental Criticality Data Part II," AHSB-S-HB-5 pt. 2 (1968).

33. J. K. Fox, et al., "Critical Parameters of U-235 and U-233 in Simple Geometry," ORNL 2842 (1959).

34. R. N. Olcott, "Homogeneous Heavy Water Moderated Critical Assemblies. Part 1. Experimental," Nuclear Science and Engineering, 1, 327 (1956).

35. A. F. Henry, "A Theoretical Method for Determining the Worth of Control Rods," WAPD-218 (1959).

36. M. Goldsmith, et al., "Experimental and Theoretical Study of Critical Slabs--Effect of Absorbing Membranes of Cadmium, Gold, and Boron," WAPD-170 (1957).

37. W. W. Engle, Jr., "A Users Manual for **ANISN**," K-1693 (1967).

38. W. W. Engle, et al., "DTF-II, A One-Dimensional, Multigroup Neutron Transport Program," NAA-SR-10951 (1966).

39. M. L. Tobias, et al., "The Twenty Grand Program for the Numerical Solution of Few Group Neutron Diffusion Equations in Two Dimensions," ORNL-3200 (1962).

40. R. K. Plebuch, "Reactor Physics of Nuclear Rocket Reactors," Sc.D. Thesis, MIT Dept. Nucl. Eng. (1963).

41. T. B. Fowler, et al., "Exterminator--A Multigroup Code for Solving Neutron Diffusion Equations in One and Two Dimensions," ORNL-TM-842 (1965).

42. T. B. Fowler, et al., "Exterminator-2: A Fortran IV Code for Solving Multigroup Diffusion Equations in Two Dimensions," ORNL-4078 (1967).

43. M. Tobias, et al., "First Order Perturbation Theory as Used in the Multigroup Diffusion Code EXTERMINATOR-2," ORNL-RM-1741 (1967).

44. E. E. Gross, and J. H. Marable, "Static and Dynamic Multiplication Factors and Their Relation to the Inhour Equation," Nucl. Sci. Eng. I (4), 281-291 (1960).

45. W. R. Cadwell, "PDQ-7 Reference Manual," WAPD-TM-678 (1967).

46. C. J. Pfeifer, "CDC-6600 Fortran Programming--Bettis Environmental Report," WAPD-TM-668 (1967).

47. J. R. Reed, and R. J. Creasy, "PDQ-7 for the IBM System/360," IBM Data Processing Division Report No. 320-3259 (1969).

48. R. J. Breen, et al., "Harmony: System for Nuclear Reactor Depletion Computation," WAPD-TM-478 (1965).

49. H. Kouts, "Personal Communication," Brookhaven National Laboratory (1968).

50. The MITR Staff, "Technical Specifications for the MIT Research Reactor,"(August, 1965).

51. D. R. Spurgeon, "Preliminary Design Studies for a High Flux MIT Reactor," Nucl. Eng. Thesis, MIT Dept Nucl. Eng. (1969).

52. R. J. Nertney, "Calculated Surface Temperature for Nuclear Systems and Analysis of Their Uncertainties," IDO-16343 (1957).

53. D.R.deBoisblanc,"Discussion on the Limitations of Steady State,High Flux Reactors,Current and Future", Seminar on Intense Neutron Sources (CONF-660925) pp.365 (1966)

54. E.A.Bergles,"Personal Communication", MIT Department of Mechanical Engineering(1968).

55. V.A.Walker,et al,"ATR Fuel Materials Development Irradiation Results",IDO-17157 (1966).

56. D.M.Goebel,"Design of a High Flux Core for the MITR", 22.90 Report,MIT Nuclear Engineering Department (August,1966).

57. " The Advanced Test Reactor",Directory of Nuclear Reactors,Vol. V,pp.107. IAEA Publication(1964)

58. K.M.M.S.Ayyangar,A.R.Reddy,G.L.Brownell,"Dosimetric Studies for Boron Capture Therapy at MITR", Trans. Am. Nucl. Soc.,12,1,pp59(June 1968).

59. H.P.Flatt and D.C.Baller,"The AIM-6 Code", NAA Program Description
January 1961.

60. "Reactor Physics Constants",ANL-5800(1963).

61. A.Kadak,"The Fuel Management of the MITR-II Core", Sc.D Thesis, MIT, Nucl. Eng. Dept. (to be Published)

62. D.H.Shaftman and R.P.Savio,"The Argonne Advanced Research Reactor",Seminar of Intense Neutron Sources, CONF-660925,pp.215 (1966).

63. A.K.Addae and T.J.Tompson, "Reactor Physics Considerations of the MIT Reactor Redesign", Trans.Am.Nucl.Scc.,12,2, pp 795 (November,1969).

APPENDIX A

MODIFICATIONS TO EXTERMINATOR-II

Exterminator-II (42) has been modified to calculate material and group dependent bucklings as well as compute few group cross-sections by the modified method mentioned in section 8.1. The two modifications are discussed in sections A.1 and A.2 respectively. The input cards necessary to execute the code are basically those given in reference 42. However, the additional cards made necessary by the modifications mentioned above are described in section A.3.

A.1 AXIAL BUCKLING CALCULATION

The basic five-point difference equations used to describe the neutron diffusion group equations in EXTERMINATOR-II are:

$$\begin{aligned} &A1_k(I,J)\,[\Phi_k(I-1,J)-\Phi_k(I,J)] \\ &+A2_k(I,J)[\Phi_k(I+1,J)-\Phi_k(I,J)] \\ &+A3_k(I,J)[\Phi_k(I,J+1)-\Phi_k(I,J)] \\ &+A4_k(I,J)[\Phi_k(I,J-1)-\Phi_k(I,J)] \end{aligned} \quad \overset{kMAX}{\underset{N=k}{+\Sigma A5(N,k)(I,J)\Phi(I,J)-}}$$

$$-A6_k(I,J)\Phi_k(I,J)+X_k\lambda\Sigma_k A7_k(I,J)\Phi_k(I,J)=0, \qquad k=1,2,kMAX \qquad \ldots A.1.1$$

where

I, J	Denotes the Ith row and Jth column of the mesh
$\Phi_k(I,J)$	Group k flux at mesh point (I,J)
$A1_k$	$\frac{1}{2\Delta Y_T}(pD_{k1}\Delta X_R+qD_{k2}\Delta X_L)$
$A2_k$	$\frac{1}{2\Delta Y_B}(qD_{k3}\Delta X_L+pD_{k4}\Delta X_R)$
$A3_k$	$\frac{1}{2\Delta X_R}(rD_{k1}\Delta Y_T+rD_{k4}\Delta Y_B)$
$A4_k$	$\frac{1}{2\Delta X_L}(sD_{k2}\Delta Y_T+sD_{k3}\Delta Y_B)$
$A5(N,k)$	$\Sigma_R(N\rightarrow k)[p(\frac{\Delta X_R\Delta Y_T+\Delta X_R\Delta Y_B}{4})+q(\frac{\Delta X_L\Delta Y_T+\Delta X_L\Delta Y_B}{4})]$
$A6_k$	$[\Sigma_{Ak}+\Sigma_{Rk}+(DB^2)_k][p(\frac{\Delta X_R\Delta Y_T+\Delta X_R\Delta Y_B}{4})+q(\frac{\Delta X_L\Delta Y_T+\Delta X_L\Delta Y_B}{4})]$
$A7_k$	$\nu\Sigma_{fk}[p(\frac{\Delta X_R\Delta Y_T+\Delta X_R\Delta Y_B}{4})+q(\frac{\Delta X_L\Delta Y_T+\Delta X_L\Delta Y_B}{4})]$
ν	The number of neutrons produced per fission
Σ_{Ak}	Group k macroscopic absorption cross-section, cm^{-1}
$\Sigma_R(N\rightarrow k)$	Group N macroscopic removal cross-section into group k, cm^{-1}

$\nu\Sigma_{fk}$	ν times group k macroscopic fission cross-section, cm^{-1}
χ_k	Fraction of neutrons produced from fission that are born in group k
$(DB^2)_k$	Group k diffusion coefficient times perpendicular buckling squared
p	$\pi[2X(J)+\frac{\Delta X_R}{2}]$ for cylindrical geometry
q	$\pi[2X(J)-\frac{\Delta X_L}{2}]$ for cylindrical geometry
r	$\pi[2X(J)+\Delta X_R]$ for cylindrical geometry
s	$\pi[2X(J)-\Delta X_L]$ for cylindrical geometry
X,ΔX	Distance from left boundary and mesh increment in the X direction (or radial direction for cylindrical geometry), respectively, cm
Y,ΔY	Distance from top boundary and mesh increment in the Y direction (or axial direction for cylindrical geometry), respectively, cm
k,ι	Subscripts denoting kth or ιth group
L,R,T,B	Subscripts denoting left, right, top, bottom, respectively

It is observed from equation A.1.1 that the axial leakage terms at the point (I,J) are

$$LZ_T(I,J) = A1_k(I,J)[\Phi_k(I-1,J)-\Phi_k(I,J)$$

$$+A2_k(I,J)[\Phi_k(I+1,J)-\Phi_k(I,J)] \qquad ...A.1.2$$

The axial leakage may be represented by a point buckling term, $LZ_B(I,J)$, as

$$LZ_B(I,J) = B_k^2(I,J)A8_k(I,J)\Phi_k(I,J) \qquad ...8.1.3$$

where

$$A8_k(I,J) = D_k(I,J)[P(\frac{\Delta X_R\Delta Y_T+\Delta X_R\Delta Y_B}{4})+q(\frac{\Delta X_L\Delta Y_T+\Delta X_L\Delta Y_B}{4})]$$

$$...A.1.3$$

Equating equations A.1.2 and 8.1.3 yields

$$B_k^2(I,J) = LZ_T(I,J)/A8_k(I,J)\Phi_k(I,J) \qquad ...A.1.4$$

EXTERMINATOR-II has been modified such that for a specified I-th row, the point bucklings, $B_k^2(I,J)$ defined by equation A.1.4, are calculated for each point. The converged fluxes of an eigenvalue problem in cylindrical geometry are used in equation A.1.4 to compute $B_k^2(I,J)$. If desired the calculated point bucklings may be punched by the code. Material and group dependent bucklings are obtained by flux and volume weighting the point bucklings defined by equation A.1.4.

A.2 MODIFIED FEW GROUP TRANSPORT CROSS-SECTION

EXTERMINATOR-II has been modified to compute equivalent homogeneous microscopic transport cross-sections by two methods. First, the microscopic transport cross-sections may be directly flux and volume weighted as

$$\sigma_{tr}(G,N) = \frac{\sum_{M=M1}^{M2} CONC(M,N)V(M) \sum_{g=g1}^{g2} \sigma_{tr}(N,g)\Phi(M,g)}{\sum_{M=M1}^{M2} CONC(M,N)V(M) \sum_{g=g1}^{g2} \Phi(M,g)} \quad \ldots A.2.1$$

where M1 to M2 define the region over which the spatial averaging of $\sigma_{tr}(G,N)$ is to be done, and the rest of the terms in equation A.2.1 are defined in section 8.1.

Secondly, the reciprocal of the microscopic transport cross-sections may be flux-volume weighted as

$$\sigma_{tr}(G,N) = \frac{\sum_{M=M1}^{M2} \frac{1}{CONC(M,N)V(M)} \sum_{g=g1}^{g2} \Phi(M,g)}{\sum_{M=M1}^{M2} \frac{1}{CONC(M,N)V(M)} \sum_{g=g1}^{g2} \frac{\Phi(M,g)}{\sigma_{tr}(N,g)}} \quad \ldots A.2.2$$

A.3 EXTERMINATOR-II ADDITIONAL INPUT CARDS

The input cards necessary to execute EXTERMINATOR-II are those listed in reference 42 together with the following.

2.5 (24I2) NDDX(0,+1,+8) If equals +1, the code will expect input flux guess on cards of the format 8 E9.2, if equals +8, the code will expect input flux guess on cards of the format 5E14.7.

NDDA (0,+1,+8) If equals +1, the code will punch out group fluxes of the format 8(1P E9.2) on cards; if equals +1, the code will punch out group fluxes of the format 5E14.7 on cards.

NDDB (-1,0,+1) If equals -1, the code will update the flux-save device (logical unit 9) at the end of the iterations only. If equals 0, the code will update the flux-save device every 20 iterations. If equals +1, the flux-save device will not be updated.

NDDC (0,+1) If equals +1, no information will be initially read from the flux-save device.

NNBUC(-2,-1,0,+1,+2) If equals -2, point axial bucklings for each group are to be read in. If equals -1, material and group dependent bucklings are to be read in. If equals +1, point bucklings are to be punched out. If equals +2 then point bucklings as well as material and group dependent bucklings are to be punched out.

The point bucklings are punched out as M,K,DBSQL(J,K), DBSQR(J,K) for the two left and right quadrants, where M,K,J are the material at that point, group index, and the column index respectively. The material and group dependent bucklings are punched out as M,K,DBSQG(M,K). For the purpose of identification, the title of the problem as well as the axial row at which the bucklings have been calculated are punched out and these must be deleted when the bucklings are used as input to another problem.

NIII If NIII equals zero, no axial buckling calculation will be done. If NIII lies between 1 and 15 inclusive, axial buckling calculations will be done for NIII rows.

(III(I) I=1, NIII) This array specifies the actual indexes of the NIII rows at which axial buckling calculations are to be done.

(12.C)
12.5 24I3 (~~NDM~~NNDM(I), I=1,22) These are pairs of pairs of numbers over which spatial averaging of the few group cross-sections are to be done as defined in equation

NNDM (23) is used to define the method to be used in calculating the few group diffusion constant. If OP14 of card 2 #0, the few group microscopic transport cross-section is calculated using equation A.2.2. If NNDM (23) equals 30 or 33, the transport cross-section is calculated by using equation A.2.1. If NNDM (23) is either greater than 61 or less than -61, the transport cross-section will be calculated by both methods and a mean value taken. In addition, if NNDM (23) is either equal to 33, 43, or less than -61, the calculated microscopic cross-sections will be punched out.

NNDM (24) If less than zero, another set of card number 12.5 to be read in.

APPENDIX B

MODIFICATIONS TO THERMOS CODE

THERMOS has been modified to compute the first moment of the spectrum, V, defined by equation 2.3.13 of section 2.3.2. THERMOS has also been modified to compute self-shielding factors for isotopes in the cell as defined by equation 2.3.9 of section 2.3.1. If the computed self-shielding factors for a region are used as input to another THERMOS calculation in which that region is further homogenized (see pp. 72), then the effective microscopic cross-sections are calculated as given by equation 2.3.8. The important errors found in THERMOS are discussed below in section B.1, while the additional input cards necessary to utilize the modifications to THERMOS are described in section B.2.

B.1 IMPORTANT ERRORS FOUND IN THERMOS

A complex DO-loop in subroutine overlay 9 (19) was found to yield incorrect results on the IBM System 360. This DO-loop is

```
DO 340   J=1, 150X
```

```
      DO 340   M=1, MX
      IF(CONCTA(J,M) 333,340,333
  333 DO 340 M=1,MX
      MP = MTBL(N)
      IF(MP-M) 340,330,340
  330 DO 340   I=1, 1X
      XFM(N,I) = XFM(N,I)+CONCTA(J,M)*XFT(J,I)
      .......
  340 CONTINUE
```

It was found that if CONCTA(1,1) = 0, then the augments N and I are not initially set equal to 1, resulting in incorrect answers. This difficulty has been eliminated by separating the above DO-loop into 3 simpler ones as

```
      DO 340   J=1, ISOX
      DO 340   M=1, MX
      IF(CONCTA(J,M)) 333,340,333
  333 DO 50   M=1,NX
      MP = MTBL(M)
      IF(MP-M)  50,330,50
  330 DO 40   I=1, 1X
      XFM(M,I) = XFM(N,I)+CONCTA(J,M)*XFT(J,I)
      .......
      40 CONTINUE
      50 CONTINUE
     340 CONTINUE
```

Self-shielding factors calculation in the slab geometry has shown that this geometry option gives incorrect results. Further, according to the THERMOS manual (19), the calculated transport kernel satisfy a normalization condition such that if reflecting cell boundary conditions are used the source term, Q_{ki} defined by equations 63 and 69 of reference (19), should be about unity. THERMOS calculations have shown that this normalization condition for the calculated transport kernel is satisfied in the cylindrical geometry but not in the slab geometry.

The three subroutines which compute the slab transport kernel--namely OVERLAY 5, subroutine EI and subroutine SLABK--have been examined. Further detailed work on these three subroutines is needed in order to eliminate the error in them.

B.2 ADDITIONAL INPUT CARDS REQUIRED BY THERMOS

The input cards necessary to execute THERMOS are basically those listed in reference 19. The additional necessary cards have been constructed such that if the modifications are not to be utilized, then the cards listed in reference 19 form a complete set. If the modifications are to be utilized, then the following additional cards must be present in the sequence indicated by the

numbers assigned to them in relation to the input card numbers listed in reference (19).

4.	(20I1,I5)	(MTBL(N), N=1,20)	Mixture number (1-5) assigned to each space point N
		NSHTR	If # 0, input self-shielding factors are to be read in.

7.5 Input Self-Shielding Factors

If NSHTR = 0, ignore this card.

(I5,2I2, 2I3, 5E11.4)

ISTBA(J),ISTBB(J),	Identification numbers of isotope
M	Mixture number in which the self-shielding factors are to be applied to this isotope.
LL1, LL2	Energy groups.
(FACTR(LL), LL=LL1,LL2)	Input self-shielding factors for energy group LL1 to LL2.

These cards must end with a blank card.

19. (2I5,2E10.5)

MRXA	Region number in increasing order
NP	Number of space points in this region
TH	Thickness of this region.

	NINCH	equals zero except when NGEDM $\leq$ 0, and NRXA=1. Then if NINCH # 0, TH is assumed to be in inches.
30 (IDI5)	NRI	
	NRF	
	NXS	See item 30 of reference (19).
	MX LAST	
	NPCH	If #0, calculated microscopic cross-sections are punched out
	NSHDC	If #0, self-shielding factors are to be calculated, Card 31.7 must then be included in the input.
	NMHOM	Normally equals zero. Otherwise NMHOM is the mixture number assigned to the self-shielding factors calculated for the first homogeneous region specified on Card number 31.
	NPCHF	If #0, calculated shielding factors are to be punched out.
	NPCHM	Normally equals zero.

	NDIS	If #0, the first moment of the spectrum (equation 2.3.13) is to be calculated. Cards 31.5 and 31.6 must be included in the input if NDIS #0.
31.5 (13I5)	NDENM	Number of pairs of space points specifying the moderator region to be used in calculating the first moment of the spectrum.
	(NDEM1(I), NDEM2(I), I=1,NDENM)	Left space point for pair I. Right space point for pair I.
31.6 (13I5)	NDENF	Number of pairs of space points specifying the moderator region for the first moment of the spectrum calculation.
	(MDEN3(I), MDEN4(I), I=1,NDENF)	Left space point for pair I. Right space point for pair I.
31.7 (13I5)	NREGR	If #0, indicates another set of cards 31 and 31.7 follow.

NX1	Normally equals 0; otherwise indicates the left boundary of the boundary of the homogeneous region for which self-shielding factors are to be calculated.
MSHDR	Number of homogeneous regions specified on Card 31.
NAVFXM	Number of pairs of space points required to define the moderator region in equation 2.3.10.
(MAVFX1(L),	Left space point for pair L.
NAVFX2(L),	Right space point for pair L.
L=1,NAVFXM)	

If NREGR#0, another set of Cards 31 and 31.7 will be expected by THERMOS.

APPENDIX C

CALCULATED 3-GROUP FLUXES FOR MITR-II and MITR-I

Three-group fluxes calculated by using PDQ-7 (45) for MITR-II and MITR-I are given in sections C.1 and C.2 respectively of this appendix. The detailed core model used in the calculations as well as the dimensions and the materials corresponding to each of the regions in the calculational model are included.

C.1 CALCULATED 3-GROUP FLUXES FOR MITR-II

The 30-region calculational model used in the MITR-II core R-Z cylindrical calculations is shown in Fig. C.1. The materials corresponding to each of the 30 regions in Fig. C.1 are given in Table C.1.

Referring to Fig. C.1, region 22 is the outer absorber ring while region 9 is the inner fixed absorber ring. The active part of the core is represented by regions 1, 3, 4, 5, and 6; while the poisoned upper half is represented by regions 13 and 14. The light water in the bottom plenum is represented by region 20.

Pairs of numbers, each pair consisting of a radial point and the accumulated radius (centimeters) up to that point, are given below. A second set of pairs of numbers, each pair consisting of a point on the Z-axis and the accumulated distance

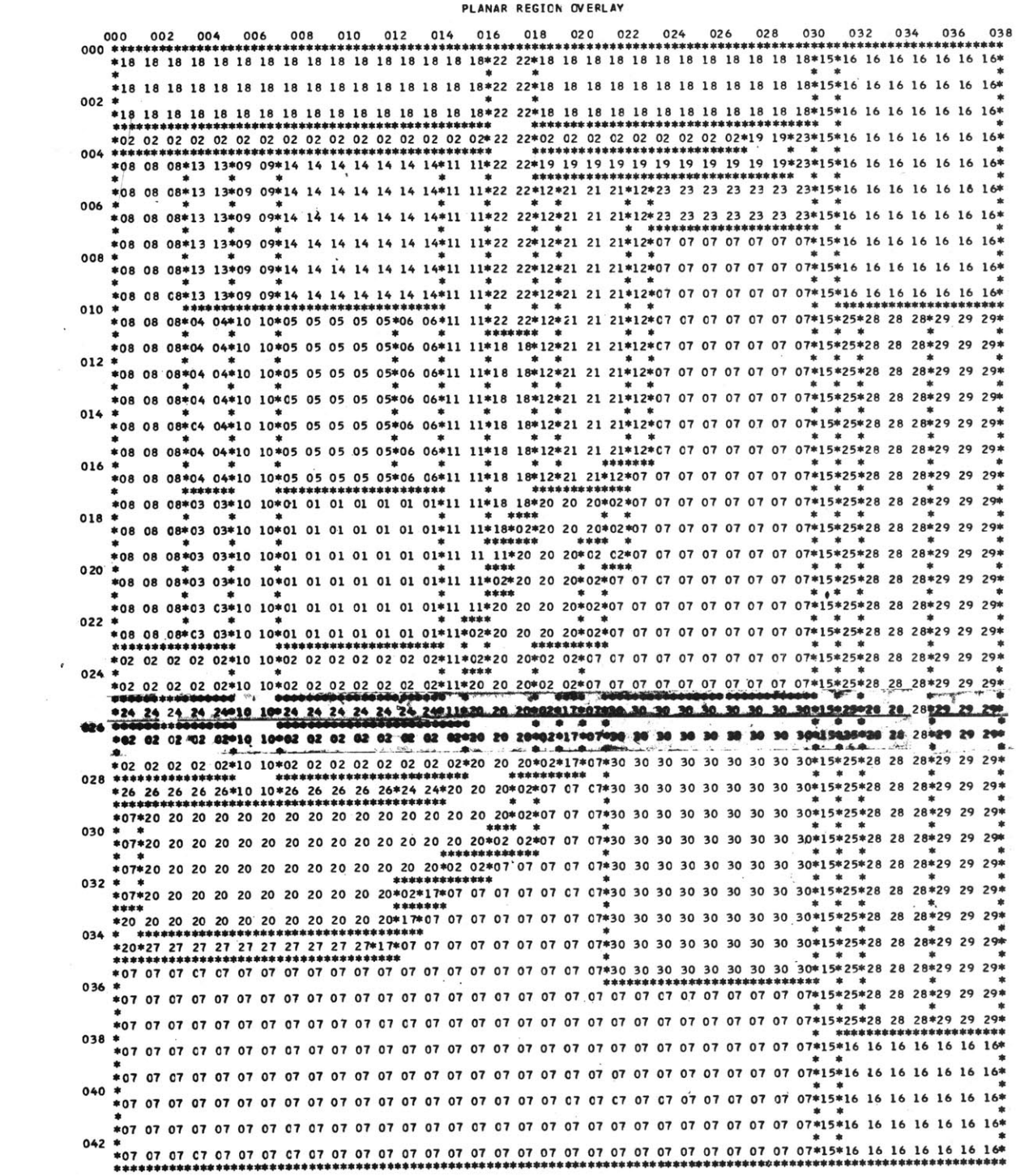

Fig. C.1 30-Region MITR-II R-Z Calculational Model

TABLE C.1

Materials Corresponding to each of the

30 Regions in the MITR-II Calculational Model

Region	Material
1	Core Composition
2	50% Al 50% H_2O
3, 4, 5, 6	Core Compositions
7	99.5% D_2O 0.5% H_2O
8	100% Lead
9	16% Cd 84% Al
10, 11, 12	100% Al
13, 14	Core Compositions
15	100% Al (Core Tank)
16	100% Graphite
17	50% D_2O 50 % Al
18	100% H_2O
19	94% H_2O 6% Al
20, 21	100% H_2O
22	16% Cd 84% Al
23	94% D_2O 6% Al
24	90% H_2O 10% Al
25	Helium
26	80% H_2O 20% Al
27	10% H_2O 90% Al
28	15.74% Void, 20% Al, 82.26% C^{12}
29	1.0% Al, 99% C^{12}
30	99.5% D_2O 0.5% H_2O

(cintimeters) from the core top up to that point, are given in the next paragraph. The calculated 3-group fluxes follow.

Accumulated Distance in the Radial Direction (cm)

1	1.0	2	2.0	3	3.51	4	4.772
5	6.034	6	6.367	7	6.701	8	9.585
9	9.585	10	11.03	11	12.47	12	14.65
13	16.84	14	19.02	15	19.97	16	20.91
17	21.23	18	21.55	19	22.02	20	22.71
21	23.40	22	24.09	23	24.72	24	27.26
25	33.61	26	39.96	27	46.31	28	52.66
29	59.01	30	61.55	31	62.19	32	64.73
33	68.54	34	76.16	35	77.04	36	92.28
37	107.5	38	122.8				

Accumulated Distance in the Z-Direction (cm)

1	10.16	2	20.32	3	30.48	4	40.64
5	45.72	6	50.80	7	55.88	8	60.96
9	66.04	10	71.12	11	74.69	12	78.26
13	81.83	14	85.40	15	88.97	16	92.54
17	96.11	18	97.80	19	98.84	20	99.88
21	100.4	22	101.0	23	101.5	24	102.1
25	102.8	26	103.4	27	104.1	28	104.7
29	105.3	30	106.0	31	106.6	32	107.2

33 107.9	34 108.5	35 109.1	36 111.7
37 114.2	38 119.3	39 129.5	40 144.7
41 159.9	42 162.0	43 164.0	

C.2 CALCULATED 3-GROUP FLUXES FOR MITR-I

The 18-region calculational model used to represent the details in each of the 11 axial planes in the 3-dimensional XYZ calculation of MITR-I is shown in Fig. C.2.

The materials corresponding to regions 1, 2, 3, 15, 16, 17, and 18 did not change from axial plane to plane, and are given in Table C.2. Regions 5, 6, 7, 11, 12, 13, and 14 were fuel element positions. The material distribution in the axial plane in these positions is as given in Fig. 10.4. Regions 8 and 9 were shim rod positions while region 10 was a regulating rod position.

The axial mesh spacing used in the calculations is identical to that given in Fig. 10.4. The mesh spacing in the XX and YY planes (Fig. 10.5) is given below. Two sets of pairs of numbers are given below. Each pair of the first set comprises a point on the XX axis and the accumulated distance (inches) up to that point, whereas each pair of the second set consists of a point on the YY axis and the accumulated distance up to that point. The calculated 3-group fluxes then follow.

POINTWISE FLUX - GROUP 1

	0	1	2	3	4	5	6	7	8	9
0	0.0	0.0	0.0	0.0	0.0	0.0	0.0	0.0	0.0	0.0
1	0.472D 11	0.471D 11	0.470D 11	0.465D 11	0.458D 11	0.450D 11	0.447D 11	0.444D 11	0.431D 11	0.415D 11
2	0.374D 12	0.374D 12	0.373D 12	0.369D 12	0.365D 12	0.359D 12	0.357D 12	0.355D 12	0.345D 12	0.333D 12
3	0.289D 13	0.289D 13	0.288D 13	0.287D 13	0.284D 13	0.281D 13	0.280D 13	0.279D 13	0.274D 13	0.266D 13
4	0.149D 14	0.149D 14	0.150D 14	0.151D 14	0.151D 14	0.150D 14	0.150D 14	0.150D 14	0.152D 14	0.152D 14
5	0.267D 14	0.267D 14	0.267D 14	0.266D 14	0.263D 14	0.259D 14	0.259D 14	0.260D 14	0.265D 14	0.265D 14
6	0.393D 14	0.393D 14	0.392D 14	0.390D 14	0.385D 14	0.380D 14	0.380D 14	0.381D 14	0.387D 14	0.387D 14
7	0.547D 14	0.546D 14	0.545D 14	0.542D 14	0.536D 14	0.529D 14	0.528D 14	0.529D 14	0.538D 14	0.538D 14
8	0.745D 14	0.744D 14	0.742D 14	0.737D 14	0.728D 14	0.718D 14	0.717D 14	0.718D 14	0.729D 14	0.728D 14
9	0.101D 15	0.101D 15	0.100D 15	0.996D 14	0.983D 14	0.967D 14	0.966D 14	0.966D 14	0.978D 14	0.973D 14
10	0.136D 15	0.136D 15	0.135D 15	0.135D 15	0.133D 15	0.131D 15	0.131D 15	0.131D 15	0.131D 15	0.129D 15
11	0.178D 15	0.178D 15	0.178D 15	0.179D 15	0.179D 15	0.176D 15	0.176D 15	0.176D 15	0.173D 15	0.168D 15
12	0.199D 15	0.199D 15	0.199D 15	0.201D 15	0.201D 15	0.198D 15	0.198D 15	0.197D 15	0.194D 15	0.188D 15
13	0.215D 15	0.215D 15	0.215D 15	0.217D 15	0.217D 15	0.214D 15	0.214D 15	0.213D 15	0.209D 15	0.203D 15
14	0.224D 15	0.224D 15	0.224D 15	0.226D 15	0.226D 15	0.224D 15	0.223D 15	0.222D 15	0.219D 15	0.212D 15
15	0.225D 15	0.225D 15	0.226D 15	0.228D 15	0.228D 15	0.225D 15	0.225D 15	0.224D 15	0.220D 15	0.214D 15
16	0.219D 15	0.219D 15	0.220D 15	0.222D 15	0.222D 15	0.220D 15	0.219D 15	0.219D 15	0.215D 15	0.208D 15
17	0.202D 15	0.203D 15	0.204D 15	0.207D 15	0.208D 15	0.206D 15	0.205D 15	0.205D 15	0.201D 15	0.195D 15
18	0.187D 15	0.187D 15	0.189D 15	0.193D 15	0.195D 15	0.193D 15	0.192D 15	0.192D 15	0.188D 15	0.182D 15
19	0.175D 15	0.175D 15	0.177D 15	0.182D 15	0.184D 15	0.182D 15	0.182D 15	0.181D 15	0.178D 15	0.172D 15
20	0.160D 15	0.160D 15	0.162D 15	0.167D 15	0.170D 15	0.168D 15	0.168D 15	0.168D 15	0.165D 15	0.159D 15
21	0.151D 15	0.152D 15	0.153D 15	0.158D 15	0.161D 15	0.160D 15	0.159D 15	0.159D 15	0.156D 15	0.151D 15
22	0.142D 15	0.142D 15	0.144D 15	0.148D 15	0.151D 15	0.149D 15	0.149D 15	0.149D 15	0.146D 15	0.141D 15
23	0.132D 15	0.132D 15	0.133D 15	0.137D 15	0.139D 15	0.138D 15	0.137D 15	0.137D 15	0.134D 15	0.130D 15
24	0.120D 15	0.120D 15	0.121D 15	0.123D 15	0.125D 15	0.124D 15	0.124D 15	0.123D 15	0.120D 15	0.116D 15
25	0.109D 15	0.109D 15	0.110D 15	0.111D 15	0.112D 15	0.112D 15	0.111D 15	0.111D 15	0.108D 15	0.104D 15
26	0.958D 14	0.960D 14	0.963D 14	0.972D 14	0.978D 14	0.984D 14	0.985D 14	0.978D 14	0.938D 14	0.900D 14
27	0.868D 14	0.869D 14	0.871D 14	0.877D 14	0.881D 14	0.885D 14	0.883D 14	0.879D 14	0.842D 14	0.807D 14
28	0.785D 14	0.785D 14	0.785D 14	0.789D 14	0.792D 14	0.794D 14	0.792D 14	0.789D 14	0.755D 14	0.723D 14
29	0.696D 14	0.693D 14	0.692D 14	0.693D 14	0.696D 14	0.705D 14	0.707D 14	0.699D 14	0.661D 14	0.632D 14
30	0.613D 14	0.609D 14	0.605D 14	0.604D 14	0.605D 14	0.607D 14	0.604D 14	0.601D 14	0.574D 14	0.549D 14
31	0.540D 14	0.536D 14	0.531D 14	0.530D 14	0.529D 14	0.526D 14	0.524D 14	0.521D 14	0.500D 14	0.479D 14
32	0.478D 14	0.474D 14	0.470D 14	0.467D 14	0.465D 14	0.461D 14	0.458D 14	0.456D 14	0.440D 14	0.422D 14
33	0.425D 14	0.422D 14	0.419D 14	0.416D 14	0.413D 14	0.408D 14	0.406D 14	0.404D 14	0.391D 14	0.375D 14
34	0.383D 14	0.380D 14	0.378D 14	0.376D 14	0.372D 14	0.367D 14	0.365D 14	0.363D 14	0.352D 14	0.339D 14
35	0.355D 14	0.357D 14	0.358D 14	0.355D 14	0.352D 14	0.346D 14	0.344D 14	0.342D 14	0.332D 14	0.320D 14
36	0.247D 14	0.247D 14	0.246D 14	0.244D 14	0.241D 14	0.237D 14	0.236D 14	0.235D 14	0.228D 14	0.220D 14
37	0.168D 14	0.168D 14	0.167D 14	0.166D 14	0.164D 14	0.161D 14	0.160D 14	0.159D 14	0.155D 14	0.149D 14
38	0.770D 13	0.769D 13	0.766D 13	0.759D 13	0.749D 13	0.736D 13	0.733D 13	0.729D 13	0.709D 13	0.686D 13
39	0.183D 13	0.183D 13	0.183D 13	0.181D 13	0.179D 13	0.176D 13	0.175D 13	0.174D 13	0.170D 13	0.165D 13
40	0.282D 12	0.282D 12	0.281D 12	0.279D 12	0.276D 12	0.272D 12	0.271D 12	0.270D 12	0.264D 12	0.257D 12
41	0.377D 11	0.377D 11	0.376D 11	0.373D 11	0.369D 11	0.364D 11	0.363D 11	0.361D 11	0.354D 11	0.345D 11
42	0.181D 11	0.181D 11	0.180D 11	0.179D 11	0.177D 11	0.175D 11	0.174D 11	0.174D 11	0.170D 11	0.166D 11

POINTWISE FLUX - GROUP 1

	10	11	12	13	14	15	16	17	18	19
0	0.0	0.0	0.0	0.0	0.0	0.0	0.0	0.0	0.0	0.0
1	0.396D 11	0.375D 11	0.340D 11	0.302D 11	0.263D 11	0.248D 11	0.232D 11	0.229D 11	0.224D 11	0.214D 11
2	0.318D 12	0.300D 12	0.269D 12	0.234D 12	0.199D 12	0.185D 12	0.171D 12	0.168D 12	0.164D 12	0.155D 12
3	0.255D 13	0.241D 13	0.213D 13	0.181D 13	0.148D 13	0.134D 13	0.121D 13	0.117D 13	0.114D 13	0.107D 13
4	0.148D 14	0.141D 14	0.124D 14	0.102D 14	0.767D 13	0.680D 13	0.595D 13	0.568D 13	0.541D 13	0.494D 13
5	0.259D 14	0.247D 14	0.217D 14	0.177D 14	0.132D 14	0.119D 14	0.107D 14	0.102D 14	0.973D 13	0.904D 13
6	0.378D 14	0.360D 14	0.317D 14	0.260D 14	0.196D 14	0.178D 14	0.161D 14	0.154D 14	0.147D 14	0.140D 14
7	0.525D 14	0.500D 14	0.440D 14	0.361D 14	0.273D 14	0.248D 14	0.224D 14	0.215D 14	0.206D 14	0.196D 14
8	0.710D 14	0.675D 14	0.593D 14	0.486D 14	0.367D 14	0.334D 14	0.302D 14	0.289D 14	0.277D 14	0.263D 14
9	0.946D 14	0.897D 14	0.786D 14	0.642D 14	0.483D 14	0.439D 14	0.396D 14	0.380D 14	0.364D 14	0.345D 14
10	0.125D 15	0.118D 15	0.103D 15	0.839D 14	0.624D 14	0.567D 14	0.511D 14	0.489D 14	0.468D 14	0.444D 14
11	0.160D 15	0.151D 15	0.133D 15	0.109D 15	0.806D 14	0.728D 14	0.653D 14	0.619D 14	0.588D 14	0.558D 14
12	0.180D 15	0.169D 15	0.150D 15	0.125D 15	0.944D 14	0.847D 14	0.757D 14	0.707D 14	0.662D 14	0.627D 14
13	0.194D 15	0.184D 15	0.164D 15	0.139D 15	0.106D 15	0.948D 14	0.844D 14	0.786D 14	0.734D 14	0.694D 14
14	0.203D 15	0.193D 15	0.173D 15	0.147D 15	0.114D 15	0.102D 15	0.903D 14	0.841D 14	0.784D 14	0.741D 14
15	0.205D 15	0.195D 15	0.176D 15	0.151D 15	0.117D 15	0.104D 15	0.928D 14	0.864D 14	0.805D 14	0.761D 14
16	0.200D 15	0.190D 15	0.172D 15	0.148D 15	0.116D 15	0.103D 15	0.914D 14	0.849D 14	0.791D 14	0.747D 14
17	0.187D 15	0.177D 15	0.160D 15	0.139D 15	0.109D 15	0.965D 14	0.855D 14	0.795D 14	0.740D 14	0.691D 14
18	0.175D 15	0.166D 15	0.150D 15	0.130D 15	0.102D 15	0.902D 14	0.798D 14	0.743D 14	0.697D 14	0.627D 14
19	0.165D 15	0.156D 15	0.141D 15	0.123D 15	0.964D 14	0.850D 14	0.748D 14	0.708D 14	0.662D 14	0.592D 14
20	0.152D 15	0.145D 15	0.131D 15	0.114D 15	0.895D 14	0.788D 14	0.695D 14	0.662D 14	0.612D 14	0.549D 14
21	0.145D 15	0.137D 15	0.124D 15	0.108D 15	0.851D 14	0.752D 14	0.664D 14	0.623D 14	0.579D 14	0.522D 14
22	0.135D 15	0.128D 15	0.116D 15	0.101D 15	0.799D 14	0.714D 14	0.626D 14	0.582D 14	0.543D 14	0.493D 14
23	0.124D 15	0.118D 15	0.106D 15	0.923D 14	0.737D 14	0.666D 14	0.577D 14	0.539D 14	0.503D 14	0.463D 14
24	0.111D 15	0.105D 15	0.948D 14	0.824D 14	0.665D 14	0.610D 14	0.525D 14	0.493D 14	0.463D 14	0.433D 14
25	0.992D 14	0.940D 14	0.847D 14	0.736D 14	0.600D 14	0.552D 14	0.472D 14	0.447D 14	0.425D 14	0.401D 14
26	0.859D 14	0.813D 14	0.733D 14	0.638D 14	0.536D 14	0.498D 14	0.427D 14	0.407D 14	0.389D 14	0.369D 14
27	0.770D 14	0.728D 14	0.657D 14	0.573D 14	0.482D 14	0.441D 14	0.385D 14	0.369D 14	0.355D 14	0.340D 14
28	0.689D 14	0.651D 14	0.588D 14	0.514D 14	0.433D 14	0.393D 14	0.347D 14	0.336D 14	0.326D 14	0.313D 14
29	0.602D 14	0.570D 14	0.513D 14	0.448D 14	0.379D 14	0.346D 14	0.313D 14	0.304D 14	0.298D 14	0.285D 14
30	0.523D 14	0.495D 14	0.447D 14	0.393D 14	0.335D 14	0.309D 14	0.283D 14	0.277D 14	0.271D 14	0.260D 14
31	0.457D 14	0.433D 14	0.392D 14	0.348D 14	0.299D 14	0.278D 14	0.260D 14	0.255D 14	0.249D 14	0.238D 14
32	0.403D 14	0.383D 14	0.348D 14	0.313D 14	0.274D 14	0.259D 14	0.241D 14	0.234D 14	0.228D 14	0.218D 14
33	0.359D 14	0.343D 14	0.317D 14	0.290D 14	0.255D 14	0.237D 14	0.220D 14	0.214D 14	0.208D 14	0.200D 14
34	0.324D 14	0.311D 14	0.292D 14	0.267D 14	0.232D 14	0.216D 14	0.201D 14	0.196D 14	0.191D 14	0.183D 14
35	0.307D 14	0.292D 14	0.269D 14	0.243D 14	0.211D 14	0.197D 14	0.183D 14	0.179D 14	0.174D 14	0.167D 14
36	0.211D 14	0.201D 14	0.185D 14	0.167D 14	0.146D 14	0.137D 14	0.128D 14	0.125D 14	0.122D 14	0.118D 14
37	0.144D 14	0.137D 14	0.126D 14	0.114D 14	0.101D 14	0.948D 13	0.890D 13	0.870D 13	0.851D 13	0.822D 13
38	0.660D 13	0.632D 13	0.583D 13	0.531D 13	0.475D 13	0.451D 13	0.426D 13	0.418D 13	0.410D 13	0.398D 13
39	0.159D 13	0.153D 13	0.143D 13	0.131D 13	0.119D 13	0.114D 13	0.109D 13	0.107D 13	0.105D 13	0.103D 13
40	0.249D 12	0.241D 12	0.226D 12	0.211D 12	0.194D 12	0.187D 12	0.180D 12	0.177D 12	0.175D 12	0.171D 12
41	0.335D 11	0.325D 11	0.307D 11	0.287D 11	0.266D 11	0.257D 11	0.248D 11	0.244D 11	0.241D 11	0.236D 11
42	0.161D 11	0.156D 11	0.148D 11	0.138D 11	0.128D 11	0.124D 11	0.119D 11	0.118D 11	0.116D 11	0.114D 11

POINTWISE FLUX - GROUP 1

	20	21	22	23	24	25	26	27	28	29
0	0.0	0.0	0.0	0.0	0.0	0.0	0.0	0.0	0.0	0.0
1	0.200D 11	0.186D 11	0.173D 11	0.162D 11	0.121D 11	0.557D 10	0.241D 10	0.990D 09	0.418D 09	0.282D 09
2	0.144D 12	0.132D 12	0.122D 12	0.113D 12	0.813D 11	0.349D 11	0.143D 11	0.550D 10	0.209D 10	0.127D 10
3	0.980D 12	0.893D 12	0.811D 12	0.741D 12	0.508D 12	0.202D 12	0.795D 11	0.281D 11	0.905D 10	0.535D 10
4	0.434D 13	0.380D 13	0.334D 13	0.295D 13	0.183D 13	0.670D 12	0.259D 12	0.982D 11	0.364D 11	0.224D 11
5	0.771D 13	0.665D 13	0.580D 13	0.535D 13	0.340D 13	0.133D 13	0.550D 12	0.232D 12	0.102D 12	0.552D 11
6	0.121D 14	0.105D 14	0.939D 13	0.893D 13	0.618D 13	0.262D 13	0.112D 13	0.488D 12	0.217D 12	0.108D 12
7	0.169D 14	0.148D 14	0.133D 14	0.127D 14	0.883D 13	0.380D 13	0.165D 13	0.717D 12	0.319D 12	0.155D 12
8	0.228D 14	0.200D 14	0.179D 14	0.170D 14	0.118D 14	0.506D 13	0.218D 13	0.946D 12	0.419D 12	0.202D 12
9	0.298D 14	0.261D 14	0.233D 14	0.222D 14	0.154D 14	0.649D 13	0.277D 13	0.119D 13	0.519D 12	0.247D 12
10	0.383D 14	0.335D 14	0.298D 14	0.284D 14	0.194D 14	0.806D 13	0.338D 13	0.143D 13	0.616D 12	0.287D 12
11	0.479D 14	0.417D 14	0.370D 14	0.351D 14	0.237D 14	0.964D 13	0.396D 13	0.165D 13	0.699D 12	0.318D 12
12	0.537D 14	0.467D 14	0.413D 14	0.392D 14	0.262D 14	0.105D 14	0.426D 13	0.175D 13	0.738D 12	0.332D 12
13	0.592D 14	0.513D 14	0.451D 14	0.428D 14	0.284D 14	0.112D 14	0.449D 13	0.183D 13	0.765D 12	0.341D 12
14	0.631D 14	0.545D 14	0.479D 14	0.453D 14	0.298D 14	0.116D 14	0.461D 13	0.187D 13	0.775D 12	0.344D 12
15	0.648D 14	0.559D 14	0.491D 14	0.465D 14	0.304D 14	0.117D 14	0.460D 13	0.186D 13	0.769D 12	0.340D 12
16	0.635D 14	0.547D 14	0.500D 14	0.462D 14	0.297D 14	0.113D 14	0.445D 13	0.179D 13	0.743D 12	0.330D 12
17	0.590D 14	0.513D 14	0.476D 14	0.426D 14	0.274D 14	0.105D 14	0.414D 13	0.168D 13	0.700D 12	0.313D 12
18	0.543D 14	0.478D 14	0.437D 14	0.393D 14	0.256D 14	0.987D 13	0.393D 13	0.160D 13	0.670D 12	0.301D 12
19	0.510D 14	0.454D 14	0.414D 14	0.371D 14	0.243D 14	0.944D 13	0.378D 13	0.155D 13	0.650D 12	0.293D 12
20	0.476D 14	0.431D 14	0.389D 14	0.348D 14	0.228D 14	0.898D 13	0.362D 13	0.149D 13	0.629D 12	0.285D 12
21	0.456D 14	0.415D 14	0.372D 14	0.335D 14	0.221D 14	0.872D 13	0.353D 13	0.146D 13	0.617D 12	0.281D 12
22	0.436D 14	0.398D 14	0.356D 14	0.321D 14	0.213D 14	0.847D 13	0.344D 13	0.143D 13	0.605D 12	0.276D 12
23	0.418D 14	0.380D 14	0.340D 14	0.307D 14	0.205D 14	0.821D 13	0.335D 13	0.139D 13	0.593D 12	0.271D 12
24	0.395D 14	0.356D 14	0.320D 14	0.290D 14	0.195D 14	0.789D 13	0.325D 13	0.135D 13	0.579D 12	0.266D 12
25	0.369D 14	0.333D 14	0.300D 14	0.273D 14	0.185D 14	0.758D 13	0.314D 13	0.132D 13	0.564D 12	0.260D 12
26	0.343D 14	0.311D 14	0.281D 14	0.256D 14	0.176D 14	0.726D 13	0.303D 13	0.128D 13	0.549D 12	0.254D 12
27	0.317D 14	0.288D 14	0.262D 14	0.239D 14	0.166D 14	0.695D 13	0.292D 13	0.124D 13	0.534D 12	0.248D 12
28	0.292D 14	0.267D 14	0.243D 14	0.223D 14	0.156D 14	0.663D 13	0.281D 13	0.119D 13	0.519D 12	0.242D 12
29	0.266D 14	0.245D 14	0.225D 14	0.207D 14	0.147D 14	0.632D 13	0.270D 13	0.115D 13	0.503D 12	0.236D 12
30	0.243D 14	0.225D 14	0.208D 14	0.192D 14	0.138D 14	0.601D 13	0.258D 13	0.111D 13	0.488D 12	0.230D 12
31	0.223D 14	0.207D 14	0.192D 14	0.178D 14	0.129D 14	0.570D 13	0.248D 13	0.107D 13	0.472D 12	0.224D 12
32	0.204D 14	0.190D 14	0.177D 14	0.165D 14	0.121D 14	0.541D 13	0.237D 13	0.103D 13	0.457D 12	0.218D 12
33	0.187D 14	0.175D 14	0.163D 14	0.152D 14	0.113D 14	0.512D 13	0.226D 13	0.993D 12	0.442D 12	0.212D 12
34	0.172D 14	0.161D 14	0.150D 14	0.140D 14	0.105D 14	0.483D 13	0.216D 13	0.953D 12	0.426D 12	0.206D 12
35	0.157D 14	0.148D 14	0.138D 14	0.129D 14	0.978D 13	0.456D 13	0.205D 13	0.914D 12	0.411D 12	0.199D 12
36	0.111D 14	0.105D 14	0.989D 13	0.933D 13	0.725D 13	0.356D 13	0.167D 13	0.764D 12	0.352D 12	0.175D 12
37	0.781D 13	0.740D 13	0.700D 13	0.664D 13	0.528D 13	0.273D 13	0.133D 13	0.627D 12	0.297D 12	0.153D 12
38	0.380D 13	0.363D 13	0.346D 13	0.331D 13	0.272D 13	0.153D 13	0.801D 12	0.403D 12	0.202D 12	0.113D 12
39	0.991D 12	0.953D 12	0.916D 12	0.882D 12	0.750D 12	0.465D 12	0.269D 12	0.149D 12	0.821D 11	0.490D 11
40	0.166D 12	0.160D 12	0.155D 12	0.150D 12	0.131D 12	0.878D 11	0.552D 11	0.333D 11	0.200D 11	0.128D 11
41	0.230D 11	0.223D 11	0.216D 11	0.210D 11	0.185D 11	0.128D 11	0.830D 10	0.519D 10	0.322D 10	0.213D 10
42	0.111D 11	0.108D 11	0.104D 11	0.101D 11	0.894D 10	0.619D 10	0.404D 10	0.253D 10	0.157D 10	0.104D 10

POINTWISE FLUX - GROUP 1

	30	31	32	33	34	35	36	37	38
0	0.0	0.0	0.0	0.0	0.0	0.0	0.0	0.0	0.0
1	0.318D 09	0.324D 09	0.364D 09	0.384D 09	0.324D 09	0.316D 09	0.131D 09	0.402D 08	0.0
2	0.136D 10	0.138D 10	0.147D 10	0.144D 10	0.108D 10	0.103D 10	0.377D 09	0.108D 09	0.0
3	0.563D 10	0.566D 10	0.554D 10	0.490D 10	0.311D 10	0.293D 10	0.915D 09	0.238D 09	0.0
4	0.226D 11	0.225D 11	0.199D 11	0.155D 11	0.816D 10	0.750D 10	0.200D 10	0.474D 09	0.0
5	0.480D 11	0.472D 11	0.379D 11	0.266D 11	0.126D 11	0.114D 11	0.282D 10	0.643D 09	0.0
6	0.846D 11	0.824D 11	0.624D 11	0.412D 11	0.183D 11	0.164D 11	0.384D 10	0.847D 09	0.0
7	0.121D 12	0.118D 12	0.882D 11	0.575D 11	0.249D 11	0.222D 11	0.503D 10	0.108D 10	0.0
8	0.156D 12	0.152D 12	0.115D 12	0.752D 11	0.323D 11	0.287D 11	0.637D 10	0.135D 10	0.0
9	0.192D 12	0.187D 12	0.145D 12	0.957D 11	0.408D 11	0.362D 11	0.786D 10	0.163D 10	0.0
10	0.219D 12	0.213D 12	0.192D 12	0.121D 12	0.505D 11	0.446D 11	0.944D 10	0.194D 10	0.0
11	0.236D 12	0.228D 12	0.213D 12	0.137D 12	0.578D 11	0.512D 11	0.107D 11	0.219D 10	0.0
12	0.244D 12	0.236D 12	0.221D 12	0.143D 12	0.607D 11	0.539D 11	0.113D 11	0.231D 10	0.0
13	0.250D 12	0.241D 12	0.225D 12	0.147D 12	0.625D 11	0.555D 11	0.117D 11	0.239D 10	0.0
14	0.251D 12	0.243D 12	0.226D 12	0.148D 12	0.631D 11	0.561D 11	0.119D 11	0.243D 10	0.0
15	0.248D 12	0.240D 12	0.224D 12	0.146D 12	0.627D 11	0.558D 11	0.118D 11	0.243D 10	0.0
16	0.241D 12	0.233D 12	0.217D 12	0.142D 12	0.613D 11	0.545D 11	0.116D 11	0.240D 10	0.0
17	0.230D 12	0.222D 12	0.207D 12	0.136D 12	0.590D 11	0.525D 11	0.113D 11	0.234D 10	0.0
18	0.222D 12	0.215D 12	0.201D 12	0.132D 12	0.574D 11	0.512D 11	0.110D 11	0.230D 10	0.0
19	0.217D 12	0.210D 12	0.196D 12	0.129D 12	0.563D 11	0.502D 11	0.109D 11	0.227D 10	0.0
20	0.211D 12	0.205D 12	0.192D 12	0.126D 12	0.552D 11	0.492D 11	0.107D 11	0.223D 10	0.0
21	0.208D 12	0.202D 12	0.189D 12	0.125D 12	0.546D 11	0.487D 11	0.106D 11	0.221D 10	0.0
22	0.205D 12	0.199D 12	0.186D 12	0.123D 12	0.539D 11	0.481D 11	0.105D 11	0.219D 10	0.0
23	0.202D 12	0.196D 12	0.184D 12	0.121D 12	0.532D 11	0.475D 11	0.104D 11	0.217D 10	0.0
24	0.199D 12	0.192D 12	0.180D 12	0.119D 12	0.525D 11	0.468D 11	0.102D 11	0.215D 10	0.0
25	0.195D 12	0.189D 12	0.177D 12	0.117D 12	0.516D 11	0.461D 11	0.101D 11	0.212D 10	0.0
26	0.191D 12	0.185D 12	0.174D 12	0.115D 12	0.508D 11	0.454D 11	0.995D 10	0.209D 10	0.0
27	0.187D 12	0.181D 12	0.170D 12	0.113D 12	0.500D 11	0.447D 11	0.981D 10	0.207D 10	0.0
28	0.183D 12	0.178D 12	0.167D 12	0.111D 12	0.491D 11	0.439D 11	0.966D 10	0.204D 10	0.0
29	0.179D 12	0.174D 12	0.163D 12	0.109D 12	0.482D 11	0.431D 11	0.951D 10	0.201D 10	0.0
30	0.175D 12	0.170D 12	0.160D 12	0.107D 12	0.473D 11	0.423D 11	0.935D 10	0.198D 10	0.0
31	0.171D 12	0.166D 12	0.156D 12	0.104D 12	0.464D 11	0.415D 11	0.920D 10	0.195D 10	0.0
32	0.167D 12	0.162D 12	0.153D 12	0.102D 12	0.455D 11	0.407D 11	0.903D 10	0.192D 10	0.0
33	0.163D 12	0.158D 12	0.149D 12	0.998D 11	0.446D 11	0.399D 11	0.887D 10	0.189D 10	0.0
34	0.159D 12	0.154D 12	0.145D 12	0.976D 11	0.436D 11	0.391D 11	0.870D 10	0.185D 10	0.0
35	0.154D 12	0.150D 12	0.142D 12	0.953D 11	0.427D 11	0.382D 11	0.854D 10	0.182D 10	0.0
36	0.138D 12	0.135D 12	0.127D 12	0.860D 11	0.388D 11	0.348D 11	0.784D 10	0.168D 10	0.0
37	0.123D 12	0.120D 12	0.114D 12	0.769D 11	0.348D 11	0.312D 11	0.711D 10	0.154D 10	0.0
38	0.964D 11	0.952D 11	0.874D 11	0.588D 11	0.268D 11	0.240D 11	0.563D 10	0.124D 10	0.0
39	0.419D 11	0.412D 11	0.341D 11	0.250D 11	0.126D 11	0.115D 11	0.300D 10	0.706D 09	0.0
40	0.112D 11	0.110D 11	0.923D 10	0.696D 10	0.379D 10	0.351D 10	0.102D 10	0.260D 09	0.0
41	0.188D 10	0.185D 10	0.156D 10	0.119D 10	0.665D 09	0.617D 09	0.186D 09	0.485D 08	0.0
42	0.921D 09	0.909D 09	0.766D 09	0.585D 09	0.328D 09	0.304D 09	0.919D 08	0.240D 08	0.0

POINTWISE FLUX - GROUP 2

	0	1	2	3	4	5	6	7	8	9
0	0.0	0.0	0.0	0.0	0.0	0.0	0.0	0.0	0.0	0.0
1	0.269D 11	0.269D 11	0.268D 11	0.265D 11	0.261D 11	0.256D 11	0.255D 11	0.253D 11	0.246D 11	0.236D 11
2	0.216D 12	0.216D 12	0.215D 12	0.213D 12	0.210D 12	0.207D 12	0.206D 12	0.205D 12	0.199D 12	0.192D 12
3	0.177D 13	0.177D 13	0.176D 13	0.175D 13	0.173D 13	0.171D 13	0.170D 13	0.169D 13	0.165D 13	0.160D 13
4	0.769D 13	0.768D 13	0.765D 13	0.756D 13	0.744D 13	0.731D 13	0.729D 13	0.728D 13	0.727D 13	0.715D 13
5	0.109D 14	0.109D 14	0.109D 14	0.108D 14	0.105D 14	0.101D 14	0.100D 14	0.101D 14	0.105D 14	0.105D 14
6	0.155D 14	0.155D 14	0.154D 14	0.153D 14	0.150D 14	0.144D 14	0.143D 14	0.144D 14	0.150D 14	0.151D 14
7	0.214D 14	0.214D 14	0.214D 14	0.213D 14	0.208D 14	0.199D 14	0.199D 14	0.199D 14	0.208D 14	0.210D 14
8	0.292D 14	0.292D 14	0.292D 14	0.290D 14	0.284D 14	0.271D 14	0.270D 14	0.271D 14	0.282D 14	0.284D 14
9	0.398D 14	0.397D 14	0.397D 14	0.394D 14	0.386D 14	0.368D 14	0.367D 14	0.368D 14	0.381D 14	0.381D 14
10	0.540D 14	0.540D 14	0.540D 14	0.540D 14	0.534D 14	0.521D 14	0.520D 14	0.520D 14	0.519D 14	0.508D 14
11	0.692D 14	0.693D 14	0.694D 14	0.698D 14	0.697D 14	0.685D 14	0.685D 14	0.684D 14	0.672D 14	0.650D 14
12	0.769D 14	0.770D 14	0.772D 14	0.778D 14	0.777D 14	0.764D 14	0.763D 14	0.763D 14	0.749D 14	0.725D 14
13	0.826D 14	0.826D 14	0.829D 14	0.835D 14	0.835D 14	0.822D 14	0.821D 14	0.820D 14	0.806D 14	0.781D 14
14	0.857D 14	0.857D 14	0.860D 14	0.868D 14	0.868D 14	0.854D 14	0.853D 14	0.853D 14	0.839D 14	0.814D 14
15	0.859D 14	0.860D 14	0.862D 14	0.870D 14	0.871D 14	0.857D 14	0.857D 14	0.856D 14	0.843D 14	0.819D 14
16	0.829D 14	0.830D 14	0.833D 14	0.841D 14	0.842D 14	0.829D 14	0.828D 14	0.827D 14	0.816D 14	0.793D 14
17	0.767D 14	0.767D 14	0.770D 14	0.777D 14	0.778D 14	0.765D 14	0.764D 14	0.764D 14	0.752D 14	0.731D 14
18	0.722D 14	0.723D 14	0.725D 14	0.729D 14	0.729D 14	0.717D 14	0.716D 14	0.716D 14	0.704D 14	0.682D 14
19	0.693D 14	0.693D 14	0.694D 14	0.697D 14	0.696D 14	0.684D 14	0.684D 14	0.683D 14	0.670D 14	0.650D 14
20	0.662D 14	0.662D 14	0.662D 14	0.663D 14	0.661D 14	0.650D 14	0.649D 14	0.649D 14	0.635D 14	0.615D 14
21	0.646D 14	0.646D 14	0.646D 14	0.645D 14	0.642D 14	0.631D 14	0.631D 14	0.630D 14	0.617D 14	0.597D 14
22	0.630D 14	0.630D 14	0.630D 14	0.628D 14	0.623D 14	0.613D 14	0.612D 14	0.612D 14	0.599D 14	0.579D 14
23	0.614D 14	0.614D 14	0.614D 14	0.611D 14	0.606D 14	0.595D 14	0.594D 14	0.594D 14	0.582D 14	0.562D 14
24	0.592D 14	0.592D 14	0.592D 14	0.590D 14	0.585D 14	0.573D 14	0.572D 14	0.572D 14	0.561D 14	0.542D 14
25	0.568D 14	0.568D 14	0.568D 14	0.567D 14	0.563D 14	0.550D 14	0.549D 14	0.549D 14	0.539D 14	0.520D 14
26	0.522D 14	0.523D 14	0.524D 14	0.524D 14	0.523D 14	0.522D 14	0.522D 14	0.521D 14	0.499D 14	0.478D 14
27	0.492D 14	0.493D 14	0.494D 14	0.496D 14	0.497D 14	0.498D 14	0.498D 14	0.497D 14	0.472D 14	0.450D 14
28	0.461D 14	0.463D 14	0.466D 14	0.468D 14	0.471D 14	0.476D 14	0.476D 14	0.475D 14	0.446D 14	0.424D 14
29	0.411D 14	0.416D 14	0.424D 14	0.426D 14	0.431D 14	0.453D 14	0.455D 14	0.451D 14	0.407D 14	0.385D 14
30	0.380D 14	0.379D 14	0.378D 14	0.378D 14	0.381D 14	0.390D 14	0.389D 14	0.386D 14	0.359D 14	0.341D 14
31	0.347D 14	0.344D 14	0.337D 14	0.336D 14	0.337D 14	0.339D 14	0.337D 14	0.335D 14	0.318D 14	0.302D 14
32	0.317D 14	0.313D 14	0.303D 14	0.299D 14	0.299D 14	0.297D 14	0.296D 14	0.294D 14	0.282D 14	0.270D 14
33	0.294D 14	0.285D 14	0.273D 14	0.269D 14	0.267D 14	0.264D 14	0.263D 14	0.261D 14	0.252D 14	0.243D 14
34	0.259D 14	0.251D 14	0.247D 14	0.244D 14	0.242D 14	0.238D 14	0.237D 14	0.236D 14	0.229D 14	0.222D 14
35	0.243D 14	0.243D 14	0.243D 14	0.240D 14	0.237D 14	0.234D 14	0.232D 14	0.231D 14	0.225D 14	0.218D 14
36	0.207D 14	0.207D 14	0.206D 14	0.204D 14	0.202D 14	0.199D 14	0.198D 14	0.197D 14	0.192D 14	0.187D 14
37	0.170D 14	0.170D 14	0.169D 14	0.167D 14	0.166D 14	0.163D 14	0.162D 14	0.162D 14	0.158D 14	0.154D 14
38	0.104D 14	0.104D 14	0.104D 14	0.103D 14	0.102D 14	0.101D 14	0.100D 14	0.997D 13	0.975D 13	0.949D 13
39	0.349D 13	0.349D 13	0.348D 13	0.345D 13	0.342D 13	0.337D 13	0.336D 13	0.334D 13	0.328D 13	0.320D 13
40	0.705D 12	0.705D 12	0.703D 12	0.698D 12	0.692D 12	0.683D 12	0.681D 12	0.678D 12	0.666D 12	0.651D 12
41	0.105D 12	0.105D 12	0.105D 12	0.104D 12	0.103D 12	0.102D 12	0.102D 12	0.101D 12	0.997D 11	0.976D 11
42	0.512D 11	0.511D 11	0.510D 11	0.507D 11	0.502D 11	0.497D 11	0.495D 11	0.493D 11	0.484D 11	0.474D 11

POINTWISE FLUX - GROUP 2

	10	11	12	13	14	15	16	17	18	19
0	0.0	0.0	0.0	0.0	0.0	0.0	0.0	0.0	0.0	0.0
1	0.226D 11	0.214D 11	0.193D 11	0.171D 11	0.148D 11	0.138D 11	0.127D 11	0.127D 11	0.126D 11	0.121D 11
2	0.183D 12	0.173D 12	0.155D 12	0.134D 12	0.113D 12	0.104D 12	0.948D 11	0.941D 11	0.935D 11	0.889D 11
3	0.153D 13	0.144D 13	0.128D 13	0.109D 13	0.889D 12	0.797D 12	0.702D 12	0.693D 12	0.687D 12	0.655D 12
4	0.691D 13	0.656D 13	0.583D 13	0.493D 13	0.397D 13	0.376D 13	0.349D 13	0.341D 13	0.335D 13	0.311D 13
5	0.103D 14	0.984D 13	0.876D 13	0.738D 13	0.589D 13	0.575D 13	0.560D 13	0.553D 13	0.549D 13	0.543D 13
6	0.148D 14	0.142D 14	0.126D 14	0.106D 14	0.846D 13	0.826D 13	0.805D 13	0.795D 13	0.789D 13	0.785D 13
7	0.205D 14	0.196D 14	0.175D 14	0.147D 14	0.117D 14	0.114D 14	0.111D 14	0.110D 14	0.109D 14	0.109D 14
8	0.278D 14	0.265D 14	0.235D 14	0.197D 14	0.156D 14	0.153D 14	0.149D 14	0.147D 14	0.146D 14	0.145D 14
9	0.370D 14	0.352D 14	0.311D 14	0.260D 14	0.204D 14	0.199D 14	0.194D 14	0.192D 14	0.190D 14	0.190D 14
10	0.488D 14	0.460D 14	0.402D 14	0.334D 14	0.261D 14	0.255D 14	0.248D 14	0.245D 14	0.244D 14	0.243D 14
11	0.620D 14	0.581D 14	0.507D 14	0.420D 14	0.332D 14	0.324D 14	0.316D 14	0.311D 14	0.307D 14	0.305D 14
12	0.691D 14	0.648D 14	0.568D 14	0.476D 14	0.382D 14	0.375D 14	0.369D 14	0.356D 14	0.344D 14	0.342D 14
13	0.746D 14	0.701D 14	0.617D 14	0.520D 14	0.420D 14	0.412D 14	0.406D 14	0.391D 14	0.376D 14	0.374D 14
14	0.778D 14	0.733D 14	0.648D 14	0.548D 14	0.443D 14	0.435D 14	0.428D 14	0.412D 14	0.397D 14	0.394D 14
15	0.784D 14	0.740D 14	0.655D 14	0.556D 14	0.450D 14	0.442D 14	0.435D 14	0.419D 14	0.403D 14	0.401D 14
16	0.759D 14	0.717D 14	0.637D 14	0.543D 14	0.440D 14	0.432D 14	0.426D 14	0.409D 14	0.392D 14	0.390D 14
17	0.700D 14	0.662D 14	0.591D 14	0.508D 14	0.415D 14	0.408D 14	0.402D 14	0.388D 14	0.374D 14	0.370D 14
18	0.654D 14	0.619D 14	0.555D 14	0.480D 14	0.395D 14	0.388D 14	0.383D 14	0.370D 14	0.359D 14	0.340D 14
19	0.622D 14	0.589D 14	0.529D 14	0.460D 14	0.382D 14	0.375D 14	0.368D 14	0.364D 14	0.352D 14	0.327D 14
20	0.589D 14	0.558D 14	0.502D 14	0.438D 14	0.368D 14	0.363D 14	0.357D 14	0.354D 14	0.335D 14	0.310D 14
21	0.572D 14	0.541D 14	0.488D 14	0.426D 14	0.361D 14	0.356D 14	0.351D 14	0.340D 14	0.322D 14	0.299D 14
22	0.554D 14	0.525D 14	0.473D 14	0.415D 14	0.354D 14	0.351D 14	0.344D 14	0.324D 14	0.307D 14	0.285D 14
23	0.538D 14	0.510D 14	0.460D 14	0.404D 14	0.345D 14	0.341D 14	0.322D 14	0.304D 14	0.287D 14	0.270D 14
24	0.518D 14	0.491D 14	0.443D 14	0.390D 14	0.335D 14	0.331D 14	0.302D 14	0.286D 14	0.270D 14	0.257D 14
25	0.496D 14	0.470D 14	0.425D 14	0.375D 14	0.325D 14	0.320D 14	0.280D 14	0.266D 14	0.253D 14	0.242D 14
26	0.455D 14	0.431D 14	0.390D 14	0.346D 14	0.313D 14	0.308D 14	0.263D 14	0.250D 14	0.239D 14	0.231D 14
27	0.429D 14	0.405D 14	0.367D 14	0.327D 14	0.293D 14	0.278D 14	0.244D 14	0.234D 14	0.226D 14	0.221D 14
28	0.403D 14	0.381D 14	0.346D 14	0.308D 14	0.274D 14	0.255D 14	0.226D 14	0.218D 14	0.214D 14	0.211D 14
29	0.366D 14	0.346D 14	0.313D 14	0.278D 14	0.245D 14	0.228D 14	0.209D 14	0.205D 14	0.203D 14	0.201D 14
30	0.324D 14	0.307D 14	0.277D 14	0.248D 14	0.219D 14	0.207D 14	0.195D 14	0.193D 14	0.193D 14	0.191D 14
31	0.288D 14	0.273D 14	0.247D 14	0.222D 14	0.199D 14	0.190D 14	0.185D 14	0.184D 14	0.184D 14	0.182D 14
32	0.258D 14	0.245D 14	0.221D 14	0.201D 14	0.187D 14	0.183D 14	0.178D 14	0.178D 14	0.177D 14	0.175D 14
33	0.233D 14	0.223D 14	0.206D 14	0.195D 14	0.183D 14	0.178D 14	0.173D 14	0.171D 14	0.170D 14	0.168D 14
34	0.214D 14	0.207D 14	0.199D 14	0.190D 14	0.178D 14	0.172D 14	0.167D 14	0.165D 14	0.163D 14	0.161D 14
35	0.211D 14	0.204D 14	0.194D 14	0.184D 14	0.171D 14	0.166D 14	0.160D 14	0.158D 14	0.157D 14	0.154D 14
36	0.181D 14	0.175D 14	0.165D 14	0.155D 14	0.143D 14	0.138D 14	0.133D 14	0.131D 14	0.130D 14	0.127D 14
37	0.149D 14	0.144D 14	0.136D 14	0.126D 14	0.117D 14	0.112D 14	0.108D 14	0.106D 14	0.105D 14	0.102D 14
38	0.921D 13	0.889D 13	0.836D 13	0.778D 13	0.717D 13	0.689D 13	0.662D 13	0.652D 13	0.643D 13	0.629D 13
39	0.310D 13	0.300D 13	0.284D 13	0.265D 13	0.246D 13	0.237D 13	0.228D 13	0.225D 13	0.222D 13	0.218D 13
40	0.634D 12	0.616D 12	0.584D 12	0.550D 12	0.514D 12	0.497D 12	0.481D 12	0.475D 12	0.470D 12	0.461D 12
41	0.952D 11	0.925D 11	0.881D 11	0.831D 11	0.779D 11	0.755D 11	0.732D 11	0.724D 11	0.715D 11	0.703D 11
42	0.463D 11	0.450D 11	0.428D 11	0.404D 11	0.379D 11	0.368D 11	0.356D 11	0.352D 11	0.348D 11	0.342D 11

POINTWISE FLUX - GROUP 2

	20	21	22	23	24	25	26	27	28	29
0	0.0	0.0	0.0	0.0	0.0	0.0	0.0	0.0	0.0	0.0
1	0.1130 11	0.1060 11	0.9830 10	0.9190 10	0.6910 10	0.3180 10	0.1380 10	0.5660 09	0.2440 09	0.2410 09
2	0.8250 11	0.7640 11	0.7050 11	0.6530 11	0.4740 11	0.2040 11	0.8400 10	0.3240 10	0.1250 10	0.1100 10
3	0.6090 12	0.5620 12	0.5170 12	0.4770 12	0.3350 12	0.1370 12	0.5490 11	0.1990 11	0.6470 10	0.6550 10
4	0.2790 13	0.2500 13	0.2230 13	0.2010 13	0.1330 13	0.5330 12	0.2230 12	0.9150 11	0.3650 11	0.3670 11
5	0.4930 13	0.4490 13	0.4150 13	0.4070 13	0.3140 13	0.1590 13	0.7960 12	0.3940 12	0.1990 12	0.1240 12
6	0.7310 13	0.6760 13	0.6280 13	0.6230 13	0.5400 13	0.3190 13	0.1730 13	0.9000 12	0.4680 12	0.2660 12
7	0.1020 14	0.9520 13	0.8930 13	0.8870 13	0.7840 13	0.4770 13	0.2640 13	0.1390 13	0.7230 12	0.4020 12
8	0.1370 14	0.1280 14	0.1210 14	0.1200 14	0.1070 14	0.6510 13	0.3600 13	0.1890 13	0.9760 12	0.5350 12
9	0.1780 14	0.1670 14	0.1570 14	0.1560 14	0.1380 14	0.8340 13	0.4560 13	0.2370 13	0.1220 13	0.6580 12
10	0.2270 14	0.2110 14	0.1970 14	0.1950 14	0.1720 14	0.1020 14	0.5520 13	0.2840 13	0.1430 13	0.7540 12
11	0.2830 14	0.2610 14	0.2400 14	0.2380 14	0.2060 14	0.1200 14	0.6380 13	0.3230 13	0.1610 13	0.8140 12
12	0.3160 14	0.2890 14	0.2640 14	0.2620 14	0.2250 14	0.1300 14	0.6810 13	0.3420 13	0.1690 13	0.8390 12
13	0.3440 14	0.3130 14	0.2840 14	0.2820 14	0.2410 14	0.1370 14	0.7120 13	0.3550 13	0.1740 13	0.8530 12
14	0.3630 14	0.3300 14	0.2980 14	0.2950 14	0.2510 14	0.1410 14	0.7280 13	0.3610 13	0.1760 13	0.8560 12
15	0.3690 14	0.3360 14	0.3040 14	0.3010 14	0.2550 14	0.1410 14	0.7270 13	0.3590 13	0.1740 13	0.8470 12
16	0.3540 14	0.3150 14	0.3070 14	0.3010 14	0.2510 14	0.1380 14	0.7050 13	0.3490 13	0.1700 13	0.8250 12
17	0.3350 14	0.3010 14	0.2950 14	0.2840 14	0.2350 14	0.1300 14	0.6650 13	0.3300 13	0.1610 13	0.7920 12
18	0.3110 14	0.2850 14	0.2730 14	0.2650 14	0.2230 14	0.1230 14	0.6370 13	0.3170 13	0.1550 13	0.7690 12
19	0.2940 14	0.2740 14	0.2620 14	0.2540 14	0.2140 14	0.1190 14	0.6170 13	0.3080 13	0.1520 13	0.7540 12
20	0.2780 14	0.2620 14	0.2510 14	0.2440 14	0.2050 14	0.1150 14	0.5960 13	0.2990 13	0.1470 13	0.7380 12
21	0.2690 14	0.2560 14	0.2460 14	0.2380 14	0.2000 14	0.1120 14	0.5850 13	0.2930 13	0.1450 13	0.7300 12
22	0.2600 14	0.2490 14	0.2400 14	0.2320 14	0.1950 14	0.1100 14	0.5730 13	0.2880 13	0.1430 13	0.7210 12
23	0.2510 14	0.2420 14	0.2340 14	0.2260 14	0.1900 14	0.1070 14	0.5610 13	0.2830 13	0.1410 13	0.7120 12
24	0.2430 14	0.2350 14	0.2260 14	0.2180 14	0.1840 14	0.1040 14	0.5470 13	0.2760 13	0.1380 13	0.7010 12
25	0.2330 14	0.2260 14	0.2190 14	0.2110 14	0.1780 14	0.1010 14	0.5320 13	0.2700 13	0.1350 13	0.6900 12
26	0.2260 14	0.2180 14	0.2110 14	0.2030 14	0.1720 14	0.9790 13	0.5170 13	0.2630 13	0.1320 13	0.6790 12
27	0.2160 14	0.2100 14	0.2020 14	0.1950 14	0.1650 14	0.9470 13	0.5030 13	0.2560 13	0.1290 13	0.6670 12
28	0.2070 14	0.2010 14	0.1940 14	0.1870 14	0.1590 14	0.9150 13	0.4870 13	0.2490 13	0.1260 13	0.6560 12
29	0.1970 14	0.1920 14	0.1860 14	0.1800 14	0.1530 14	0.8830 13	0.4720 13	0.2420 13	0.1230 13	0.6440 12
30	0.1880 14	0.1830 14	0.1770 14	0.1720 14	0.1460 14	0.8510 13	0.4570 13	0.2350 13	0.1200 13	0.6320 12
31	0.1790 14	0.1750 14	0.1690 14	0.1640 14	0.1400 14	0.8190 13	0.4420 13	0.2280 13	0.1170 13	0.6200 12
32	0.1710 14	0.1670 14	0.1620 14	0.1570 14	0.1340 14	0.7870 13	0.4260 13	0.2210 13	0.1140 13	0.6080 12
33	0.1640 14	0.1590 14	0.1540 14	0.1490 14	0.1280 14	0.7560 13	0.4110 13	0.2140 13	0.1100 13	0.5960 12
34	0.1560 14	0.1520 14	0.1470 14	0.1430 14	0.1220 14	0.7250 13	0.3960 13	0.2070 13	0.1070 13	0.5840 12
35	0.1490 14	0.1450 14	0.1400 14	0.1360 14	0.1160 14	0.6940 13	0.3810 13	0.2010 13	0.1040 13	0.5720 12
36	0.1230 14	0.1190 14	0.1150 14	0.1110 14	0.9510 13	0.5780 13	0.3240 13	0.1730 13	0.9200 12	0.5250 12
37	0.9890 13	0.9560 13	0.9220 13	0.8900 13	0.7650 13	0.4740 13	0.2710 13	0.1480 13	0.8020 12	0.4790 12
38	0.6080 13	0.5880 13	0.5670 13	0.5490 13	0.4740 13	0.3040 13	0.1810 13	0.1030 13	0.5890 12	0.3910 12
39	0.2110 13	0.2050 13	0.1980 13	0.1920 13	0.1690 13	0.1140 13	0.7250 12	0.4420 12	0.2700 12	0.1830 12
40	0.4490 12	0.4370 12	0.4240 12	0.4130 12	0.3680 12	0.2620 12	0.1760 12	0.1150 12	0.7470 11	0.5260 11
41	0.6860 11	0.6680 11	0.6500 11	0.6340 11	0.5690 11	0.4120 11	0.2840 11	0.1890 11	0.1260 11	0.9040 10
42	0.3340 11	0.3250 11	0.3170 11	0.3090 11	0.2770 11	0.2010 11	0.1390 11	0.9260 10	0.6190 10	0.4450 10

POINTWISE FLUX - GROUP 2

	30	31	32	33	34	35	36	37	38
0	0.0	0.0	0.0	0.0	0.0	0.0	0.0	0.0	0.0
1	0.580D 09	0.600D 09	0.863D 09	0.111D 10	0.117D 10	0.116D 10	0.572D 09	0.194D 09	0.0
2	0.242D 10	0.249D 10	0.338D 10	0.407D 10	0.380D 10	0.373D 10	0.162D 10	0.513D 09	0.0
3	0.109D 11	0.111D 11	0.131D 11	0.139D 11	0.108D 11	0.104D 11	0.384D 10	0.111D 10	0.0
4	0.494D 11	0.499D 11	0.505D 11	0.451D 11	0.282D 11	0.265D 11	0.825D 10	0.217D 10	0.0
5	0.120D 12	0.119D 12	0.103D 12	0.800D 11	0.437D 11	0.404D 11	0.116D 11	0.292D 10	0.0
6	0.223D 12	0.220D 12	0.177D 12	0.126D 12	0.636D 11	0.581D 11	0.157D 11	0.382D 10	0.0
7	0.330D 12	0.325D 12	0.257D 12	0.179D 12	0.868D 11	0.789D 11	0.204D 11	0.484D 10	0.0
8	0.436D 12	0.431D 12	0.340D 12	0.237D 12	0.113D 12	0.102D 12	0.257D 11	0.598D 10	0.0
9	0.536D 12	0.529D 12	0.431D 12	0.302D 12	0.142D 12	0.128D 12	0.314D 11	0.719D 10	0.0
10	0.602D 12	0.593D 12	0.581D 12	0.379D 12	0.172D 12	0.155D 12	0.372D 11	0.844D 10	0.0
11	0.619D 12	0.606D 12	0.598D 12	0.411D 12	0.193D 12	0.174D 12	0.417D 11	0.946D 10	0.0
12	0.626D 12	0.612D 12	0.604D 12	0.421D 12	0.200D 12	0.181D 12	0.437D 11	0.992D 10	0.0
13	0.629D 12	0.614D 12	0.606D 12	0.425D 12	0.204D 12	0.185D 12	0.450D 11	0.102D 11	0.0
14	0.627D 12	0.612D 12	0.603D 12	0.424D 12	0.206D 12	0.187D 12	0.456D 11	0.104D 11	0.0
15	0.619D 12	0.604D 12	0.596D 12	0.420D 12	0.205D 12	0.186D 12	0.457D 11	0.105D 11	0.0
16	0.605D 12	0.590D 12	0.582D 12	0.411D 12	0.201D 12	0.183D 12	0.452D 11	0.104D 11	0.0
17	0.585D 12	0.571D 12	0.564D 12	0.398D 12	0.196D 12	0.178D 12	0.441D 11	0.102D 11	0.0
18	0.572D 12	0.560D 12	0.552D 12	0.390D 12	0.192D 12	0.175D 12	0.434D 11	0.100D 11	0.0
19	0.564D 12	0.552D 12	0.545D 12	0.385D 12	0.189D 12	0.172D 12	0.429D 11	0.991D 10	0.0
20	0.555D 12	0.543D 12	0.536D 12	0.380D 12	0.187D 12	0.170D 12	0.423D 11	0.978D 10	0.0
21	0.550D 12	0.539D 12	0.532D 12	0.376D 12	0.185D 12	0.169D 12	0.420D 11	0.972D 10	0.0
22	0.545D 12	0.534D 12	0.528D 12	0.373D 12	0.184D 12	0.167D 12	0.417D 11	0.965D 10	0.0
23	0.540D 12	0.530D 12	0.523D 12	0.370D 12	0.182D 12	0.166D 12	0.413D 11	0.957D 10	0.0
24	0.535D 12	0.524D 12	0.518D 12	0.366D 12	0.180D 12	0.164D 12	0.409D 11	0.948D 10	0.0
25	0.529D 12	0.518D 12	0.512D 12	0.363D 12	0.178D 12	0.162D 12	0.405D 11	0.939D 10	0.0
26	0.522D 12	0.512D 12	0.506D 12	0.359D 12	0.176D 12	0.161D 12	0.401D 11	0.929D 10	0.0
27	0.516D 12	0.507D 12	0.501D 12	0.355D 12	0.174D 12	0.159D 12	0.396D 11	0.919D 10	0.0
28	0.510D 12	0.501D 12	0.495D 12	0.351D 12	0.172D 12	0.157D 12	0.392D 11	0.909D 10	0.0
29	0.504D 12	0.495D 12	0.489D 12	0.346D 12	0.170D 12	0.155D 12	0.387D 11	0.898D 10	0.0
30	0.497D 12	0.489D 12	0.483D 12	0.342D 12	0.168D 12	0.153D 12	0.382D 11	0.887D 10	0.0
31	0.491D 12	0.483D 12	0.477D 12	0.338D 12	0.166D 12	0.151D 12	0.377D 11	0.876D 10	0.0
32	0.484D 12	0.477D 12	0.471D 12	0.334D 12	0.164D 12	0.149D 12	0.372D 11	0.864D 10	0.0
33	0.478D 12	0.471D 12	0.466D 12	0.329D 12	0.161D 12	0.147D 12	0.366D 11	0.852D 10	0.0
34	0.471D 12	0.464D 12	0.460D 12	0.325D 12	0.159D 12	0.145D 12	0.361D 11	0.840D 10	0.0
35	0.465D 12	0.458D 12	0.454D 12	0.321D 12	0.157D 12	0.143D 12	0.355D 11	0.828D 10	0.0
36	0.439D 12	0.434D 12	0.430D 12	0.303D 12	0.147D 12	0.133D 12	0.332D 11	0.775D 10	0.0
37	0.415D 12	0.412D 12	0.408D 12	0.284D 12	0.136D 12	0.123D 12	0.307D 11	0.719D 10	0.0
38	0.373D 12	0.374D 12	0.368D 12	0.243D 12	0.112D 12	0.101D 12	0.253D 11	0.597D 10	0.0
39	0.165D 12	0.164D 12	0.140D 12	0.107D 12	0.564D 11	0.519D 11	0.144D 11	0.358D 10	0.0
40	0.477D 11	0.473D 11	0.404D 11	0.314D 11	0.180D 11	0.168D 11	0.519D 10	0.139D 10	0.0
41	0.824D 10	0.818D 10	0.701D 10	0.549D 10	0.322D 10	0.301D 10	0.964D 09	0.264D 09	0.0
42	0.406D 10	0.403D 10	0.345D 10	0.271D 10	0.159D 10	0.149D 10	0.477D 09	0.131D 09	0.0

POINTWISE FLUX - GROUP 3

	0	1	2	3	4	5	6	7	8	9
0	0.0	0.0	0.0	0.0	0.0	0.0	0.0	0.0	0.0	0.0
1	0.308D 12	0.307D 12	0.306D 12	0.302D 12	0.297D 12	0.291D 12	0.289D 12	0.287D 12	0.277D 12	0.265D 12
2	0.210D 13	0.210D 13	0.209D 13	0.206D 13	0.203D 13	0.199D 13	0.198D 13	0.197D 13	0.190D 13	0.182D 13
3	0.992D 13	0.990D 13	0.985D 13	0.971D 13	0.954D 13	0.933D 13	0.928D 13	0.923D 13	0.902D 13	0.870D 13
4	0.682D 13	0.674D 13	0.649D 13	0.578D 13	0.380D 13	0.823D 12	0.411D 12	0.102D 13	0.457D 13	0.600D 13
5	0.414D 13	0.411D 13	0.402D 13	0.378D 13	0.256D 13	0.317D 12	0.769D 10	0.420D 12	0.305D 13	0.394D 13
6	0.446D 13	0.445D 13	0.442D 13	0.433D 13	0.327D 13	0.423D 12	0.105D 11	0.581D 12	0.418D 13	0.537D 13
7	0.587D 13	0.586D 13	0.584D 13	0.577D 13	0.445D 13	0.580D 12	0.145D 11	0.804D 12	0.578D 13	0.742D 13
8	0.802D 13	0.800D 13	0.797D 13	0.788D 13	0.607D 13	0.790D 12	0.197D 11	0.109D 13	0.784D 13	0.100D 14
9	0.112D 14	0.112D 14	0.111D 14	0.109D 14	0.834D 13	0.108D 13	0.268D 11	0.148D 13	0.105D 14	0.134D 14
10	0.163D 14	0.163D 14	0.162D 14	0.159D 14	0.123D 14	0.232D 13	0.206D 13	0.251D 13	0.144D 14	0.179D 14
11	0.245D 14	0.246D 14	0.246D 14	0.248D 14	0.247D 14	0.227D 14	0.226D 14	0.227D 14	0.246D 14	0.247D 14
12	0.284D 14	0.284D 14	0.285D 14	0.287D 14	0.289D 14	0.279D 14	0.279D 14	0.279D 14	0.284D 14	0.278D 14
13	0.311D 14	0.312D 14	0.312D 14	0.314D 14	0.316D 14	0.308D 14	0.308D 14	0.308D 14	0.309D 14	0.301D 14
14	0.329D 14	0.329D 14	0.330D 14	0.331D 14	0.331D 14	0.323D 14	0.323D 14	0.323D 14	0.322D 14	0.314D 14
15	0.340D 14	0.340D 14	0.340D 14	0.340D 14	0.337D 14	0.329D 14	0.329D 14	0.329D 14	0.326D 14	0.317D 14
16	0.354D 14	0.353D 14	0.352D 14	0.347D 14	0.336D 14	0.329D 14	0.329D 14	0.329D 14	0.319D 14	0.308D 14
17	0.389D 14	0.387D 14	0.382D 14	0.368D 14	0.336D 14	0.340D 14	0.340D 14	0.340D 14	0.303D 14	0.284D 14
18	0.436D 14	0.433D 14	0.425D 14	0.402D 14	0.350D 14	0.377D 14	0.377D 14	0.376D 14	0.305D 14	0.277D 14
19	0.480D 14	0.477D 14	0.468D 14	0.440D 14	0.378D 14	0.424D 14	0.424D 14	0.422D 14	0.327D 14	0.294D 14
20	0.538D 14	0.535D 14	0.526D 14	0.497D 14	0.430D 14	0.498D 14	0.499D 14	0.497D 14	0.381D 14	0.346D 14
21	0.572D 14	0.570D 14	0.562D 14	0.537D 14	0.479D 14	0.552D 14	0.554D 14	0.551D 14	0.436D 14	0.403D 14
22	0.61CD 14	0.608D 14	0.602D 14	0.587D 14	0.554D 14	0.619D 14	0.620D 14	0.617D 14	0.521D 14	0.495D 14
23	0.651D 14	0.649D 14	0.645D 14	0.648D 14	0.677D 14	0.699D 14	0.699D 14	0.698D 14	0.654D 14	0.638D 14
24	0.888D 14	0.885D 14	0.879D 14	0.867D 14	0.853D 14	0.799D 14	0.798D 14	0.799D 14	0.840D 14	0.843D 14
25	0.108D 15	0.108D 15	0.107D 15	0.104D 15	0.996D 14	0.891D 14	0.890D 14	0.892D 14	0.991D 14	0.101D 15
26	0.133D 15	0.132D 15	0.131D 15	0.126D 15	0.116D 15	0.977D 14	0.975D 14	0.979D 14	0.117D 15	0.122D 15
27	0.143D 15	0.142D 15	0.140D 15	0.134D 15	0.124D 15	0.104D 15	0.104D 15	0.105D 15	0.125D 15	0.130D 15
28	0.151D 15	0.151D 15	0.149D 15	0.143D 15	0.131D 15	0.110D 15	0.110D 15	0.110D 15	0.132D 15	0.138D 15
29	0.161D 15	0.161D 15	0.160D 15	0.154D 15	0.142D 15	0.114D 15	0.114D 15	0.115D 15	0.143D 15	0.148D 15
30	0.163D 15	0.163D 15	0.166D 15	0.162D 15	0.153D 15	0.139D 15	0.138D 15	0.139D 15	0.152D 15	0.154D 15
31	0.163D 15	0.164D 15	0.166D 15	0.163D 15	0.157D 15	0.150D 15	0.149D 15	0.149D 15	0.154D 15	0.155D 15
32	0.162D 15	0.162D 15	0.163D 15	0.160D 15	0.156D 15	0.152D 15	0.151D 15	0.151D 15	0.153D 15	0.152D 15
33	0.159D 15	0.158D 15	0.156D 15	0.154D 15	0.151D 15	0.148D 15	0.148D 15	0.148D 15	0.147D 15	0.146D 15
34	0.150D 15	0.146D 15	0.145D 15	0.144D 15	0.143D 15	0.141D 15	0.141D 15	0.140D 15	0.139D 15	0.137D 15
35	0.145D 15	0.144D 15	0.144D 15	0.143D 15	0.142D 15	0.140D 15	0.140D 15	0.140D 15	0.138D 15	0.136D 15
36	0.139D 15	0.139D 15	0.139D 15	0.138D 15	0.137D 15	0.136D 15	0.136D 15	0.136D 15	0.134D 15	0.132D 15
37	0.133D 15	0.133D 15	0.133D 15	0.132D 15	0.132D 15	0.131D 15	0.130D 15	0.130D 15	0.129D 15	0.127D 15
38	0.118D 15	0.118D 15	0.118D 15	0.117D 15	0.117D 15	0.116D 15	0.116D 15	0.115D 15	0.114D 15	0.113D 15
39	0.833D 14	0.833D 14	0.832D 14	0.829D 14	0.826D 14	0.821D 14	0.820D 14	0.818D 14	0.811D 14	0.803D 14
40	0.410D 14	0.410D 14	0.409D 14	0.408D 14	0.407D 14	0.405D 14	0.404D 14	0.403D 14	0.400D 14	0.397D 14
41	0.836D 13	0.836D 13	0.835D 13	0.833D 13	0.830D 13	0.826D 13	0.825D 13	0.823D 13	0.818D 13	0.811D 13
42	0.417D 13	0.417D 13	0.416D 13	0.415D 13	0.414D 13	0.412D 13	0.411D 13	0.411D 13	0.408D 13	0.404D 13

POINTWISE FLUX - GROUP 3

	10	11	12	13	14	15	16	17	18	19
0	0.0	0.0	0.0	0.0	0.0	0.0	0.0	0.0	0.0	0.0
1	0.250D 12	0.232D 12	0.198D 12	0.153D 12	0.885D 11	0.500D 11	0.307D 10	0.569D 08	0.214D 10	0.186D 11
2	0.172D 13	0.160D 13	0.136D 13	0.105D 13	0.611D 12	0.346D 12	0.214D 11	0.395D 09	0.147D 11	0.127D 12
3	0.826D 13	0.768D 13	0.651D 13	0.492D 13	0.276D 13	0.156D 13	0.135D 12	0.256D 10	0.983D 11	0.618D 12
4	0.642D 13	0.631D 13	0.549D 13	0.396D 13	0.118D 13	0.779D 12	0.308D 12	0.777D 10	0.395D 12	0.225D 13
5	0.415D 13	0.405D 13	0.355D 13	0.261D 13	0.579D 12	0.422D 12	0.258D 12	0.140D 11	0.101D 13	0.159D 13
6	0.564D 13	0.550D 13	0.483D 13	0.355D 13	0.722D 12	0.514D 12	0.313D 12	0.168D 11	0.120D 13	0.158D 13
7	0.779D 13	0.759D 13	0.665D 13	0.490D 13	0.984D 12	0.699D 12	0.426D 12	0.221D 11	0.156D 13	0.205D 13
8	0.105D 14	0.102D 14	0.896D 13	0.658D 13	0.132D 13	0.940D 12	0.572D 12	0.288D 11	0.202D 13	0.265D 13
9	0.140D 14	0.136D 14	0.118D 14	0.866D 13	0.178D 13	0.128D 13	0.779D 12	0.370D 11	0.254D 13	0.334D 13
10	0.184D 14	0.176D 14	0.150D 14	0.109D 14	0.274D 13	0.207D 13	0.130D 13	0.508D 11	0.327D 13	0.427D 13
11	0.238D 14	0.222D 14	0.188D 14	0.145D 14	0.800D 13	0.716D 13	0.547D 13	0.105D 13	0.860D 13	0.101D 14
12	0.266D 14	0.250D 14	0.216D 14	0.192D 14	0.230D 14	0.237D 14	0.250D 14	0.377D 14	0.467D 14	0.473D 14
13	0.288D 14	0.271D 14	0.239D 14	0.228D 14	0.337D 14	0.351D 14	0.369D 14	0.531D 14	0.653D 14	0.659D 14
14	0.301D 14	0.284D 14	0.253D 14	0.252D 14	0.405D 14	0.423D 14	0.444D 14	0.620D 14	0.754D 14	0.761D 14
15	0.303D 14	0.287D 14	0.258D 14	0.264D 14	0.449D 14	0.469D 14	0.491D 14	0.672D 14	0.811D 14	0.818D 14
16	0.294D 14	0.279D 14	0.253D 14	0.267D 14	0.479D 14	0.501D 14	0.523D 14	0.703D 14	0.841D 14	0.848D 14
17	0.270D 14	0.256D 14	0.238D 14	0.265D 14	0.511D 14	0.535D 14	0.557D 14	0.731D 14	0.866D 14	0.876D 14
18	0.261D 14	0.248D 14	0.236D 14	0.271D 14	0.538D 14	0.563D 14	0.584D 14	0.731D 14	0.823D 14	0.968D 14
19	0.277D 14	0.264D 14	0.252D 14	0.287D 14	0.561D 14	0.587D 14	0.612D 14	0.629D 14	0.748D 14	0.934D 14
20	0.328D 14	0.314D 14	0.298D 14	0.326D 14	0.588D 14	0.612D 14	0.632D 14	0.642D 14	0.795D 14	0.957D 14
21	0.386D 14	0.370D 14	0.350D 14	0.370D 14	0.608D 14	0.628D 14	0.646D 14	0.731D 14	0.852D 14	0.985D 14
22	0.477D 14	0.459D 14	0.432D 14	0.439D 14	0.633D 14	0.645D 14	0.662D 14	0.802D 14	0.908D 14	0.102D 15
23	0.620D 14	0.598D 14	0.561D 14	0.549D 14	0.669D 14	0.679D 14	0.790D 14	0.890D 14	0.975D 14	0.104D 15
24	0.826D 14	0.797D 14	0.744D 14	0.706D 14	0.713D 14	0.719D 14	0.881D 14	0.960D 14	0.102D 15	0.106D 15
25	0.996D 14	0.962D 14	0.896D 14	0.832D 14	0.752D 14	0.755D 14	0.968D 14	0.102D 15	0.106D 15	0.110D 15
26	0.121D 15	0.117D 15	0.109D 15	0.990D 14	0.786D 14	0.784D 14	0.102D 15	0.106D 15	0.109D 15	0.111D 15
27	0.130D 15	0.126D 15	0.117D 15	0.106D 15	0.914D 14	0.938D 14	0.107D 15	0.109D 15	0.111D 15	0.112D 15
28	0.137D 15	0.133D 15	0.123D 15	0.113D 15	0.101D 15	0.104D 15	0.111D 15	0.112D 15	0.112D 15	0.112D 15
29	0.146D 15	0.142D 15	0.132D 15	0.121D 15	0.111D 15	0.112D 15	0.114D 15	0.113D 15	0.113D 15	0.113D 15
30	0.152D 15	0.147D 15	0.136D 15	0.126D 15	0.117D 15	0.116D 15	0.115D 15	0.114D 15	0.114D 15	0.114D 15
31	0.152D 15	0.147D 15	0.136D 15	0.126D 15	0.119D 15	0.117D 15	0.115D 15	0.115D 15	0.115D 15	0.114D 15
32	0.149D 15	0.144D 15	0.132D 15	0.124D 15	0.120D 15	0.118D 15	0.116D 15	0.115D 15	0.115D 15	0.115D 15
33	0.143D 15	0.139D 15	0.128D 15	0.123D 15	0.120D 15	0.118D 15	0.116D 15	0.116D 15	0.115D 15	0.115D 15
34	0.135D 15	0.132D 15	0.128D 15	0.123D 15	0.119D 15	0.118D 15	0.116D 15	0.116D 15	0.115D 15	0.114D 15
35	0.134D 15	0.131D 15	0.127D 15	0.123D 15	0.119D 15	0.118D 15	0.116D 15	0.115D 15	0.115D 15	0.114D 15
36	0.130D 15	0.128D 15	0.124D 15	0.121D 15	0.117D 15	0.115D 15	0.113D 15	0.113D 15	0.112D 15	0.111D 15
37	0.125D 15	0.123D 15	0.120D 15	0.116D 15	0.112D 15	0.111D 15	0.109D 15	0.108D 15	0.108D 15	0.107D 15
38	0.111D 15	0.110D 15	0.107D 15	0.104D 15	0.100D 15	0.989D 14	0.974D 14	0.968D 14	0.963D 14	0.955D 14
39	0.794D 14	0.783D 14	0.765D 14	0.745D 14	0.723D 14	0.712D 14	0.702D 14	0.698D 14	0.695D 14	0.689D 14
40	0.393D 14	0.388D 14	0.380D 14	0.372D 14	0.362D 14	0.357D 14	0.353D 14	0.351D 14	0.349D 14	0.347D 14
41	0.803D 13	0.794D 13	0.778D 13	0.761D 13	0.741D 13	0.732D 13	0.723D 13	0.720D 13	0.717D 13	0.712D 13
42	0.400D 13	0.396D 13	0.388D 13	0.380D 13	0.370D 13	0.365D 13	0.361D 13	0.359D 13	0.358D 13	0.355D 13

POINTWISE FLUX - GROUP 3

	20	21	22	23	24	25	26	27	28	29
0	0.0	0.0	0.0	0.0	0.0	0.0	0.0	0.0	0.0	0.0
1	0.366D 11	0.496D 11	0.585D 11	0.642D 11	0.675D 11	0.383D 11	0.188D 11	0.123D 11	0.332D 11	0.210D 12
2	0.248D 12	0.332D 12	0.390D 12	0.425D 12	0.438D 12	0.246D 12	0.122D 12	0.681D 11	0.107D 12	0.553D 12
3	0.121D 13	0.165D 13	0.197D 13	0.219D 13	0.241D 13	0.154D 13	0.889D 12	0.515D 12	0.521D 12	0.225D 13
4	0.438D 13	0.597D 13	0.713D 13	0.789D 13	0.872D 13	0.644D 13	0.457D 13	0.343D 13	0.292D 13	0.588D 13
5	0.109D 14	0.182D 14	0.242D 14	0.246D 14	0.268D 14	0.256D 14	0.219D 14	0.179D 14	0.142D 14	0.112D 14
6	0.138D 14	0.229D 14	0.299D 14	0.301D 14	0.329D 14	0.334D 14	0.297D 14	0.248D 14	0.199D 14	0.157D 14
7	0.180D 14	0.294D 14	0.377D 14	0.379D 14	0.415D 14	0.426D 14	0.383D 14	0.320D 14	0.257D 14	0.200D 14
8	0.230D 14	0.374D 14	0.474D 14	0.477D 14	0.522D 14	0.534D 14	0.477D 14	0.396D 14	0.315D 14	0.242D 14
9	0.289D 14	0.465D 14	0.583D 14	0.587D 14	0.638D 14	0.644D 14	0.569D 14	0.468D 14	0.367D 14	0.279D 14
10	0.356D 14	0.568D 14	0.704D 14	0.708D 14	0.764D 14	0.755D 14	0.656D 14	0.533D 14	0.412D 14	0.306D 14
11	0.467D 14	0.703D 14	0.844D 14	0.848D 14	0.898D 14	0.860D 14	0.734D 14	0.587D 14	0.447D 14	0.322D 14
12	0.736D 14	0.886D 14	0.948D 14	0.950D 14	0.980D 14	0.918D 14	0.775D 14	0.615D 14	0.464D 14	0.328D 14
13	0.894D 14	0.101D 15	0.103D 15	0.104D 15	0.105D 15	0.967D 14	0.808D 14	0.637D 14	0.477D 14	0.334D 14
14	0.987D 14	0.109D 15	0.110D 15	0.110D 15	0.111D 15	0.100D 15	0.833D 14	0.653D 14	0.486D 14	0.337D 14
15	0.104D 15	0.113D 15	0.114D 15	0.114D 15	0.114D 15	0.103D 15	0.848D 14	0.663D 14	0.492D 14	0.339D 14
16	0.105D 15	0.114D 15	0.115D 15	0.115D 15	0.116D 15	0.104D 15	0.853D 14	0.666D 14	0.494D 14	0.340D 14
17	0.106D 15	0.114D 15	0.115D 15	0.115D 15	0.116D 15	0.103D 15	0.849D 14	0.662D 14	0.491D 14	0.339D 14
18	0.110D 15	0.115D 15	0.115D 15	0.116D 15	0.115D 15	0.103D 15	0.843D 14	0.658D 14	0.489D 14	0.338D 14
19	0.108D 15	0.113D 15	0.115D 15	0.115D 15	0.115D 15	0.102D 15	0.838D 14	0.654D 14	0.487D 14	0.337D 14
20	0.109D 15	0.112D 15	0.114D 15	0.115D 15	0.114D 15	0.101D 15	0.832D 14	0.650D 14	0.484D 14	0.336D 14
21	0.109D 15	0.113D 15	0.114D 15	0.114D 15	0.114D 15	0.101D 15	0.829D 14	0.648D 14	0.483D 14	0.335D 14
22	0.110D 15	0.113D 15	0.113D 15	0.114D 15	0.113D 15	0.100D 15	0.825D 14	0.645D 14	0.481D 14	0.335D 14
23	0.111D 15	0.112D 15	0.113D 15	0.114D 15	0.113D 15	0.999D 14	0.821D 14	0.642D 14	0.479D 14	0.334D 14
24	0.111D 15	0.112D 15	0.113D 15	0.114D 15	0.113D 15	0.994D 14	0.816D 14	0.639D 14	0.477D 14	0.333D 14
25	0.111D 15	0.112D 15	0.113D 15	0.113D 15	0.112D 15	0.988D 14	0.811D 14	0.635D 14	0.475D 14	0.332D 14
26	0.111D 15	0.112D 15	0.113D 15	0.113D 15	0.112D 15	0.981D 14	0.806D 14	0.632D 14	0.473D 14	0.331D 14
27	0.112D 15	0.113D 15	0.113D 15	0.113D 15	0.111D 15	0.974D 14	0.800D 14	0.628D 14	0.471D 14	0.330D 14
28	0.113D 15	0.113D 15	0.113D 15	0.113D 15	0.110D 15	0.967D 14	0.795D 14	0.624D 14	0.468D 14	0.329D 14
29	0.113D 15	0.113D 15	0.113D 15	0.112D 15	0.110D 15	0.960D 14	0.788D 14	0.619D 14	0.465D 14	0.328D 14
30	0.114D 15	0.113D 15	0.113D 15	0.112D 15	0.109D 15	0.952D 14	0.782D 14	0.615D 14	0.463D 14	0.327D 14
31	0.114D 15	0.113D 15	0.113D 15	0.112D 15	0.109D 15	0.944D 14	0.776D 14	0.610D 14	0.460D 14	0.326D 14
32	0.114D 15	0.113D 15	0.112D 15	0.112D 15	0.108D 15	0.936D 14	0.769D 14	0.605D 14	0.457D 14	0.325D 14
33	0.114D 15	0.113D 15	0.112D 15	0.111D 15	0.107D 15	0.927D 14	0.762D 14	0.601D 14	0.454D 14	0.323D 14
34	0.113D 15	0.112D 15	0.111D 15	0.110D 15	0.106D 15	0.918D 14	0.755D 14	0.595D 14	0.451D 14	0.322D 14
35	0.113D 15	0.112D 15	0.111D 15	0.110D 15	0.105D 15	0.909D 14	0.747D 14	0.590D 14	0.448D 14	0.321D 14
36	0.110D 15	0.109D 15	0.108D 15	0.106D 15	0.101D 15	0.870D 14	0.716D 14	0.568D 14	0.434D 14	0.315D 14
37	0.106D 15	0.104D 15	0.103D 15	0.102D 15	0.968D 14	0.828D 14	0.682D 14	0.544D 14	0.419D 14	0.309D 14
38	0.943D 14	0.931D 14	0.919D 14	0.907D 14	0.860D 14	0.736D 14	0.610D 14	0.491D 14	0.385D 14	0.293D 14
39	0.681D 14	0.673D 14	0.665D 14	0.657D 14	0.625D 14	0.541D 14	0.456D 14	0.374D 14	0.300D 14	0.234D 14
40	0.343D 14	0.340D 14	0.336D 14	0.333D 14	0.318D 14	0.280D 14	0.240D 14	0.201D 14	0.164D 14	0.130D 14
41	0.705D 13	0.698D 13	0.690D 13	0.683D 13	0.655D 13	0.577D 13	0.497D 13	0.418D 13	0.342D 13	0.272D 13
42	0.352D 13	0.348D 13	0.345D 13	0.341D 13	0.327D 13	0.288D 13	0.248D 13	0.209D 13	0.171D 13	0.136D 13

POINTWISE FLUX - GROUP 3

	30	31	32	33	34	35	36	37	38
0	0.0	0.0	0.0	0.0	0.0	0.0	0.0	0.0	0.0
1	0.592D 12	0.598D 12	0.693D 12	0.801D 12	0.892D 12	0.894D 12	0.695D 12	0.350D 12	0.0
2	0.144D 13	0.145D 13	0.167D 13	0.189D 13	0.203D 13	0.202D 13	0.150D 13	0.735D 12	0.0
3	0.304D 13	0.306D 13	0.340D 13	0.369D 13	0.369D 13	0.366D 13	0.249D 13	0.118D 13	0.0
4	0.667D 13	0.669D 13	0.695D 13	0.694D 13	0.617D 13	0.606D 13	0.373D 13	0.168D 13	0.0
5	0.105D 14	0.105D 14	0.100D 14	0.931D 13	0.773D 13	0.754D 13	0.439D 13	0.193D 13	0.0
6	0.143D 14	0.143D 14	0.133D 14	0.119D 14	0.940D 13	0.913D 13	0.507D 13	0.218D 13	0.0
7	0.180D 14	0.179D 14	0.165D 14	0.146D 14	0.111D 14	0.107D 14	0.571D 13	0.240D 13	0.0
8	0.216D 14	0.215D 14	0.197D 14	0.171D 14	0.127D 14	0.123D 14	0.628D 13	0.258D 13	0.0
9	0.248D 14	0.247D 14	0.228D 14	0.196D 14	0.142D 14	0.136D 14	0.672D 13	0.271D 13	0.0
10	0.271D 14	0.269D 14	0.267D 14	0.220D 14	0.154D 14	0.147D 14	0.698D 13	0.277D 13	0.0
11	0.275D 14	0.273D 14	0.272D 14	0.229D 14	0.160D 14	0.153D 14	0.712D 13	0.279D 13	0.0
12	0.278D 14	0.275D 14	0.274D 14	0.232D 14	0.163D 14	0.156D 14	0.719D 13	0.280D 13	0.0
13	0.280D 14	0.277D 14	0.276D 14	0.235D 14	0.165D 14	0.158D 14	0.725D 13	0.281D 13	0.0
14	0.282D 14	0.279D 14	0.277D 14	0.237D 14	0.167D 14	0.160D 14	0.730D 13	0.282D 13	0.0
15	0.283D 14	0.280D 14	0.278D 14	0.237D 14	0.168D 14	0.161D 14	0.733D 13	0.282D 13	0.0
16	0.283D 14	0.280D 14	0.279D 14	0.238D 14	0.168D 14	0.161D 14	0.734D 13	0.282D 13	0.0
17	0.282D 14	0.279D 14	0.278D 14	0.237D 14	0.168D 14	0.161D 14	0.733D 13	0.282D 13	0.0
18	0.282D 14	0.279D 14	0.278D 14	0.237D 14	0.168D 14	0.161D 14	0.732D 13	0.281D 13	0.0
19	0.281D 14	0.278D 14	0.277D 14	0.237D 14	0.168D 14	0.160D 14	0.731D 13	0.281D 13	0.0
20	0.281D 14	0.278D 14	0.277D 14	0.236D 14	0.167D 14	0.160D 14	0.730D 13	0.280D 13	0.0
21	0.280D 14	0.278D 14	0.276D 14	0.236D 14	0.167D 14	0.160D 14	0.729D 13	0.280D 13	0.0
22	0.280D 14	0.277D 14	0.276D 14	0.236D 14	0.167D 14	0.160D 14	0.728D 13	0.280D 13	0.0
23	0.280D 14	0.277D 14	0.276D 14	0.235D 14	0.167D 14	0.160D 14	0.727D 13	0.280D 13	0.0
24	0.279D 14	0.277D 14	0.275D 14	0.235D 14	0.166D 14	0.159D 14	0.726D 13	0.279D 13	0.0
25	0.279D 14	0.276D 14	0.275D 14	0.235D 14	0.166D 14	0.159D 14	0.725D 13	0.279D 13	0.0
26	0.278D 14	0.276D 14	0.274D 14	0.234D 14	0.166D 14	0.159D 14	0.724D 13	0.279D 13	0.0
27	0.278D 14	0.275D 14	0.274D 14	0.234D 14	0.166D 14	0.158D 14	0.723D 13	0.278D 13	0.0
28	0.277D 14	0.275D 14	0.274D 14	0.233D 14	0.165D 14	0.158D 14	0.722D 13	0.278D 13	0.0
29	0.277D 14	0.274D 14	0.273D 14	0.233D 14	0.165D 14	0.158D 14	0.720D 13	0.277D 13	0.0
30	0.276D 14	0.274D 14	0.273D 14	0.233D 14	0.164D 14	0.157D 14	0.719D 13	0.277D 13	0.0
31	0.276D 14	0.273D 14	0.272D 14	0.232D 14	0.164D 14	0.157D 14	0.717D 13	0.276D 13	0.0
32	0.275D 14	0.273D 14	0.272D 14	0.231D 14	0.164D 14	0.156D 14	0.716D 13	0.276D 13	0.0
33	0.275D 14	0.272D 14	0.271D 14	0.231D 14	0.163D 14	0.156D 14	0.714D 13	0.276D 13	0.0
34	0.274D 14	0.272D 14	0.270D 14	0.230D 14	0.163D 14	0.156D 14	0.712D 13	0.275D 13	0.0
35	0.273D 14	0.271D 14	0.270D 14	0.230D 14	0.162D 14	0.155D 14	0.711D 13	0.275D 13	0.0
36	0.271D 14	0.269D 14	0.267D 14	0.227D 14	0.160D 14	0.153D 14	0.703D 13	0.272D 13	0.0
37	0.268D 14	0.266D 14	0.265D 14	0.224D 14	0.157D 14	0.150D 14	0.695D 13	0.270D 13	0.0
38	0.263D 14	0.262D 14	0.259D 14	0.215D 14	0.150D 14	0.144D 14	0.677D 13	0.265D 13	0.0
39	0.210D 14	0.209D 14	0.192D 14	0.167D 14	0.123D 14	0.118D 14	0.590D 13	0.237D 13	0.0
40	0.117D 14	0.116D 14	0.107D 14	0.937D 13	0.709D 13	0.685D 13	0.358D 13	0.148D 13	0.0
41	0.245D 13	0.244D 13	0.225D 13	0.198D 13	0.150D 13	0.145D 13	0.765D 12	0.318D 12	0.0
42	0.123D 13	0.122D 13	0.112D 13	0.988D 12	0.751D 12	0.726D 12	0.383D 12	0.159D 12	0.0

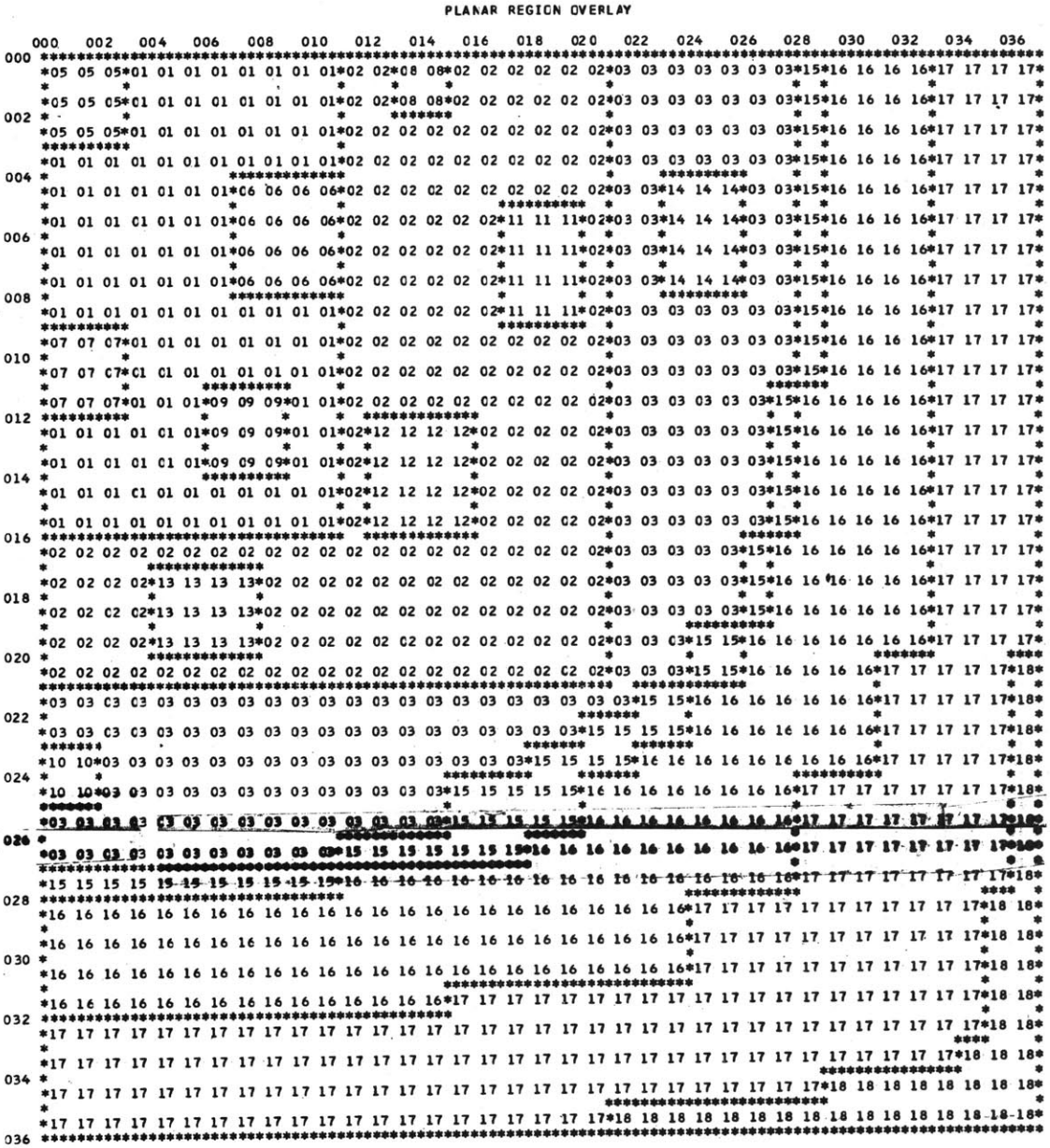

Fig.C.2 18-Planar Region MITR-I 3-Dimensional XYZ Calculational Model

TABLE C.2

Materials Corresponding to each of the 18 Regions in the MITR-I Calculational Model

Region	Material
1, 2, 3	99.5% D_2O 0.5% H_2O
5, 6, 7	105 gram elements
8, 9	shim rod positions
10	regulating rod position
11, 12, 13	160 gram elements
14	105 gram elements
15	Homogenized core tank
16, 17	grahpite**
18	neutron absorber

** Between planes 3 and 7, 17.34% void and 2.0% aluminum was included in the graphite in region 16, while 1.0% aluminum was included in the graphite in region 17.

Accumulated Distance in the XX Direction (inches)

1	0.45	2	0.90	3	1.50	4	1.92
5	2.842	6	3.750	7	4.02	8	4.92
9	5.525	10	6.272	11	7.02	12	7.87
13	8.35	14	9.25	15	10.15	16	10.87
17	11.30	18	12.3	19	13.30	20	14.30
21	15.05	22	16.30	23	17.05	24	18.05
25	26.70	26	29.00	27	21.00	28	22.75
29	24.50	30	25.70	31	26.70	32	29.00
33	32.00	34	33.50	35	39.50	36	45.50
37	48.50						

Accumulated Distance in the YY Direction (inches)

1	0.45	2	0.90	3	1.50	4	1.687
5	1.92	6	2.842	7	3.765	8	4.687
9	4.897	10	5.998	11	7.099	12	7.874
13	8.376	14	8.877	15	9.862	16	10.85
17	11.28	18	12.28	19	13.28	20	14.28
21	15.71	22	17.14	23	18.58	24	19.48
25	20.38	26	20.98	27	22.73	28	24.48
29	25.68	30	26.68	31	28.98	32	31.98
33	33.48	34	39.48	35	45.48	36	48.48

POINTWISE FLUX - GROUP 1 - PLANE 6

	0	1	2	3	4	5	6	7	8	9
0	0.799D 14	0.790D 14	0.765D 14	0.699D 14	0.633D 14	0.556D 14	0.535D 14	0.532D 14	0.532D 14	0.524D 14
1	0.790D 14	0.782D 14	0.757D 14	0.693D 14	0.629D 14	0.556D 14	0.539D 14	0.537D 14	0.539D 14	0.532D 14
2	0.765D 14	0.757D 14	0.735D 14	0.676D 14	0.617D 14	0.556D 14	0.550D 14	0.553D 14	0.564D 14	0.559D 14
3	0.699D 14	0.693D 14	0.676D 14	0.631D 14	0.591D 14	0.556D 14	0.578D 14	0.592D 14	0.626D 14	0.626D 14
4	0.666D 14	0.661D 14	0.646D 14	0.610D 14	0.582D 14	0.556D 14	0.588D 14	0.612D 14	0.655D 14	0.656D 14
5	0.632D 14	0.628D 14	0.616D 14	0.589D 14	0.570D 14	0.556D 14	0.600D 14	0.631D 14	0.683D 14	0.685D 14
6	0.559D 14	0.557D 14	0.552D 14	0.542D 14	0.539D 14	0.551D 14	0.624D 14	0.664D 14	0.732D 14	0.738D 14
7	0.558D 14	0.556D 14	0.550D 14	0.538D 14	0.532D 14	0.541D 14	0.609D 14	0.648D 14	0.714D 14	0.720D 14
8	0.633D 14	0.628D 14	0.613D 14	0.577D 14	0.550D 14	0.523D 14	0.553D 14	0.578D 14	0.623D 14	0.626D 14
9	0.664D 14	0.659D 14	0.641D 14	0.596D 14	0.555D 14	0.518D 14	0.537D 14	0.550D 14	0.583D 14	0.586D 14
10	0.731D 14	0.723D 14	0.698D 14	0.633D 14	0.568D 14	0.489D 14	0.462D 14	0.459D 14	0.459D 14	0.458D 14
11	0.698D 14	0.690D 14	0.665D 14	0.602D 14	0.537D 14	0.454D 14	0.416D 14	0.410D 14	0.403D 14	0.405D 14
12	0.612D 14	0.606D 14	0.587D 14	0.538D 14	0.492D 14	0.429D 14	0.398D 14	0.392D 14	0.386D 14	0.391D 14
13	0.531D 14	0.526D 14	0.514D 14	0.485D 14	0.460D 14	0.418D 14	0.393D 14	0.388D 14	0.382D 14	0.389D 14
14	0.475D 14	0.473D 14	0.466D 14	0.451D 14	0.439D 14	0.413D 14	0.395D 14	0.391D 14	0.385D 14	0.390D 14
15	0.424D 14	0.424D 14	0.426D 14	0.429D 14	0.432D 14	0.433D 14	0.426D 14	0.422D 14	0.407D 14	0.403D 14
16	0.416D 14	0.419D 14	0.430D 14	0.456D 14	0.479D 14	0.515D 14	0.513D 14	0.506D 14	0.462D 14	0.427D 14
17	0.416D 14	0.421D 14	0.437D 14	0.477D 14	0.524D 14	0.582D 14	0.582D 14	0.573D 14	0.505D 14	0.440D 14
18	0.415D 14	0.423D 14	0.446D 14	0.505D 14	0.571D 14	0.648D 14	0.650D 14	0.637D 14	0.547D 14	0.448D 14
19	0.388D 14	0.396D 14	0.419D 14	0.477D 14	0.541D 14	0.617D 14	0.617D 14	0.604D 14	0.513D 14	0.412D 14
20	0.333D 14	0.339D 14	0.355D 14	0.394D 14	0.436D 14	0.492D 14	0.491D 14	0.480D 14	0.406D 14	0.335D 14
21	0.230D 14	0.232D 14	0.237D 14	0.248D 14	0.256D 14	0.269D 14	0.265D 14	0.260D 14	0.232D 14	0.207D 14
22	0.148D 14	0.148D 14	0.149D 14	0.152D 14	0.153D 14	0.155D 14	0.151D 14	0.148D 14	0.136D 14	0.125D 14
23	0.918D 13	0.919D 13	0.920D 13	0.923D 13	0.923D 13	0.915D 13	0.884D 13	0.870D 13	0.808D 13	0.758D 13
24	0.674D 13	0.674D 13	0.674D 13	0.672D 13	0.670D 13	0.659D 13	0.635D 13	0.625D 13	0.585D 13	0.552D 13
25	0.493D 13	0.493D 13	0.492D 13	0.490D 13	0.487D 13	0.477D 13	0.459D 13	0.452D 13	0.425D 13	0.403D 13
26	0.400D 13	0.400D 13	0.399D 13	0.396D 13	0.393D 13	0.384D 13	0.370D 13	0.365D 13	0.344D 13	0.328D 13
27	0.228D 13	0.228D 13	0.227D 13	0.226D 13	0.224D 13	0.218D 13	0.211D 13	0.208D 13	0.198D 13	0.191D 13
28	0.145D 13	0.145D 13	0.144D 13	0.143D 13	0.142D 13	0.139D 13	0.135D 13	0.133D 13	0.127D 13	0.123D 13
29	0.105D 13	0.105D 13	0.104D 13	0.103D 13	0.103D 13	0.100D 13	0.974D 12	0.964D 12	0.925D 12	0.896D 12
30	0.793D 12	0.793D 12	0.790D 12	0.785D 12	0.779D 12	0.763D 12	0.741D 12	0.733D 12	0.705D 12	0.684D 12
31	0.429D 12	0.428D 12	0.427D 12	0.424D 12	0.421D 12	0.413D 12	0.402D 12	0.399D 12	0.385D 12	0.374D 12
32	0.195D 12	0.195D 12	0.194D 12	0.193D 12	0.192D 12	0.188D 12	0.184D 12	0.182D 12	0.176D 12	0.172D 12
33	0.119D 12	0.119D 12	0.119D 12	0.118D 12	0.118D 12	0.116D 12	0.113D 12	0.112D 12	0.109D 12	0.106D 12
34	0.263D 11	0.263D 11	0.263D 11	0.261D 11	0.260D 11	0.256D 11	0.251D 11	0.249D 11	0.242D 11	0.237D 11
35	0.523D 10	0.523D 10	0.522D 10	0.519D 10	0.517D 10	0.509D 10	0.498D 10	0.495D 10	0.481D 10	0.470D 10
36	0.0	0.0	0.0	0.0	0.0	0.0	0.0	0.0	0.0	0.0

POINTWISE FLUX - GROUP 1 - PLANE 6

	10	11	12	13	14	15	16	17	18	19
0	0.503D 14	0.471D 14	0.431D 14	0.414D 14	0.399D 14	0.406D 14	0.422D 14	0.433D 14	0.453D 14	0.446D 14
1	0.511D 14	0.477D 14	0.434D 14	0.417D 14	0.401D 14	0.409D 14	0.427D 14	0.439D 14	0.461D 14	0.454D 14
2	0.535D 14	0.495D 14	0.444D 14	0.424D 14	0.406D 14	0.417D 14	0.441D 14	0.457D 14	0.486D 14	0.478D 14
3	0.598D 14	0.540D 14	0.465D 14	0.438D 14	0.418D 14	0.435D 14	0.473D 14	0.503D 14	0.548D 14	0.538D 14
4	0.627D 14	0.560D 14	0.472D 14	0.443D 14	0.421D 14	0.441D 14	0.486D 14	0.524D 14	0.577D 14	0.566D 14
5	0.655D 14	0.581D 14	0.481D 14	0.448D 14	0.426D 14	0.448D 14	0.501D 14	0.555D 14	0.618D 14	0.605D 14
6	0.706D 14	0.623D 14	0.504D 14	0.466D 14	0.442D 14	0.474D 14	0.548D 14	0.620D 14	0.699D 14	0.682D 14
7	0.695D 14	0.611D 14	0.499D 14	0.464D 14	0.444D 14	0.477D 14	0.550D 14	0.622D 14	0.698D 14	0.679D 14
8	0.604D 14	0.546D 14	0.471D 14	0.447D 14	0.434D 14	0.458D 14	0.511D 14	0.564D 14	0.620D 14	0.598D 14
9	0.567D 14	0.521D 14	0.464D 14	0.444D 14	0.433D 14	0.454D 14	0.498D 14	0.538D 14	0.586D 14	0.563D 14
10	0.454D 14	0.446D 14	0.437D 14	0.434D 14	0.432D 14	0.433D 14	0.436D 14	0.437D 14	0.429D 14	0.397D 14
11	0.414D 14	0.432D 14	0.463D 14	0.478D 14	0.488D 14	0.471D 14	0.440D 14	0.416D 14	0.362D 14	0.312D 14
12	0.410D 14	0.449D 14	0.528D 14	0.569D 14	0.593D 14	0.562D 14	0.493D 14	0.436D 14	0.342D 14	0.276D 14
13	0.412D 14	0.461D 14	0.567D 14	0.620D 14	0.648D 14	0.611D 14	0.526D 14	0.449D 14	0.332D 14	0.258D 14
14	0.414D 14	0.467D 14	0.585D 14	0.642D 14	0.672D 14	0.631D 14	0.538D 14	0.452D 14	0.322D 14	0.242D 14
15	0.415D 14	0.459D 14	0.568D 14	0.622D 14	0.648D 14	0.605D 14	0.510D 14	0.423D 14	0.292D 14	0.212D 14
16	0.407D 14	0.420D 14	0.482D 14	0.519D 14	0.532D 14	0.492D 14	0.414D 14	0.348D 14	0.245D 14	0.178D 14
17	0.401D 14	0.396D 14	0.423D 14	0.438D 14	0.441D 14	0.405D 14	0.347D 14	0.305D 14	0.222D 14	0.163D 14
18	0.376D 14	0.339D 14	0.323D 14	0.317D 14	0.303D 14	0.274D 14	0.241D 14	0.219D 14	0.169D 14	0.129D 14
19	0.332D 14	0.284D 14	0.252D 14	0.238D 14	0.217D 14	0.193D 14	0.171D 14	0.158D 14	0.126D 14	0.988D 13
20	0.272D 14	0.228D 14	0.195D 14	0.181D 14	0.159D 14	0.139D 14	0.124D 14	0.114D 14	0.934D 13	0.748D 13
21	0.178D 14	0.154D 14	0.131D 14	0.121D 14	0.104D 14	0.902D 13	0.798D 13	0.740D 13	0.613D 13	0.501D 13
22	0.112D 14	0.988D 13	0.857D 13	0.791D 13	0.682D 13	0.588D 13	0.521D 13	0.484D 13	0.405D 13	0.337D 13
23	0.695D 13	0.621D 13	0.548D 13	0.509D 13	0.443D 13	0.385D 13	0.343D 13	0.320D 13	0.271D 13	0.230D 13
24	0.507D 13	0.462D 13	0.412D 13	0.385D 13	0.337D 13	0.294D 13	0.264D 13	0.248D 13	0.214D 13	0.186D 13
25	0.374D 13	0.344D 13	0.310D 13	0.291D 13	0.259D 13	0.229D 13	0.209D 13	0.197D 13	0.173D 13	0.152D 13
26	0.306D 13	0.282D 13	0.257D 13	0.243D 13	0.217D 13	0.195D 13	0.179D 13	0.170D 13	0.151D 13	0.133D 13
27	0.182D 13	0.173D 13	0.163D 13	0.156D 13	0.143D 13	0.130D 13	0.120D 13	0.114D 13	0.102D 13	0.899D 12
28	0.118D 13	0.112D 13	0.105D 13	0.101D 13	0.927D 12	0.849D 12	0.788D 12	0.753D 12	0.674D 12	0.600D 12
29	0.858D 12	0.817D 12	0.767D 12	0.739D 12	0.684D 12	0.629D 12	0.586D 12	0.561D 12	0.504D 12	0.451D 12
30	0.656D 12	0.626D 12	0.589D 12	0.568D 12	0.528D 12	0.488D 12	0.456D 12	0.437D 12	0.394D 12	0.354D 12
31	0.360D 12	0.345D 12	0.326D 12	0.316D 12	0.295D 12	0.275D 12	0.258D 12	0.248D 12	0.225D 12	0.203D 12
32	0.166D 12	0.159D 12	0.151D 12	0.147D 12	0.137D 12	0.128D 12	0.119D 12	0.115D 12	0.104D 12	0.947D 11
33	0.103D 12	0.988D 11	0.941D 11	0.913D 11	0.859D 11	0.802D 11	0.757D 11	0.730D 11	0.668D 11	0.608D 11
34	0.230D 11	0.222D 11	0.212D 11	0.207D 11	0.195D 11	0.184D 11	0.174D 11	0.168D 11	0.155D 11	0.142D 11
35	0.455D 10	0.438D 10	0.416D 10	0.403D 10	0.375D 10	0.343D 10	0.314D 10	0.294D 10	0.242D 10	0.175D 10
36	0.0	0.0	0.0	0.0	0.0	0.0	0.0	0.0	0.0	0.0

POINTWISE FLUX - GROUP 1 - PLANE 6

	20	21	22	23	24	25	26	27	28	29
0	0.414D 14	0.385D 14	0.348D 14	0.335D 14	0.318D 14	0.286D 14	0.238D 14	0.187D 14	0.111D 14	0.707D 13
1	0.419D 14	0.388D 14	0.351D 14	0.339D 14	0.323D 14	0.291D 14	0.241D 14	0.188D 14	0.111D 14	0.706D 13
2	0.436D 14	0.399D 14	0.359D 14	0.351D 14	0.339D 14	0.306D 14	0.252D 14	0.192D 14	0.112D 14	0.705D 13
3	0.478D 14	0.422D 14	0.376D 14	0.380D 14	0.379D 14	0.345D 14	0.278D 14	0.200D 14	0.112D 14	0.701D 13
4	0.497D 14	0.430D 14	0.382D 14	0.392D 14	0.397D 14	0.363D 14	0.289D 14	0.203D 14	0.112D 14	0.699D 13
5	0.524D 14	0.440D 14	0.388D 14	0.406D 14	0.415D 14	0.380D 14	0.302D 14	0.206D 14	0.112D 14	0.695D 13
6	0.581D 14	0.468D 14	0.405D 14	0.429D 14	0.445D 14	0.409D 14	0.322D 14	0.211D 14	0.111D 14	0.675D 13
7	0.574D 14	0.458D 14	0.390D 14	0.412D 14	0.426D 14	0.391D 14	0.307D 14	0.200D 14	0.105D 14	0.638D 13
8	0.505D 14	0.408D 14	0.343D 14	0.351D 14	0.356D 14	0.324D 14	0.254D 14	0.173D 14	0.942D 13	0.584D 13
9	0.477D 14	0.393D 14	0.330D 14	0.329D 14	0.327D 14	0.296D 14	0.235D 14	0.166D 14	0.914D 13	0.570D 13
10	0.344D 14	0.302D 14	0.254D 14	0.238D 14	0.221D 14	0.196D 14	0.161D 14	0.125D 14	0.755D 13	0.491D 13
11	0.265D 14	0.233D 14	0.193D 14	0.176D 14	0.156D 14	0.136D 14	0.114D 14	0.920D 13	0.613D 13	0.413D 13
12	0.227D 14	0.197D 14	0.160D 14	0.143D 14	0.125D 14	0.107D 14	0.903D 13	0.748D 13	0.525D 13	0.359D 13
13	0.207D 14	0.178D 14	0.142D 14	0.126D 14	0.108D 14	0.927D 13	0.781D 13	0.655D 13	0.472D 13	0.327D 13
14	0.190D 14	0.161D 14	0.127D 14	0.111D 14	0.946D 13	0.805D 13	0.680D 13	0.575D 13	0.424D 13	0.298D 13
15	0.161D 14	0.134D 14	0.102D 14	0.882D 13	0.737D 13	0.621D 13	0.525D 13	0.450D 13	0.342D 13	0.246D 13
16	0.134D 14	0.110D 14	0.827D 13	0.706D 13	0.582D 13	0.487D 13	0.413D 13	0.361D 13	0.278D 13	0.202D 13
17	0.123D 14	0.101D 14	0.753D 13	0.640D 13	0.525D 13	0.439D 13	0.373D 13	0.328D 13	0.253D 13	0.185D 13
18	0.984D 13	0.811D 13	0.603D 13	0.511D 13	0.418D 13	0.349D 13	0.298D 13	0.264D 13	0.204D 13	0.151D 13
19	0.770D 13	0.641D 13	0.480D 13	0.407D 13	0.333D 13	0.280D 13	0.243D 13	0.214D 13	0.165D 13	0.124D 13
20	0.594D 13	0.500D 13	0.379D 13	0.324D 13	0.268D 13	0.228D 13	0.199D 13	0.174D 13	0.134D 13	0.101D 13
21	0.407D 13	0.346D 13	0.270D 13	0.235D 13	0.200D 13	0.173D 13	0.150D 13	0.130D 13	0.100D 13	0.757D 12
22	0.279D 13	0.243D 13	0.195D 13	0.174D 13	0.151D 13	0.130D 13	0.112D 13	0.975D 12	0.749D 12	0.568D 12
23	0.197D 13	0.176D 13	0.146D 13	0.131D 13	0.114D 13	0.976D 12	0.841D 12	0.729D 12	0.561D 12	0.426D 12
24	0.162D 13	0.146D 13	0.122D 13	0.109D 13	0.942D 12	0.812D 12	0.699D 12	0.607D 12	0.468D 12	0.355D 12
25	0.133D 13	0.120D 13	0.101D 13	0.902D 12	0.780D 12	0.673D 12	0.581D 12	0.504D 12	0.388D 12	0.293D 12
26	0.117D 13	0.105D 13	0.883D 12	0.793D 12	0.687D 12	0.593D 12	0.512D 12	0.445D 12	0.342D 12	0.258D 12
27	0.791D 12	0.716D 12	0.605D 12	0.545D 12	0.474D 12	0.411D 12	0.356D 12	0.309D 12	0.238D 12	0.178D 12
28	0.531D 12	0.483D 12	0.411D 12	0.372D 12	0.326D 12	0.284D 12	0.246D 12	0.214D 12	0.164D 12	0.123D 12
29	0.401D 12	0.366D 12	0.313D 12	0.284D 12	0.249D 12	0.216D 12	0.187D 12	0.162D 12	0.125D 12	0.944D 11
30	0.315D 12	0.289D 12	0.247D 12	0.225D 12	0.197D 12	0.171D 12	0.148D 12	0.129D 12	0.990D 11	0.753D 11
31	0.183D 12	0.168D 12	0.145D 12	0.132D 12	0.115D 12	0.100D 12	0.869D 11	0.758D 11	0.586D 11	0.448D 11
32	0.854D 11	0.787D 11	0.683D 11	0.625D 11	0.552D 11	0.485D 11	0.424D 11	0.372D 11	0.290D 11	0.222D 11
33	0.550D 11	0.509D 11	0.444D 11	0.408D 11	0.362D 11	0.319D 11	0.280D 11	0.246D 11	0.192D 11	0.146D 11
34	0.128D 11	0.119D 11	0.103D 11	0.944D 10	0.829D 10	0.717D 10	0.605D 10	0.495D 10	0.277D 10	0.147D 08
35	0.879D 09	0.154D 08	0.237D 07	0.213D 07	0.187D 07	0.162D 07	0.136D 07	0.112D 07	0.626D 06	0.164D 04
36	0.0	0.0	0.0	0.0	0.0	0.0	0.0	0.0	0.0	0.0

POINTWISE FLUX - GROUP 1 - PLANE 6

	30	31	32	33	34	35	36	37
0	C.5C5D 13	C.378D 13	0.199D 13	0.881D 12	C.530D 12	0.113C 12	0.221C 11	0.0
1	C.5C4C 13	0.378D 13	0.199D 13	C.880D 12	0.529D 12	C.113D 12	C.221D 11	0.0
2	C.5C2C 13	C.376D 13	0.198D 13	0.876D 12	C.527C 12	C.113D 12	0.220D 11	0.0
3	C.498D 13	0.372D 13	0.196D 13	0.867D 12	C.522D 12	0.112D 12	0.218D 11	C.0
4	C.496C 13	0.371C 13	0.195D 13	C.864D 12	C.520D 12	C.111D 12	C.218D 11	0.0
5	C.493D 13	C.368D 13	0.194D 13	C.858D 12	0.518D 12	0.111D 12	0.217D 11	0.0
6	0.476D 13	0.355D 13	0.187D 13	0.832D 12	C.503D 12	0.108D 12	C.212D 11	C.0
7	C.450D 13	0.337D 13	0.178C 13	0.797D 12	0.484D 12	0.105D 12	0.205C 11	0.0
8	C.416D 13	0.312D 13	0.167D 13	C.753D 12	C.460D 12	0.100D 12	C.197C 11	0.0
9	C.4C7C 13	0.307C 13	0.164D 13	0.743D 12	0.454D 12	C.993D 11	C.195D 11	C.0
10	0.358C 13	0.273D 13	0.149D 13	0.681D 12	0.420D 12	C.931D 11	0.183D 11	0.0
11	C.3C6D 13	0.237D 13	0.132C 13	0.615D 12	0.383C 12	0.861D 11	0.169D 11	C.0
12	0.271C 13	0.212D 13	0.120D 13	0.566D 12	0.356D 12	0.809D 11	0.158D 11	0.0
13	C.249C 13	0.196D 13	0.112D 13	0.535D 12	0.338D 12	C.775D 11	C.150D 11	0.0
14	C.228D 13	C.181D 13	0.105D 13	0.504D 12	0.320D 12	C.740D 11	0.142D 11	0.0
15	0.191C 13	0.154D 13	0.909D 12	0.445D 12	0.286D 12	0.672D 11	C.125D 11	C.0
16	C.159D 13	0.129D 13	C.780D 12	0.389D 12	0.253D 12	0.604D 11	0.106C 11	0.0
17	C.147C 13	0.120C 13	0.728D 12	C.366D 12	C.239D 12	0.575D 11	C.964D 10	0.0
18	C.121C 13	C.996D 12	0.617D 12	0.315D 12	C.208D 12	0.508D 11	0.715D 10	C.0
19	C.997D 12	0.826D 12	0.519D 12	0.269D 12	C.180D 12	0.446D 11	0.406D 10	0.0
20	C.82CD 12	0.685D 12	0.435D 12	0.228D 12	0.154C 12	0.387D 11	0.488D C8	0.0
21	0.618D 12	C.518D 12	0.331D 12	0.176D 12	0.122D 12	0.313D 11	0.714D 07	0.0
22	C.465D 12	0.391C 12	0.251D 12	0.136D 12	C.953D 11	0.248D 11	C.560D C7	C.0
23	C.349C 12	0.293D 12	0.190D 12	0.104D 12	0.736D 11	C.192D 11	0.434D C7	0.0
24	C.291C 12	0.244D 12	0.158C 12	0.874D 11	0.623C 11	0.161D 11	0.363D 07	0.0
25	C.240D 12	0.201D 12	0.132D 12	C.734D 11	C.526D 11	0.131D 11	C.296D 07	0.0
26	C.211C 12	0.177C 12	0.117D 12	0.652D 11	0.468D 11	0.112D 11	0.254D 07	C.0
27	C.146D 12	0.123D 12	0.816D 11	0.461D 11	C.331D 11	0.592C 10	0.134D 07	0.0
28	0.101D 12	0.849D 11	0.568D 11	0.322D 11	C.230D 11	C.291D C8	C.332D 04	C.0
29	C.775D 11	0.654D 11	0.439D 11	0.250D 11	0.178D 11	0.205D C7	0.126D 01	0.0
30	C.620D 11	0.524C 11	0.353D 11	0.200D 11	0.143D 11	0.161D C7	C.958D C0	0.0
31	C.37CD 11	C.314D 11	0.212D 11	0.119D 11	0.831D 10	0.938D 06	0.558D 00	0.0
32	0.184D 11	C.156D 11	0.104D 11	0.515D 10	C.292D 10	C.330D C6	0.196D 00	0.0
33	C.121D 11	C.102D 11	0.662D 10	0.258D 10	C.310D 07	0.107D 03	0.641D-04	C.0
34	C.13EC C7	0.115C 07	0.747C 06	0.291D C6	C.990C C2	0.919D-C4	C.833D-10	0.0
35	C.843C C0	C.685D CC	0.444D C0	0.173D 00	C.594D-C4	0.812C-10	C.978C-16	0.0
36	C.C	0.0	0.0	0.0	0.0	C.C	0.0	0.0

POINTWISE FLUX - GROUP 2 - PLANE 6

	0	1	2	3	4	5	6	7	8	9
0	0.522D 14	0.522D 14	0.522D 14	0.522D 14	0.522D 14	0.515D 14	0.507D 14	0.505D 14	0.497D 14	0.490D 14
1	0.522D 14	0.522D 14	0.522D 14	0.522D 14	0.521D 14	0.515D 14	0.507D 14	0.505D 14	0.497D 14	0.490D 14
2	0.522D 14	0.521D 14	0.521D 14	0.521D 14	0.520D 14	0.514D 14	0.507D 14	0.504D 14	0.496D 14	0.490D 14
3	0.521D 14	0.521D 14	0.521D 14	0.519D 14	0.518D 14	0.512D 14	0.505D 14	0.502D 14	0.494D 14	0.488D 14
4	0.521D 14	0.521D 14	0.520D 14	0.519D 14	0.517D 14	0.511D 14	0.504D 14	0.501D 14	0.493D 14	0.486D 14
5	0.521D 14	0.520D 14	0.520D 14	0.517D 14	0.516D 14	0.510D 14	0.503D 14	0.499D 14	0.491D 14	0.485D 14
6	0.513D 14	0.513D 14	0.512D 14	0.510D 14	0.508D 14	0.504D 14	0.497D 14	0.494D 14	0.485D 14	0.480D 14
7	0.504D 14	0.504D 14	0.503D 14	0.501D 14	0.500D 14	0.495D 14	0.490D 14	0.486D 14	0.479D 14	0.474D 14
8	0.493D 14	0.493D 14	0.492D 14	0.491D 14	0.490D 14	0.485D 14	0.479D 14	0.477D 14	0.471D 14	0.466D 14
9	0.485D 14	0.485D 14	0.485D 14	0.488D 14	0.487D 14	0.482D 14	0.476D 14	0.474D 14	0.469D 14	0.464D 14
10	0.475D 14	0.475D 14	0.474D 14	0.474D 14	0.473D 14	0.465D 14	0.457D 14	0.455D 14	0.448D 14	0.444D 14
11	0.460D 14	0.460D 14	0.459D 14	0.457D 14	0.455D 14	0.446D 14	0.437D 14	0.434D 14	0.427D 14	0.424D 14
12	0.450D 14	0.450D 14	0.449D 14	0.446D 14	0.442D 14	0.432D 14	0.423D 14	0.421D 14	0.414D 14	0.411D 14
13	0.442D 14	0.441D 14	0.440D 14	0.436D 14	0.433D 14	0.424D 14	0.416D 14	0.413D 14	0.407D 14	0.403D 14
14	0.431D 14	0.431D 14	0.430D 14	0.427D 14	0.424D 14	0.416D 14	0.409D 14	0.406D 14	0.400D 14	0.396D 14
15	0.412D 14	0.411D 14	0.411D 14	0.409D 14	0.407D 14	0.402D 14	0.396D 14	0.394D 14	0.387D 14	0.382D 14
16	0.394D 14	0.393D 14	0.393D 14	0.392D 14	0.391D 14	0.387D 14	0.381D 14	0.379D 14	0.372D 14	0.366D 14
17	0.385D 14	0.385D 14	0.385D 14	0.384D 14	0.381D 14	0.376D 14	0.370D 14	0.368D 14	0.362D 14	0.357D 14
18	0.364D 14	0.364D 14	0.364D 14	0.363D 14	0.360D 14	0.355D 14	0.349D 14	0.347D 14	0.341D 14	0.333D 14
19	0.336D 14	0.337D 14	0.337D 14	0.337D 14	0.335D 14	0.330D 14	0.324D 14	0.322D 14	0.314D 14	0.304D 14
20	0.301D 14	0.301D 14	0.302D 14	0.304D 14	0.304D 14	0.303D 14	0.297D 14	0.294D 14	0.282D 14	0.269D 14
21	0.240D 14	0.240D 14	0.240D 14	0.240D 14	0.240D 14	0.238D 14	0.232D 14	0.229D 14	0.218D 14	0.208D 14
22	0.180D 14	0.180D 14	0.179D 14	0.179D 14	0.178D 14	0.176D 14	0.171D 14	0.169D 14	0.160D 14	0.153D 14
23	0.129D 14	0.129D 14	0.129D 14	0.128D 14	0.128D 14	0.125D 14	0.121D 14	0.120D 14	0.114D 14	0.109D 14
24	0.104D 14	0.104D 14	0.104D 14	0.103D 14	0.102D 14	0.100D 14	0.969D 13	0.958D 13	0.913D 13	0.878D 13
25	0.828D 13	0.828D 13	0.825D 13	0.820D 13	0.814D 13	0.797D 13	0.772D 13	0.763D 13	0.728D 13	0.702D 13
26	0.711D 13	0.710D 13	0.708D 13	0.703D 13	0.699D 13	0.683D 13	0.662D 13	0.655D 13	0.626D 13	0.604D 13
27	0.463D 13	0.462D 13	0.461D 13	0.458D 13	0.455D 13	0.445D 13	0.433D 13	0.429D 13	0.413D 13	0.402D 13
28	0.330D 13	0.330D 13	0.329D 13	0.327D 13	0.324D 13	0.318D 13	0.310D 13	0.307D 13	0.297D 13	0.289D 13
29	0.253D 13	0.252D 13	0.252D 13	0.250D 13	0.249D 13	0.244D 13	0.238D 13	0.236D 13	0.228D 13	0.223D 13
30	0.201D 13	0.201D 13	0.201D 13	0.200D 13	0.198D 13	0.195D 13	0.190D 13	0.189D 13	0.183D 13	0.178D 13
31	0.120D 13	0.120D 13	0.119D 13	0.119D 13	0.118D 13	0.116D 13	0.114D 13	0.113D 13	0.109D 13	0.107D 13
32	0.606D 12	0.606D 12	0.604D 12	0.601D 12	0.598D 12	0.589D 12	0.577D 12	0.573D 12	0.557D 12	0.545D 12
33	0.399D 12	0.399D 12	0.398D 12	0.396D 12	0.394D 12	0.389D 12	0.381D 12	0.378D 12	0.368D 12	0.360D 12
34	0.101D 12	0.101D 12	0.100D 12	0.100D 12	0.995D 11	0.982D 11	0.964D 11	0.957D 11	0.934D 11	0.916D 11
35	0.216D 11	0.215D 11	0.215D 11	0.214D 11	0.213D 11	0.210D 11	0.206D 11	0.205D 11	0.199D 11	0.195D 11
36	0.0	0.0	0.0	0.0	0.0	0.0	0.0	0.0	0.0	0.0

POINTWISE FLUX - GROUP 2 - PLANE 6

	10	11	12	13	14	15	16	17	18	19
0	0.480D 14	0.468D 14	0.454D 14	0.447D 14	0.436D 14	0.428D 14	0.424D 14	0.421D 14	0.413D 14	0.399D 14
1	0.480D 14	0.468D 14	0.454D 14	0.447D 14	0.436D 14	0.429D 14	0.424D 14	0.421D 14	0.413D 14	0.399D 14
2	0.480D 14	0.469D 14	0.455D 14	0.448D 14	0.437D 14	0.429D 14	0.424D 14	0.421D 14	0.413D 14	0.399D 14
3	0.479D 14	0.469D 14	0.456D 14	0.448D 14	0.437D 14	0.430D 14	0.425D 14	0.421D 14	0.412D 14	0.398D 14
4	0.478D 14	0.469D 14	0.456D 14	0.448D 14	0.437D 14	0.430D 14	0.424D 14	0.420D 14	0.411D 14	0.397D 14
5	0.477D 14	0.469D 14	0.456D 14	0.449D 14	0.437D 14	0.430D 14	0.424D 14	0.419D 14	0.409D 14	0.395D 14
6	0.473D 14	0.467D 14	0.455D 14	0.447D 14	0.436D 14	0.428D 14	0.422D 14	0.415D 14	0.403D 14	0.388D 14
7	0.467D 14	0.461D 14	0.449D 14	0.443D 14	0.432D 14	0.424D 14	0.416D 14	0.409D 14	0.395D 14	0.380D 14
8	0.459D 14	0.452D 14	0.441D 14	0.434D 14	0.424D 14	0.415D 14	0.407D 14	0.401D 14	0.387D 14	0.369D 14
9	0.457D 14	0.449D 14	0.438D 14	0.432D 14	0.422D 14	0.413D 14	0.405D 14	0.399D 14	0.385D 14	0.366D 14
10	0.438D 14	0.432D 14	0.423D 14	0.419D 14	0.409D 14	0.398D 14	0.388D 14	0.381D 14	0.362D 14	0.338D 14
11	0.419D 14	0.415D 14	0.409D 14	0.405D 14	0.395D 14	0.382D 14	0.369D 14	0.360D 14	0.335D 14	0.306D 14
12	0.407D 14	0.404D 14	0.397D 14	0.391D 14	0.381D 14	0.367D 14	0.355D 14	0.345D 14	0.316D 14	0.285D 14
13	0.400D 14	0.396D 14	0.389D 14	0.383D 14	0.371D 14	0.357D 14	0.346D 14	0.335D 14	0.304D 14	0.271D 14
14	0.393D 14	0.389D 14	0.380D 14	0.374D 14	0.362D 14	0.347D 14	0.335D 14	0.324D 14	0.291D 14	0.257D 14
15	0.377D 14	0.372D 14	0.362D 14	0.355D 14	0.342D 14	0.326D 14	0.312D 14	0.300D 14	0.265D 14	0.230D 14
16	0.358D 14	0.350D 14	0.340D 14	0.334D 14	0.320D 14	0.302D 14	0.284D 14	0.270D 14	0.236D 14	0.203D 14
17	0.348D 14	0.338D 14	0.328D 14	0.321D 14	0.306D 14	0.287D 14	0.268D 14	0.255D 14	0.222D 14	0.191D 14
18	0.321D 14	0.307D 14	0.292D 14	0.284D 14	0.267D 14	0.247D 14	0.229D 14	0.217D 14	0.189D 14	0.163D 14
19	0.288D 14	0.272D 14	0.255D 14	0.245D 14	0.227D 14	0.208D 14	0.192D 14	0.182D 14	0.159D 14	0.137D 14
20	0.252D 14	0.235D 14	0.217D 14	0.207D 14	0.190D 14	0.172D 14	0.158D 14	0.150D 14	0.131D 14	0.113D 14
21	0.195D 14	0.181D 14	0.166D 14	0.158D 14	0.143D 14	0.129D 14	0.119D 14	0.112D 14	0.981D 13	0.851D 13
22	0.144D 14	0.134D 14	0.123D 14	0.117D 14	0.106D 14	0.954D 13	0.874D 13	0.828D 13	0.727D 13	0.635D 13
23	0.103D 14	0.966D 13	0.890D 13	0.847D 13	0.769D 13	0.695D 13	0.638D 13	0.606D 13	0.536D 13	0.475D 13
24	0.830D 13	0.780D 13	0.721D 13	0.688D 13	0.627D 13	0.567D 13	0.524D 13	0.500D 13	0.449D 13	0.405D 13
25	0.666D 13	0.627D 13	0.583D 13	0.558D 13	0.513D 13	0.469D 13	0.438D 13	0.421D 13	0.383D 13	0.348D 13
26	0.575D 13	0.542D 13	0.507D 13	0.487D 13	0.450D 13	0.415D 13	0.390D 13	0.376D 13	0.346D 13	0.316D 13
27	0.388D 13	0.377D 13	0.361D 13	0.350D 13	0.328D 13	0.305D 13	0.288D 13	0.277D 13	0.253D 13	0.229D 13
28	0.279D 13	0.268D 13	0.253D 13	0.245D 13	0.230D 13	0.215D 13	0.202D 13	0.195D 13	0.179D 13	0.162D 13
29	0.215D 13	0.207D 13	0.196D 13	0.190D 13	0.179D 13	0.167D 13	0.158D 13	0.152D 13	0.140D 13	0.127D 13
30	0.172D 13	0.166D 13	0.158D 13	0.153D 13	0.144D 13	0.135D 13	0.128D 13	0.123D 13	0.113D 13	0.104D 13
31	0.104D 13	0.999D 12	0.954D 12	0.928D 12	0.878D 12	0.828D 12	0.785D 12	0.760D 12	0.701D 12	0.642D 12
32	0.528D 12	0.510D 12	0.488D 12	0.475D 12	0.449D 12	0.422D 12	0.398D 12	0.385D 12	0.355D 12	0.325D 12
33	0.350D 12	0.338D 12	0.324D 12	0.316D 12	0.299D 12	0.282D 12	0.268D 12	0.260D 12	0.240D 12	0.221D 12
34	0.891D 11	0.863D 11	0.830D 11	0.810D 11	0.770D 11	0.728D 11	0.694D 11	0.673D 11	0.624D 11	0.574D 11
35	0.189D 11	0.183D 11	0.174D 11	0.169D 11	0.157D 11	0.144D 11	0.132D 11	0.124D 11	0.102D 11	0.739D 10
36	0.0	0.0	0.0	0.0	0.0	0.0	0.0	0.0	0.0	0.0

POINTWISE FLUX - GROUP 2 - PLANE 6

	20	21	22	23	24	25	26	27	28	29
0	0.379D 14	0.362D 14	0.329D 14	0.309D 14	0.282D 14	0.254D 14	0.223D 14	0.192D 14	0.138D 14	0.102D 14
1	0.380D 14	0.362D 14	0.329D 14	0.309D 14	0.282D 14	0.254D 14	0.223D 14	0.192D 14	0.137D 14	0.102D 14
2	0.380D 14	0.362D 14	0.328D 14	0.308D 14	0.281D 14	0.253D 14	0.223D 14	0.191D 14	0.137D 14	0.102D 14
3	0.380D 14	0.362D 14	0.327D 14	0.305D 14	0.278D 14	0.251D 14	0.223D 14	0.191D 14	0.136D 14	0.101D 14
4	0.379D 14	0.361D 14	0.326D 14	0.303D 14	0.277D 14	0.250D 14	0.223D 14	0.190D 14	0.135D 14	0.100D 14
5	0.378D 14	0.361D 14	0.325D 14	0.301D 14	0.275D 14	0.249D 14	0.222D 14	0.190D 14	0.135D 14	0.998D 13
6	0.374D 14	0.356D 14	0.319D 14	0.294D 14	0.268D 14	0.242D 14	0.218D 14	0.185D 14	0.131D 14	0.968D 13
7	0.364D 14	0.345D 14	0.307D 14	0.283D 14	0.257D 14	0.232D 14	0.208D 14	0.177D 14	0.125D 14	0.924D 13
8	0.348D 14	0.327D 14	0.290D 14	0.268D 14	0.245D 14	0.220D 14	0.194D 14	0.164D 14	0.116D 14	0.867D 13
9	0.344D 14	0.322D 14	0.285D 14	0.264D 14	0.240D 14	0.215D 14	0.189D 14	0.160D 14	0.114D 14	0.853D 13
10	0.311D 14	0.290D 14	0.254D 14	0.235D 14	0.211D 14	0.187D 14	0.163D 14	0.140D 14	0.102D 14	0.773D 13
11	0.277D 14	0.255D 14	0.221D 14	0.203D 14	0.180D 14	0.159D 14	0.138D 14	0.119D 14	0.907D 13	0.689D 13
12	0.254D 14	0.232D 14	0.199D 14	0.181D 14	0.160D 14	0.140D 14	0.122D 14	0.106D 14	0.825D 13	0.624D 13
13	0.239D 14	0.218D 14	0.185D 14	0.168D 14	0.148D 14	0.129D 14	0.112D 14	0.977D 13	0.773D 13	0.585D 13
14	0.225D 14	0.204D 14	0.172D 14	0.156D 14	0.136D 14	0.119D 14	0.103D 14	0.903D 13	0.721D 13	0.547D 13
15	0.199D 14	0.178D 14	0.149D 14	0.133D 14	0.116D 14	0.101D 14	0.878D 13	0.775D 13	0.626D 13	0.478D 13
16	0.174D 14	0.154D 14	0.128D 14	0.114D 14	0.984D 13	0.855D 13	0.747D 13	0.671D 13	0.543D 13	0.415D 13
17	0.162D 14	0.145D 14	0.119D 14	0.106D 14	0.915D 13	0.795D 13	0.697D 13	0.629D 13	0.506D 13	0.389D 13
18	0.139D 14	0.123D 14	0.101D 14	0.897D 13	0.773D 13	0.673D 13	0.594D 13	0.539D 13	0.431D 13	0.335D 13
19	0.117D 14	0.103D 14	0.848D 13	0.755D 13	0.650D 13	0.570D 13	0.511D 13	0.462D 13	0.368D 13	0.287D 13
20	0.969D 13	0.862D 13	0.709D 13	0.634D 13	0.551D 13	0.489D 13	0.440D 13	0.393D 13	0.313D 13	0.245D 13
21	0.734D 13	0.656D 13	0.546D 13	0.495D 13	0.442D 13	0.396D 13	0.354D 13	0.313D 13	0.248D 13	0.195D 13
22	0.552D 13	0.499D 13	0.426D 13	0.392D 13	0.354D 13	0.314D 13	0.278D 13	0.247D 13	0.196D 13	0.154D 13
23	0.424D 13	0.391D 13	0.342D 13	0.316D 13	0.282D 13	0.248D 13	0.219D 13	0.194D 13	0.155D 13	0.121D 13
24	0.368D 13	0.341D 13	0.297D 13	0.271D 13	0.241D 13	0.213D 13	0.188D 13	0.166D 13	0.133D 13	0.104D 13
25	0.316D 13	0.291D 13	0.253D 13	0.232D 13	0.206D 13	0.182D 13	0.161D 13	0.142D 13	0.114D 13	0.886D 12
26	0.285D 13	0.262D 13	0.227D 13	0.208D 13	0.185D 13	0.164D 13	0.144D 13	0.128D 13	0.102D 13	0.794D 12
27	0.206D 13	0.190D 13	0.165D 13	0.151D 13	0.135D 13	0.120D 13	0.106D 13	0.937D 12	0.745D 12	0.577D 12
28	0.147D 13	0.136D 13	0.119D 13	0.109D 13	0.977D 12	0.868D 12	0.768D 12	0.680D 12	0.538D 12	0.416D 12
29	0.116D 13	0.107D 13	0.938D 12	0.864D 12	0.773D 12	0.683D 12	0.603D 12	0.534D 12	0.423D 12	0.329D 12
30	0.941D 12	0.873D 12	0.767D 12	0.707D 12	0.632D 12	0.558D 12	0.492D 12	0.435D 12	0.345D 12	0.270D 12
31	0.586D 12	0.545D 12	0.479D 12	0.442D 12	0.394D 12	0.348D 12	0.306D 12	0.271D 12	0.215D 12	0.169D 12
32	0.297D 12	0.277D 12	0.245D 12	0.226D 12	0.203D 12	0.181D 12	0.160D 12	0.142D 12	0.113D 12	0.888D 11
33	0.202D 12	0.189D 12	0.167D 12	0.155D 12	0.139D 12	0.124D 12	0.110D 12	0.982D 11	0.779D 11	0.606D 11
34	0.524D 11	0.487D 11	0.428D 11	0.394D 11	0.348D 11	0.303D 11	0.257D 11	0.211D 11	0.119D 11	0.485D 08
35	0.369D 10	0.503D 08	0.761D 07	0.690D 07	0.611D 07	0.531D 07	0.451D 07	0.371D 07	0.208D 07	0.421D 04
36	0.0	0.0	0.0	0.0	0.0	0.0	0.0	0.0	0.0	0.0

POINTWISE FLUX - GROUP 2 - PLANE 6

	30	31	32	33	34	35	36	37
0	0.8CCD 13	0.647D 13	0.394D 13	0.203D 13	0.135C 13	0.348D 12	0.751D 11	0.0
1	0.799C 13	0.646C 13	0.393D 13	0.203D 13	0.135D 13	0.347D 12	0.750C 11	0.0
2	0.795D 13	0.643C 13	0.391D 13	0.202D 13	0.135D 13	0.346D 12	0.748D 11	0.0
3	0.788D 13	0.637D 13	0.388D 13	0.200D 13	0.134D 13	0.344C 12	0.743D 11	0.0
4	0.784C 13	0.634C 13	0.386D 13	0.200D 13	0.133D 13	0.343D 12	0.741D 11	0.0
5	0.78CD 13	0.631D 13	0.384D 13	0.199D 13	0.133D 13	0.342D 12	0.738D 11	0.0
6	0.756D 13	0.612C 13	0.374D 13	0.194D 13	0.130D 13	0.335D 12	0.723D 11	0.0
7	0.723D 13	0.586D 13	0.359D 13	0.187D 13	0.125D 13	0.325D 12	0.703D 11	0.0
8	0.682C 13	0.554D 13	0.341D 13	0.179D 13	0.120D 13	0.314D 12	0.678D 11	0.0
9	0.671D 13	0.546D 13	0.337C 13	0.176D 13	0.119D 13	0.311D 12	0.672D 11	0.0
10	0.612C 13	0.501D 13	0.312D 13	0.165D 13	0.112D 13	0.294C 12	0.634C 11	0.0
11	0.549C 13	0.451C 13	0.284D 13	0.152D 13	0.103D 13	0.275D 12	0.589D 11	0.0
12	0.502D 13	0.415D 13	0.264D 13	0.142D 13	0.973D 12	0.261C 12	0.554D 11	0.0
13	0.473C 13	0.393D 13	0.251D 13	0.136D 13	0.932D 12	0.251D 12	0.529D 11	0.0
14	0.444D 13	0.370D 13	0.238D 13	0.129D 13	0.892C 12	0.241D 12	0.502D 11	0.0
15	0.390C 13	0.327C 13	0.213D 13	0.117D 13	0.812D 12	0.222D 12	0.444D 11	0.0
16	0.341D 13	0.287D 13	0.189D 13	0.105D 13	0.732D 12	0.202D 12	0.377D 11	0.0
17	0.321C 13	0.271D 13	0.179D 13	0.998D 12	0.699D 12	0.193D 12	0.344D 11	0.0
18	0.277D 13	0.235C 13	0.157D 13	0.883D 12	0.622D 12	0.174D 12	0.256D 11	0.0
19	0.239C 13	0.203D 13	0.137D 13	0.776D 12	0.550D 12	0.155D 12	0.145D 11	0.0
20	0.205C 13	0.175C 13	0.119D 13	0.675D 12	0.482D 12	0.136D 12	0.136D 09	0.0
21	0.163D 13	0.140D 13	0.947D 12	0.544D 12	0.394D 12	0.113D 12	0.199D 08	0.0
22	0.129C 13	0.111D 13	0.752D 12	0.435D 12	0.319D 12	0.914D 11	0.160D 08	0.0
23	0.102D 13	0.874D 12	0.593D 12	0.345D 12	0.254C 12	0.722D 11	0.127D 08	0.0
24	0.875C 12	0.748D 12	0.508D 12	0.297D 12	0.220D 12	0.611D 11	0.107C 08	0.0
25	0.742D 12	0.635D 12	0.435D 12	0.255D 12	0.189D 12	0.505D 11	0.885D 07	0.0
26	0.664C 12	0.569D 12	0.391D 12	0.230D 12	0.171D 12	0.435D 11	0.763D 07	0.0
27	0.482C 12	0.413D 12	0.285D 12	0.169D 12	0.125C 12	0.232D 11	0.407D 07	0.0
28	0.348D 12	0.298D 12	0.207D 12	0.122D 12	0.897D 11	0.886D 08	0.787D 04	0.0
29	0.276C 12	0.237D 12	0.164D 12	0.972D 11	0.709D 11	0.631D 07	0.385D 01	0.0
30	0.226D 12	0.194D 12	0.135D 12	0.796D 11	0.578D 11	0.507D 07	0.302D 01	0.0
31	0.142C 12	0.122D 12	0.848D 11	0.490D 11	0.349D 11	0.306D 07	0.182D 01	0.0
32	0.745D 11	0.639C 11	0.434D 11	0.220D 11	0.126D 11	0.110D 07	0.655D 00	0.0
33	0.506D 11	0.432D 11	0.285D 11	0.113D 11	0.104D 08	0.279D 03	0.168D-03	0.0
34	0.449D 07	0.379D 07	0.250D 07	0.987D 06	0.261D 03	0.241D-03	0.218D-09	0.0
35	0.272D 01	0.225D 01	0.149D 01	0.587D 00	0.157D-03	0.213D-09	0.257D-15	0.0
36	0.0	0.0	0.0	0.0	0.0	0.0	0.0	0.0

POINTWISE FLUX - GROUP 3 - PLANE 6

	0	1	2	3	4	5	6	7	8	9
0	0.784D 14	0.792D 14	0.818D 14	0.883D 14	0.956D 14	0.104D 15	0.105D 15	0.105D 15	0.103D 15	0.103D 15
1	0.792D 14	0.800D 14	0.825D 14	0.889D 14	0.960D 14	0.104D 15	0.104D 15	0.104D 15	0.102D 15	0.102D 15
2	0.817D 14	0.825D 14	0.848D 14	0.907D 14	0.971D 14	0.103D 15	0.103D 15	0.102D 15	0.994D 14	0.989D 14
3	0.882D 14	0.888D 14	0.906D 14	0.953D 14	0.998D 14	0.103D 15	0.991D 14	0.970D 14	0.917D 14	0.907D 14
4	0.917D 14	0.922D 14	0.938D 14	0.976D 14	0.101D 15	0.103D 15	0.977D 14	0.944D 14	0.882D 14	0.871D 14
5	0.954D 14	0.958D 14	0.971D 14	0.999D 14	0.102D 15	0.103D 15	0.961D 14	0.921D 14	0.852D 14	0.839D 14
6	0.103D 15	0.103D 15	0.103D 15	0.104D 15	0.104D 15	0.102D 15	0.923D 14	0.873D 14	0.790D 14	0.774D 14
7	0.101D 15	0.101D 15	0.102D 15	0.103D 15	0.104D 15	0.102D 15	0.926D 14	0.878D 14	0.796D 14	0.779D 14
8	0.903D 14	0.909D 14	0.925D 14	0.964D 14	0.994D 14	0.102D 15	0.972D 14	0.939D 14	0.877D 14	0.862D 14
9	0.862D 14	0.868D 14	0.888D 14	0.936D 14	0.983D 14	0.102D 15	0.987D 14	0.968D 14	0.916D 14	0.902D 14
10	0.769D 14	0.777D 14	0.802D 14	0.868D 14	0.940D 14	0.103D 15	0.105D 15	0.105D 15	0.103D 15	0.102D 15
11	0.773D 14	0.781D 14	0.806D 14	0.870D 14	0.943D 14	0.103D 15	0.107D 15	0.107D 15	0.107D 15	0.105D 15
12	0.838D 14	0.844D 14	0.864D 14	0.916D 14	0.967D 14	0.103D 15	0.106D 15	0.106D 15	0.106D 15	0.104D 15
13	0.905D 14	0.913D 14	0.926D 14	0.957D 14	0.983D 14	0.103D 15	0.105D 15	0.105D 15	0.104D 15	0.102D 15
14	0.951D 14	0.953D 14	0.960D 14	0.975D 14	0.987D 14	0.101D 15	0.102D 15	0.102D 15	0.101D 15	0.991D 14
15	0.962D 14	0.962D 14	0.958D 14	0.952D 14	0.946D 14	0.936D 14	0.933D 14	0.934D 14	0.936D 14	0.927D 14
16	0.919D 14	0.914D 14	0.900D 14	0.866D 14	0.837D 14	0.787D 14	0.778D 14	0.782D 14	0.818D 14	0.845D 14
17	0.895D 14	0.888D 14	0.868D 14	0.818D 14	0.761D 14	0.688D 14	0.677D 14	0.684D 14	0.745D 14	0.807D 14
18	0.838D 14	0.829D 14	0.801D 14	0.732D 14	0.657D 14	0.569D 14	0.558D 14	0.568D 14	0.649D 14	0.745D 14
19	0.810D 14	0.801D 14	0.774D 14	0.706D 14	0.634D 14	0.550D 14	0.540D 14	0.550D 14	0.632D 14	0.730D 14
20	0.813D 14	0.806D 14	0.787D 14	0.740D 14	0.693D 14	0.627D 14	0.618D 14	0.626D 14	0.691D 14	0.758D 14
21	0.841D 14	0.839D 14	0.832D 14	0.817D 14	0.805D 14	0.782D 14	0.776D 14	0.778D 14	0.796D 14	0.813D 14
22	0.840D 14	0.839D 14	0.837D 14	0.831D 14	0.827D 14	0.817D 14	0.811D 14	0.810D 14	0.810D 14	0.811D 14
23	0.801D 14	0.801D 14	0.799D 14	0.797D 14	0.794D 14	0.787D 14	0.780D 14	0.778D 14	0.771D 14	0.766D 14
24	0.763D 14	0.762D 14	0.761D 14	0.759D 14	0.757D 14	0.751D 14	0.743D 14	0.741D 14	0.732D 14	0.725D 14
25	0.716D 14	0.716D 14	0.715D 14	0.713D 14	0.711D 14	0.705D 14	0.697D 14	0.695D 14	0.685D 14	0.677D 14
26	0.682D 14	0.681D 14	0.680D 14	0.679D 14	0.677D 14	0.671D 14	0.664D 14	0.661D 14	0.651D 14	0.643D 14
27	0.570D 14	0.569D 14	0.569D 14	0.567D 14	0.566D 14	0.561D 14	0.555D 14	0.552D 14	0.544D 14	0.537D 14
28	0.480D 14	0.479D 14	0.479D 14	0.478D 14	0.476D 14	0.473D 14	0.468D 14	0.466D 14	0.459D 14	0.454D 14
29	0.427D 14	0.427D 14	0.427D 14	0.426D 14	0.425D 14	0.421D 14	0.417D 14	0.416D 14	0.410D 14	0.406D 14
30	0.387D 14	0.387D 14	0.387D 14	0.386D 14	0.385D 14	0.382D 14	0.378D 14	0.377D 14	0.372D 14	0.368D 14
31	0.306D 14	0.306D 14	0.305D 14	0.305D 14	0.304D 14	0.302D 14	0.299D 14	0.298D 14	0.294D 14	0.291D 14
32	0.218D 14	0.218D 14	0.218D 14	0.217D 14	0.217D 14	0.215D 14	0.213D 14	0.212D 14	0.210D 14	0.207D 14
33	0.178D 14	0.178D 14	0.178D 14	0.178D 14	0.177D 14	0.176D 14	0.174D 14	0.174D 14	0.171D 14	0.170D 14
34	0.795D 13	0.795D 13	0.794D 13	0.792D 13	0.790D 13	0.784D 13	0.775D 13	0.772D 13	0.761D 13	0.752D 13
35	0.232D 13	0.232D 13	0.232D 13	0.231D 13	0.231D 13	0.228D 13	0.225D 13	0.224D 13	0.219D 13	0.216D 13
36	0.0	0.0	0.0	0.0	0.0	0.0	0.0	0.0	0.0	0.0

POINTWISE FLUX - GROUP 3 - PLANE 6

	10	11	12	13	14	15	16	17	18	19
0	0.104D 15	0.106D 15	0.109D 15	0.109D 15	0.108D 15	0.103D 15	0.98CD 14	0.945D 14	0.869D 14	0.822D 14
1	0.103D 15	0.106D 15	0.108D 15	0.109D 15	0.108D 15	0.103D 15	0.973D 14	0.938D 14	0.860D 14	0.812D 14
2	0.100D 15	0.103D 15	0.107D 15	0.108D 15	0.107D 15	0.102D 15	0.955D 14	0.914D 14	0.829D 14	0.783D 14
3	0.924D 14	0.974D 14	0.104D 15	0.106D 15	0.105D 15	0.992D 14	0.912D 14	0.857D 14	0.755D 14	0.712D 14
4	0.889D 14	0.949D 14	0.103D 15	0.105D 15	0.104D 15	0.982D 14	0.896D 14	0.830D 14	0.722D 14	0.681D 14
5	0.859D 14	0.923D 14	0.102D 15	0.104D 15	0.104D 15	0.971D 14	0.875D 14	0.791D 14	0.675D 14	0.636D 14
6	0.794D 14	0.865D 14	0.978D 14	0.101D 15	0.100D 15	0.927D 14	0.809D 14	0.707D 14	0.581D 14	0.548D 14
7	0.797D 14	0.863D 14	0.967D 14	0.992D 14	0.983D 14	0.907D 14	0.791D 14	0.691D 14	0.568D 14	0.539D 14
8	0.871D 14	0.917D 14	0.979D 14	0.991D 14	0.973D 14	0.908D 14	0.816D 14	0.736D 14	0.633D 14	0.608D 14
9	0.908D 14	0.940D 14	0.982D 14	0.989D 14	0.970D 14	0.908D 14	0.825D 14	0.760D 14	0.663D 14	0.639D 14
10	0.101D 15	0.998D 14	0.982D 14	0.969D 14	0.938D 14	0.900D 14	0.866D 14	0.846D 14	0.810D 14	0.798D 14
11	0.102D 15	0.975D 14	0.911D 14	0.878D 14	0.834D 14	0.818D 14	0.826D 14	0.835D 14	0.854D 14	0.864D 14
12	0.993D 14	0.924D 14	0.805D 14	0.743D 14	0.687D 14	0.689D 14	0.739D 14	0.785D 14	0.850D 14	0.879D 14
13	0.970D 14	0.890D 14	0.742D 14	0.672D 14	0.613D 14	0.622D 14	0.687D 14	0.754D 14	0.843D 14	0.872D 14
14	0.944D 14	0.860D 14	0.701D 14	0.629D 14	0.569D 14	0.583D 14	0.656D 14	0.732D 14	0.835D 14	0.881D 14
15	0.895D 14	0.823D 14	0.677D 14	0.609D 14	0.555D 14	0.573D 14	0.647D 14	0.723D 14	0.828D 14	0.874D 14
16	0.851D 14	0.818D 14	0.726D 14	0.676D 14	0.635D 14	0.649D 14	0.708D 14	0.762D 14	0.836D 14	0.867D 14
17	0.836D 14	0.823D 14	0.770D 14	0.741D 14	0.711D 14	0.721D 14	0.759D 14	0.788D 14	0.841D 14	0.863D 14
18	0.810D 14	0.834D 14	0.831D 14	0.824D 14	0.813D 14	0.815D 14	0.826D 14	0.834D 14	0.850D 14	0.851D 14
19	0.804D 14	0.842D 14	0.857D 14	0.859D 14	0.855D 14	0.852D 14	0.850D 14	0.849D 14	0.844D 14	0.831D 14
20	0.814D 14	0.847D 14	0.863D 14	0.866D 14	0.863D 14	0.855D 14	0.846D 14	0.840D 14	0.823D 14	0.800D 14
21	0.831D 14	0.842D 14	0.846D 14	0.844D 14	0.835D 14	0.821D 14	0.806D 14	0.797D 14	0.771D 14	0.741D 14
22	0.811D 14	0.809D 14	0.802D 14	0.796D 14	0.781D 14	0.761D 14	0.743D 14	0.731D 14	0.702D 14	0.668D 14
23	0.758D 14	0.749D 14	0.736D 14	0.727D 14	0.708D 14	0.685D 14	0.665D 14	0.652D 14	0.621D 14	0.589D 14
24	0.715D 14	0.703D 14	0.687D 14	0.677D 14	0.657D 14	0.631D 14	0.611D 14	0.599D 14	0.572D 14	0.546D 14
25	0.665D 14	0.651D 14	0.634D 14	0.624D 14	0.604D 14	0.581D 14	0.564D 14	0.553D 14	0.529D 14	0.506D 14
26	0.630D 14	0.615D 14	0.597D 14	0.587D 14	0.568D 14	0.549D 14	0.534D 14	0.524D 14	0.503D 14	0.481D 14
27	0.528D 14	0.518D 14	0.506D 14	0.499D 14	0.485D 14	0.470D 14	0.457D 14	0.450D 14	0.432D 14	0.415D 14
28	0.447D 14	0.440D 14	0.431D 14	0.425D 14	0.414D 14	0.402D 14	0.392D 14	0.385D 14	0.371D 14	0.355D 14
29	0.400D 14	0.393D 14	0.385D 14	0.380D 14	0.370D 14	0.359D 14	0.350D 14	0.345D 14	0.332D 14	0.318D 14
30	0.363D 14	0.357D 14	0.349D 14	0.345D 14	0.336D 14	0.326D 14	0.318D 14	0.313D 14	0.301D 14	0.288D 14
31	0.287D 14	0.282D 14	0.276D 14	0.273D 14	0.265D 14	0.258D 14	0.251D 14	0.247D 14	0.237D 14	0.227D 14
32	0.204D 14	0.201D 14	0.196D 14	0.194D 14	0.188D 14	0.182D 14	0.176D 14	0.173D 14	0.166D 14	0.158D 14
33	0.167D 14	0.164D 14	0.160D 14	0.158D 14	0.154D 14	0.149D 14	0.145D 14	0.142D 14	0.136D 14	0.130D 14
34	0.740D 13	0.726D 13	0.708D 13	0.697D 13	0.675D 13	0.651D 13	0.630D 13	0.617D 13	0.585D 13	0.552D 13
35	0.211D 13	0.205D 13	0.196D 13	0.191D 13	0.179D 13	0.165D 13	0.152D 13	0.143D 13	0.117D 13	0.946D 12
36	0.0	0.0	0.0	0.0	0.0	0.0	0.0	0.0	0.0	0.0

POINTWISE FLUX - GROUP 3 - PLANE 6

	20	21	22	23	24	25	26	27	28	29
0	0.800D 14	0.766D 14	0.745D 14	0.709D 14	0.663D 14	0.634D 14	0.625D 14	0.621D 14	0.584D 14	0.526D 14
1	0.792D 14	0.781D 14	0.741D 14	0.704D 14	0.656D 14	0.628D 14	0.621D 14	0.619D 14	0.584D 14	0.526D 14
2	0.772D 14	0.768D 14	0.729D 14	0.687D 14	0.635D 14	0.609D 14	0.608D 14	0.613D 14	0.582D 14	0.525D 14
3	0.722D 14	0.737D 14	0.704D 14	0.647D 14	0.585D 14	0.561D 14	0.576D 14	0.601D 14	0.579D 14	0.524D 14
4	0.700D 14	0.727D 14	0.696D 14	0.629D 14	0.563D 14	0.540D 14	0.562D 14	0.597D 14	0.578D 14	0.523D 14
5	0.669D 14	0.714D 14	0.686D 14	0.611D 14	0.543D 14	0.522D 14	0.549D 14	0.593D 14	0.577D 14	0.522D 14
6	0.600D 14	0.673D 14	0.657D 14	0.575D 14	0.505D 14	0.486D 14	0.520D 14	0.579D 14	0.572D 14	0.519D 14
7	0.596D 14	0.672D 14	0.662D 14	0.584D 14	0.515D 14	0.495D 14	0.527D 14	0.581D 14	0.569D 14	0.515D 14
8	0.655D 14	0.714D 14	0.703D 14	0.642D 14	0.578D 14	0.553D 14	0.570D 14	0.598D 14	0.569D 14	0.510D 14
9	0.681D 14	0.727D 14	0.715D 14	0.666D 14	0.607D 14	0.581D 14	0.588D 14	0.603D 14	0.569D 14	0.509D 14
10	0.804D 14	0.808D 14	0.785D 14	0.755D 14	0.711D 14	0.675D 14	0.650D 14	0.628D 14	0.568D 14	0.503D 14
11	0.866D 14	0.860D 14	0.831D 14	0.804D 14	0.762D 14	0.719D 14	0.678D 14	0.637D 14	0.563D 14	0.494D 14
12	0.885D 14	0.879D 14	0.847D 14	0.820D 14	0.777D 14	0.731D 14	0.683D 14	0.634D 14	0.556D 14	0.487D 14
13	0.890D 14	0.884D 14	0.852D 14	0.824D 14	0.781D 14	0.733D 14	0.682D 14	0.630D 14	0.551D 14	0.481D 14
14	0.891D 14	0.884D 14	0.852D 14	0.824D 14	0.780D 14	0.731D 14	0.678D 14	0.624D 14	0.544D 14	0.474D 14
15	0.884D 14	0.876D 14	0.841D 14	0.812D 14	0.767D 14	0.717D 14	0.662D 14	0.608D 14	0.529D 14	0.460D 14
16	0.869D 14	0.858D 14	0.820D 14	0.790D 14	0.744D 14	0.693D 14	0.637D 14	0.587D 14	0.511D 14	0.444D 14
17	0.861D 14	0.848D 14	0.808D 14	0.778D 14	0.731D 14	0.680D 14	0.624D 14	0.577D 14	0.502D 14	0.436D 14
18	0.838D 14	0.820D 14	0.776D 14	0.744D 14	0.697D 14	0.647D 14	0.594D 14	0.551D 14	0.481D 14	0.418D 14
19	0.808D 14	0.785D 14	0.737D 14	0.704D 14	0.655D 14	0.607D 14	0.562D 14	0.523D 14	0.458D 14	0.398D 14
20	0.771D 14	0.745D 14	0.695D 14	0.661D 14	0.613D 14	0.570D 14	0.530D 14	0.495D 14	0.434D 14	0.377D 14
21	0.706D 14	0.678D 14	0.626D 14	0.595D 14	0.555D 14	0.519D 14	0.485D 14	0.454D 14	0.399D 14	0.347D 14
22	0.631D 14	0.603D 14	0.559D 14	0.534D 14	0.502D 14	0.471D 14	0.441D 14	0.413D 14	0.363D 14	0.316D 14
23	0.558D 14	0.536D 14	0.500D 14	0.479D 14	0.452D 14	0.425D 14	0.398D 14	0.373D 14	0.328D 14	0.285D 14
24	0.519D 14	0.499D 14	0.467D 14	0.448D 14	0.422D 14	0.397D 14	0.373D 14	0.349D 14	0.307D 14	0.266D 14
25	0.482D 14	0.465D 14	0.435D 14	0.418D 14	0.394D 14	0.371D 14	0.347D 14	0.326D 14	0.286D 14	0.246D 14
26	0.459D 14	0.443D 14	0.415D 14	0.398D 14	0.376D 14	0.353D 14	0.331D 14	0.310D 14	0.272D 14	0.234D 14
27	0.397D 14	0.382D 14	0.359D 14	0.344D 14	0.325D 14	0.305D 14	0.286D 14	0.268D 14	0.234D 14	0.201D 14
28	0.340D 14	0.328D 14	0.307D 14	0.295D 14	0.278D 14	0.261D 14	0.244D 14	0.228D 14	0.199D 14	0.170D 14
29	0.304D 14	0.293D 14	0.274D 14	0.263D 14	0.248D 14	0.231D 14	0.216D 14	0.201D 14	0.175D 14	0.151D 14
30	0.276D 14	0.266D 14	0.249D 14	0.238D 14	0.224D 14	0.209D 14	0.194D 14	0.181D 14	0.158D 14	0.136D 14
31	0.217D 14	0.209D 14	0.195D 14	0.186D 14	0.175D 14	0.163D 14	0.151D 14	0.141D 14	0.122D 14	0.105D 14
32	0.151D 14	0.145D 14	0.135D 14	0.129D 14	0.121D 14	0.113D 14	0.105D 14	0.973D 13	0.838D 13	0.710D 13
33	0.124D 14	0.119D 14	0.111D 14	0.106D 14	0.990D 13	0.922D 13	0.853D 13	0.789D 13	0.671D 13	0.558D 13
34	0.516D 13	0.498D 13	0.442D 13	0.413D 13	0.373D 13	0.331D 13	0.285D 13	0.237D 13	0.134D 13	0.445D 10
35	0.418D 12	0.473D 10	0.673D 09	0.621D 09	0.561D 09	0.497D 09	0.428D 09	0.356D 09	0.201D 09	0.337D 06
36	0.0	0.0	0.0	0.0	0.0	0.0	0.0	0.0	0.0	0.0

POINTWISE FLUX - GROUP 3 - PLANE 6

	30	31	32	33	34	35	36	37
0	0.484D 14	0.449D 14	0.368D 14	0.271D 14	0.225D 14	0.102D 14	0.300D 13	0.0
1	0.484D 14	0.449D 14	0.368D 14	0.271D 14	0.225D 14	0.102D 14	0.300D 13	0.0
2	0.483D 14	0.448D 14	0.367D 14	0.270D 14	0.224D 14	0.102D 14	0.299D 13	0.0
3	0.482D 14	0.447D 14	0.367D 14	0.270D 14	0.224D 14	0.102D 14	0.298D 13	0.0
4	0.482D 14	0.447D 14	0.366D 14	0.269D 14	0.224D 14	0.102D 14	0.298D 13	0.0
5	0.481D 14	0.446D 14	0.366D 14	0.269D 14	0.223D 14	0.101D 14	0.297D 13	0.0
6	0.478D 14	0.443D 14	0.363D 14	0.267D 14	0.221D 14	0.101D 14	0.293D 13	0.0
7	0.474D 14	0.439D 14	0.359D 14	0.264D 14	0.219D 14	0.992D 13	0.288D 13	0.0
8	0.469D 14	0.433D 14	0.354D 14	0.260D 14	0.216D 14	0.976D 13	0.282D 13	0.0
9	0.467D 14	0.432D 14	0.353D 14	0.259D 14	0.215D 14	0.972D 13	0.280D 13	0.0
10	0.460D 14	0.424D 14	0.345D 14	0.253D 14	0.210D 14	0.947D 13	0.270D 13	0.0
11	0.450D 14	0.414D 14	0.337D 14	0.247D 14	0.204D 14	0.918D 13	0.256D 13	0.0
12	0.442D 14	0.406D 14	0.330D 14	0.241D 14	0.200D 14	0.895D 13	0.245D 13	0.0
13	0.436D 14	0.401D 14	0.325D 14	0.237D 14	0.196D 14	0.878D 13	0.236D 13	0.0
14	0.430D 14	0.395D 14	0.320D 14	0.234D 14	0.193D 14	0.861D 13	0.226D 13	0.0
15	0.416D 14	0.382D 14	0.309D 14	0.225D 14	0.186D 14	0.825D 13	0.204D 13	0.0
16	0.401D 14	0.368D 14	0.297D 14	0.216D 14	0.179D 14	0.785D 13	0.176D 13	0.0
17	0.394D 14	0.361D 14	0.292D 14	0.212D 14	0.175D 14	0.767D 13	0.162D 13	0.0
18	0.377D 14	0.346D 14	0.278D 14	0.202D 14	0.167D 14	0.723D 13	0.121D 13	0.0
19	0.359D 14	0.329D 14	0.264D 14	0.192D 14	0.158D 14	0.676D 13	0.693D 12	0.0
20	0.341D 14	0.312D 14	0.249D 14	0.180D 14	0.149D 14	0.628D 13	0.549D 10	0.0
21	0.313D 14	0.286D 14	0.227D 14	0.163D 14	0.136D 14	0.560D 13	0.847D 09	0.0
22	0.285D 14	0.260D 14	0.205D 14	0.147D 14	0.122D 14	0.490D 13	0.736D 09	0.0
23	0.257D 14	0.234D 14	0.184D 14	0.132D 14	0.109D 14	0.416D 13	0.625D 09	0.0
24	0.239D 14	0.218D 14	0.172D 14	0.123D 14	0.101D 14	0.366D 13	0.551D 09	0.0
25	0.221D 14	0.201D 14	0.159D 14	0.113D 14	0.935D 13	0.314D 13	0.472D 09	0.0
26	0.210D 14	0.191D 14	0.151D 14	0.108D 14	0.884D 13	0.276D 13	0.415D 09	0.0
27	0.180D 14	0.163D 14	0.129D 14	0.910D 13	0.739D 13	0.154D 13	0.232D 09	0.0
28	0.152D 14	0.138D 14	0.109D 14	0.758D 13	0.603D 13	0.507D 10	0.386D 06	0.0
29	0.135D 14	0.123D 14	0.964D 13	0.661D 13	0.521D 13	0.396D 09	0.240D 03	0.0
30	0.122D 14	0.110D 14	0.863D 13	0.585D 13	0.457D 13	0.343D 09	0.204D 03	0.0
31	0.936D 13	0.846D 13	0.652D 13	0.422D 13	0.317D 13	0.238D 09	0.142D 03	0.0
32	0.626D 13	0.559D 13	0.411D 13	0.220D 13	0.127D 13	0.956D 08	0.568D 02	0.0
33	0.487D 13	0.431D 13	0.305D 13	0.124D 13	0.945D 09	0.212D 05	0.128D-01	0.0
34	0.370D 09	0.324D 09	0.229D 09	0.935D 08	0.209D 05	0.188D-01	0.169D-07	0.0
35	0.224D 03	0.192D 03	0.136D 03	0.556D 02	0.126D-01	0.168D-07	0.200D-13	0.0
36	0.0	0.0	0.0	0.0	0.0	0.0	0.0	0.0

POINTWISE FLUX - GROUP 1 - PLANE 5

	0	1	2	3	4	5	6	7	8	9
0	0.740D 14	0.733D 14	0.710D 14	0.650D 14	0.590D 14	0.520D 14	0.500D 14	0.498D 14	0.496D 14	0.489D 14
1	0.733D 14	0.726D 14	0.703D 14	0.645D 14	0.587D 14	0.520D 14	0.504D 14	0.502D 14	0.503D 14	0.497D 14
2	0.710D 14	0.703D 14	0.683D 14	0.629D 14	0.576D 14	0.520D 14	0.514D 14	0.516D 14	0.525D 14	0.520D 14
3	0.650D 14	0.645D 14	0.629D 14	0.589D 14	0.552D 14	0.520D 14	0.539D 14	0.551D 14	0.580D 14	0.579D 14
4	0.621D 14	0.616D 14	0.603D 14	0.570D 14	0.544D 14	0.520D 14	0.548D 14	0.568D 14	0.606D 14	0.606D 14
5	0.590D 14	0.586D 14	0.575D 14	0.551D 14	0.533D 14	0.519D 14	0.558D 14	0.586D 14	0.630D 14	0.632D 14
6	0.523D 14	0.521D 14	0.516D 14	0.508D 14	0.504D 14	0.514D 14	0.578D 14	0.614D 14	0.674D 14	0.679D 14
7	0.521D 14	0.519D 14	0.513D 14	0.502D 14	0.497D 14	0.504D 14	0.564D 14	0.599D 14	0.657D 14	0.663D 14
8	0.586D 14	0.582D 14	0.568D 14	0.537D 14	0.512D 14	0.488D 14	0.514D 14	0.536D 14	0.576D 14	0.579D 14
9	0.614D 14	0.609D 14	0.593D 14	0.553D 14	0.516D 14	0.483D 14	0.500D 14	0.511D 14	0.541D 14	0.543D 14
10	0.672D 14	0.664D 14	0.642D 14	0.585D 14	0.527D 14	0.456D 14	0.432D 14	0.430D 14	0.430D 14	0.429D 14
11	0.642D 14	0.635D 14	0.613D 14	0.556D 14	0.499D 14	0.425D 14	0.391D 14	0.386D 14	0.379D 14	0.381D 14
12	0.565D 14	0.560D 14	0.543D 14	0.499D 14	0.458D 14	0.402D 14	0.374D 14	0.370D 14	0.364D 14	0.369D 14
13	0.493D 14	0.489D 14	0.478D 14	0.452D 14	0.430D 14	0.392D 14	0.370D 14	0.366D 14	0.361D 14	0.367D 14
14	0.444D 14	0.442D 14	0.436D 14	0.422D 14	0.411D 14	0.388D 14	0.372D 14	0.369D 14	0.364D 14	0.369D 14
15	0.398D 14	0.399D 14	0.400D 14	0.403D 14	0.406D 14	0.407D 14	0.400D 14	0.397D 14	0.384D 14	0.380D 14
16	0.392D 14	0.395D 14	0.405D 14	0.428D 14	0.449D 14	0.481D 14	0.480D 14	0.473D 14	0.433D 14	0.403D 14
17	0.392D 14	0.397D 14	0.411D 14	0.448D 14	0.490D 14	0.542D 14	0.542D 14	0.533D 14	0.473D 14	0.414D 14
18	0.391D 14	0.398D 14	0.419D 14	0.473D 14	0.533D 14	0.602D 14	0.604D 14	0.592D 14	0.511D 14	0.421D 14
19	0.367D 14	0.374D 14	0.395D 14	0.447D 14	0.506D 14	0.574D 14	0.575D 14	0.563D 14	0.480D 14	0.388D 14
20	0.316D 14	0.321D 14	0.335D 14	0.372D 14	0.409D 14	0.461D 14	0.460D 14	0.450D 14	0.382D 14	0.317D 14
21	0.220D 14	0.221D 14	0.226D 14	0.235D 14	0.243D 14	0.255D 14	0.251D 14	0.247D 14	0.220D 14	0.198D 14
22	0.142D 14	0.142D 14	0.143D 14	0.145D 14	0.147D 14	0.148D 14	0.144D 14	0.142D 14	0.130D 14	0.129D 14
23	0.888D 13	0.889D 13	0.890D 13	0.892D 13	0.892D 13	0.884D 13	0.854D 13	0.841D 13	0.782D 13	0.734D 13
24	0.655D 13	0.655D 13	0.654D 13	0.653D 13	0.651D 13	0.640D 13	0.617D 13	0.608D 13	0.569D 13	0.537D 13
25	0.482D 13	0.481D 13	0.480D 13	0.478D 13	0.475D 13	0.465D 13	0.448D 13	0.442D 13	0.415D 13	0.395D 13
26	0.391D 13	0.391D 13	0.390D 13	0.388D 13	0.385D 13	0.376D 13	0.362D 13	0.357D 13	0.337D 13	0.321D 13
27	0.225D 13	0.225D 13	0.224D 13	0.222D 13	0.221D 13	0.216D 13	0.208D 13	0.206D 13	0.196D 13	0.189D 13
28	0.144D 13	0.144D 13	0.143D 13	0.142D 13	0.141D 13	0.138D 13	0.134D 13	0.132D 13	0.127D 13	0.122D 13
29	0.104D 13	0.104D 13	0.104D 13	0.103D 13	0.102D 13	0.100D 13	0.972D 12	0.962D 12	0.924D 12	0.895D 12
30	0.794D 12	0.794D 12	0.791D 12	0.786D 12	0.780D 12	0.764D 12	0.742D 12	0.735D 12	0.707D 12	0.686D 12
31	0.432D 12	0.432D 12	0.431D 12	0.428D 12	0.425D 12	0.417D 12	0.406D 12	0.403D 12	0.389D 12	0.378D 12
32	0.198D 12	0.198D 12	0.198D 12	0.196D 12	0.195D 12	0.192D 12	0.187D 12	0.186D 12	0.180D 12	0.175D 12
33	0.122D 12	0.122D 12	0.122D 12	0.121D 12	0.121D 12	0.119D 12	0.116D 12	0.115D 12	0.111D 12	0.109D 12
34	0.272D 11	0.272D 11	0.271D 11	0.270D 11	0.269D 11	0.265D 11	0.259D 11	0.257D 11	0.250D 11	0.245D 11
35	0.543D 10	0.542D 10	0.541D 10	0.539D 10	0.536D 10	0.528D 10	0.517D 10	0.514D 10	0.499D 10	0.488D 10
36	0.0	0.0	0.0	0.0	0.0	0.0	0.0	0.0	0.0	0.0

POINTWISE FLUX - GROUP 1 - PLANE 5

	10	11	12	13	14	15	16	17	18	19
0	C.47CD 14	0.441D 14	0.406D 14	C.391D 14	C.378D 14	0.386D 14	0.402D 14	0.413D 14	0.432D 14	0.427D 14
1	C.477D 14	0.446D 14	0.409D 14	0.393D 14	0.380D 14	0.388D 14	C.406D 14	0.418D 14	0.440D 14	0.434D 14
2	C.499D 14	C.463D 14	0.417D 14	C.400D 14	0.385D 14	0.396D 14	C.419D 14	C.435D 14	0.462D 14	C.457D 14
3	0.554D 14	0.503D 14	0.436D 14	C.413D 14	0.395D 14	C.412D 14	C.449D 14	0.476D 14	0.519D 14	C.512D 14
4	C.58CD 14	C.520D 14	0.443D 14	0.417D 14	C.399D 14	0.418D 14	C.460D 14	C.495D 14	0.545D 14	C.537D 14
5	C.6C4D 14	0.539D 14	0.450D 14	0.422D 14	C.4C3D 14	0.425D 14	C.474D 14	0.524D 14	C.583D 14	0.573D 14
6	C.65CD 14	0.576D 14	0.471D 14	0.438D 14	0.418D 14	0.448D 14	0.517D 14	C.583D 14	0.657D 14	0.644D 14
7	C.63ED 14	C.566D 14	0.467D 14	0.437D 14	C.420D 14	0.451D 14	0.519D 14	0.585D 14	0.656D 14	0.641D 14
8	C.559D 14	0.508D 14	0.442D 14	0.422D 14	C.411D 14	C.434D 14	0.483D 14	C.533D 14	0.585D 14	0.567D 14
9	C.526D 14	C.486D 14	0.436D 14	0.419D 14	0.410D 14	0.430D 14	0.472D 14	0.509D 14	0.554D 14	0.535D 14
10	C.426D 14	0.419D 14	0.412D 14	0.410D 14	C.410D 14	0.412D 14	C.415D 14	C.416D 14	C.409D 14	0.380D 14
11	C.391D 14	0.4CED 14	0.437D 14	0.450D 14	0.461D 14	0.447D 14	0.418D 14	0.396D 14	0.346D 14	0.300D 14
12	C.387D 14	0.423D 14	0.496D 14	0.534D 14	C.556D 14	C.529D 14	0.466D 14	0.414D 14	0.327D 14	0.266D 14
13	C.389D 14	0.434D 14	0.531D 14	0.579D 14	C.607D 14	0.574D 14	0.497D 14	0.425D 14	0.318D 14	0.249D 14
14	0.391D 14	0.44CD 14	0.547D 14	0.600D 14	C.629D 14	0.593D 14	0.5C8D 14	0.428D 14	0.308D 14	0.234D 14
15	C.392D 14	C.433D 14	0.532D 14	0.581D 14	0.607D 14	0.568D 14	0.482D 14	C.401D 14	C.279D 14	0.205D 14
16	C.385D 14	0.397D 14	0.454D 14	C.487D 14	C.500D 14	0.464D 14	0.392D 14	C.331D 14	C.235D 14	0.173D 14
17	C.379D 14	0.375D 14	0.4C0D 14	0.414D 14	C.417D 14	C.384D 14	C.330D 14	C.291D 14	C.213D 14	0.158D 14
18	C.356D 14	C.322D 14	0.307D 14	0.302D 14	0.288D 14	0.262D 14	C.231D 14	0.210D 14	0.163D 14	C.125D 14
19	C.315D 14	0.27CD 14	0.240D 14	0.228D 14	C.208D 14	0.185D 14	C.165D 14	0.152D 14	0.122D 14	0.963D 13
20	C.25ED 14	C.21ED 14	0.187D 14	0.174D 14	C.153D 14	0.135D 14	0.120D 14	C.111D 14	C.909D 13	0.732D 13
21	C.171D 14	0.148D 14	0.127D 14	0.117D 14	0.1C1D 14	C.876D 13	0.777D 13	0.722D 13	0.600D 13	0.493D 13
22	C.1C8D 14	0.955D 13	0.831D 13	0.768D 13	0.665D 13	C.575D 13	C.511D 13	C.475D 13	0.399D 13	0.333D 13
23	C.67CD 13	0.605D 13	0.534D 13	0.498D 13	C.434D 13	0.378D 13	0.337D 13	0.315D 13	0.268D 13	0.229D 13
24	C.495D 13	0.451D 13	0.403D 13	0.377D 13	C.332D 13	0.290D 13	C.261D 13	0.245D 13	0.213D 13	0.185D 13
25	C.366D 13	0.337D 13	0.305D 13	0.287D 13	C.255D 13	0.226D 13	0.207D 13	0.196D 13	0.172D 13	0.151D 13
26	C.3C0D 13	0.278D 13	0.253D 13	0.240D 13	0.215D 13	C.193D 13	0.177D 13	C.169D 13	0.150D 13	0.133D 13
27	C.18CD 13	0.172D 13	0.162D 13	C.155D 13	0.142D 13	0.129D 13	C.120D 13	0.114D 13	C.102D 13	0.902D 12
28	0.117D 13	0.112D 13	0.105D 13	C.100D 13	C.927D 12	C.851D 12	0.791D 12	0.756D 12	0.678D 12	0.605D 12
29	C.858D 12	0.818D 12	0.769D 12	0.741D 12	0.687D 12	0.633D 12	C.591D 12	0.566D 12	C.510D 12	0.456D 12
30	C.658D 12	0.629D 12	0.593D 12	0.572D 12	C.532D 12	C.492D 12	0.461D 12	0.442D 12	0.399D 12	0.359D 12
31	C.364D 12	0.349D 12	0.331D 12	0.320D 12	C.300D 12	C.279D 12	C.263D 12	0.253D 12	0.230D 12	0.208D 12
32	C.169D 12	0.163D 12	0.154D 12	0.150D 12	C.140D 12	0.131D 12	0.122D 12	C.118D 12	0.107D 12	0.973D 11
33	C.1C5D 12	0.101D 12	0.966D 11	0.937D 11	C.882D 11	C.825D 11	C.779D 11	0.751D 11	0.688D 11	0.627D 11
34	C.238D 11	C.23CD 11	0.220D 11	0.214D 11	0.202D 11	0.190D 11	0.181D 11	C.175D 11	C.161D 11	0.147D 11
35	C.472D 10	0.455D 10	0.432D 10	C.419D 10	C.390D 10	C.357D 10	C.326D 10	C.3C6D 10	0.251D 10	0.182D 10
36	C.C	0.0	0.C	0.0	0.0	0.0	0.0	C.0	C.C	0.0

POINTWISE FLUX - GROUP 1 - PLANE 5

	20	21	22	23	24	25	26	27	28	29
0	0.399D 14	0.373D 14	0.341D 14	0.329D 14	0.314D 14	0.284D 14	0.237D 14	0.187D 14	0.113D 14	0.722D 13
1	0.404D 14	0.377D 14	0.343D 14	0.333D 14	0.319D 14	0.289D 14	0.241D 14	0.188D 14	0.113D 14	0.722D 13
2	0.420D 14	0.386D 14	0.351D 14	0.344D 14	0.334D 14	0.304D 14	0.251D 14	0.192D 14	0.113D 14	0.720D 13
3	0.459D 14	0.408D 14	0.368D 14	0.372D 14	0.373D 14	0.341D 14	0.276D 14	0.200D 14	0.114D 14	0.716D 13
4	0.476D 14	0.415D 14	0.373D 14	0.384D 14	0.390D 14	0.358D 14	0.287D 14	0.203D 14	0.114D 14	0.714D 13
5	0.501D 14	0.424D 14	0.379D 14	0.397D 14	0.407D 14	0.374D 14	0.299D 14	0.206D 14	0.114D 14	0.711D 13
6	0.554D 14	0.450D 14	0.394D 14	0.419D 14	0.435D 14	0.401D 14	0.318D 14	0.211D 14	0.112D 14	0.689D 13
7	0.547D 14	0.441D 14	0.380D 14	0.402D 14	0.417D 14	0.384D 14	0.303D 14	0.200D 14	0.106D 14	0.651D 13
8	0.483D 14	0.393D 14	0.335D 14	0.344D 14	0.349D 14	0.319D 14	0.252D 14	0.173D 14	0.953D 13	0.597D 13
9	0.456D 14	0.379D 14	0.322D 14	0.322D 14	0.321D 14	0.292D 14	0.233D 14	0.166D 14	0.926D 13	0.583D 13
10	0.332D 14	0.293D 14	0.249D 14	0.235D 14	0.219D 14	0.195D 14	0.161D 14	0.125D 14	0.767D 13	0.503D 13
11	0.256D 14	0.227D 14	0.190D 14	0.173D 14	0.155D 14	0.136D 14	0.114D 14	0.927D 13	0.624D 13	0.424D 13
12	0.220D 14	0.192D 14	0.158D 14	0.142D 14	0.124D 14	0.108D 14	0.908D 13	0.756D 13	0.535D 13	0.369D 13
13	0.201D 14	0.174D 14	0.140D 14	0.125D 14	0.108D 14	0.929D 13	0.787D 13	0.663D 13	0.482D 13	0.337D 13
14	0.185D 14	0.158D 14	0.125D 14	0.110D 14	0.943D 13	0.808D 13	0.685D 13	0.583D 13	0.433D 13	0.306D 13
15	0.157D 14	0.131D 14	0.101D 14	0.876D 13	0.736D 13	0.624D 13	0.531D 13	0.457D 13	0.350D 13	0.253D 13
16	0.131D 14	0.108D 14	0.818D 13	0.701D 13	0.582D 13	0.490D 13	0.417D 13	0.367D 13	0.285D 13	0.209D 13
17	0.120D 14	0.990D 13	0.745D 13	0.636D 13	0.526D 13	0.442D 13	0.378D 13	0.334D 13	0.259D 13	0.191D 13
18	0.962D 13	0.797D 13	0.597D 13	0.509D 13	0.418D 13	0.351D 13	0.302D 13	0.269D 13	0.209D 13	0.156D 13
19	0.755D 13	0.631D 13	0.476D 13	0.406D 13	0.334D 13	0.282D 13	0.246D 13	0.218D 13	0.169D 13	0.128D 13
20	0.585D 13	0.494D 13	0.377D 13	0.323D 13	0.269D 13	0.231D 13	0.202D 13	0.177D 13	0.138D 13	0.104D 13
21	0.462D 13	0.345D 13	0.269D 13	0.235D 13	0.202D 13	0.175D 13	0.153D 13	0.133D 13	0.103D 13	0.784D 12
22	0.277D 13	0.242D 13	0.195D 13	0.174D 13	0.152D 13	0.132D 13	0.114D 13	0.997D 12	0.771D 12	0.589D 12
23	0.196D 13	0.176D 13	0.147D 13	0.132D 13	0.115D 13	0.991D 12	0.857D 12	0.746D 12	0.578D 12	0.442D 12
24	0.162D 13	0.146D 13	0.123D 13	0.110D 13	0.953D 12	0.825D 12	0.714D 12	0.622D 12	0.483D 12	0.369D 12
25	0.133D 13	0.121D 13	0.101D 13	0.911D 12	0.791D 12	0.685D 12	0.593D 12	0.517D 12	0.400D 12	0.304D 12
26	0.117D 13	0.106D 13	0.891D 12	0.802D 12	0.697D 12	0.605D 12	0.524D 12	0.456D 12	0.353D 12	0.268D 12
27	0.796D 12	0.723D 12	0.613D 12	0.554D 12	0.483D 12	0.420D 12	0.365D 12	0.318D 12	0.246D 12	0.185D 12
28	0.537D 12	0.490D 12	0.418D 12	0.379D 12	0.333D 12	0.291D 12	0.253D 12	0.221D 12	0.170D 12	0.128D 12
29	0.407D 12	0.372D 12	0.319D 12	0.290D 12	0.255D 12	0.221D 12	0.192D 12	0.168D 12	0.129D 12	0.983D 11
30	0.321D 12	0.294D 12	0.253D 12	0.230D 12	0.202D 12	0.176D 12	0.152D 12	0.133D 12	0.103D 12	0.785D 11
31	0.187D 12	0.172D 12	0.148D 12	0.135D 12	0.119D 12	0.103D 12	0.899D 11	0.785D 11	0.609D 11	0.468D 11
32	0.878D 11	0.811D 11	0.705D 11	0.646D 11	0.572D 11	0.503D 11	0.440D 11	0.387D 11	0.302D 11	0.232D 11
33	0.568D 11	0.526D 11	0.460D 11	0.422D 11	0.375D 11	0.332D 11	0.292D 11	0.257D 11	0.200D 11	0.153D 11
34	0.133D 11	0.123D 11	0.107D 11	0.983D 10	0.864D 10	0.748D 10	0.631D 10	0.517D 10	0.290D 10	0.154D 08
35	0.914D 09	0.161D 08	0.247D 07	0.222D 07	0.155D 07	0.169D 07	0.142D 07	0.117D 07	0.654D 06	0.171D 04
36	0.0	0.0	0.0	0.0	0.0	0.0	0.0	0.0	0.0	0.0

POINTWISE FLUX - GROUP 1 - PLANE 5

	30	31	32	33	34	35	36	37
0	C.519D 13	C.391D 13	0.208D 13	C.928D 12	C.561D 12	0.121D 12	C.236D 11	C.0
1	C.519D 13	0.391D 13	0.208D 13	C.926D 12	C.560D 12	0.121D 12	C.236D 11	C.0
2	C.517D 13	C.389D 13	0.207D 13	0.922D 12	0.558D 12	0.120D 12	0.235D 11	C.0
3	0.512D 13	C.385D 13	0.204D 13	C.913D 12	C.553D 12	0.119D 12	C.233D 11	0.0
4	C.510D 13	0.383D 13	0.203D 13	0.909D 12	0.551D 12	0.119D 12	0.233D 11	0.0
5	C.507D 13	0.381D 13	0.202D 13	C.904D 12	C.548D 12	0.118D 12	0.232D 11	0.0
6	C.495D 13	0.367D 13	0.195D 13	0.876D 12	0.533D 12	C.115D 12	0.227D 11	0.0
7	C.463D 13	C.348D 13	0.186D 13	C.839D 12	C.512D 12	0.112D 12	C.220D 11	C.0
8	0.428D 13	0.324D 13	0.175D 13	0.794D 12	C.487D 12	C.107D 12	0.211D 11	0.0
9	C.419D 13	0.318D 13	C.172D 13	0.783D 12	0.481D 12	0.106D 12	C.209D 11	C.0
10	C.369D 13	0.283D 13	0.155D 13	0.718D 12	C.445D 12	C.993D 11	C.196D 11	C.0
11	C.316D 13	C.246D 13	0.138D 13	0.648D 12	0.406D 12	0.919D 11	C.181D 11	C.0
12	C.28CD 13	C.22CD 13	0.126D 13	C.598D 12	C.377D 12	C.863D 11	0.169D 11	0.0
13	C.258D 13	C.204D 13	0.118D 13	0.565D 12	0.358D 12	C.827D 11	C.161D 11	C.0
14	C.236D 13	C.188D 13	0.11CD 13	0.532D 12	C.340D 12	0.790D 11	0.152D 11	0.0
15	C.198D 13	0.160D 13	0.952D 12	C.470D 12	0.303D 12	0.717D 11	0.134D 11	0.0
16	C.165D 13	C.135D 13	C.818D 12	0.411D 12	C.268D 12	0.644D 11	0.113D 11	0.0
17	C.152D 13	0.125D 13	0.764D 12	C.387D 12	0.254D 12	C.613D 11	0.103D 11	C.0
18	C.126D 13	0.104D 13	0.647D 12	0.333D 12	C.221D 12	0.543D 11	C.765D 10	C.0
19	C.104D 13	C.861D 12	0.545D 12	0.285D 12	C.191D 12	0.476D 11	C.434D 10	0.0
20	C.852D 12	C.715D 12	0.457D 12	0.241D 12	0.164D 12	0.413D 11	0.522D C8	0.0
21	C.643D 12	0.541D 12	0.348D 12	0.187D 12	C.129D 12	C.334D 11	0.761D C7	0.0
22	0.484D 12	0.408D 12	0.264D 12	0.144D 12	0.101D 12	0.265D 11	0.598D C7	0.0
23	C.363D 12	C.306D 12	0.199D 12	0.110D 12	C.781D 11	0.205D 11	0.462D 07	C.0
24	C.303D 12	0.255D 12	0.167D 12	C.925D 11	C.661D 11	0.171D 11	0.387D 07	0.0
25	C.25CD 12	C.211D 12	0.139D 12	C.776D 11	0.558D 11	0.140D 11	0.316D 07	0.0
26	C.220D 12	0.185D 12	0.123D 12	C.690D 11	C.496D 11	C.12CD 11	0.270D C7	C.0
27	C.152D 12	0.128D 12	C.858D 11	0.487D 11	0.351D 11	0.631D 10	C.142D C7	0.0
28	0.105D 12	C.88ED 11	0.597D 11	0.340D 11	C.244D 11	0.309D 08	0.353D C4	0.0
29	C.8C9D 11	C.685D 11	0.462D 11	0.264D 11	0.189D 11	0.217D 07	0.134D 01	C.0
30	C.647D 11	C.549D 11	0.371D 11	0.212D 11	C.151D 11	0.17CD C7	0.101D 01	0.0
31	C.387D 11	0.329C 11	0.223D 11	0.126D 11	C.879D 10	C.993D C6	C.591D C0	0.0
32	C.193D 11	0.163D 11	0.109D 11	0.543D 10	0.309D 10	0.349D 06	0.208D C0	C.0
33	0.127D 11	C.1C7D 11	0.696D 1C	0.272D 1C	C.328D C7	C.113D C3	0.678D-04	0.0
34	C.145D C7	C.121D 07	0.786D C6	0.307D C6	C.104D C3	C.97CD-C4	C.880D-10	C.0
35	C.883D CC	C.719D C0	0.467D 00	0.183D C0	C.627D-C4	C.857D-10	0.103D-15	0.0
36	C.C	C.0	0.0	0.0	0.0	C.C	C.0	C.0

POINTWISE FLUX - GROUP 2 - PLANE 5

	0	1	2	3	4	5	6	7	8	9
0	0.499D 14	0.499D 14	0.499D 14	0.499D 14	0.498D 14	0.492D 14	0.485D 14	0.482D 14	0.474D 14	0.468D 14
1	0.499D 14	0.499D 14	0.499D 14	0.499D 14	0.498D 14	0.492D 14	0.484D 14	0.482D 14	0.474D 14	0.468D 14
2	0.499D 14	0.499D 14	0.498D 14	0.498D 14	0.497D 14	0.491D 14	0.484D 14	0.482D 14	0.474D 14	0.468D 14
3	0.498D 14	0.498D 14	0.498D 14	0.496D 14	0.495D 14	0.489D 14	0.482D 14	0.480D 14	0.472D 14	0.466D 14
4	0.498D 14	0.498D 14	0.497D 14	0.496D 14	0.494D 14	0.488D 14	0.481D 14	0.478D 14	0.470D 14	0.465D 14
5	0.498D 14	0.497D 14	0.496D 14	0.494D 14	0.493D 14	0.487D 14	0.480D 14	0.477D 14	0.469D 14	0.463D 14
6	0.490D 14	0.490D 14	0.489D 14	0.487D 14	0.485D 14	0.481D 14	0.475D 14	0.471D 14	0.464D 14	0.459D 14
7	0.481D 14	0.481D 14	0.480D 14	0.479D 14	0.477D 14	0.473D 14	0.467D 14	0.464D 14	0.457D 14	0.453D 14
8	0.471D 14	0.470D 14	0.470D 14	0.469D 14	0.467D 14	0.462D 14	0.457D 14	0.455D 14	0.450D 14	0.446D 14
9	0.467D 14	0.467D 14	0.466D 14	0.466D 14	0.465D 14	0.460D 14	0.454D 14	0.453D 14	0.448D 14	0.443D 14
10	0.453D 14	0.453D 14	0.452D 14	0.452D 14	0.451D 14	0.444D 14	0.436D 14	0.434D 14	0.428D 14	0.425D 14
11	0.439D 14	0.439D 14	0.438D 14	0.437D 14	0.435D 14	0.426D 14	0.417D 14	0.415D 14	0.409D 14	0.406D 14
12	0.430D 14	0.430D 14	0.428D 14	0.426D 14	0.422D 14	0.413D 14	0.405D 14	0.403D 14	0.397D 14	0.394D 14
13	0.422D 14	0.421D 14	0.420D 14	0.417D 14	0.414D 14	0.406D 14	0.398D 14	0.396D 14	0.390D 14	0.387D 14
14	0.412D 14	0.412D 14	0.411D 14	0.408D 14	0.405D 14	0.398D 14	0.391D 14	0.389D 14	0.383D 14	0.380D 14
15	0.394D 14	0.394D 14	0.393D 14	0.392D 14	0.390D 14	0.385D 14	0.379D 14	0.377D 14	0.371D 14	0.367D 14
16	0.377D 14	0.377D 14	0.377D 14	0.376D 14	0.375D 14	0.370D 14	0.365D 14	0.363D 14	0.357D 14	0.351D 14
17	0.369D 14	0.369D 14	0.369D 14	0.368D 14	0.365D 14	0.360D 14	0.355D 14	0.353D 14	0.348D 14	0.343D 14
18	0.350D 14	0.350D 14	0.350D 14	0.349D 14	0.346D 14	0.341D 14	0.335D 14	0.333D 14	0.328D 14	0.321D 14
19	0.323D 14	0.324D 14	0.324D 14	0.324D 14	0.322D 14	0.318D 14	0.312D 14	0.310D 14	0.302D 14	0.293D 14
20	0.290D 14	0.290D 14	0.291D 14	0.293D 14	0.293D 14	0.292D 14	0.286D 14	0.284D 14	0.272D 14	0.259D 14
21	0.232D 14	0.232D 14	0.232D 14	0.232D 14	0.232D 14	0.230D 14	0.225D 14	0.222D 14	0.211D 14	0.202D 14
22	0.175D 14	0.175D 14	0.175D 14	0.174D 14	0.174D 14	0.171D 14	0.166D 14	0.164D 14	0.156D 14	0.150D 14
23	0.126D 14	0.126D 14	0.126D 14	0.126D 14	0.125D 14	0.122D 14	0.119D 14	0.117D 14	0.112D 14	0.107D 14
24	0.102D 14	0.102D 14	0.102D 14	0.101D 14	0.100D 14	0.983D 13	0.952D 13	0.941D 13	0.897D 13	0.863D 13
25	0.815D 13	0.815D 13	0.812D 13	0.807D 13	0.802D 13	0.785D 13	0.760D 13	0.752D 13	0.718D 13	0.692D 13
26	0.701D 13	0.701D 13	0.699D 13	0.694D 13	0.689D 13	0.674D 13	0.654D 13	0.646D 13	0.619D 13	0.598D 13
27	0.459D 13	0.459D 13	0.457D 13	0.454D 13	0.451D 13	0.442D 13	0.430D 13	0.426D 13	0.411D 13	0.400D 13
28	0.329D 13	0.328D 13	0.328D 13	0.325D 13	0.323D 13	0.317D 13	0.309D 13	0.307D 13	0.296D 13	0.289D 13
29	0.253D 13	0.252D 13	0.252D 13	0.250D 13	0.249D 13	0.244D 13	0.238D 13	0.236D 13	0.229D 13	0.223D 13
30	0.202D 13	0.202D 13	0.201D 13	0.200D 13	0.199D 13	0.196D 13	0.191D 13	0.189D 13	0.184D 13	0.179D 13
31	0.121D 13	0.121D 13	0.121D 13	0.120D 13	0.119D 13	0.117D 13	0.115D 13	0.114D 13	0.111D 13	0.108D 13
32	0.617D 12	0.616D 12	0.615D 12	0.612D 12	0.609D 12	0.600D 12	0.587D 12	0.583D 12	0.567D 12	0.555D 12
33	0.408D 12	0.408D 12	0.407D 12	0.405D 12	0.403D 12	0.398D 12	0.390D 12	0.387D 12	0.377D 12	0.369D 12
34	0.104D 12	0.104D 12	0.104D 12	0.103D 12	0.103D 12	0.101D 12	0.994D 11	0.988D 11	0.963D 11	0.945D 11
35	0.223D 11	0.223D 11	0.223D 11	0.222D 11	0.221D 11	0.218D 11	0.214D 11	0.212D 11	0.207D 11	0.202D 11
36	0.0	0.0	0.0	0.0	0.0	0.0	0.0	0.0	0.0	0.0

POINTWISE FLUX - GROUP 2 - PLANE 5

	10	11	12	13	14	15	16	17	18	19
0	0.459D 14	0.448D 14	0.435D 14	0.429D 14	0.419D 14	0.413D 14	0.410D 14	0.407D 14	0.401D 14	0.389D 14
1	0.459D 14	0.448D 14	0.436D 14	0.429D 14	0.419D 14	0.413D 14	0.410D 14	0.407D 14	0.401D 14	0.389D 14
2	0.459D 14	0.449D 14	0.436D 14	0.430D 14	0.420D 14	0.414D 14	0.410D 14	0.408D 14	0.401D 14	0.389D 14
3	0.458D 14	0.449D 14	0.437D 14	0.430D 14	0.420D 14	0.414D 14	0.410D 14	0.408D 14	0.400D 14	0.388D 14
4	0.457D 14	0.449D 14	0.437D 14	0.430D 14	0.421D 14	0.414D 14	0.410D 14	0.407D 14	0.399D 14	0.387D 14
5	0.456D 14	0.449D 14	0.437D 14	0.431D 14	0.421D 14	0.414D 14	0.410D 14	0.406D 14	0.397D 14	0.385D 14
6	0.452D 14	0.447D 14	0.436D 14	0.430D 14	0.420D 14	0.413D 14	0.408D 14	0.402D 14	0.391D 14	0.379D 14
7	0.447D 14	0.441D 14	0.431D 14	0.425D 14	0.416D 14	0.409D 14	0.403D 14	0.396D 14	0.384D 14	0.370D 14
8	0.440D 14	0.433D 14	0.423D 14	0.418D 14	0.408D 14	0.401D 14	0.394D 14	0.389D 14	0.376D 14	0.360D 14
9	0.437D 14	0.431D 14	0.421D 14	0.415D 14	0.406D 14	0.399D 14	0.392D 14	0.387D 14	0.374D 14	0.357D 14
10	0.420D 14	0.414D 14	0.407D 14	0.403D 14	0.394D 14	0.385D 14	0.376D 14	0.370D 14	0.352D 14	0.331D 14
11	0.402D 14	0.399D 14	0.393D 14	0.390D 14	0.381D 14	0.370D 14	0.358D 14	0.350D 14	0.326D 14	0.300D 14
12	0.391D 14	0.388D 14	0.382D 14	0.377D 14	0.367D 14	0.355D 14	0.344D 14	0.335D 14	0.308D 14	0.279D 14
13	0.384D 14	0.381D 14	0.374D 14	0.369D 14	0.358D 14	0.346D 14	0.335D 14	0.325D 14	0.296D 14	0.265D 14
14	0.377D 14	0.374D 14	0.366D 14	0.360D 14	0.349D 14	0.336D 14	0.325D 14	0.315D 14	0.284D 14	0.252D 14
15	0.362D 14	0.357D 14	0.348D 14	0.342D 14	0.330D 14	0.316D 14	0.303D 14	0.291D 14	0.259D 14	0.226D 14
16	0.344D 14	0.337D 14	0.328D 14	0.323D 14	0.310D 14	0.293D 14	0.276D 14	0.263D 14	0.230D 14	0.199D 14
17	0.335D 14	0.326D 14	0.316D 14	0.310D 14	0.297D 14	0.279D 14	0.261D 14	0.248D 14	0.217D 14	0.187D 14
18	0.309D 14	0.297D 14	0.283D 14	0.275D 14	0.259D 14	0.240D 14	0.223D 14	0.212D 14	0.186D 14	0.160D 14
19	0.278D 14	0.263D 14	0.247D 14	0.238D 14	0.221D 14	0.203D 14	0.187D 14	0.178D 14	0.156D 14	0.135D 14
20	0.244D 14	0.228D 14	0.211D 14	0.202D 14	0.185D 14	0.169D 14	0.155D 14	0.147D 14	0.129D 14	0.112D 14
21	0.189D 14	0.177D 14	0.162D 14	0.155D 14	0.141D 14	0.127D 14	0.117D 14	0.111D 14	0.970D 13	0.844D 13
22	0.141D 14	0.131D 14	0.121D 14	0.115D 14	0.104D 14	0.941D 13	0.864D 13	0.820D 13	0.721D 13	0.632D 13
23	0.101D 14	0.950D 13	0.877D 13	0.836D 13	0.760D 13	0.688D 13	0.633D 13	0.602D 13	0.534D 13	0.475D 13
24	0.818D 13	0.769D 13	0.712D 13	0.680D 13	0.621D 13	0.563D 13	0.521D 13	0.497D 13	0.448D 13	0.406D 13
25	0.658D 13	0.621D 13	0.578D 13	0.554D 13	0.509D 13	0.467D 13	0.437D 13	0.420D 13	0.383D 13	0.348D 13
26	0.569D 13	0.538D 13	0.503D 13	0.484D 13	0.447D 13	0.414D 13	0.390D 13	0.376D 13	0.347D 13	0.317D 13
27	0.387D 13	0.375D 13	0.360D 13	0.350D 13	0.328D 13	0.306D 13	0.288D 13	0.278D 13	0.255D 13	0.230D 13
28	0.279D 13	0.268D 13	0.254D 13	0.246D 13	0.231D 13	0.216D 13	0.204D 13	0.197D 13	0.180D 13	0.164D 13
29	0.216D 13	0.207D 13	0.197D 13	0.191D 13	0.180D 13	0.169D 13	0.159D 13	0.154D 13	0.141D 13	0.129D 13
30	0.173D 13	0.167D 13	0.159D 13	0.154D 13	0.146D 13	0.137D 13	0.129D 13	0.125D 13	0.115D 13	0.105D 13
31	0.105D 13	0.101D 13	0.968D 12	0.942D 12	0.892D 12	0.842D 12	0.799D 12	0.774D 12	0.714D 12	0.656D 12
32	0.539D 12	0.521D 12	0.498D 12	0.485D 12	0.459D 12	0.432D 12	0.408D 12	0.394D 12	0.364D 12	0.334D 12
33	0.358D 12	0.347D 12	0.333D 12	0.324D 12	0.307D 12	0.290D 12	0.276D 12	0.267D 12	0.247D 12	0.228D 12
34	0.919D 11	0.892D 11	0.857D 11	0.836D 11	0.796D 11	0.753D 11	0.718D 11	0.696D 11	0.646D 11	0.594D 11
35	0.196D 11	0.189D 11	0.180D 11	0.175D 11	0.163D 11	0.150D 11	0.137D 11	0.129D 11	0.106D 11	0.767D 10
36	0.0	0.0	0.0	0.0	0.0	0.0	0.0	0.0	0.0	0.0

POINTWISE FLUX - GROUP 2 - PLANE 5

	20	21	22	23	24	25	26	27	28	29
0	0.372D 14	0.356D 14	0.326D 14	0.307D 14	0.282D 14	0.255D 14	0.225D 14	0.194D 14	0.140D 14	0.105D 14
1	0.372D 14	0.356D 14	0.326D 14	0.307D 14	0.282D 14	0.255D 14	0.225D 14	0.194D 14	0.140D 14	0.105D 14
2	0.372D 14	0.356D 14	0.325D 14	0.306D 14	0.281D 14	0.254D 14	0.225D 14	0.194D 14	0.140D 14	0.104D 14
3	0.372D 14	0.356D 14	0.324D 14	0.303D 14	0.278D 14	0.252D 14	0.224D 14	0.193D 14	0.139D 14	0.103D 14
4	0.371D 14	0.355D 14	0.323D 14	0.302D 14	0.276D 14	0.251D 14	0.224D 14	0.193D 14	0.138D 14	0.103D 14
5	0.370D 14	0.355D 14	0.322D 14	0.300D 14	0.275D 14	0.249D 14	0.224D 14	0.192D 14	0.137D 14	0.102D 14
6	0.366D 14	0.350D 14	0.316D 14	0.292D 14	0.267D 14	0.243D 14	0.219D 14	0.188D 14	0.133D 14	0.993D 13
7	0.356D 14	0.339D 14	0.304D 14	0.281D 14	0.257D 14	0.233D 14	0.210D 14	0.179D 14	0.127D 14	0.948D 13
8	0.341D 14	0.322D 14	0.287D 14	0.267D 14	0.244D 14	0.221D 14	0.195D 14	0.166D 14	0.119D 14	0.891D 13
9	0.337D 14	0.317D 14	0.282D 14	0.263D 14	0.240D 14	0.216D 14	0.191D 14	0.162D 14	0.117D 14	0.877D 13
10	0.306D 14	0.285D 14	0.252D 14	0.234D 14	0.211D 14	0.188D 14	0.165D 14	0.142D 14	0.105D 14	0.795D 13
11	0.272D 14	0.252D 14	0.220D 14	0.202D 14	0.180D 14	0.160D 14	0.139D 14	0.120D 14	0.927D 13	0.709D 13
12	0.250D 14	0.229D 14	0.198D 14	0.181D 14	0.160D 14	0.141D 14	0.123D 14	0.107D 14	0.845D 13	0.642D 13
13	0.236D 14	0.215D 14	0.184D 14	0.168D 14	0.148D 14	0.130D 14	0.114D 14	0.994D 13	0.791D 13	0.602D 13
14	0.222D 14	0.202D 14	0.171D 14	0.156D 14	0.137D 14	0.120D 14	0.105D 14	0.919D 13	0.738D 13	0.563D 13
15	0.196D 14	0.176D 14	0.148D 14	0.134D 14	0.116D 14	0.102D 14	0.891D 13	0.789D 13	0.642D 13	0.492D 13
16	0.171D 14	0.153D 14	0.127D 14	0.114D 14	0.990D 13	0.864D 13	0.758D 13	0.684D 13	0.557D 13	0.428D 13
17	0.161D 14	0.143D 14	0.119D 14	0.106D 14	0.921D 13	0.804D 13	0.708D 13	0.641D 13	0.519D 13	0.402D 13
18	0.137D 14	0.122D 14	0.101D 14	0.899D 13	0.778D 13	0.681D 13	0.604D 13	0.549D 13	0.443D 13	0.345D 13
19	0.116D 14	0.103D 14	0.848D 13	0.757D 13	0.655D 13	0.577D 13	0.520D 13	0.471D 13	0.377D 13	0.296D 13
20	0.962D 13	0.858D 13	0.710D 13	0.637D 13	0.556D 13	0.496D 13	0.448D 13	0.401D 13	0.321D 13	0.253D 13
21	0.731D 13	0.655D 13	0.548D 13	0.498D 13	0.446D 13	0.402D 13	0.360D 13	0.319D 13	0.255D 13	0.201D 13
22	0.551D 13	0.500D 13	0.429D 13	0.395D 13	0.358D 13	0.319D 13	0.284D 13	0.252D 13	0.202D 13	0.159D 13
23	0.424D 13	0.393D 13	0.345D 13	0.319D 13	0.286D 13	0.252D 13	0.223D 13	0.199D 13	0.159D 13	0.126D 13
24	0.369D 13	0.343D 13	0.300D 13	0.274D 13	0.244D 13	0.217D 13	0.192D 13	0.170D 13	0.137D 13	0.108D 13
25	0.317D 13	0.293D 13	0.256D 13	0.235D 13	0.209D 13	0.185D 13	0.164D 13	0.146D 13	0.117D 13	0.917D 12
26	0.287D 13	0.264D 13	0.230D 13	0.211D 13	0.188D 13	0.167D 13	0.148D 13	0.131D 13	0.105D 13	0.822D 12
27	0.208D 13	0.192D 13	0.167D 13	0.154D 13	0.137D 13	0.122D 13	0.108D 13	0.962D 12	0.769D 12	0.598D 12
28	0.149D 13	0.138D 13	0.121D 13	0.111D 13	0.998D 12	0.889D 12	0.788D 12	0.700D 12	0.556D 12	0.432D 12
29	0.117D 13	0.109D 13	0.957D 12	0.883D 12	0.791D 12	0.701D 12	0.620D 12	0.551D 12	0.438D 12	0.342D 12
30	0.958D 12	0.890D 12	0.783D 12	0.723D 12	0.648D 12	0.573D 12	0.506D 12	0.449D 12	0.357D 12	0.280D 12
31	0.599D 12	0.558D 12	0.492D 12	0.454D 12	0.405D 12	0.358D 12	0.316D 12	0.281D 12	0.223D 12	0.176D 12
32	0.306D 12	0.285D 12	0.252D 12	0.233D 12	0.209D 12	0.187D 12	0.166D 12	0.148D 12	0.118D 12	0.926D 11
33	0.209D 12	0.195D 12	0.173D 12	0.160D 12	0.144D 12	0.129D 12	0.115D 12	0.102D 12	0.811D 11	0.632D 11
34	0.543D 11	0.506D 11	0.445D 11	0.409D 11	0.362D 11	0.315D 11	0.267D 11	0.220D 11	0.124D 11	0.506D 08
35	0.383D 10	0.522D 08	0.791D 07	0.717D 07	0.635D 07	0.553D 07	0.469D 07	0.386D 07	0.217D 07	0.439D 04
36	0.0	0.0	0.0	0.0	0.0	0.0	0.0	0.0	0.0	0.0

POINTWISE FLUX - GROUP 2 - PLANE 5

	30	31	32	33	34	35	36	37
0	0.825D 13	0.669D 13	0.410D 13	0.213D 13	0.143D 13	0.369D 12	0.798D 11	0.0
1	0.824D 13	0.668D 13	0.410D 13	0.213D 13	0.143D 13	0.368D 12	0.797D 11	0.0
2	0.820D 13	0.666D 13	0.408D 13	0.212D 13	0.142D 13	0.367D 12	0.795D 11	0.0
3	0.812D 13	0.659D 13	0.404D 13	0.210D 13	0.141D 13	0.365D 12	0.790D 11	0.0
4	0.809D 13	0.656D 13	0.403D 13	0.209D 13	0.141D 13	0.364D 12	0.788D 11	0.0
5	0.804D 13	0.653D 13	0.401D 13	0.208D 13	0.140D 13	0.362D 12	0.785D 11	0.0
6	0.780D 13	0.633D 13	0.389D 13	0.203D 13	0.137D 13	0.355D 12	0.769D 11	0.0
7	0.746D 13	0.607D 13	0.374D 13	0.196D 13	0.132D 13	0.345D 12	0.748D 11	0.0
8	0.703D 13	0.574D 13	0.356D 13	0.187D 13	0.127D 13	0.333D 12	0.721D 11	0.0
9	0.693D 13	0.565D 13	0.351D 13	0.185D 13	0.125D 13	0.330D 12	0.714D 11	0.0
10	0.632D 13	0.519D 13	0.325D 13	0.173D 13	0.118D 13	0.312D 12	0.674D 11	0.0
11	0.567D 13	0.468D 13	0.296D 13	0.159D 13	0.109D 13	0.292D 12	0.627D 11	0.0
12	0.519D 13	0.431D 13	0.276D 13	0.149D 13	0.103D 13	0.276D 12	0.589D 11	0.0
13	0.489D 13	0.407D 13	0.262D 13	0.143D 13	0.984D 12	0.266D 12	0.562D 11	0.0
14	0.459D 13	0.384D 13	0.248D 13	0.136D 13	0.941D 12	0.256D 12	0.534D 11	0.0
15	0.404D 13	0.339D 13	0.222D 13	0.123D 13	0.856D 12	0.235D 12	0.473D 11	0.0
16	0.353D 13	0.298D 13	0.197D 13	0.110D 13	0.773D 12	0.214D 12	0.401D 11	0.0
17	0.332D 13	0.281D 13	0.187D 13	0.105D 13	0.737D 12	0.205D 12	0.366D 11	0.0
18	0.287D 13	0.244D 13	0.164D 13	0.929D 12	0.657D 12	0.184D 12	0.272D 11	0.0
19	0.247D 13	0.211D 13	0.143D 13	0.816D 12	0.581D 12	0.164D 12	0.155D 11	0.0
20	0.212D 13	0.182D 13	0.124D 13	0.711D 12	0.509D 12	0.145D 12	0.144D 09	0.0
21	0.169D 13	0.146D 13	0.991D 12	0.572D 12	0.416D 12	0.119D 12	0.211D 08	0.0
22	0.134D 13	0.116D 13	0.787D 12	0.458D 12	0.336D 12	0.969D 11	0.170D 08	0.0
23	0.106D 13	0.910D 12	0.620D 12	0.363D 12	0.269D 12	0.766D 11	0.134D 08	0.0
24	0.968D 12	0.779D 12	0.532D 12	0.313D 12	0.232D 12	0.648D 11	0.114D 08	0.0
25	0.770D 12	0.661D 12	0.455D 12	0.269D 12	0.199D 12	0.535D 11	0.938D 07	0.0
26	0.690D 12	0.593D 12	0.409D 12	0.242D 12	0.180D 12	0.461D 11	0.808D 07	0.0
27	0.501D 12	0.431D 12	0.299D 12	0.178D 12	0.132D 12	0.246D 11	0.431D 07	0.0
28	0.362D 12	0.311D 12	0.216D 12	0.129D 12	0.945D 11	0.938D 08	0.833D 04	0.0
29	0.287D 12	0.247D 12	0.172D 12	0.102D 12	0.747D 11	0.666D 07	0.406D 01	0.0
30	0.235D 12	0.203D 12	0.141D 12	0.837D 11	0.609D 11	0.534D 07	0.318D 01	0.0
31	0.148D 12	0.128D 12	0.889D 11	0.516D 11	0.367D 11	0.322D 07	0.192D 01	0.0
32	0.778D 11	0.668D 11	0.455D 11	0.231D 11	0.132D 11	0.116D 07	0.690D 00	0.0
33	0.529D 11	0.452D 11	0.299D 11	0.118D 11	0.110D 08	0.294D 03	0.177D-03	0.0
34	0.469D 07	0.396D 07	0.262D 07	0.104D 07	0.274D 03	0.253D-03	0.230D-09	0.0
35	0.284D 01	0.236D 01	0.156D 01	0.616D 00	0.165D-03	0.224D-09	0.270D-15	0.0
36	0.0	0.0	0.0	0.0	0.0	0.0	0.0	0.0

POINTWISE FLUX - GROUP 3 - PLANE 5

	0	1	2	3	4	5	6	7	8	9
0	0.693D 14	0.700D 14	0.723D 14	0.782D 14	0.847D 14	0.918D 14	0.928D 14	0.926D 14	0.910D 14	0.905D 14
1	0.700D 14	0.707D 14	0.730D 14	0.787D 14	0.850D 14	0.918D 14	0.923D 14	0.920D 14	0.901D 14	0.895D 14
2	0.723D 14	0.730D 14	0.750D 14	0.803D 14	0.860D 14	0.916D 14	0.908D 14	0.901D 14	0.873D 14	0.866D 14
3	0.781D 14	0.786D 14	0.803D 14	0.845D 14	0.884D 14	0.911D 14	0.874D 14	0.854D 14	0.804D 14	0.793D 14
4	0.812D 14	0.817D 14	0.831D 14	0.865D 14	0.892D 14	0.910D 14	0.861D 14	0.831D 14	0.773D 14	0.761D 14
5	0.845D 14	0.849D 14	0.860D 14	0.885D 14	0.902D 14	0.908D 14	0.847D 14	0.810D 14	0.746D 14	0.733D 14
6	0.911D 14	0.912D 14	0.917D 14	0.924D 14	0.924D 14	0.901D 14	0.812D 14	0.766D 14	0.690D 14	0.675D 14
7	0.894D 14	0.896D 14	0.901D 14	0.911D 14	0.914D 14	0.896D 14	0.812D 14	0.768D 14	0.695D 14	0.679D 14
8	0.794D 14	0.799D 14	0.813D 14	0.847D 14	0.873D 14	0.894D 14	0.850D 14	0.820D 14	0.764D 14	0.751D 14
9	0.757D 14	0.762D 14	0.779D 14	0.821D 14	0.863D 14	0.894D 14	0.863D 14	0.845D 14	0.799D 14	0.786D 14
10	0.671D 14	0.678D 14	0.700D 14	0.757D 14	0.821D 14	0.896D 14	0.912D 14	0.912D 14	0.898D 14	0.890D 14
11	0.673D 14	0.680D 14	0.702D 14	0.758D 14	0.821D 14	0.898D 14	0.925D 14	0.928D 14	0.922D 14	0.910D 14
12	0.731D 14	0.737D 14	0.754D 14	0.798D 14	0.843D 14	0.898D 14	0.918D 14	0.919D 14	0.912D 14	0.898D 14
13	0.795D 14	0.799D 14	0.810D 14	0.836D 14	0.858D 14	0.892D 14	0.905D 14	0.906D 14	0.898D 14	0.882D 14
14	0.834D 14	0.836D 14	0.841D 14	0.853D 14	0.862D 14	0.879D 14	0.885D 14	0.885D 14	0.878D 14	0.862D 14
15	0.849D 14	0.847D 14	0.844D 14	0.837D 14	0.831D 14	0.819D 14	0.815D 14	0.815D 14	0.818D 14	0.813D 14
16	0.815D 14	0.810D 14	0.797D 14	0.766D 14	0.739D 14	0.693D 14	0.684D 14	0.688D 14	0.722D 14	0.748D 14
17	0.795D 14	0.789D 14	0.771D 14	0.725D 14	0.673D 14	0.607D 14	0.597D 14	0.604D 14	0.660D 14	0.718D 14
18	0.750D 14	0.741D 14	0.716D 14	0.653D 14	0.585D 14	0.506D 14	0.496D 14	0.505D 14	0.580D 14	0.669D 14
19	0.730D 14	0.722D 14	0.697D 14	0.636D 14	0.571D 14	0.494D 14	0.486D 14	0.495D 14	0.572D 14	0.663D 14
20	0.739D 14	0.733D 14	0.716D 14	0.673D 14	0.630D 14	0.569D 14	0.562D 14	0.570D 14	0.632D 14	0.695D 14
21	0.773D 14	0.771D 14	0.765D 14	0.751D 14	0.740D 14	0.720D 14	0.716D 14	0.718D 14	0.736D 14	0.753D 14
22	0.778D 14	0.777D 14	0.775D 14	0.770D 14	0.766D 14	0.757D 14	0.753D 14	0.753D 14	0.754D 14	0.756D 14
23	0.745D 14	0.745D 14	0.744D 14	0.742D 14	0.739D 14	0.734D 14	0.728D 14	0.727D 14	0.722D 14	0.718D 14
24	0.711D 14	0.711D 14	0.710D 14	0.708D 14	0.707D 14	0.702D 14	0.695D 14	0.694D 14	0.686D 14	0.681D 14
25	0.669D 14	0.669D 14	0.668D 14	0.666D 14	0.665D 14	0.660D 14	0.654D 14	0.652D 14	0.643D 14	0.637D 14
26	0.638D 14	0.637D 14	0.637D 14	0.635D 14	0.634D 14	0.629D 14	0.623D 14	0.621D 14	0.612D 14	0.605D 14
27	0.534D 14	0.534D 14	0.533D 14	0.532D 14	0.531D 14	0.527D 14	0.522D 14	0.520D 14	0.512D 14	0.507D 14
28	0.450D 14	0.450D 14	0.449D 14	0.448D 14	0.447D 14	0.444D 14	0.440D 14	0.438D 14	0.433D 14	0.428D 14
29	0.401D 14	0.401D 14	0.401D 14	0.400D 14	0.399D 14	0.396D 14	0.393D 14	0.391D 14	0.386D 14	0.383D 14
30	0.364D 14	0.364D 14	0.364D 14	0.363D 14	0.362D 14	0.359D 14	0.356D 14	0.355D 14	0.350D 14	0.347D 14
31	0.288D 14	0.288D 14	0.287D 14	0.287D 14	0.286D 14	0.284D 14	0.282D 14	0.281D 14	0.277D 14	0.274D 14
32	0.205D 14	0.205D 14	0.205D 14	0.204D 14	0.204D 14	0.203D 14	0.201D 14	0.200D 14	0.197D 14	0.195D 14
33	0.168D 14	0.168D 14	0.167D 14	0.167D 14	0.167D 14	0.166D 14	0.164D 14	0.163D 14	0.161D 14	0.160D 14
34	0.743D 13	0.743D 13	0.742D 13	0.740D 13	0.738D 13	0.733D 13	0.725D 13	0.722D 13	0.712D 13	0.704D 13
35	0.217D 13	0.217D 13	0.216D 13	0.216D 13	0.215D 13	0.213D 13	0.210D 13	0.209D 13	0.205D 13	0.201D 13
36	0.0	0.0	0.0	0.0	0.0	0.0	0.0	0.0	0.0	0.0

POINTWISE FLUX - GROUP 3 - PLANE 5

	10	11	12	13	14	15	16	17	18	19
0	0.910D 14	0.925D 14	0.943D 14	0.946D 14	0.934D 14	0.898D 14	0.857D 14	0.831D 14	0.774D 14	0.741D 14
1	0.901D 14	0.918D 14	0.939D 14	0.943D 14	0.932D 14	0.895D 14	0.852D 14	0.824D 14	0.765D 14	0.733D 14
2	0.874D 14	0.898D 14	0.928D 14	0.935D 14	0.926D 14	0.886D 14	0.836D 14	0.804D 14	0.739D 14	0.707D 14
3	0.806D 14	0.848D 14	0.904D 14	0.919D 14	0.913D 14	0.866D 14	0.801D 14	0.755D 14	0.673D 14	0.643D 14
4	0.775D 14	0.826D 14	0.896D 14	0.914D 14	0.909D 14	0.859D 14	0.787D 14	0.732D 14	0.643D 14	0.615D 14
5	0.748D 14	0.804D 14	0.886D 14	0.907D 14	0.903D 14	0.850D 14	0.769D 14	0.698D 14	0.601D 14	0.574D 14
6	0.692D 14	0.755D 14	0.856D 14	0.882D 14	0.880D 14	0.817D 14	0.716D 14	0.627D 14	0.519D 14	0.495D 14
7	0.695D 14	0.755D 14	0.849D 14	0.873D 14	0.869D 14	0.805D 14	0.704D 14	0.616D 14	0.510D 14	0.490D 14
8	0.761D 14	0.804D 14	0.863D 14	0.875D 14	0.864D 14	0.810D 14	0.731D 14	0.662D 14	0.573D 14	0.557D 14
9	0.793D 14	0.824D 14	0.866D 14	0.875D 14	0.862D 14	0.811D 14	0.740D 14	0.684D 14	0.602D 14	0.586D 14
10	0.881D 14	0.876D 14	0.867D 14	0.859D 14	0.837D 14	0.809D 14	0.783D 14	0.768D 14	0.742D 14	0.738D 14
11	0.888D 14	0.855D 14	0.804D 14	0.778D 14	0.746D 14	0.738D 14	0.751D 14	0.762D 14	0.787D 14	0.804D 14
12	0.865D 14	0.811D 14	0.710D 14	0.659D 14	0.614D 14	0.623D 14	0.673D 14	0.720D 14	0.787D 14	0.821D 14
13	0.846D 14	0.781D 14	0.655D 14	0.596D 14	0.549D 14	0.563D 14	0.627D 14	0.692D 14	0.782D 14	0.825D 14
14	0.826D 14	0.757D 14	0.621D 14	0.559D 14	0.511D 14	0.529D 14	0.600D 14	0.674D 14	0.777D 14	0.825D 14
15	0.788D 14	0.729D 14	0.603D 14	0.545D 14	0.501D 14	0.523D 14	0.595D 14	0.669D 14	0.773D 14	0.822D 14
16	0.758D 14	0.732D 14	0.654D 14	0.611D 14	0.579D 14	0.597D 14	0.655D 14	0.709D 14	0.784D 14	0.818D 14
17	0.747D 14	0.740D 14	0.697D 14	0.673D 14	0.650D 14	0.665D 14	0.704D 14	0.734D 14	0.789D 14	0.815D 14
18	0.732D 14	0.756D 14	0.759D 14	0.756D 14	0.750D 14	0.757D 14	0.771D 14	0.780D 14	0.800D 14	0.806D 14
19	0.734D 14	0.772D 14	0.789D 14	0.793D 14	0.795D 14	0.795D 14	0.797D 14	0.798D 14	0.797D 14	0.798D 14
20	0.749D 14	0.782D 14	0.800D 14	0.805D 14	0.806D 14	0.802D 14	0.796D 14	0.792D 14	0.779D 14	0.761D 14
21	0.771D 14	0.784D 14	0.790D 14	0.790D 14	0.785D 14	0.774D 14	0.762D 14	0.754D 14	0.732D 14	0.706D 14
22	0.758D 14	0.757D 14	0.753D 14	0.748D 14	0.736D 14	0.720D 14	0.705D 14	0.694D 14	0.668D 14	0.638D 14
23	0.712D 14	0.704D 14	0.693D 14	0.686D 14	0.669D 14	0.649D 14	0.632D 14	0.620D 14	0.592D 14	0.563D 14
24	0.672D 14	0.662D 14	0.649D 14	0.640D 14	0.622D 14	0.599D 14	0.581D 14	0.570D 14	0.546D 14	0.521D 14
25	0.627D 14	0.615D 14	0.600D 14	0.591D 14	0.573D 14	0.552D 14	0.536D 14	0.527D 14	0.505D 14	0.483D 14
26	0.594D 14	0.580D 14	0.565D 14	0.556D 14	0.539D 14	0.522D 14	0.508D 14	0.499D 14	0.479D 14	0.459D 14
27	0.499D 14	0.490D 14	0.479D 14	0.473D 14	0.460D 14	0.446D 14	0.435D 14	0.428D 14	0.412D 14	0.396D 14
28	0.422D 14	0.416D 14	0.408D 14	0.403D 14	0.393D 14	0.382D 14	0.372D 14	0.367D 14	0.353D 14	0.339D 14
29	0.377D 14	0.371D 14	0.364D 14	0.360D 14	0.351D 14	0.341D 14	0.333D 14	0.328D 14	0.316D 14	0.303D 14
30	0.342D 14	0.337D 14	0.330D 14	0.326D 14	0.318D 14	0.310D 14	0.302D 14	0.298D 14	0.287D 14	0.275D 14
31	0.271D 14	0.266D 14	0.261D 14	0.258D 14	0.251D 14	0.244D 14	0.238D 14	0.234D 14	0.225D 14	0.216D 14
32	0.193D 14	0.189D 14	0.185D 14	0.183D 14	0.178D 14	0.172D 14	0.167D 14	0.164D 14	0.157D 14	0.150D 14
33	0.157D 14	0.155D 14	0.151D 14	0.149D 14	0.145D 14	0.141D 14	0.137D 14	0.134D 14	0.129D 14	0.123D 14
34	0.692D 13	0.680D 13	0.663D 13	0.653D 13	0.633D 13	0.610D 13	0.591D 13	0.579D 13	0.549D 13	0.518D 13
35	0.197D 13	0.191D 13	0.183D 13	0.178D 13	0.168D 13	0.155D 13	0.142D 13	0.133D 13	0.110D 13	0.781D 12
36	0.0	0.0	0.0	0.0	0.0	0.0	0.0	0.0	0.0	0.0

POINTWISE FLUX - GROUP 3 - PLANE 5

	20	21	22	23	24	25	26	27	28	29
0	0.731D 14	0.724D 14	0.695D 14	0.665D 14	0.626D 14	0.603D 14	0.598D 14	0.598D 14	0.567D 14	0.512D 14
1	0.725D 14	0.720D 14	0.691D 14	0.660D 14	0.619D 14	0.597D 14	0.594D 14	0.596D 14	0.566D 14	0.512D 14
2	0.706D 14	0.707D 14	0.680D 14	0.644D 14	0.600D 14	0.579D 14	0.582D 14	0.591D 14	0.565D 14	0.511D 14
3	0.660D 14	0.680D 14	0.656D 14	0.606D 14	0.552D 14	0.533D 14	0.551D 14	0.579D 14	0.562D 14	0.510D 14
4	0.640D 14	0.670D 14	0.649D 14	0.589D 14	0.531D 14	0.513D 14	0.538D 14	0.575D 14	0.561D 14	0.509D 14
5	0.612D 14	0.659D 14	0.639D 14	0.573D 14	0.512D 14	0.496D 14	0.524D 14	0.571D 14	0.560D 14	0.509D 14
6	0.550D 14	0.622D 14	0.613D 14	0.540D 14	0.476D 14	0.461D 14	0.497D 14	0.558D 14	0.555D 14	0.505D 14
7	0.548D 14	0.623D 14	0.620D 14	0.549D 14	0.486D 14	0.470D 14	0.504D 14	0.560D 14	0.552D 14	0.501D 14
8	0.606D 14	0.665D 14	0.661D 14	0.606D 14	0.548D 14	0.527D 14	0.547D 14	0.577D 14	0.552D 14	0.497D 14
9	0.630D 14	0.678D 14	0.673D 14	0.629D 14	0.577D 14	0.554D 14	0.564D 14	0.582D 14	0.552D 14	0.496D 14
10	0.750D 14	0.758D 14	0.743D 14	0.717D 14	0.678D 14	0.647D 14	0.626D 14	0.607D 14	0.552D 14	0.490D 14
11	0.812D 14	0.811D 14	0.789D 14	0.766D 14	0.729D 14	0.691D 14	0.654D 14	0.616D 14	0.547D 14	0.481D 14
12	0.833D 14	0.830D 14	0.806D 14	0.783D 14	0.745D 14	0.704D 14	0.660D 14	0.614D 14	0.540D 14	0.474D 14
13	0.839D 14	0.836D 14	0.811D 14	0.788D 14	0.749D 14	0.706D 14	0.659D 14	0.611D 14	0.535D 14	0.468D 14
14	0.841D 14	0.838D 14	0.812D 14	0.788D 14	0.749D 14	0.704D 14	0.656D 14	0.605D 14	0.529D 14	0.462D 14
15	0.836D 14	0.832D 14	0.804D 14	0.779D 14	0.738D 14	0.691D 14	0.641D 14	0.590D 14	0.514D 14	0.448D 14
16	0.824D 14	0.817D 14	0.785D 14	0.758D 14	0.716D 14	0.669D 14	0.616D 14	0.569D 14	0.496D 14	0.432D 14
17	0.818D 14	0.808D 14	0.774D 14	0.747D 14	0.704D 14	0.657D 14	0.604D 14	0.559D 14	0.488D 14	0.425D 14
18	0.797D 14	0.782D 14	0.744D 14	0.715D 14	0.671D 14	0.625D 14	0.575D 14	0.534D 14	0.467D 14	0.406D 14
19	0.770D 14	0.750D 14	0.708D 14	0.677D 14	0.631D 14	0.587D 14	0.544D 14	0.507D 14	0.445D 14	0.387D 14
20	0.736D 14	0.713D 14	0.667D 14	0.636D 14	0.592D 14	0.551D 14	0.513D 14	0.480D 14	0.421D 14	0.366D 14
21	0.675D 14	0.649D 14	0.601D 14	0.573D 14	0.535D 14	0.502D 14	0.469D 14	0.439D 14	0.387D 14	0.336D 14
22	0.604D 14	0.578D 14	0.537D 14	0.514D 14	0.484D 14	0.455D 14	0.426D 14	0.400D 14	0.352D 14	0.306D 14
23	0.535D 14	0.514D 14	0.480D 14	0.461D 14	0.435D 14	0.410D 14	0.385D 14	0.361D 14	0.318D 14	0.276D 14
24	0.497D 14	0.478D 14	0.448D 14	0.430D 14	0.407D 14	0.383D 14	0.359D 14	0.337D 14	0.297D 14	0.258D 14
25	0.461D 14	0.445D 14	0.418D 14	0.401D 14	0.379D 14	0.357D 14	0.335D 14	0.314D 14	0.276D 14	0.238D 14
26	0.439D 14	0.424D 14	0.398D 14	0.383D 14	0.361D 14	0.340D 14	0.319D 14	0.299D 14	0.263D 14	0.226D 14
27	0.379D 14	0.366D 14	0.344D 14	0.330D 14	0.312D 14	0.294D 14	0.275D 14	0.258D 14	0.226D 14	0.193D 14
28	0.325D 14	0.313D 14	0.294D 14	0.283D 14	0.267D 14	0.251D 14	0.235D 14	0.219D 14	0.191D 14	0.164D 14
29	0.290D 14	0.280D 14	0.263D 14	0.252D 14	0.237D 14	0.222D 14	0.207D 14	0.193D 14	0.168D 14	0.145D 14
30	0.263D 14	0.254D 14	0.238D 14	0.228D 14	0.214D 14	0.200D 14	0.186D 14	0.174D 14	0.151D 14	0.130D 14
31	0.206D 14	0.199D 14	0.186D 14	0.178D 14	0.167D 14	0.155D 14	0.144D 14	0.134D 14	0.117D 14	0.100D 14
32	0.143D 14	0.137D 14	0.128D 14	0.123D 14	0.115D 14	0.107D 14	0.997D 13	0.926D 13	0.797D 13	0.675D 13
33	0.117D 14	0.113D 14	0.105D 14	0.100D 14	0.938D 13	0.874D 13	0.810D 13	0.748D 13	0.637D 13	0.529D 13
34	0.485D 13	0.459D 13	0.416D 13	0.389D 13	0.352D 13	0.312D 13	0.268D 13	0.223D 13	0.126D 13	0.420D 10
35	0.391D 12	0.444D 10	0.633D 09	0.585D 09	0.528D 09	0.468D 09	0.403D 09	0.335D 09	0.189D 09	0.318D 06
36	0.0	0.0	0.0	0.0	0.0	0.0	0.0	0.0	0.0	0.0

POINTWISE FLUX - GROUP 3 - PLANE 5

	30	31	32	33	34	35	36	37
0	0.472D 14	0.438D 14	0.360D 14	0.265D 14	0.220D 14	0.992D 13	0.290D 13	0.0
1	0.472D 14	0.438D 14	0.360D 14	0.265D 14	0.220D 14	0.992D 13	0.290D 13	0.0
2	0.471D 14	0.437D 14	0.359D 14	0.264D 14	0.219D 14	0.991D 13	0.290D 13	0.0
3	0.470D 14	0.436D 14	0.358D 14	0.264D 14	0.219D 14	0.988D 13	0.288D 13	0.0
4	0.470D 14	0.436D 14	0.358D 14	0.263D 14	0.218D 14	0.986D 13	0.288D 13	0.0
5	0.469D 14	0.435D 14	0.357D 14	0.263D 14	0.218D 14	0.985D 13	0.287D 13	0.0
6	0.466D 14	0.432D 14	0.355D 14	0.261D 14	0.216D 14	0.976D 13	0.284D 13	0.0
7	0.462D 14	0.428D 14	0.351D 14	0.258D 14	0.214D 14	0.963D 13	0.279D 13	0.0
8	0.457D 14	0.423D 14	0.346D 14	0.254D 14	0.211D 14	0.947D 13	0.273D 13	0.0
9	0.456D 14	0.422D 14	0.345D 14	0.253D 14	0.210D 14	0.943D 13	0.271D 13	0.0
10	0.448D 14	0.414D 14	0.338D 14	0.248D 14	0.205D 14	0.919D 13	0.261D 13	0.0
11	0.439D 14	0.404D 14	0.329D 14	0.241D 14	0.199D 14	0.890D 13	0.248D 13	0.0
12	0.431D 14	0.396D 14	0.322D 14	0.236D 14	0.195D 14	0.868D 13	0.236D 13	0.0
13	0.425D 14	0.391D 14	0.317D 14	0.232D 14	0.192D 14	0.852D 13	0.228D 13	0.0
14	0.419D 14	0.385D 14	0.312D 14	0.228D 14	0.188D 14	0.835D 13	0.219D 13	0.0
15	0.406D 14	0.372D 14	0.301D 14	0.220D 14	0.181D 14	0.799D 13	0.197D 13	0.0
16	0.391D 14	0.359D 14	0.290D 14	0.211D 14	0.174D 14	0.766D 13	0.170D 13	0.0
17	0.384D 14	0.352D 14	0.284D 14	0.207D 14	0.171D 14	0.743D 13	0.156D 13	0.0
18	0.367D 14	0.337D 14	0.271D 14	0.197D 14	0.162D 14	0.699D 13	0.117D 13	0.0
19	0.350D 14	0.320D 14	0.257D 14	0.186D 14	0.154D 14	0.654D 13	0.670D 12	0.0
20	0.331D 14	0.303D 14	0.243D 14	0.175D 14	0.145D 14	0.607D 13	0.531D 10	0.0
21	0.304D 14	0.278D 14	0.220D 14	0.158D 14	0.132D 14	0.541D 13	0.818D 09	0.0
22	0.276D 14	0.252D 14	0.199D 14	0.143D 14	0.119D 14	0.472D 13	0.710D 09	0.0
23	0.249D 14	0.227D 14	0.178D 14	0.128D 14	0.106D 14	0.401D 13	0.602D 09	0.0
24	0.232D 14	0.211D 14	0.166D 14	0.118D 14	0.978D 13	0.353D 13	0.530D 09	0.0
25	0.214D 14	0.195D 14	0.154D 14	0.109D 14	0.902D 13	0.302D 13	0.454D 09	0.0
26	0.203D 14	0.185D 14	0.146D 14	0.104D 14	0.851D 13	0.266D 13	0.400D 09	0.0
27	0.173D 14	0.157D 14	0.125D 14	0.876D 13	0.710D 13	0.148D 13	0.223D 09	0.0
28	0.146D 14	0.133D 14	0.105D 14	0.727D 13	0.579D 13	0.487D 10	0.371D 06	0.0
29	0.130D 14	0.118D 14	0.924D 13	0.634D 13	0.499D 13	0.380D 09	0.230D 03	0.0
30	0.116D 14	0.106D 14	0.827D 13	0.560D 13	0.437D 13	0.328D 09	0.195D 03	0.0
31	0.894D 13	0.808D 13	0.623D 13	0.403D 13	0.303D 13	0.228D 09	0.135D 03	0.0
32	0.596D 13	0.532D 13	0.391D 13	0.209D 13	0.121D 13	0.910D 08	0.542D 02	0.0
33	0.462D 13	0.409D 13	0.289D 13	0.118D 13	0.899D 09	0.202D 05	0.122D-01	0.0
34	0.351D 09	0.307D 09	0.217D 09	0.888D 08	0.159D 05	0.179D-01	0.160D-07	0.0
35	0.213D 03	0.183D 03	0.129D 03	0.528D 02	0.120D-01	0.160D-07	0.190D-13	0.0
36	0.0	0.0	0.0	0.0	0.0	0.0	0.0	0.0